[redacted]

UNCLASSIFIED

[redacted]

Studies in Radar Cross-Sections XIX

Radar Cross-Section of a Ballistic Missile - II

by K. M. Siegel, M. L. Barasch, H. Brysk,
J. W. Crispin, T. B. Curtz, and T. A. Kaplan

Contract AF 04(645)-33

January 1956

2428-3-T

2428-3-T = RL-2050

The University of Michigan
Engineering Research Institute
Willow Run Laboratories
Willow Run Airport
Ypsilanti, Michigan

[redacted]

UNCLASSIFIED

[redacted]

STUDIES IN RADAR CROSS-SECTIONS

I Scattering by a Prolate Spheroid, F.V. Schultz (UMM-42, March 1950), W 33(038)-ac-14222. UNCLASSIFIED

II The Zeros of the Associated Legendre Functions $P_n^m(\mu')$ of Non-Integral Degree, K.M. Siegel, D.M. Brown, H.E. Hunter, H.A. Alperin, and C.W. Quillen (UMM-82, April 1951), W 33(038)-ac-14222. UNCLASSIFIED

III Scattering by a Cone, K.M. Siegel and H.A. Alperin (UMM-87, January 1952), AF 30(602)-9. UNCLASSIFIED

IV Comparison Between Theory and Experiment of the Cross-Section of a Cone, K.M. Siegel, H.A. Alperin, J.W. Crispin, H.E. Hunter, R.E. Kleinman, W.C. Orthwein, and C.E. Schensted (UMM-92, February 1953), AF 30(602)-9. UNCLASSIFIED

V An Examination of Bistatic Early Warning Radars, K.M. Siegel (UMM-98, August 1952), W-33(038)-ac-14222. SECRET

VI Cross-Sections of Corner Reflectors and Other Multiple Scatterers at Microwave Frequencies, R.R. Bonkowski, C.R. Lubitz, and C.E. Schensted (UMM-106, October 1953), AF 30(602)-9. SECRET (UNCLASSIFIED when Appendix is removed)

VII Summary of Radar Cross-Section Studies Under Project Wizard, K.M. Siegel, J.W. Crispin, and R.E. Kleinman (UMM-108, November 1952), W 33(038)-ac-14222. SECRET

VIII Theoretical Cross-Sections as a Function of Separation Angle Between Transmitter and Receiver at Small Wavelengths, K.M. Siegel, H.A. Alperin, R.R. Bonkowski, J.W. Crispin, A.L. Maffett, C.E. Schensted, and I.V. Schensted (UMM-115, October 1953), W 33(038)-ac-14222. UNCLASSIFIED

IX Electromagnetic Scattering by an Oblate Spheroid, L.M. Rauch (UMM-116, October 1953), AF 30(602)-9. UNCLASSIFIED

X The Radar Cross-Section of a Sphere, H. Weil (2255-20-T, to be published), AF 30(602)-1070. UNCLASSIFIED

XI The Numerical Determination of the Radar Cross-Section of a Prolate Spheroid, K.M. Siegel, B.H. Gere, I. Marx, and F.B. Sleator (UMM-126, December 1953), AF 30(602)-9. UNCLASSIFIED

XII Summary of Radar Cross-Section Studies Under Project MIRO, K.M. Siegel, M.E. Anderson, R.R. Bonkowski, and W.C. Orthwein (UMM-127, December 1953), AF 30(602)-9. SECRET

XIII Description of a Dynamic Measurement Program, K.M. Siegel and J.M. Wolf (UMM-128, July 1954) W 33(038)-ac-14222. CONFIDENTIAL

XIV Radar Cross-Section of a Ballistic Missile, K.M. Siegel, M.L. Barasch, J.W. Crispin, I.V. Schensted, W.C. Orthwein, and H. Weil (UMM-134, September 1954), W 33(038)-ac-14222. SECRET

XV Radar Cross-Sections of B-47 and B-52 Aircraft, C.E. Schensted, J.W. Crispin, and K.M. Siegel (2260-1-T, August 1954), AF 33(616)-2531. CONFIDENTIAL

XVI Microwave Reflection Characteristics of Buildings, H. Weil, R.R. Bonkowski, T.A. Kaplan, and M. Leichter (2255-12-T, May 1955), AF 30(602)-1070. SECRET

XVII Complete Scattering Matrices and Circular Polarization Cross-Sections for the B-47 Aircraft at S-Band, A.L. Maffett, M.L. Barasch, W.E. Burdick, R.F. Goodrich, W.C. Orthwein, C.E. Schensted, and K.M. Siegel (2260-6-T, June 1955), AF 33(616)-2531. CONFIDENTIAL

XVIII Airborne Passive Measures and Countermeasures (Offense with, and Defense Against, Bomber Decoys (s)), K.M. Siegel, M.L. Barasch, J.W. Crispin, R.F. Goodrich, A.H. Halpin, A.L. Maffett, W.C. Orthwein, C.E. Schensted, and C.J. Titus (2260-29-F, December 1955). AF 33(616)-2531 . SECRET

XIX Radar Cross-Section of a Ballistic Missile – II, K. M. Siegel, M. L. Barasch, H. Brysk J. W. Crispin, T. B. Curtz, and T. A. Kaplan (2428-3-T, January 1956), AF 04(645)-33. SECRET

PREFACE

This paper is the nineteenth in a series of reports growing out of studies of radar cross-sections at the Willow Run Laboratories of the Engineering Research Institute of The University of Michigan. The primary aims of this program are:

1. To show that radar cross-sections can be determined analytically.
2. To elaborate means for computing cross-sections of various objects of military interest.
3. To demonstrate that these theoretical cross-sections are in agreement with experimentally determined values.

Intermediate objectives are:

1. To compute the exact theoretical cross-sections of various simple bodies by solution of the appropriate boundary-value problems arising from electromagnetic theory.
2. To examine the various approximations possible in this problem and to determine the limits of their validity and utility.
3. To find means of combining the simple-body solutions in order to determine the cross-sections of composite bodies.
4. To tabulate various formulas and functions necessary to enable such computations to be done quickly for arbitrary objects.
5. To collect, summarize, and evaluate existing experimental data.

Titles of the papers already published or presently in process of publication are listed on the preceding page.

The major portion of the studies summarized in this paper were performed under Contract No. AF 04(645)-33, a prime contract of the

Western Development Division of the Air Research and Development Command (University of Michigan Project 2428); the contract was under the technical management of the Ramo-Wooldridge Corporation. Appendix F was done under Purchase Order No. S-96527 (University of Michigan Project 2355) sponsored by the Radio Division of the Bendix Aircraft Corporation. Other work was done under Purchase Order No. 7540 (University of Michigan Project 2360) under the sponsorship of the Ramo-Wooldridge Corporation.

K. M. Siegel

TABLE OF CONTENTS

LIST OF FIGURES

LIST OF FIGURES (Cont.)

LIST OF FIGURES (Cont.)

LIST OF FIGURES (Cont.)

LIST OF FIGURES (Cont.)

LIST OF TABLES

I

INTRODUCTION AND SUMMARY

This report is a continuation of the radar cross-section study of ballistic missiles begun in Reference 1. In this report the radar cross-sections of a new ICBM for several parameterizations have been found for aspect angles out to 60 degrees off-nose, from 200 Mc through S-band. It is concluded that there are several methods, which appear to be feasible from the cross-section point of view, for significantly reducing the radar cross-section of this new warhead; future systems analysis will determine if these changes will unduly disturb the over-all system. A major point established in this report is that fission waste-products are not suitable for camouflage purposes.

The new ICBM warhead referred to above was designed as the result of studies carried out by leading experts in hydrodynamics, thermodynamics, aerodynamics, and upper-atmosphere physics under the leadership of the Ramo-Wooldridge Corporation. They felt that the third stage of an ICBM as previously designed might vaporize upon re-entry into the atmosphere. As a result, new parameterizations of the third stage of the ICBM were developed by the staff members and consultants of the Ramo-Wooldridge Corporation. The University was requested to determine the radar cross-section of these vehicles. The cross-sections determined and the analyses performed are presented in Appendix A; a brief summary of the results is presented in the body of this report (Sec. II).

Enough analysis of the countermeasure problem has been performed to indicate that, if the modifications suggested in this report are made, the radar cross-section of the new ICBM warhead will be significantly reduced. The modifications involve certain changes in the shape of the vehicle while it is out of the atmosphere, without disturbing the vehicle's geometry upon re-entry into the sensible atmosphere. It is assumed that, for effective warning, the search radars must look for the ICBM long before re-entry takes place.

Design of perturbations to Rudolph[1] to perform this function has been carried out; scale drawings of the new shapes and perturbations to them and computations of their cross-sections appear in Appendix B. It is shown there that perturbing the Rudolph shape in the proper manner can result in a reduction of the nose-on cross-section by a factor of 10^5 at S-band.

The perturbation method of reducing the detectability of Rudolph requires that the warhead be in approximately a nose-on attitude to the enemy search radar. This in turn requires knowledge of the location of the enemy search radars and means to point the warhead in the proper direction while it is in flight out of the atmosphere. There are three other methods of reducing the detectability of an ICBM which are discussed here: decoys, camouflage, and chaff.

Since the aircraft decoy problem has been studied quite thoroughly (Ref. 2), little additional work seemed necessary from the reflectivity point of view to design decoys for the ICBM with the exception of considering certain problems in the decoy field which are essentially different for aircraft in the atmosphere and for missiles out of the atmosphere. As a result, only two efforts other than the perturbation-protuberance method were made in this field. These involved the analysis of the latest proposed camouflage material for aircraft and missiles (App. C), and the possibility of the use of radioactive wastes to serve either as an ionized medium itself or as an inducer of ionization in the atmosphere (App. D). Reference 2 contains a discussion of the possibility of the defense determining the difference between decoys and aircraft. Since the same methods of differentiating decoys from aircraft are available for use in defense against missiles, and since it was felt that these problems warrant further study, these methods are summarized in Appendix E.

---

[1]Since no name had been given to the new third stage of the ICBM, the authors have coined the name Rudolph because of the "red nose" upon re-entry.

One subject discussed in Appendix E in regard to decoys is the necessity for foreseeing the possible methods available for distinguishing between decoys and actual missiles or airplanes. One proposed method uses the differences in the fine structure of the radar return (scintillation and glint) to make this distinction. Since the auto-correlation functions and power spectra associated with the radar cross-sections of ballistic missiles have not been obtained previously, and since this information might prove important in more sophisticated methods of detection, these quantities were computed using The University of Michigan drop-test data. The drop-test experiment is summarized in Reference 3; the experimental cross-section data is presented in Reference 1; and the analysis of this data which yields the power spectra and the auto-correlation functions is presented in Appendix F.

One must consider the cross-section and trajectory of the terminal propulsion unit (tanks) as compared with the cross-section and trajectory of the third stage to see if the knowledge of one will give away the location of the other. As a first step in this direction the radar cross-section of the tanks was determined. Also, some analysis was made of different ways of changing the enclosure which previously housed the third stage, in order to reduce the nose-on cross-section of the tanks. Computations for the tanks are given in Appendix G.

Additional study has been carried out on the analysis of reflections from ionic trails such as those from meteors and, since it is clear that these trails are worthy of strong consideration by the defensive people in the ICBM field, a summary of thinking on this problem and on other related topics is given in Section IV and Appendix H.

Recommendations for future research on the radar-reflection problem for offensive ICBM study appear in Section V.

II

THE RADAR CROSS-SECTION OF THE RUDOLPH MISSILE

The primary purpose in the design of the Rudolph warhead was to make sure that it would not vaporize upon re-entry into the atmosphere. It is expected that any low-drag supersonic missile traveling at the velocity of Rudolph would vaporize away upon re-entry. (Typical trajectories of an ICBM are shown in Figure 2-1.) The change in configuration was designed to produce a high-drag shape to replace the low-drag shapes previously under investigation (e.g., the 7-OC warhead). As a result, the small conical nose was replaced by a spherical one[1]. Of course, this aerodynamic difference changed the radar cross-section picture and at small wavelengths increased the cross-sections of the ICBM warhead. The detailed analysis of the cross-section work for the different parameterizations of the Warhead is given in Appendix A. For the sake of clarity and brevity, one parameterization of the six considered in Appendix A is dealt with here; this particular third stage is referred to in Appendix A as Configuration I and is presented in Figure 2-2.

In Appendix A the cross-sections of the various parameterizations of the Rudolph warhead are given out to 60 degrees off-nose for wavelengths between 10 cm and 150 cm (i.e., for frequencies between 3000 Mc and 200 Mc). For these conditions Configuration I yields the smallest cross-sections. The cross-sections of Configuration I are shown in Figure 2-3.

The cross-section of the terminal propulsion unit (the "tanks," Fig. 2-4) of Rudolph is discussed in Appendix G. Several different variations of the surface of the enclosure exposed, when the Rudolph warhead has

[1]The 7-OC warhead has a conical nose of half-angle 15 degrees. An earlier configuration, referred to in Reference 1 as the "needle-nose warhead," had a conical nose with total-angle equal to 7 degrees.

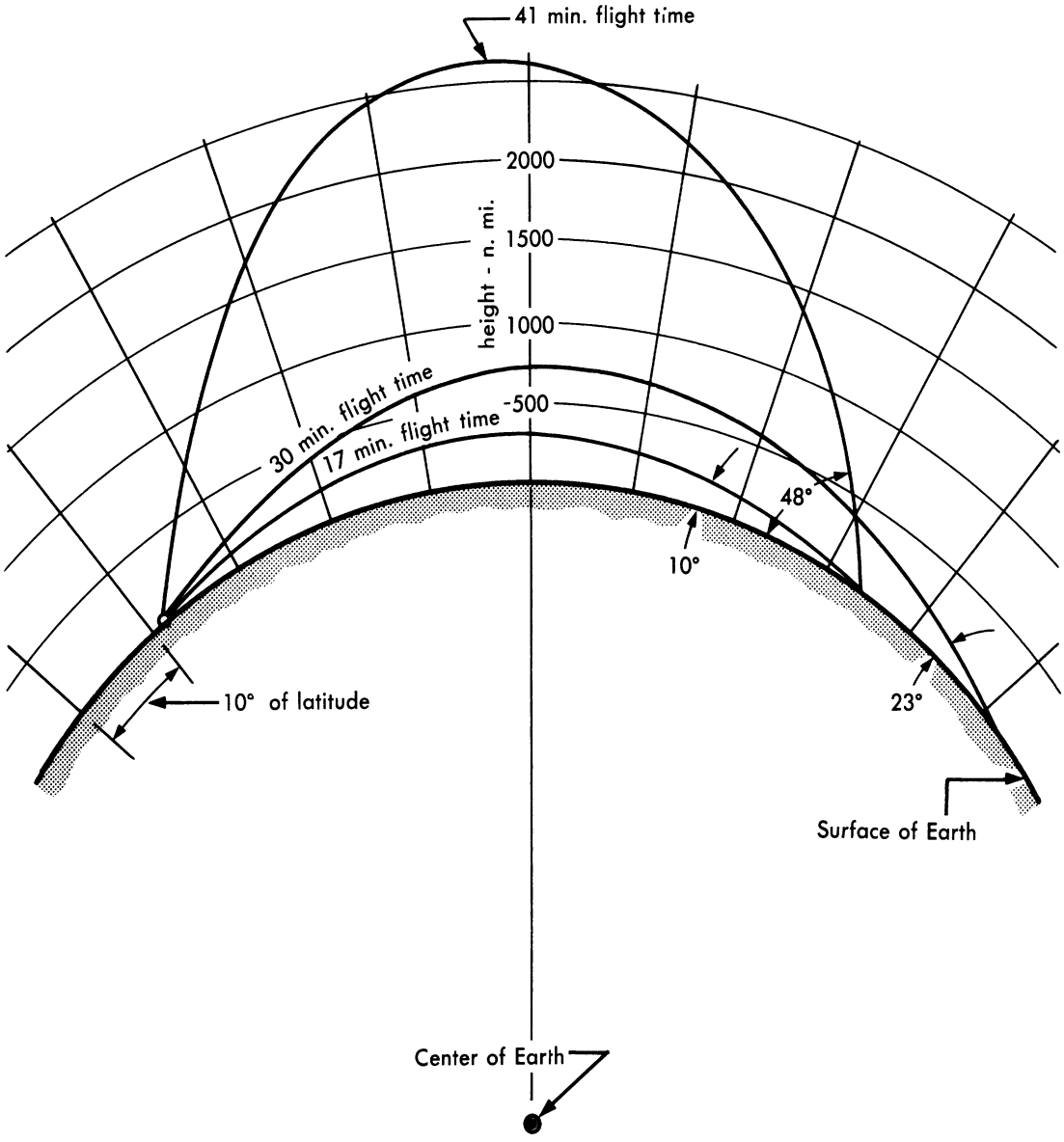

FIG. 2-1 TYPICAL TRAJECTORIES OF AN ICBM (Information for this Figure was obtained from Ref. 4)

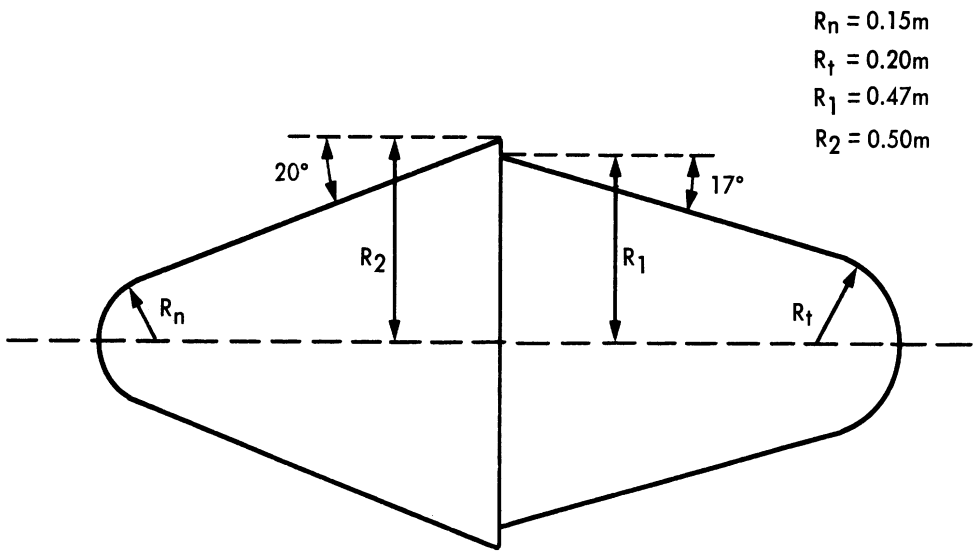

FIG. 2-2 A TYPICAL PARAMETERIZATION FOR THE RUDOLPH WARHEAD (CONFIGURATION I)

separated, are discussed. These variations are:

a. The hole filled with an absorbing material so that only a negligible contribution to the cross-section is received from the interior of the hole.

b. The hole lined on the inside with an inverted hemisphere.

c. The hole considered empty up to the end of the hat section, so that for the nose-on aspect the return from the hole would be like that from a flat plate.

d. The interior of the hole lined as the inverse of the rear portion of the warhead.

The first and last of these variations yield the smallest nose-on cross-sections.

The results (with the warhead removed) are summarized in Figure 2-5.

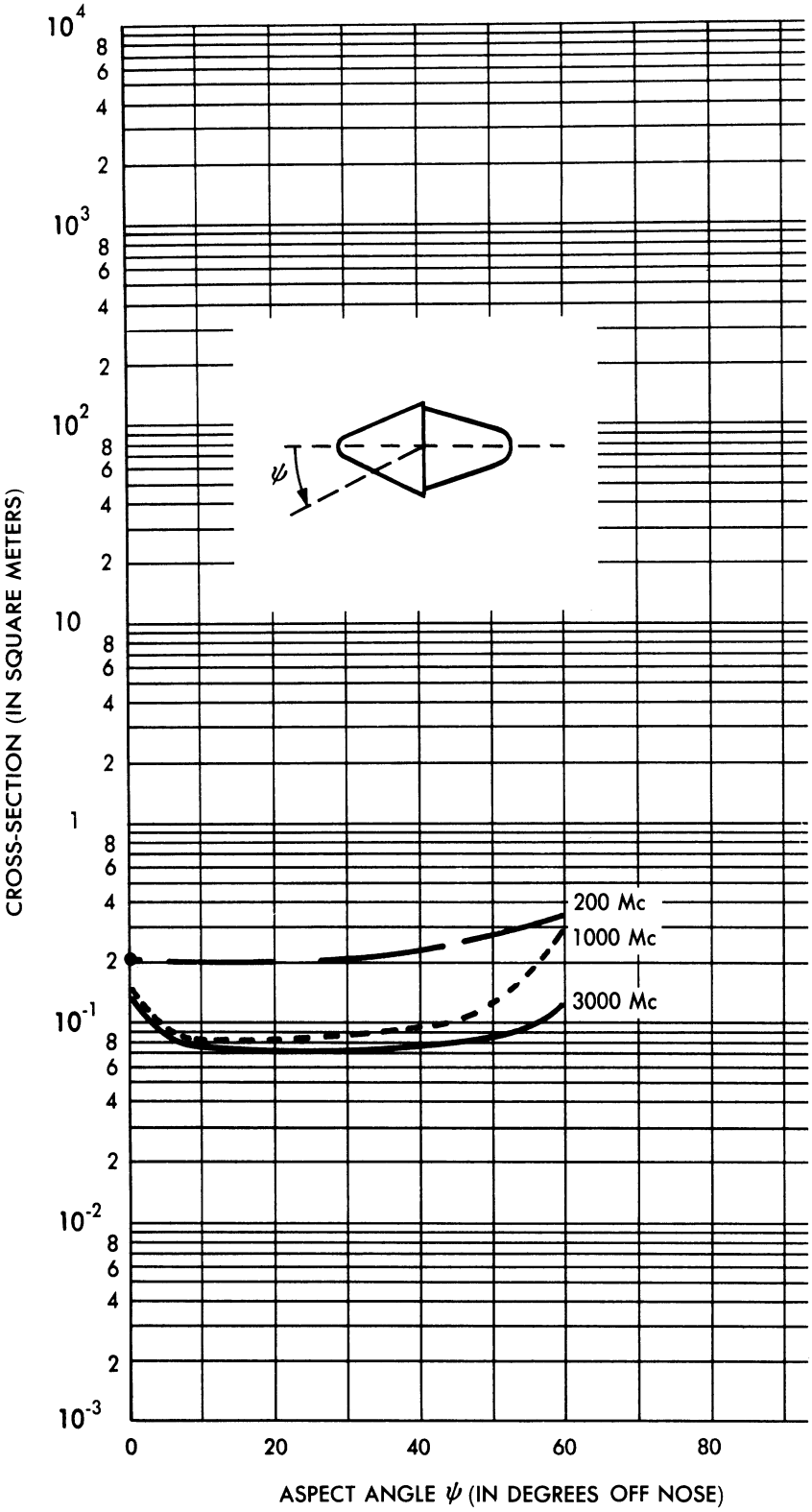

FIG. 2-3 CROSS-SECTION OF ONE OF THE PARAMETERIZATIONS FOR THE RUDOLPH WARHEAD (CONFIGURATION I) AS A FUNCTION OF ASPECT AND FREQUENCY

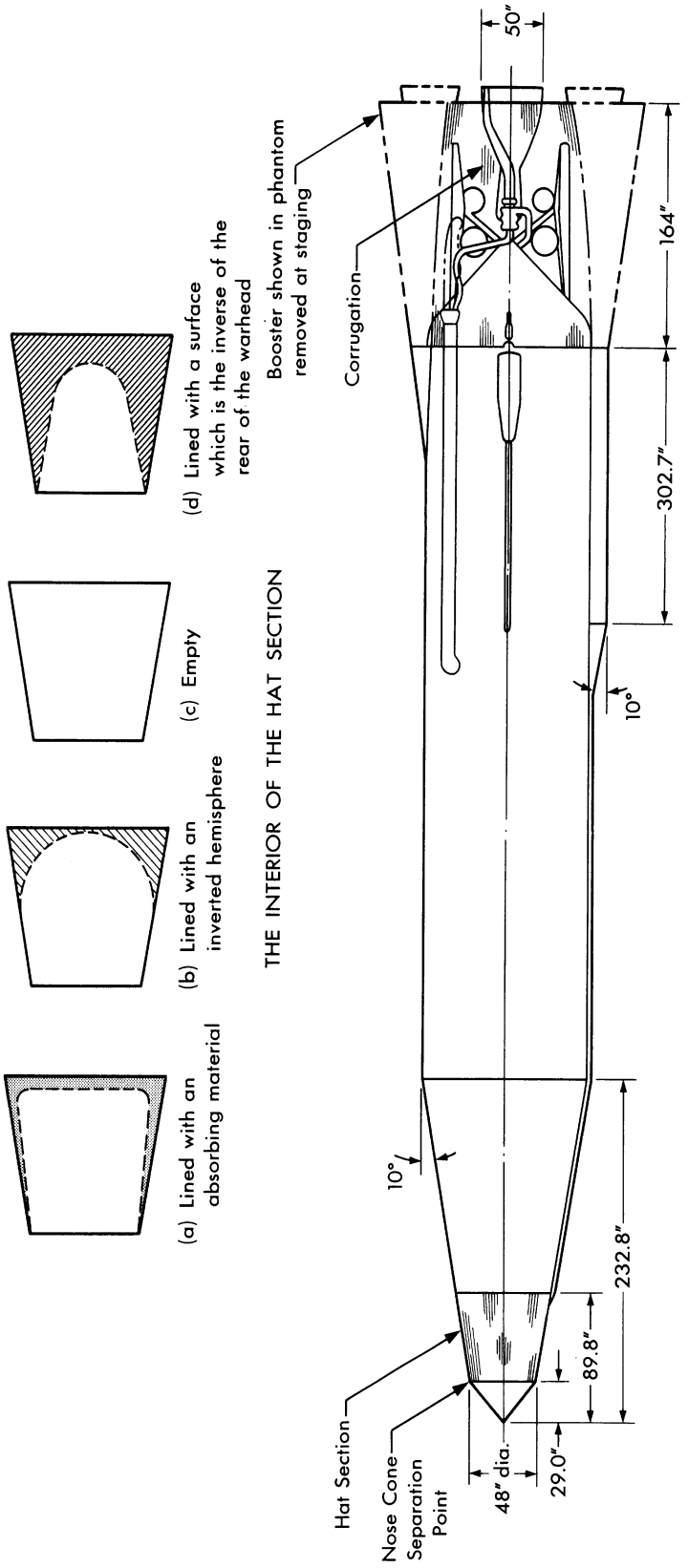

FIG. 2 - 4 THE TERMINAL PROPULSION UNIT (TANKS)
(The tanks are shown here with a nose cone rather than with one of the Rudolph parameterizations)

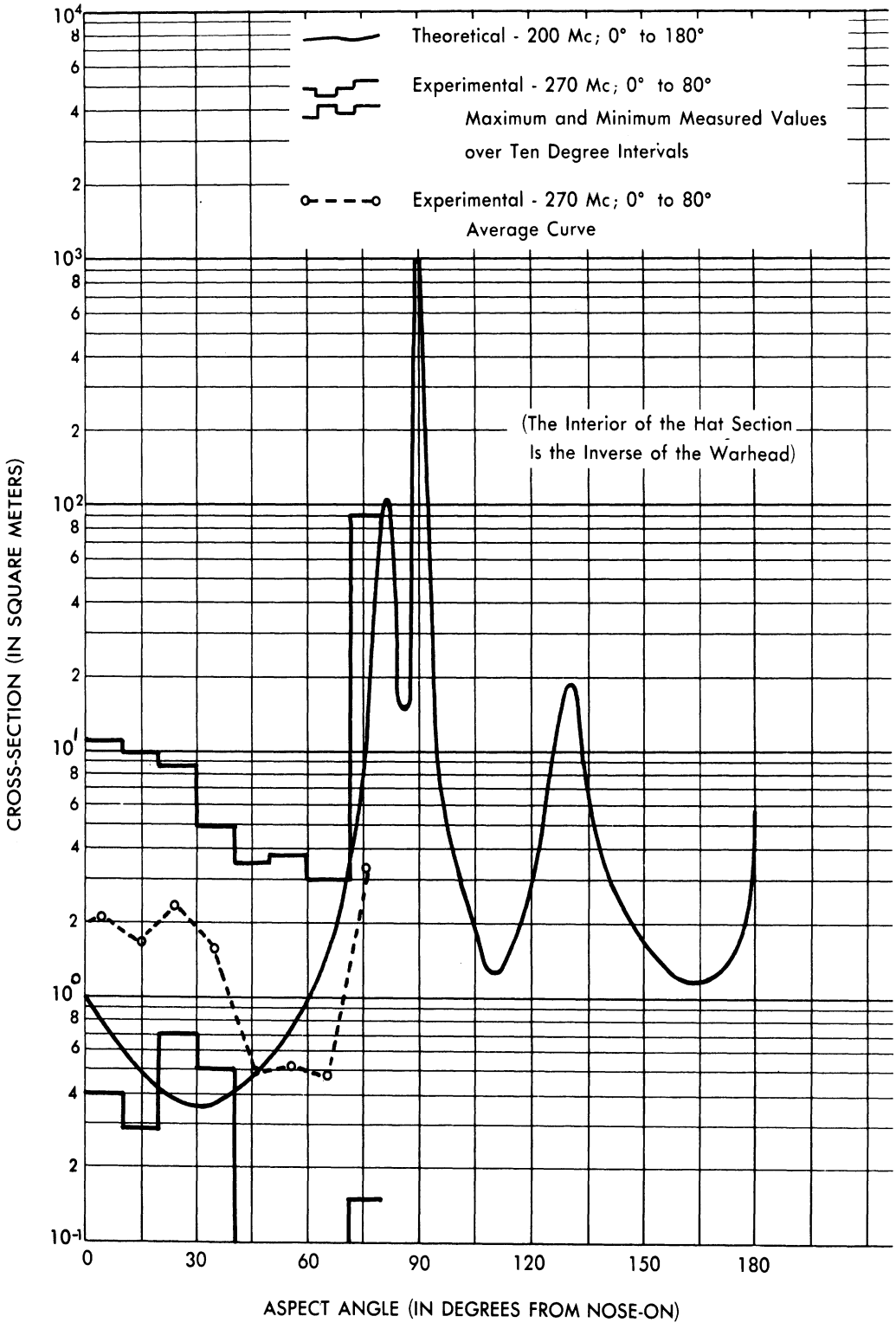

FIG. 2-5 CROSS SECTION OF THE TANKS (WARHEAD REMOVED) AT 200 & 270 Mc(See Appendix G for Details)

III

REDUCTION OF THE DETECTABILITY OF THE RUDOLPH MISSILE

There are four approaches to the problem of reducing the detectability of the Rudolph missile:

1. If it is possible to choose the orientation of the warhead with respect to the radar within certain broad limits (5 to 20 degrees) when it is out of the atmosphere, the best method available seems to be to reduce the cross-section of the Rudolph warhead by the addition of structures which will vaporize readily upon re-entry into the atmosphere, thus re-establishing the desired shape.
2. A large number of false Rudolphs could be produced so that the enemy could not discriminate between the actual warhead and the decoys.
3. Camouflage materials could be applied to reduce the cross-section of the missile.
4. The warhead could be hidden in an almost continuous column of ionized particles or in chaff.

3.1 PERTURBATION OF THE SHAPE OF THE WARHEAD

The discussion of perturbation of the shape of the warhead must be broken up into three cases:

a. The assumption that the tanks would not have to be separated from the warhead until after the search phase was ended,

b. The assumption that the tanks could be separated from the warhead by a large distance (the tanks could then be blown up), and

c. The assumption that the separation would occur, but that the tanks would remain near the warhead.

Let us consider (c) first. In that case the defense could fix its search radars on the tanks and predict the trajectory of the warhead to within small bounds. Thus perturbation of the shape of the warhead by itself is not sufficient.

Under case (b) the most economical method available for reducing the cross-section of the warhead is to put a thin sheet of tin around Rudolph (Fig. 3-1). It is expected that the tin will vaporize almost immediately upon re-entry, and as a result one will obtain the aerodynamic shape required for re-entry. If properly done, this will reduce the cross-section of the warhead while it is outside the atmosphere by a factor of approximately 10^5 at S-band in the nose-on region. In Figure 3-2 we have plotted the average cross-section of the Rudolph warhead (Configuration I) within ±5 degrees of nose-on as a function of wavelength, with and without the tin structural perturbation. Figure 3-2 also contains the cross-sections of the 7-OC and Needle-Nose warheads as a function of wavelength. In this figure observe that the cross-section of the Rudolph warhead has not only been decreased by a factor of approximately 10^5 at S-band, but, simultaneously, this cross-section has been reduced by a factor of about 10^2 at 200 Mc (App. B).

Under case (a) the cross-section of the entire missile at the nose-on aspect will be comparable to the cross-section of the warhead alone above 200 Mc[1].

3.2 THE USE OF DECOYS

If additional load capacity is available in the Rudolph missile, this space can be used for decoys having the same cross-section as the Rudolph warhead, and adequate aerodynamic characteristics. For a discussion of the use of decoys see References 2, 5, and 6. This work is summarized

[1]At lower frequencies the nose-on cross-section of the warhead alone will be less than that of the entire missile because the warhead is in the Rayleigh region.

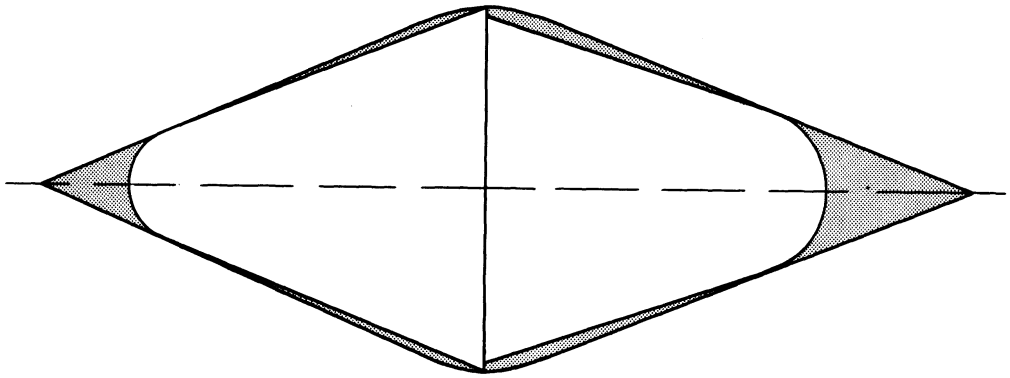

FIG. 3-1 CONFIGURATION I WITH PERTURBATIONS

The shaded portions indicate the perturbations which would vaporize upon re-entry. This perturbation is the one which is referred to as Configuration G in Appendix B.

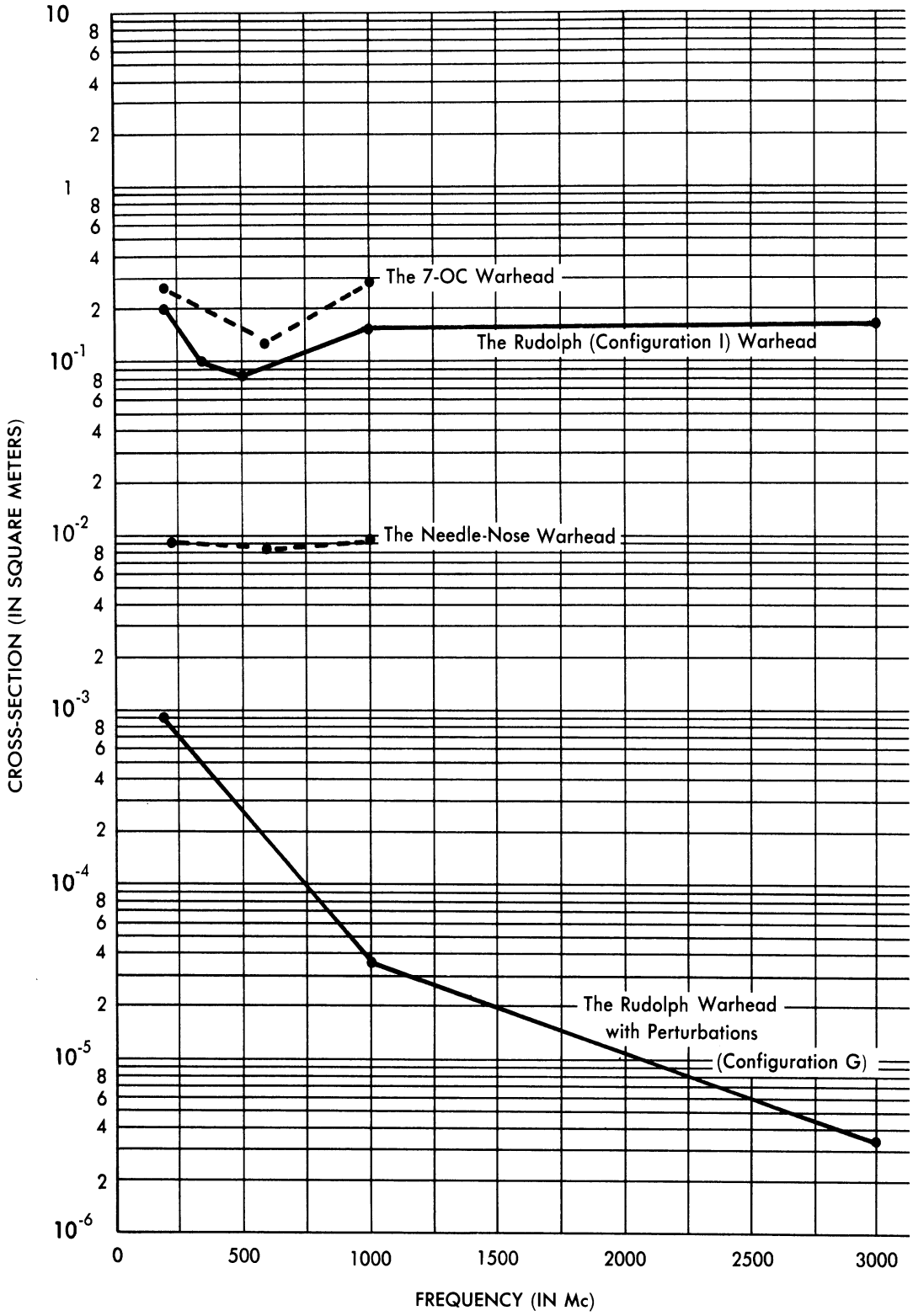

FIG. 3-2 THEORETICAL NOSE-ON CROSS-SECTIONS AS A FUNCTION OF FREQUENCY

in Appendix E. It is shown in Appendix D that fission waste-products cannot be used to enhance the cross-section of the decoys.

3.3 THE APPLICATION OF CAMOUFLAGE MATERIALS

The University of Michigan's examination of the camouflage field has consisted of a continuous but limited study, under Air Force Contract AF 33(602)-1070, over the past 18 months. A portion of this study is summarized in Reference 7. Additional studies were made since the completion of Reference 7. One of these additional studies consisted of an examination of thick and heavy materials (approximately 8 inches thick and 1 1/2 lbs/ft^2) for which large reductions in cross-sections can be obtained for operation at frequencies above 500 Mc (Ref. 8).

Recently a new camouflage material has been developed by Deutsche Magnesit, AG, Munich, Germany. This new material seems to be the best presently available for aircraft and missile applications. Tests on this camouflage material, carried out at the Rome Air Development Center, are discussed in Appendix C. This material is effective in reducing the back-scattering cross-section over small frequency bands. Unfortunately, its effectiveness may be due not so much to absorbent qualities as to the fact that it scatters the electromagnetic energy into angles other than the back-scattering direction.

The above studies are still in process and it is too early to state that there is a camouflage material presently available which is suitable for use on missiles.

3.4 THE USE OF CHAFF OR IONIZED PARTICLES

It is clearly not possible to carry enough chaff to cover the space required to camouflage the Rudolph warhead over a significant portion of of its trajectory. The alternative possiblity of using fission waste-products to hide the warhead can be discounted on the basis of the results contained in Appendix D.

IV

CONTINUATION OF THE BASIC ANALYSIS INVOLVING THE CROSS-SECTIONS OF BALLISTIC MISSILES

4.1 POWER SPECTRA ANALYSIS

One method of discriminating between ballistic missiles and ballistic-missile decoys might be based upon scintillation and glint. Recently, for the Bendix Aviation Corporation, The University of Michigan computed the auto-correlation function and power spectra of the cross-section measurements obtained for one-third scale V-2 models (Ref. 1 and 3). The results of this investigation are given in Appendix F.

4.2 IONIZATION AND SHOCK WAVE CONSIDERATIONS

In Appendix H we have summarized the work presented in Reference 1, and information on the analysis performed by the Massachusetts Institute of Technology on the effects of ionization of the atmosphere by the missile. Also included is a discussion of the shape of shock waves formed by a missile as it leaves the atmosphere, as compared to the shape of the shock wave upon re-entry.

4.3 EXPERIMENTAL WORK ON HIGH SPEED PELLETS

It has been discovered recently by Dr. T. C. Poulter (of the Poulter Laboratories) that one may obtain experimental velocities in the neighborhood of 15 km/sec. These experiments were performed at Stanford Research Institute. The results are summarized in Appendix H.

V

CONCLUSIONS AND RECOMMENDATIONS FOR FUTURE WORK

The radar cross-section study of ballistic missiles begun in Reference 1 has been continued in the present report. In this report the radar cross-section of several parameterizations of the Rudolph warhead have been found from 200 Mc through S-band for aspect angles out to 60 degrees off-nose. It has been concluded here that there are several methods for significantly reducing the radar cross-section of the Rudolph warhead; future systems analysis will determine if these changes will unduly disturb the over-all system. A major point established in this report is that fission waste-products should not be used for camouflage purposes.

It is recommended that future work on the radar cross-section problem for the ICBM should include:

1. A thorough analysis of the decoy problem for the ICBM (similar to the thorough analysis given to the decoy problem for aircraft (Ref. 2)),
2. A continuing analysis of the reflection characteristics of ionized media (as associated with problems of propulsion, as well as with ionization of the atmosphere during the re-entry portion of the missile trajectory),
3. A continuation of the perturbation analysis presented in this report (The University of Michigan expects to do this on an extension of Air Force Contract AF 04(645)-33.),
4. An experimental check on the cross-section computations performed on the perturbations to Rudolph warhead shapes (It is planned also to include these experimental checks in the extension of Air Force Contract AF 04(645)-33.),
5. The determination of the bistatic cross-section of the ICBM (due to the advantages to the defense that bistatic operation would yield), and

6. Further analysis of camouflage materials, including the considerations of the idea of rotating the polarization of the reflected energy.

APPENDIX A

THE RADAR CROSS-SECTION OF THE R-W RE-ENTRY BODIES (CONFIGURATIONS I – VI)

A.1 INTRODUCTION

This appendix contains the analysis involved, and the results obtained, in the computation of the radar cross-sections of the six Ramo-Wooldridge Corporation re-entry designs. The six configurations are shown in Figures A.1-1 and A.1-2.(Throughout this report, they are referred to as Configurations I–VI.)

Cross-section computations have been performed for 200, 350, 500, 1000, and 3000 Mc for aspect angles (ψ) out to 60 degrees off-nose (in the case of 3000 Mc, the aspect angle ψ ranged from 0 to 180 degrees). Section A.2 contains the 200 – 500 Mc data and analysis, and Section A.3 contains a discussion of the 1000 and 3000 Mc considerations.

Section A.4 is devoted to a consideration of experimental data at 200 Mc for shapes whose dimensions are comparable to those of Configurations I–VI. This is done because of the inapplicability of physical optics to the study of the cross-sections of these configurations at 200 Mc.

In estimating the cross-sections of the Configurations I–VI at 1000 Mc and at 3000 Mc, the methods of physical optics were used exclusively. At the lower frequencies, due to the inapplicability of physical optics, other methods of approximation were required.[1] For the nose-on aspect an approach based upon the creeping wave method was employed; in the

[1]At these lower frequencies the ratio of the characteristic dimension of the body to the wavelength is approximately equal to one. When this ratio is much greater than one, the methods of physical optics can be applied, and when the ratio is much less than one, the Rayleigh approximation is valid.

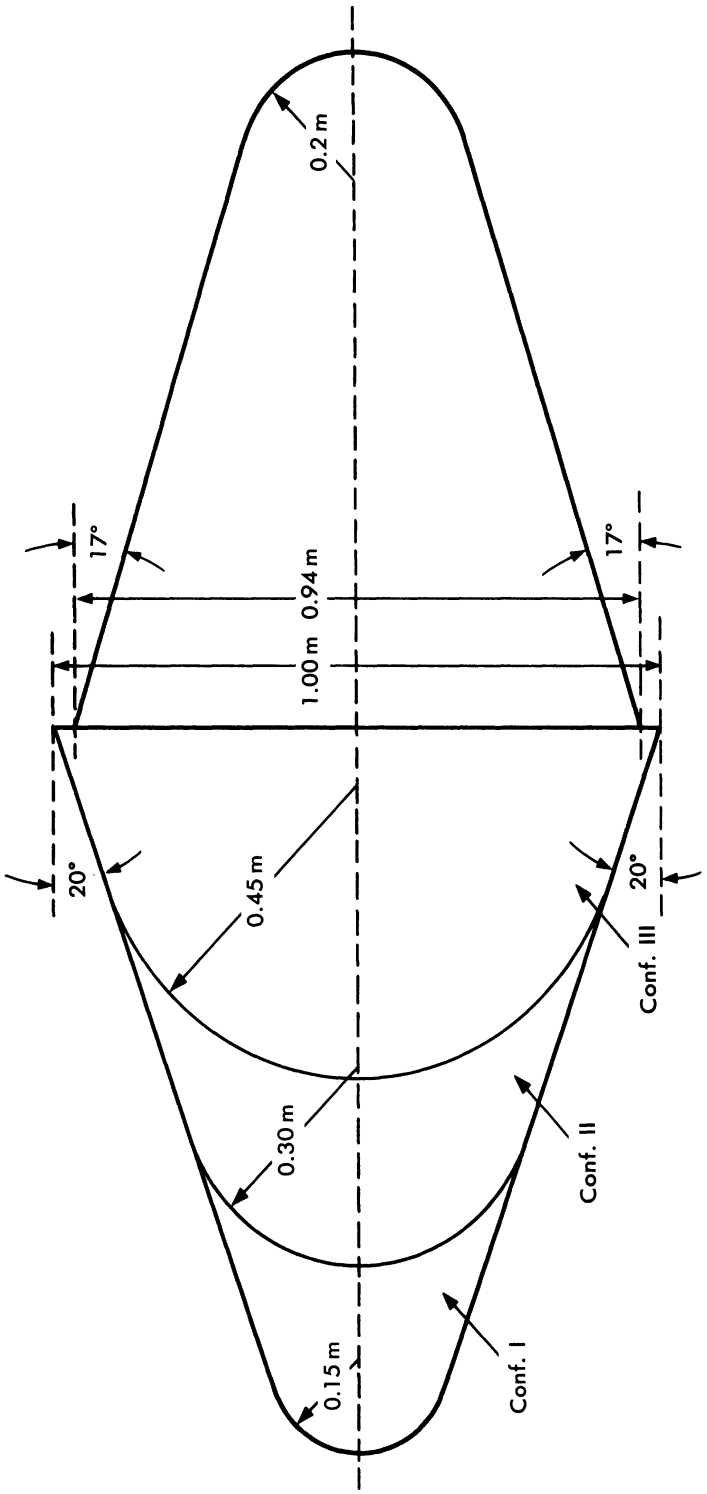

FIG. A.1-1 CONFIGURATIONS I, II, AND III

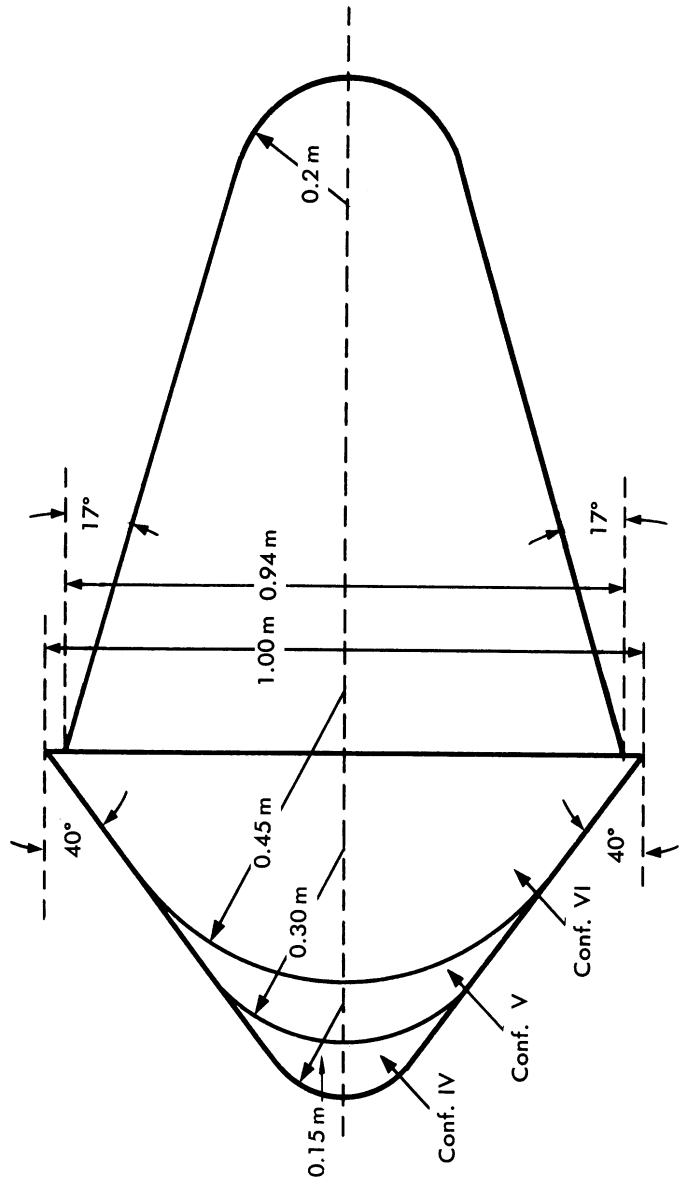

FIG. A.1-2 CONFIGURATIONS IV, V, AND VI

aspect range $0 < \psi \leq 60^{\circ}$, cross-section estimates were obtained based upon the results of the study of experimental data (Sec. A.4), physical optics results, and the data obtained in the study of the nose-on case.

The over-all results of any such approximation method should be accurate within a factor of 10. It is of course hoped that the approximations will be better in many cases, but this maximum error is tolerable[1] because the range of detection varies as the fourth root of the cross-section. In other words, if the radar cross-section is known within a factor of 10, the range performance of the radar system is known within a factor of 1.78.

A.2 CROSS-SECTIONS AT 200 TO 500 Mc

A.2.1 Cross-Sections for the Nose-On Aspect ($\psi = 0$)

Each of the Configurations I–VI has a maximum diameter, D, and length, L, such that at 200 Mc, $D/\lambda = 0.67$, and $0.93 \leqslant L/\lambda \leqslant 1.43$; at 350 Mc, $D/\lambda = 1.17$, and $1.63 \leqslant L/\lambda \leqslant 2.50$; and at 500 Mc, $D/\lambda = 1.67$, and $2.33 \leqslant L/\lambda \leqslant 3.57$. Reference to the theoretical sphere curve in Kerr (Ref. 9) and the 10:1 prolate spheroid curve (Ref. 10), indicates that these values of D/λ and L/λ are in the resonance region. These ratios are of such magnitude that neither physical optics nor Rayleigh scattering can be considered to be applicable (although at 500 Mc we are approaching values of these ratios for which physical optics could be applied). Thus some other method of approximation must be applied to estimate the nose-on cross-sections of Configurations I–VI for these frequencies.

The method applied is similar to the one which was successfully used by Franz and Deppermann (Ref. 11) for the cylinder and is the same as that applied in Reference 1 for the determination of the nose-on cross-section of the 7-OC warhead. (The 7-OC calculations yielded results which agreed with experimental data to within a factor of 2.) Briefly, the method involves considering the back scattering cross-section to be the sum of two contributions. One is due to the radiation scattered from the first Fresnel zone on the body or, in the case of a pointed body, from the tip, and the other is due to the radiation which creeps around

[1]The accuracy of the results obtainable depends only upon the amount of time and money one wishes to expend in obtaining the results.

the rear of the body and comes back to interfere coherently with the radiation scattered from the forward part of the body. An estimate of the contribution from the rear was obtained in Reference 1 through the study of sphere cross-sections. To do this the cross-section of a sphere at a peak was written

$$\sigma_{peak} = \left[A_{g.o.} + A_{rear} \right]^2 ,$$

where σ_{peak} is the sphere cross-section at a peak in the resonance region, $A_{g.o.}$ is proportional to the field amplitude due to the first Fresnel zone, and A_{rear} is the contribution due to the radiation which creeps about the rear of the body. Taking $(A_{g.o.})^2 = \pi a^2$, where a = the radius of the sphere, and reading values of σ_{peak} off existing sphere graphs such as the one found in Kerr (Ref. 9, p. 453), it was found that in the region of interest $(A_{rear})^2$ is given by $0.033\lambda^2 (\lambda/a)^{1/2}$.

Applying this procedure to Configurations I–VI and considering the contribution from the rear to be approximated by that from a sphere of radius equal to 0.5 m, we obtain for each of the six configurations

$$(A_{rear})^2 = 0.128 \ m^2 \text{ at } 200 \text{ Mc},$$

$$(A_{rear})^2 = 0.0317 \ m^2 \text{ at } 350 \text{ Mc, and}$$

$$(A_{rear})^2 = 0.0130 \ m^2 \text{ at } 500 \text{ Mc.}$$

From the physical optics methods applied for the 1000 and 3000 Mc cases, the contribution from the first Fresnel zone is

$0.0707 \ m^2$ for Configurations I and IV,

$0.283 \ m^2$ for Configurations II and V, and

$0.636 \ m^2$ for Configurations III and VI,

for all three frequencies[1]

From these computed values "average" cross-sections can now be obtained by merely taking the sum of the two contributions, an upper bound by assuming complete reinforcement, and a lower bound by assuming complete interference between the two contributions; i.e., if σ_1 is the contribution from the front and σ_2 is the contribution from the rear, we have $(\sigma_1 + \sigma_2)$ as the "average" value, $(\sqrt{\sigma_1} - \sqrt{\sigma_2})^2$ as the lower bound, and $(\sqrt{\sigma_1} + \sqrt{\sigma_2})^2$ as the upper bound. The results appear in Table A.2-1.

At 500 Mc the ratios of L/λ are approaching values which would permit the application of physical optics. It is of interest to compare the values for 500 Mc given in Table A.2-1 with those which are obtained through the application of physical optics. The following average values are yielded by the physical optics method for $\lambda = 0.6$ m:

$$\sigma_I = 0.17 \text{ m}^2, \ \sigma_{II} = 0.39 \text{ m}^2, \ \sigma_{III} = 0.74 \text{ m}^2,$$

$$\sigma_{IV} = 0.64 \text{ m}^2, \ \sigma_V = 0.84 \text{ m}^2, \text{ and } \sigma_{VI} = 1.19 \text{ m}^2.$$

It should be noted that these physical optics cross-sections are larger than those given in Table A.2-1 by factors ranging from one up to eight.

A.2.2 Cross-Sections for the Off-Nose Aspects ($0 < \psi \leqslant 60^o$)

The "creeping-wave" approach used for the nose-on aspect cannot conveniently be applied for $\psi > 0$ since the use of a sphere to determine the contribution from the "rear" for $\psi > 0$ is a poor geometric approximation to the actual shape. However, estimates of the manner in which the cross-section varies over the interval $0 \leqslant \psi \leqslant 60^o$ can be obtained through the use of

1. The results obtained for $\lambda = 0.1$ m and $\lambda = 0.3$ m (Sec. A.3),
2. The physical optics estimate at 500 Mc,

[1]This contribution is given by πR_n^2 where R_n equals the radius of the front spherical section of the missile (see Fig. A.1-1 and A.1-2).

TABLE A.2-1

NOSE-ON CROSS-SECTIONS OF CONFIGURATIONS I–VI

(In Square Meters)

CONFIGURATION	200 Mc			350 Mc			500 Mc		
	Lower Bound	Av.	Upper Bound	Lower Bound	Av.	Upper Bound	Lower Bound	Av.	Upper Bound
I and IV	.0083	.20	.39	.0074	.10	.20	.023	.084	.14
II and V	.030	.41	.79	.13	.31	.50	.17	.30	.42
III and VI	.19	.76	1.3	.38	.67	.95	.47	.65	.83

3. The geometric optics prolate spheroid (a = L/2, b = D/2) curve in the region $0 \leqslant \psi \leqslant 60^{o}$ (Ref. 10), and

4. The results of the examination of experimental data (Sec. A.4) which indicated that at 200 Mc $\sigma(\psi)$ should not vary much in the interval $0 \leqslant \psi \leqslant 60^{o}$ for these configurations,

combined with the computed nose-on values given in Table A.2-1. Cross-section curves are given in Figures A.2-1 through A.2-6. Each figure contains, for a given configuration, the cross-section curves at 3000 Mc (λ = 0.1 m) and 1000 Mc (λ = 0.3 m) (Sec. A.3), the curves for the prolate spheroid (geometric optics), and points obtained through physical optics at 500 Mc. With these as a guide, estimates of the cross-section curves at 200 Mc, 350 Mc, and 500 Mc are made with the $\sigma(0^{o})$ point determined from Table A.2-1.

A.2.3 The Wavelength Dependence in the Region From 200 to 500 Mc

Some idea of the manner in which the cross-sections of Configurations I—VI vary as a function of frequency in the region from 200 to 500 Mc is obtained by an examination of Figures A.2-1 through A.2-6. However, a better idea may be obtained by analogy with the variations with frequency of the cross-section of the theoretical sphere (Ref. 9) and the theoretical 10:1 prolate spheroid curves (Ref. 10). These shapes display an oscillation of σ as a function of λ in this frequency interval. It is to be expected that the nose-on cross-section of Configurations I—VI will oscillate as a function of λ in a somewhat similar manner. Figure A.2-7 shows the cross-section of a sphere (of diameter equal to the diameter of Configurations I—VI) as a function of $1/(2\lambda)$, together with the computed "average", lower bound, and upper bound σ at 200, 350, and 500 Mc, for Configuration VI. Examination of this figure yields a fairly good picture of how the nose-on cross-section of Configuration VI varies in the 200 to 500 Mc frequency region, which can be considered to be typical of the variations for all six configurations.

Experimental data obtained by the Radar Research and Development Establishment (Ref. 12) and by the Sperry Gyroscope Company (Ref. 13)

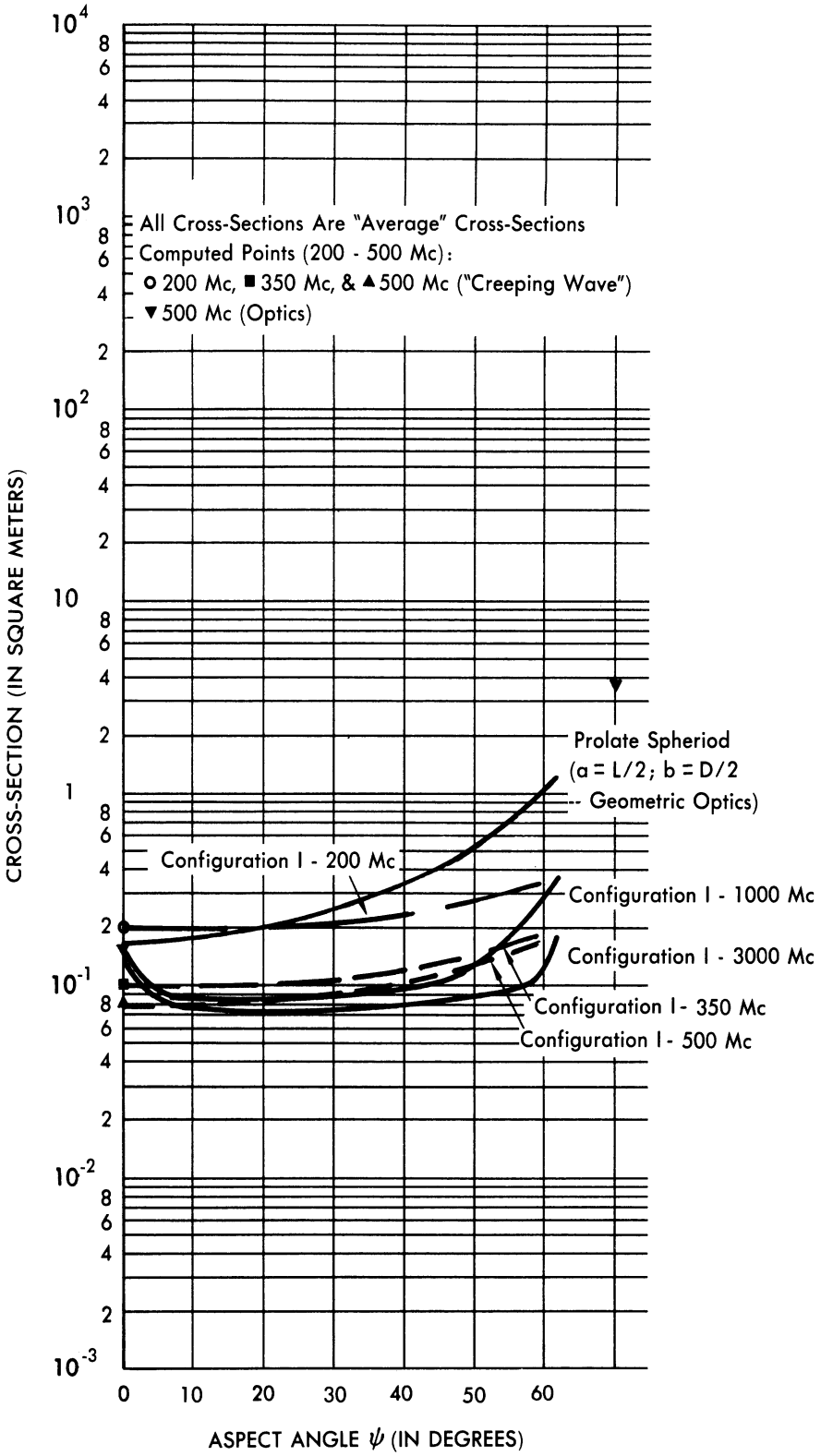

FIG. A.2-1 RADAR CROSS-SECTION OF CONFIGURATION I

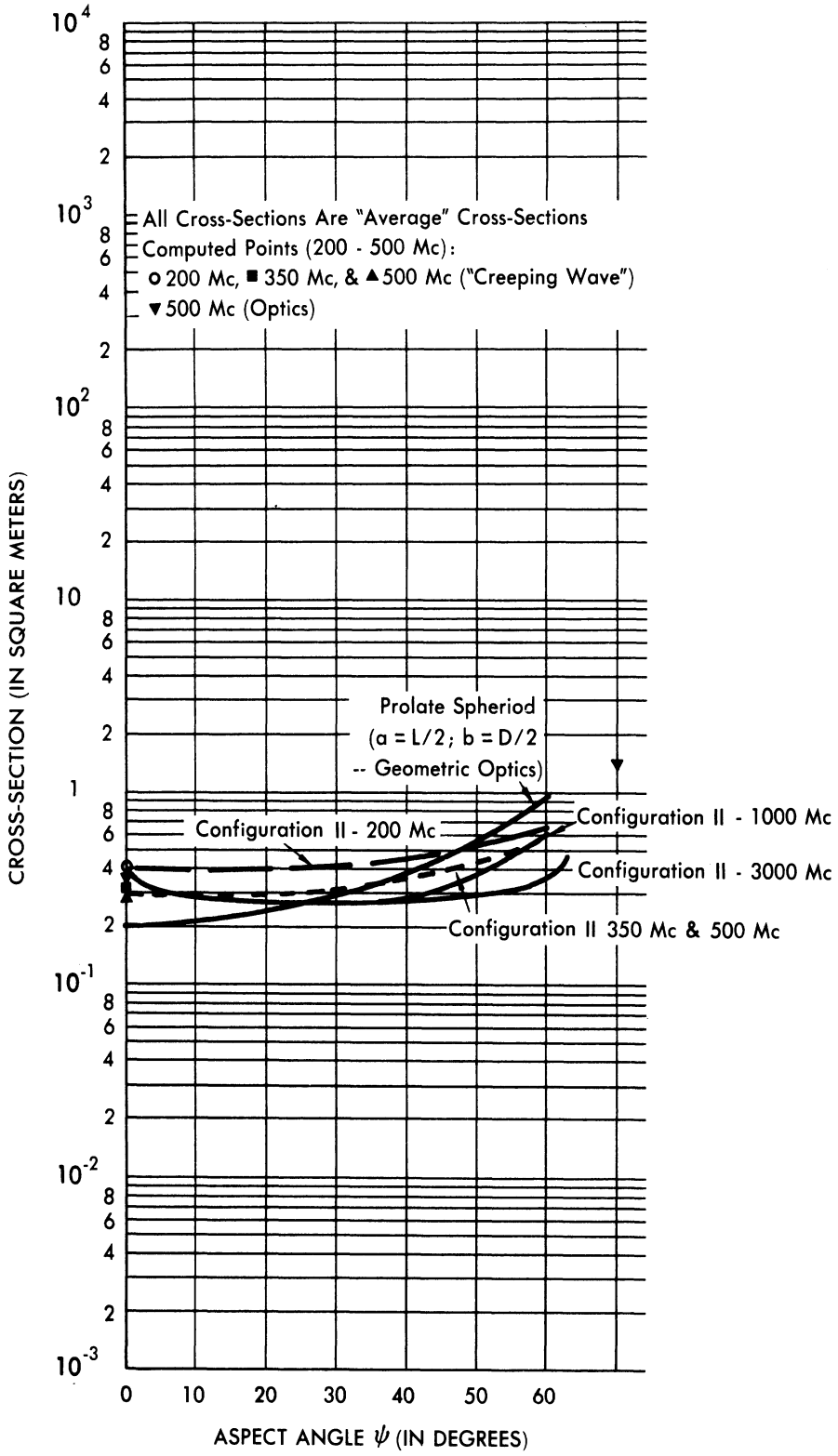

FIG. A.2-2 RADAR CROSS-SECTION OF CONFIGURATION II

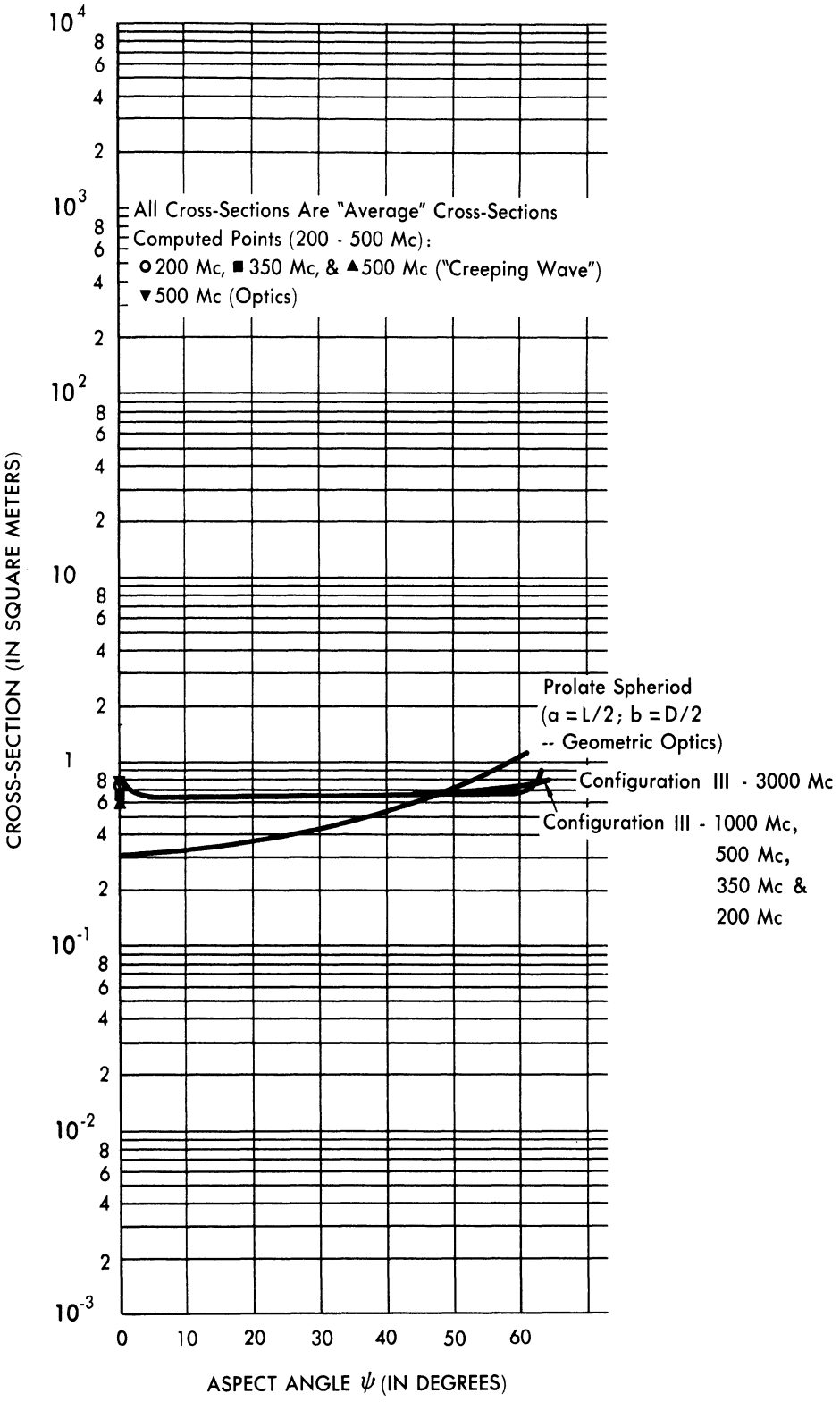

FIG. A.2-3 RADAR CROSS-SECTION OF CONFIGURATION III

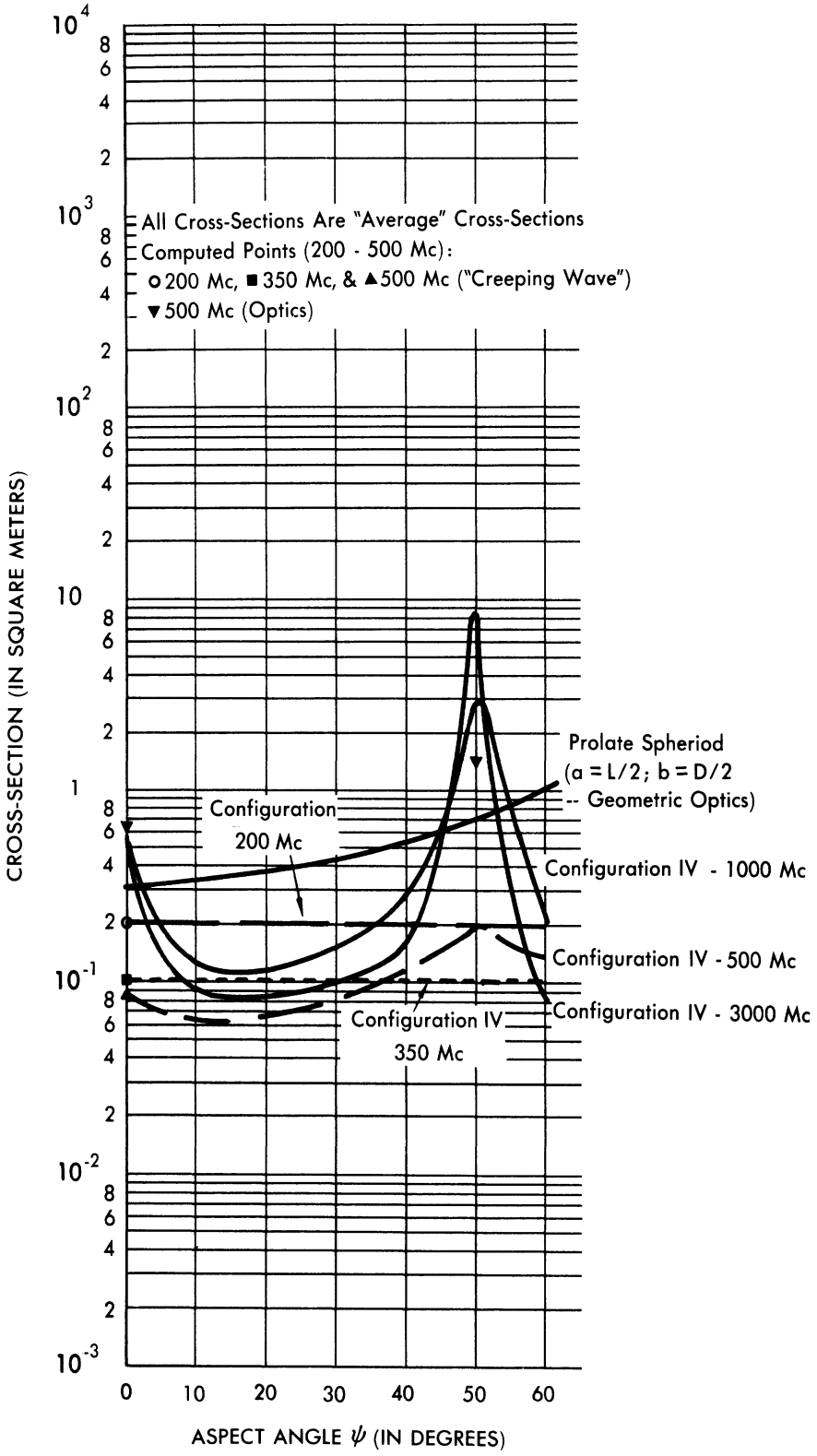

FIG. A.2-4 RADAR CROSS-SECTION OF CONFIGURATION IV

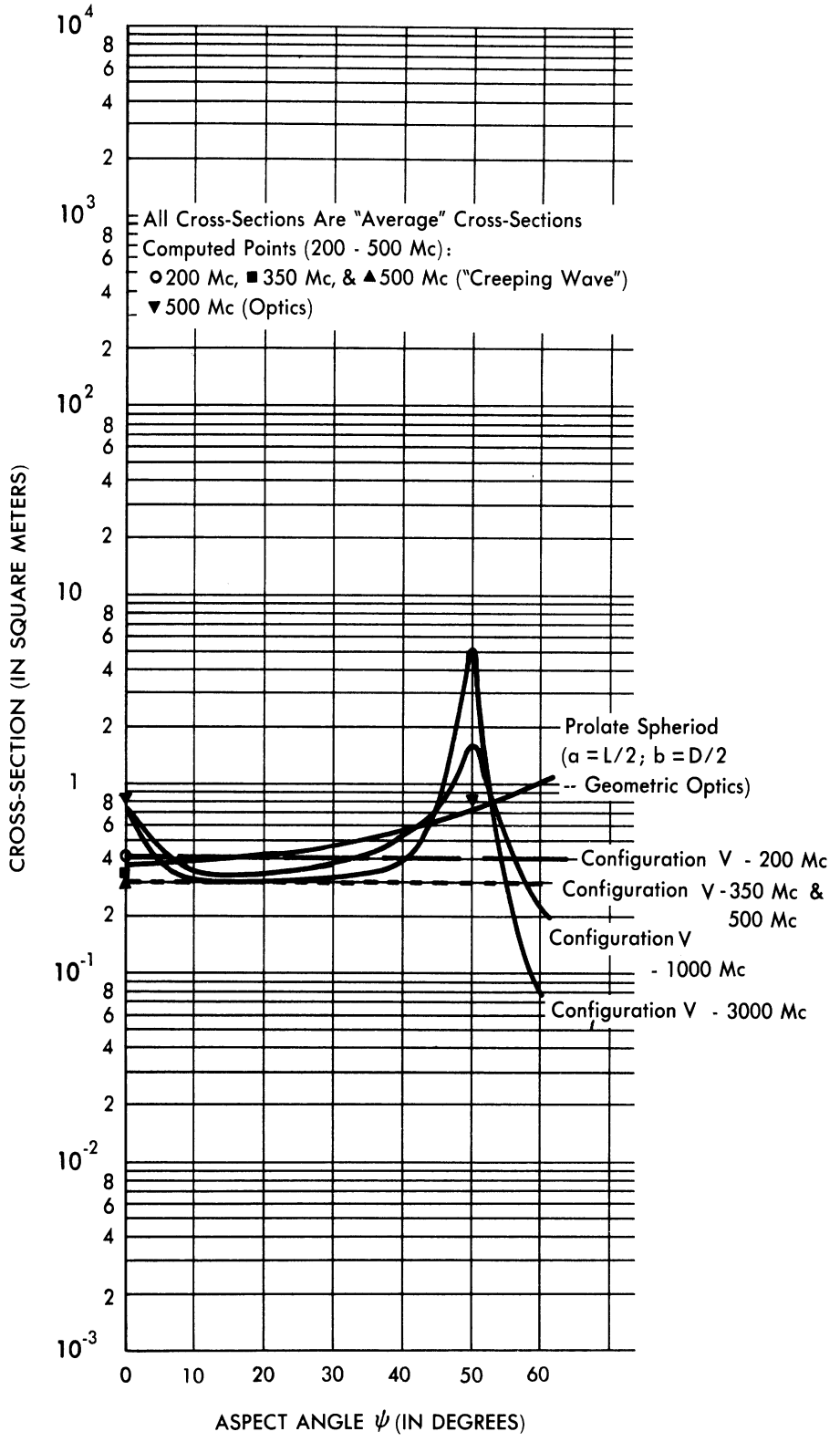

FIG. A.2-5 RADAR CROSS-SECTION OF CONFIGURATION V

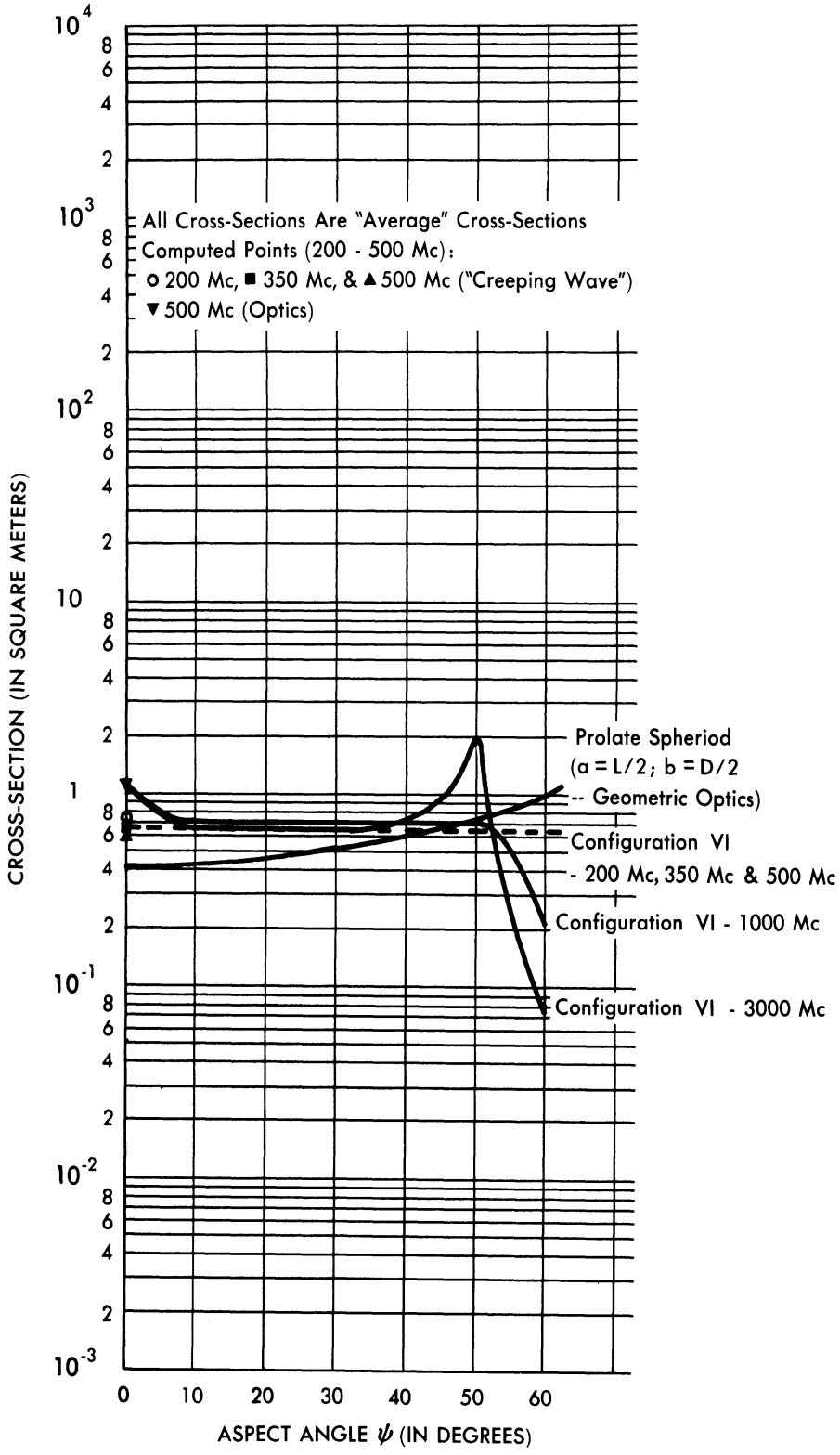

FIG. A.2-6 RADAR CROSS-SECTION OF CONFIGURATION VI

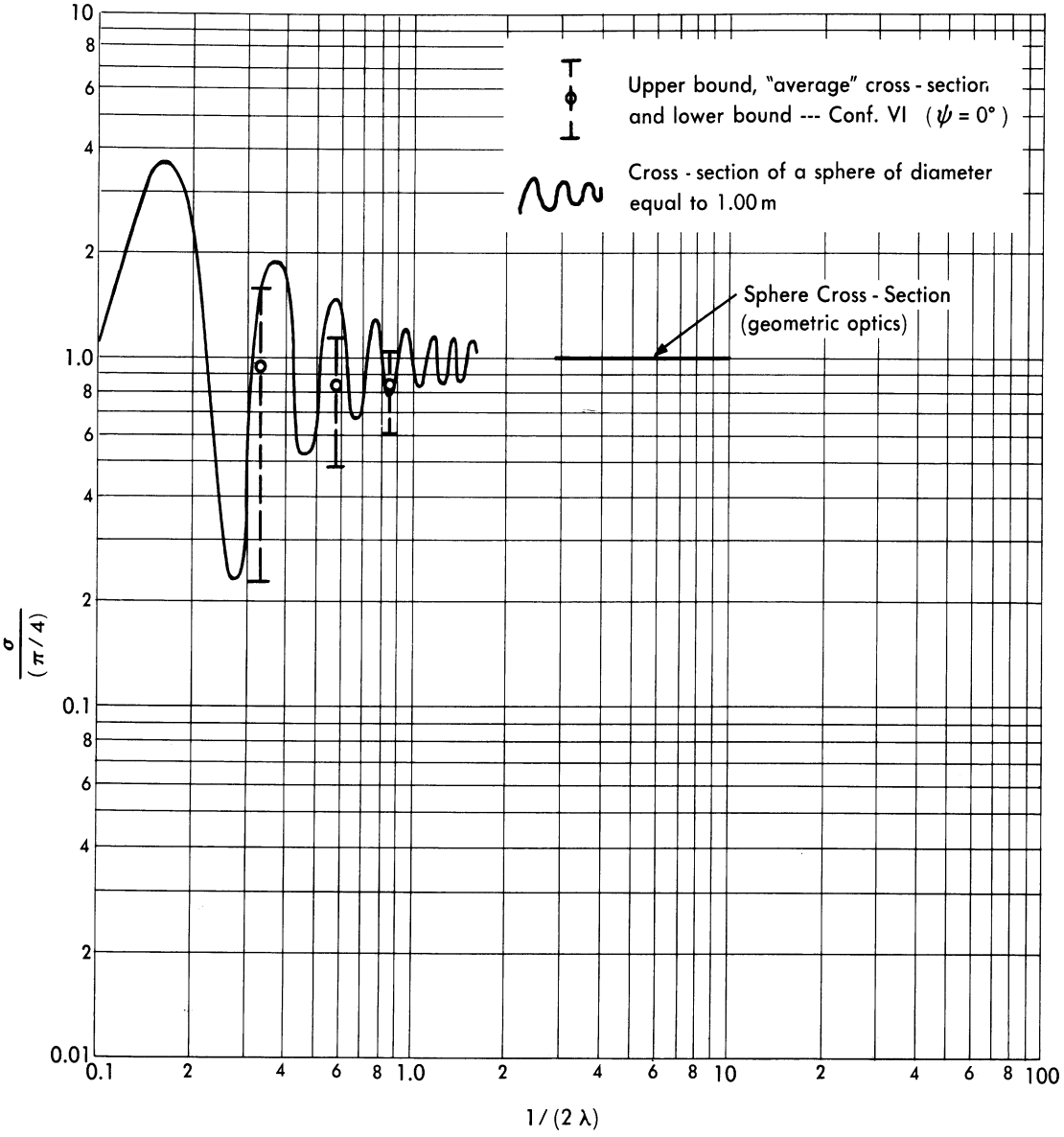

FIG. A.2-7 COMPARISON OF THE CROSS-SECTION OF CONFIGURATION VI WITH THE CROSS-SECTION OF A SPHERE OF DIAMETER EQUAL TO THE MAXIMUM DIAMETER OF CONFIGURATION VI (ψ=0°)

add additional information relative to the oscillation of σ with changing frequency. The RRDE data is reproduced in Figure A.2-8 and the Sperry data in Figure A.2-9. The configurations in these experiments have L/D ratios of from 6:1 to approximately 10:1. An examination of the above data, the theoretical sphere data, and the theoretical 10:1 prolate spheroid data, indicates that Configurations I – VI have a total fluctuation in cross-section (as a function of frequency) of less than a factor of ten in the 200 to 500 Mc range.

A.3 CROSS-SECTIONS AT 1000 AND 3000 Mc

The cross-sections of Configurations I–VI at 1000 and 3000 Mc were computed by two methods. Method I yields "average cross-sections," and Method II yields cross-sections for which the oscillations due to phase differences are estimated. Since the computations were performed in connection with the perturbations to the six re-entry designs, the computational procedures and equations involved for both sets of calculations appear in Appendix B.

The computational procedures followed closely the methods and techniques outlined in Appendix A of Reference 5, and the results obtained are shown in Figures A.3-1 through A.3-9. Figures A.3-1 through A.3-8 cover the aspect interval $0 \leqslant \psi \leqslant 60^{\circ}$ and include the data for two of the perturbations (Configurations A and B) discussed in Appendix B. Figure A.3-9 contains 3000 Mc data in the aspect range from 60 to 180 degrees. Examination of the data contained in these figures indicates that of the six configurations, Configuration I has the smallest cross-sections at all of the frequencies and aspects considered.

A.4 EXPERIMENTAL DATA AT 200 Mc FOR SHAPES COMPARABLE TO CONFIGURATIONS I–VI

A.4.1 Introduction

An examination of experimental data for configurations having body dimension to wavelength ratios similar to those for Configurations I–VI should give information relative to the magnitudes of the Rudolph cross-sections.

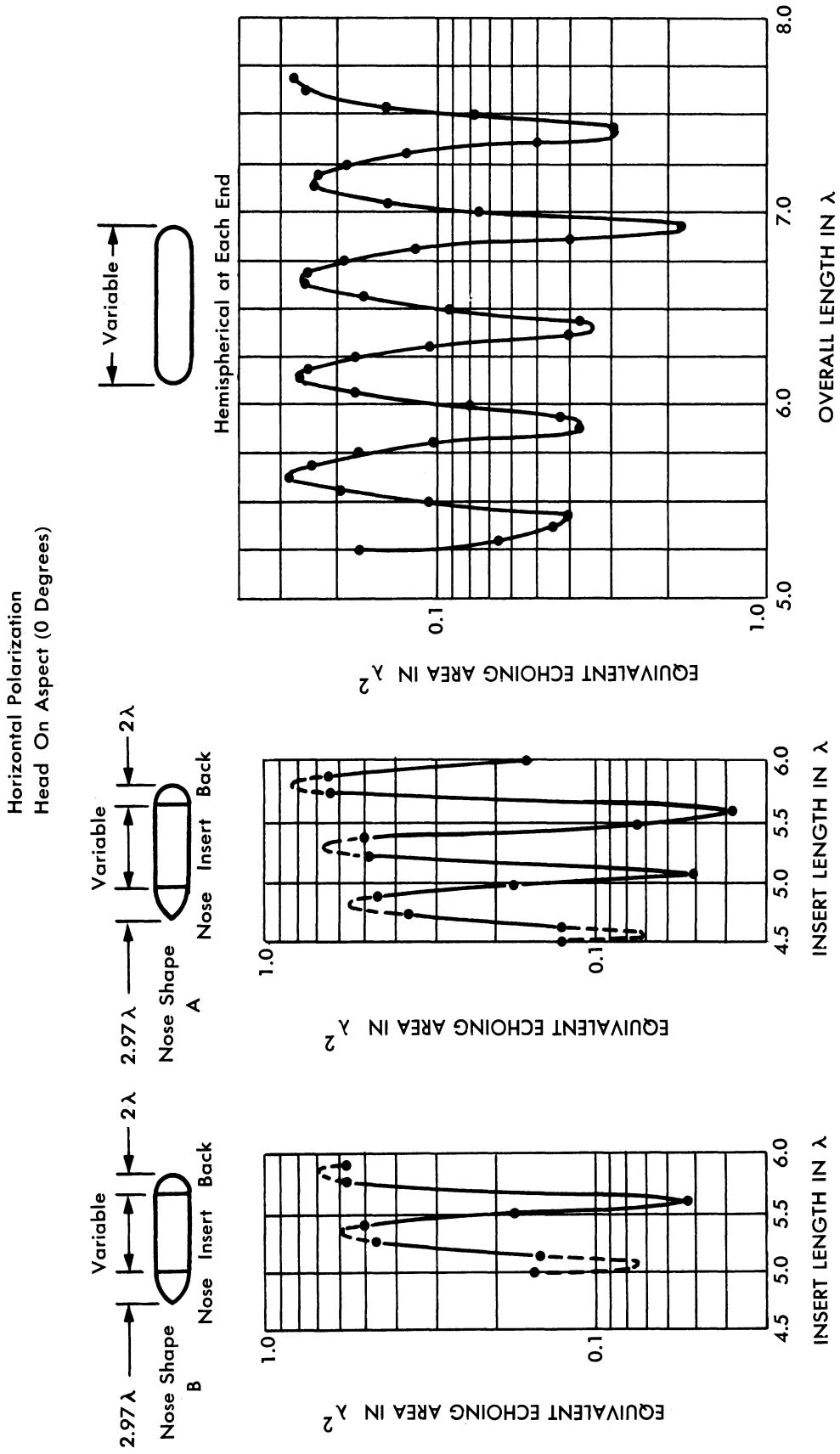

FIG. A.2-8 R.R.D.E. EXPERIMENTAL DATA - EQUIVALENT ECHOING AREA OF FINLESS MISSILE MODEL OF 1.17 λ DIAMETER
(Figures 5A, 5B, & 6 of Ref.12)

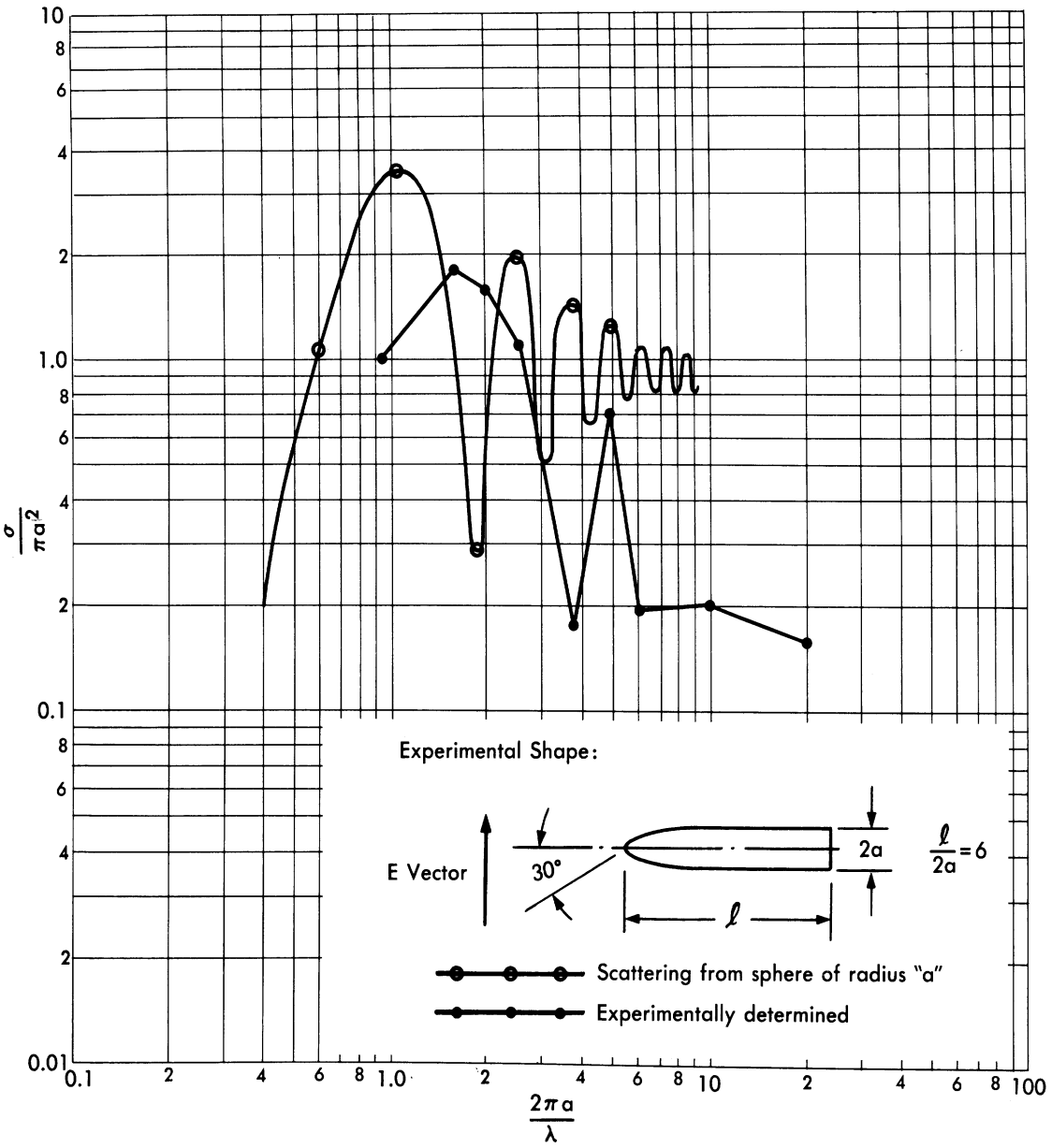

FIG. A.2-9 EXPERIMENTAL DATA — SPERRY GYROSCOPE COMPANY (From Ref. 13)

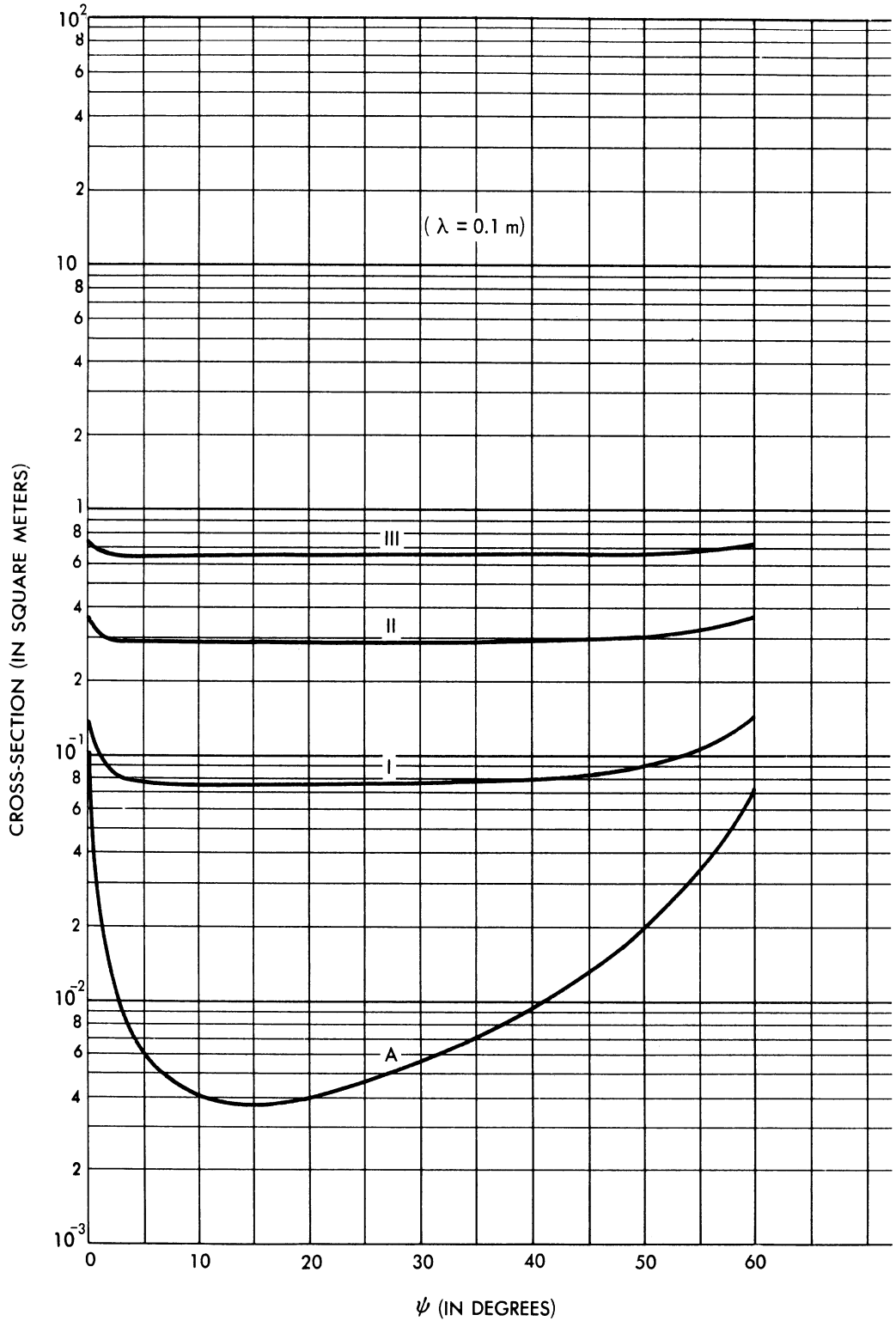

FIG. A.3-1 CROSS-SECTIONS OF CONFIGURATIONS I, II, III, AND A AT 3000 Mc (METHOD I)

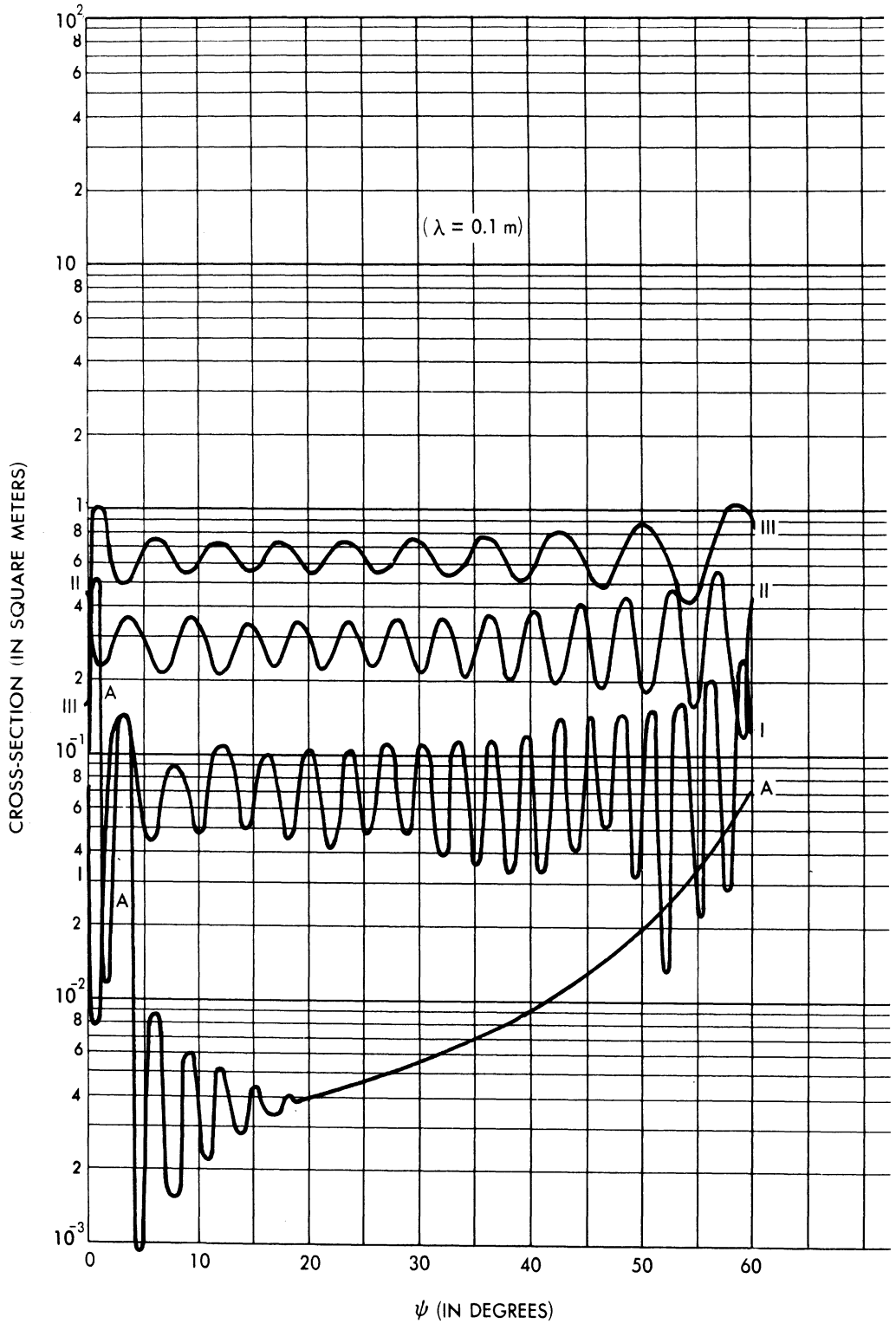

FIG. A.3-2 CROSS-SECTIONS OF CONFIGURATIONS I, II, III, AND A AT 3000 Mc (METHOD II)

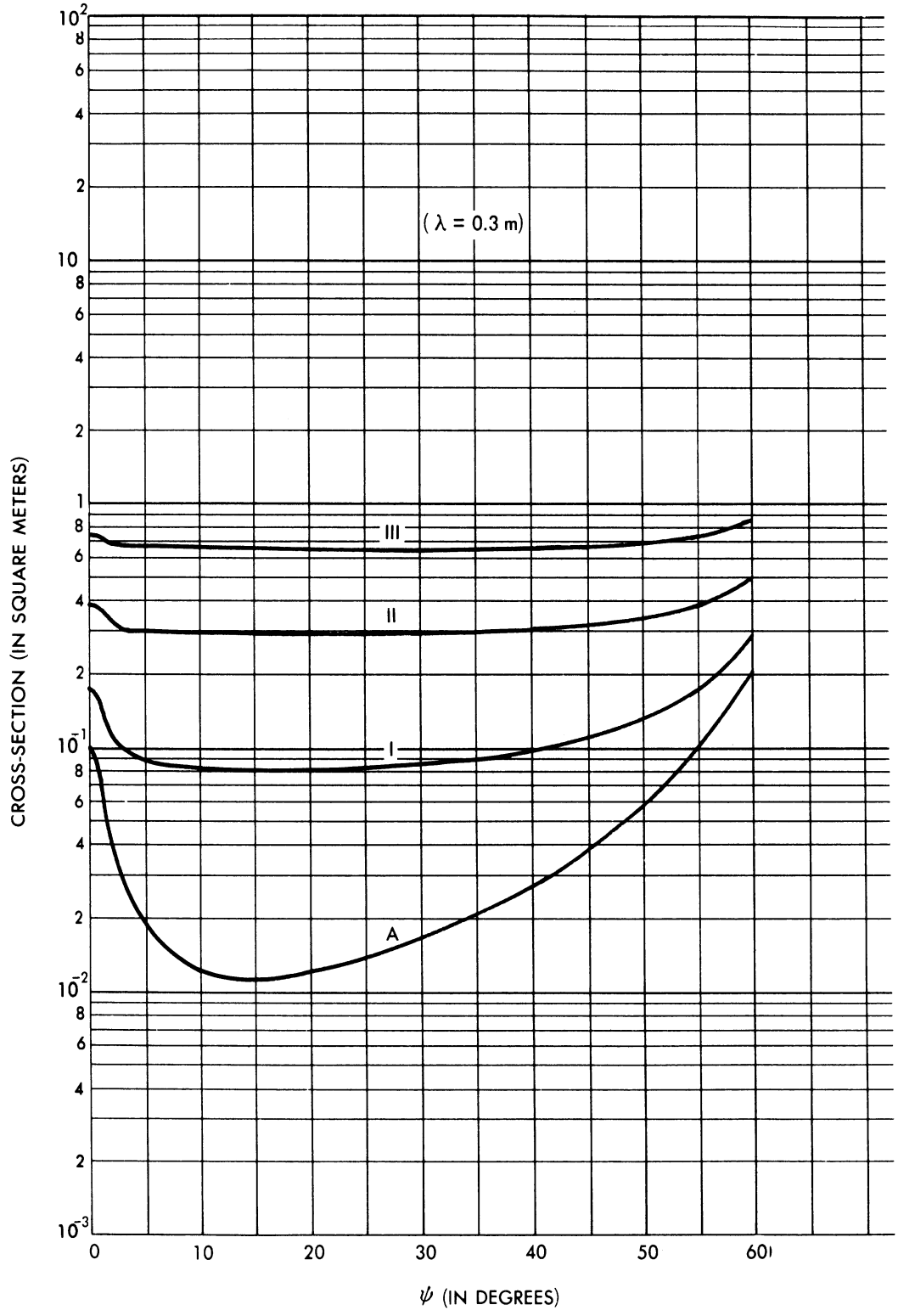

FIG. A.3-3 CROSS-SECTIONS OF CONFIGURATIONS I, II, III, AND A AT 1000 Mc (METHOD I)

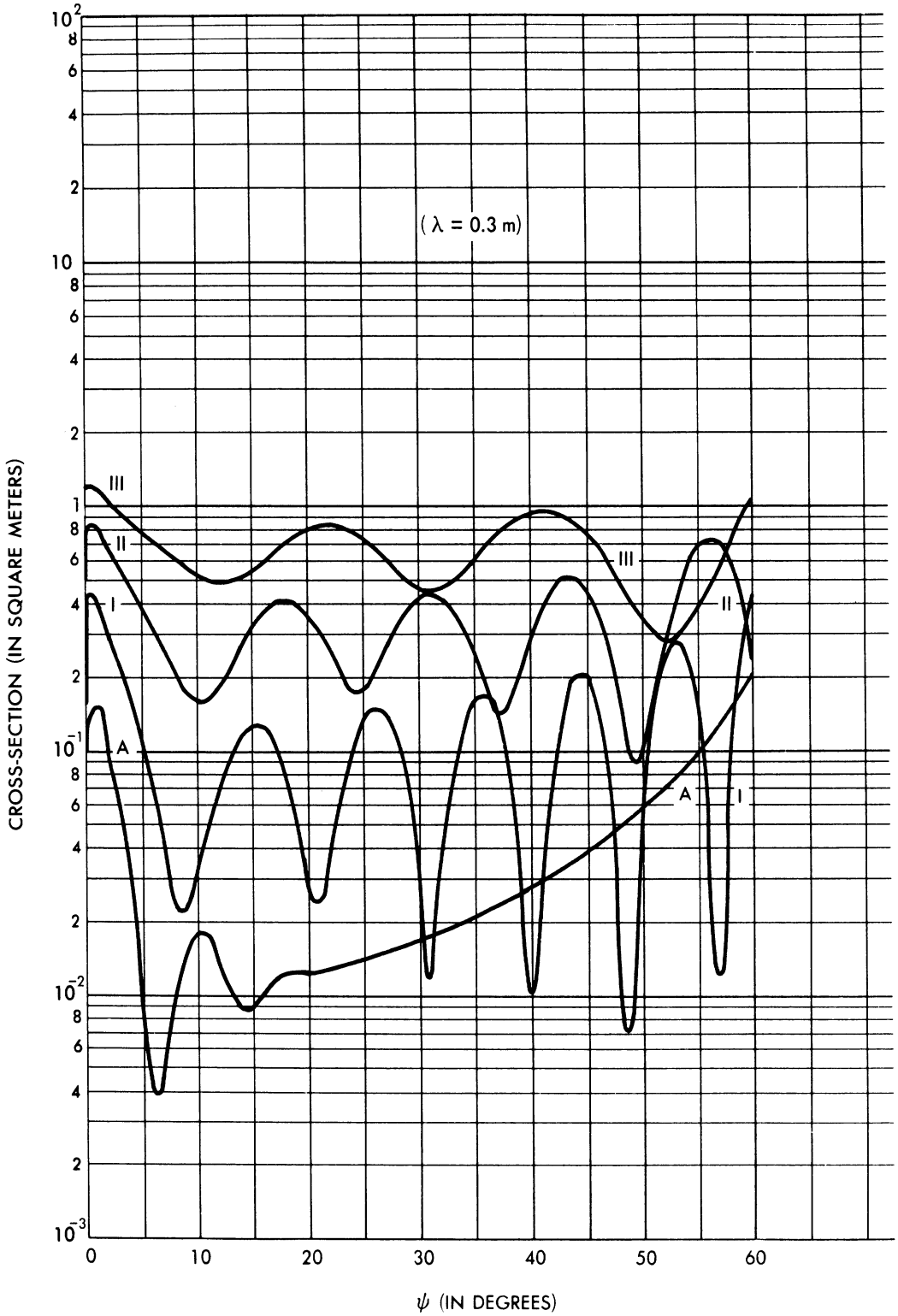

FIG. A.3-4 CROSS-SECTIONS OF CONFIGURATIONS I, II, III, AND A AT 1000 Mc (METHOD II)

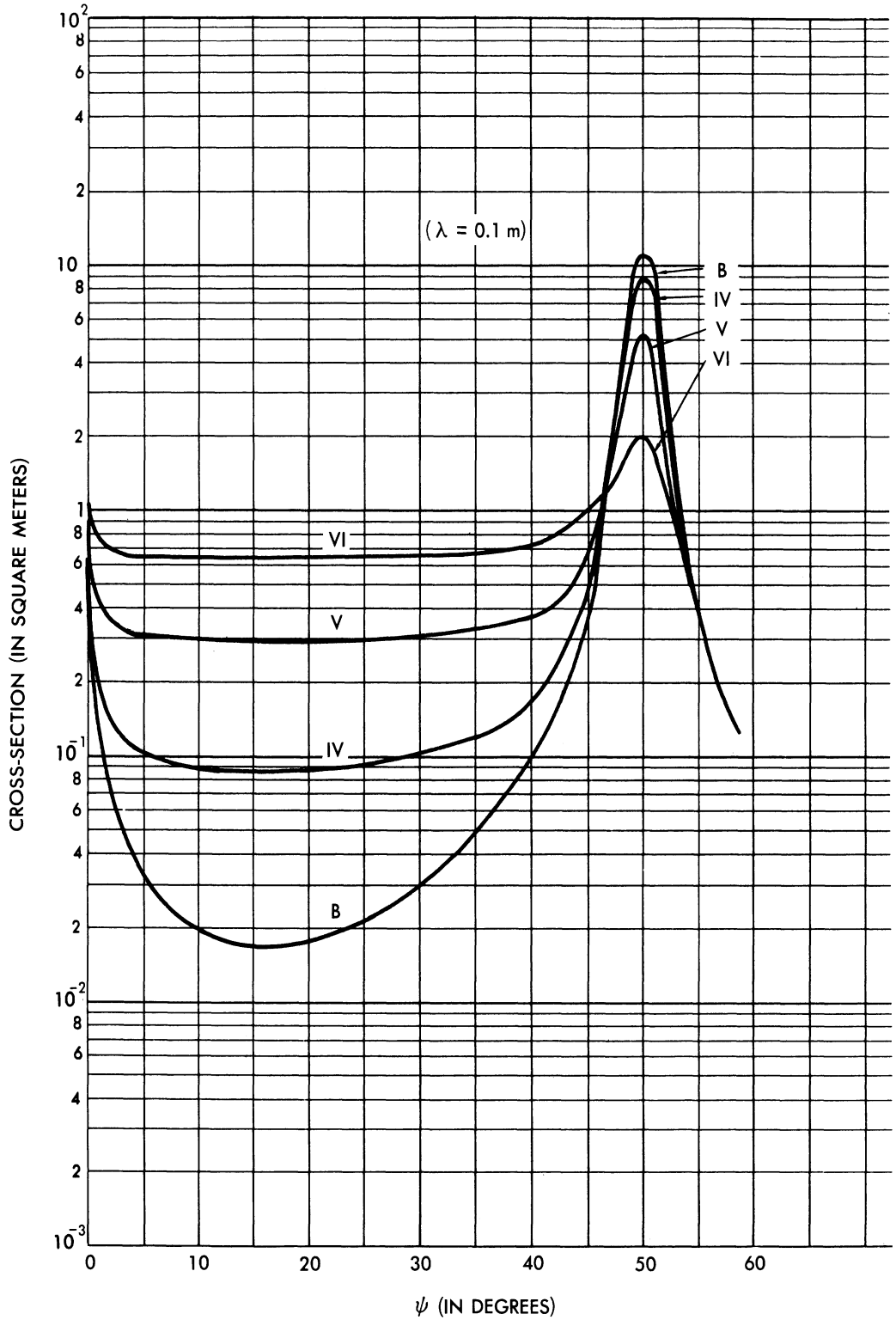

FIG. A.3-5 CROSS-SECTIONS OF CONFIGURATIONS IV, V, VI, AND B AT 3000 Mc (METHOD I)

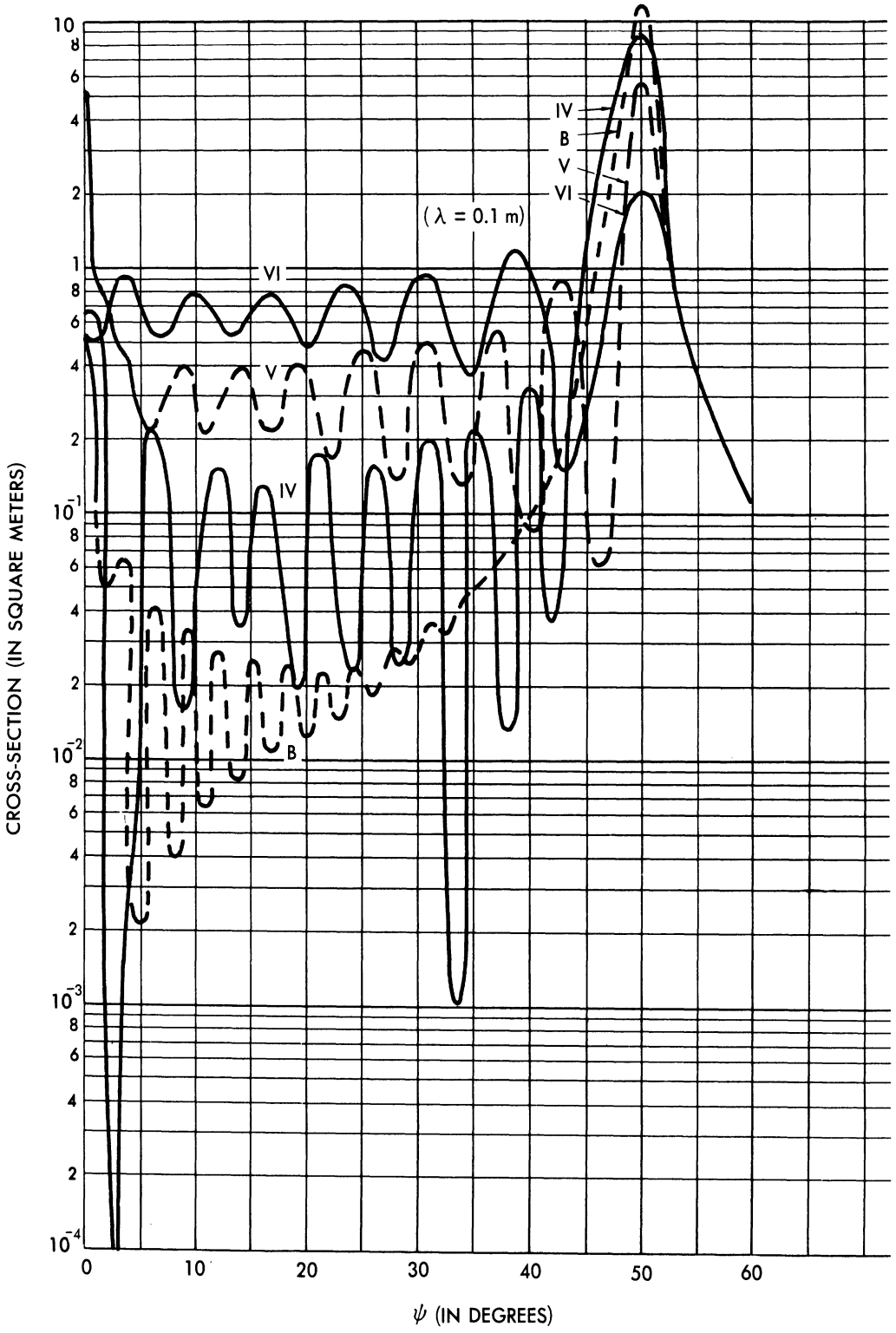

FIG. A.3-6 CROSS-SECTIONS OF CONFIGURATIONS IV, V, VI, AND B AT 3000 Mc (METHOD II)

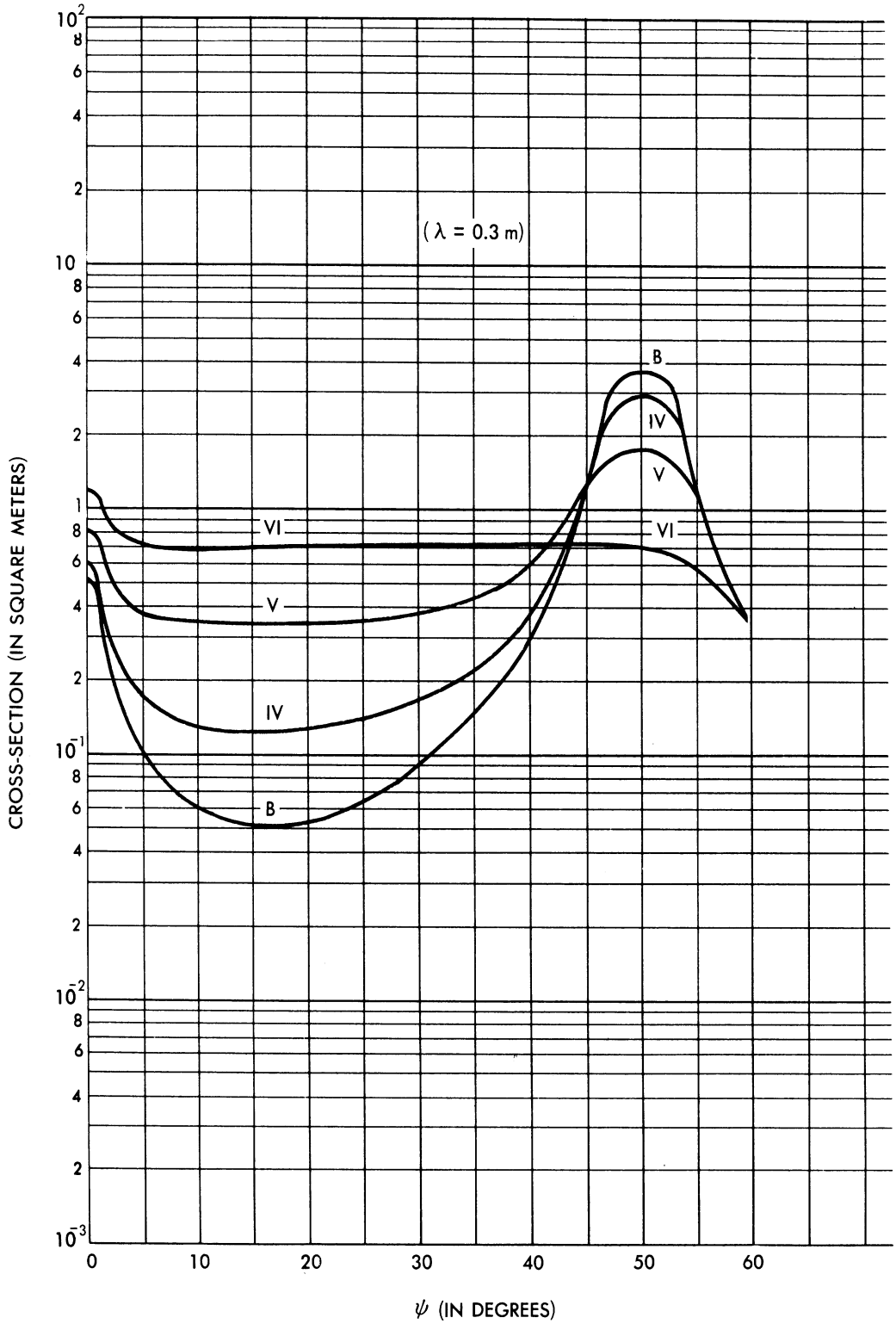

FIG. A.3-7 CROSS-SECTIONS OF CONFIGURATIONS IV, V, VI, AND B AT 1000 Mc (METHOD I)

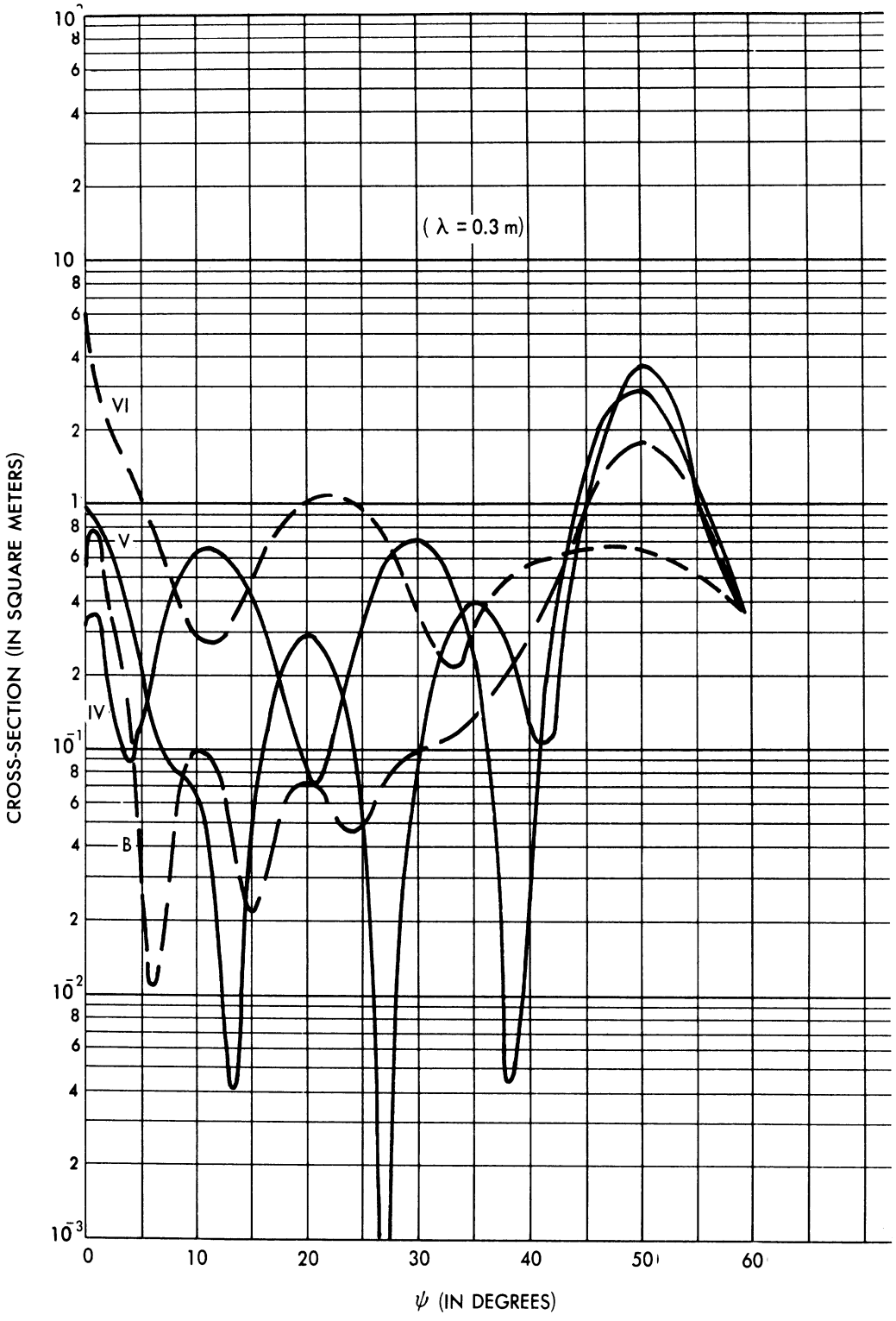

FIG. A.3-8 CROSS-SECTIONS OF CONFIGURATIONS IV, V, VI, AND B AT 1000 Mc (METHOD II)

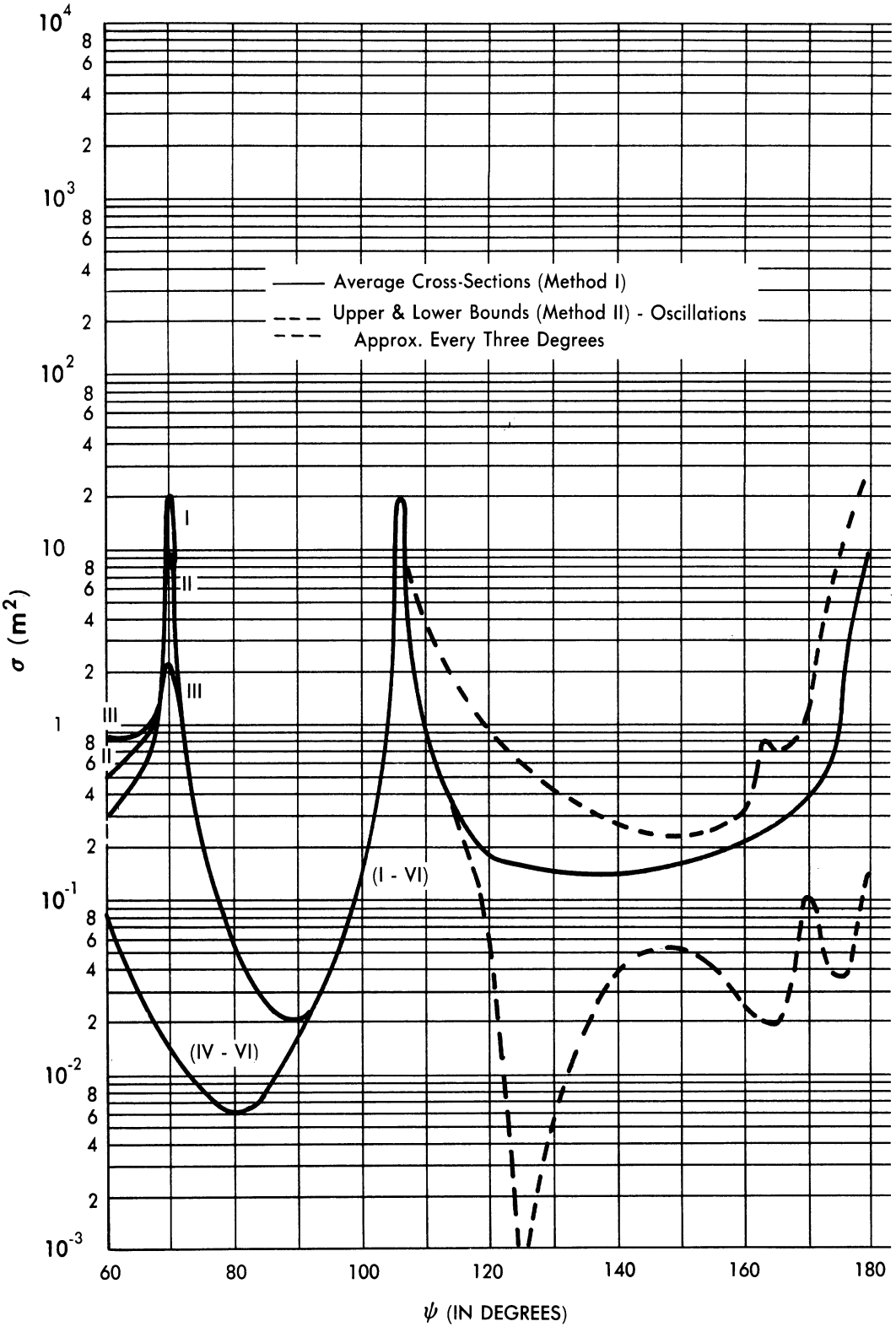

FIG. A.3-9 CROSS-SECTIONS OF CONFIGURATIONS I - VI
AT 3000 Mc IN THE ASPECT RANGE $60° \leqslant \psi \leqslant 180°$

A.4.2 Experimental Data for Carrots and Cones

The Microwave Radiation Company, Inc. has performed cross-section measurements for the Cornell Aeronautical Laboratory, Inc. under Contract DA-30-115-ORD-543 between the Cornell Aeronautical Laboratory and the Department of Defense. These experiments were conducted at a frequency of 9375 Mc on models which were 2, 4, 8, and 32 wavelengths long. Two of the models involved were a "Carrot" and a finite cone (Fig. A.4-1). This section contains some of the 2λ model data scaled to 200 Mc. This results in full scale configurations which are all 3 meters long with a maximum diameter = 0.66 m and 0.75 m.[1]

To examine the effect of configuration shape on the model cross-sections, these two models are considered as four; i.e., the Carrot with the cone tip in front, the Carrot with the spherical bulb in front, the Cone with the tip in front, and the Cone with its base in front. These four configurations have approximately the same length-to-diameter ratio, but otherwise differ in many respects.

The experimental data (Ref. 23) scaled to 200 Mc are displayed graphically in Figure A.4-2.

Average curves can be fitted to this 200 Mc data which serve to predict most of the experimental points to within a factor of three. These curves, together with maximum and minimum curves, are shown in Figure A.4-3. For horizontal polarization the average curve is within a factor of three of all the experimental data for aspects out to 20 degrees from the front and is always within a factor of eight of the remaining data in the 25 to 60 degree aspect range. For vertical polarization the average curve is within a factor of three of all the data, except for the aspect of 40 degrees, at which the average is within a factor of five of the extremes.

[1]This may be compared with lengths between 2.16 and 1.40 meters and a maximum diameter of 1 meter for the six configurations of interest here.

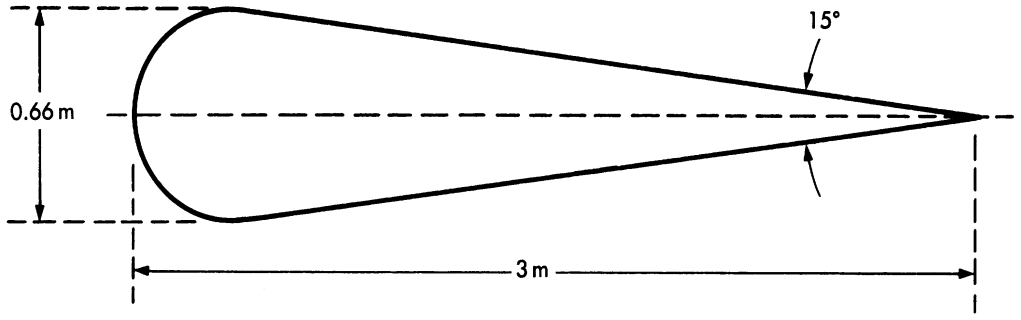

Carrot

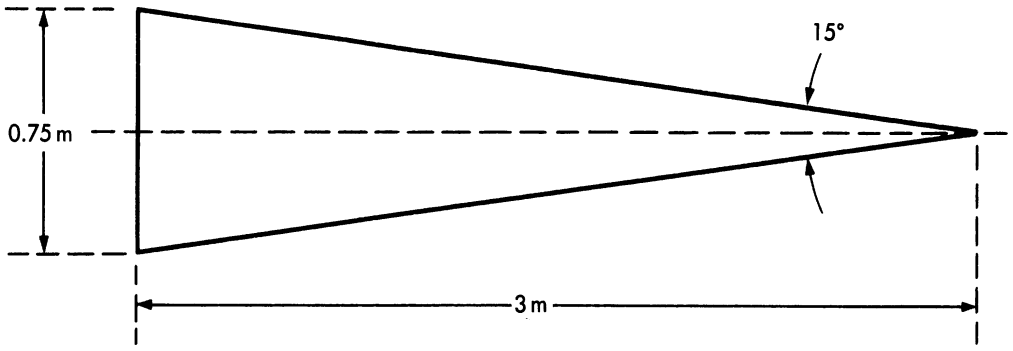

Cone

FIG. A.4-1 CARROT AND CONE MODELS
(Scaled to 200 Mc size)

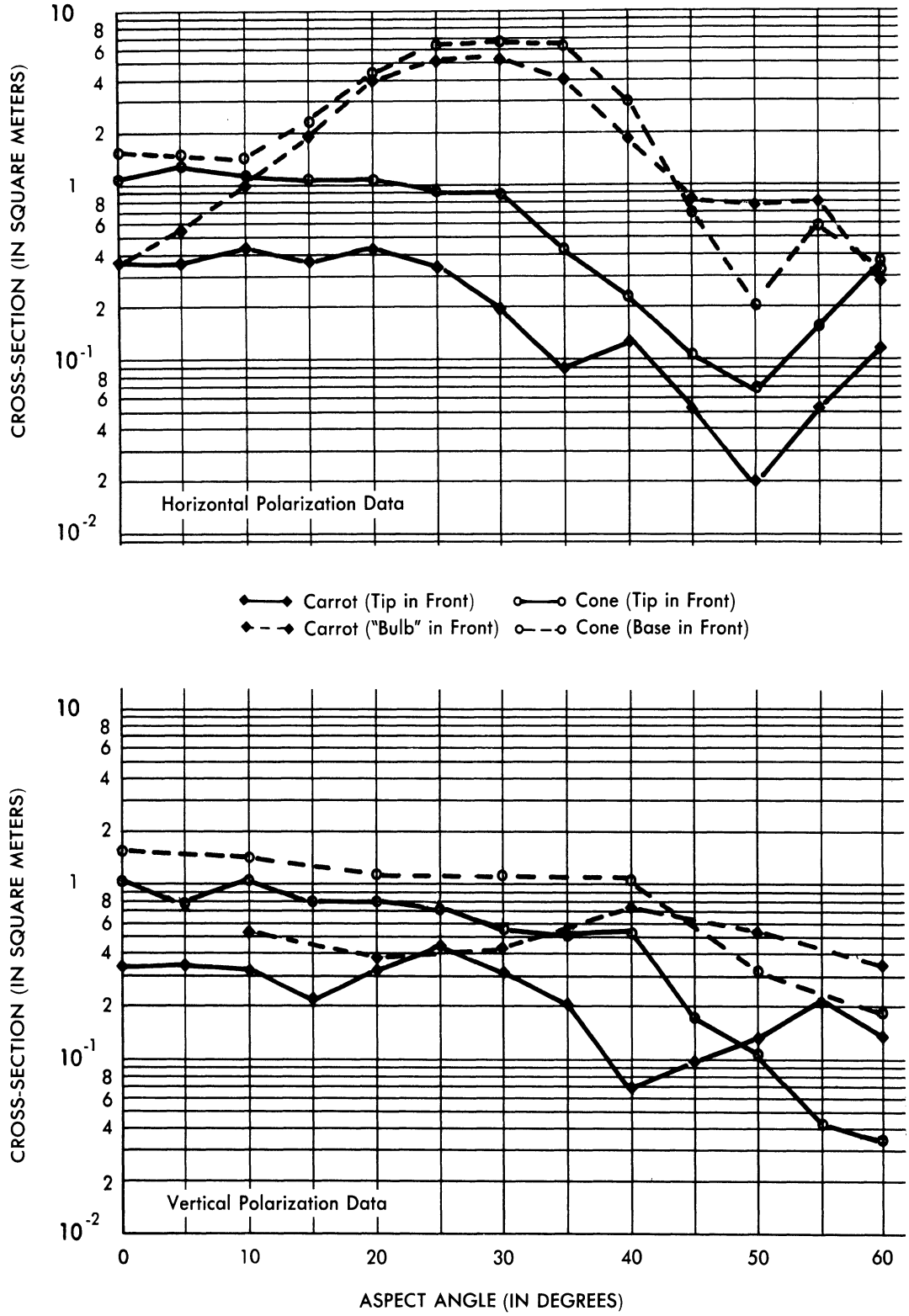

FIG. A.4-2 CROSS-SECTION vs. ASPECT ANGLE FOR CARROT AND CONE DATA (200 Mc)

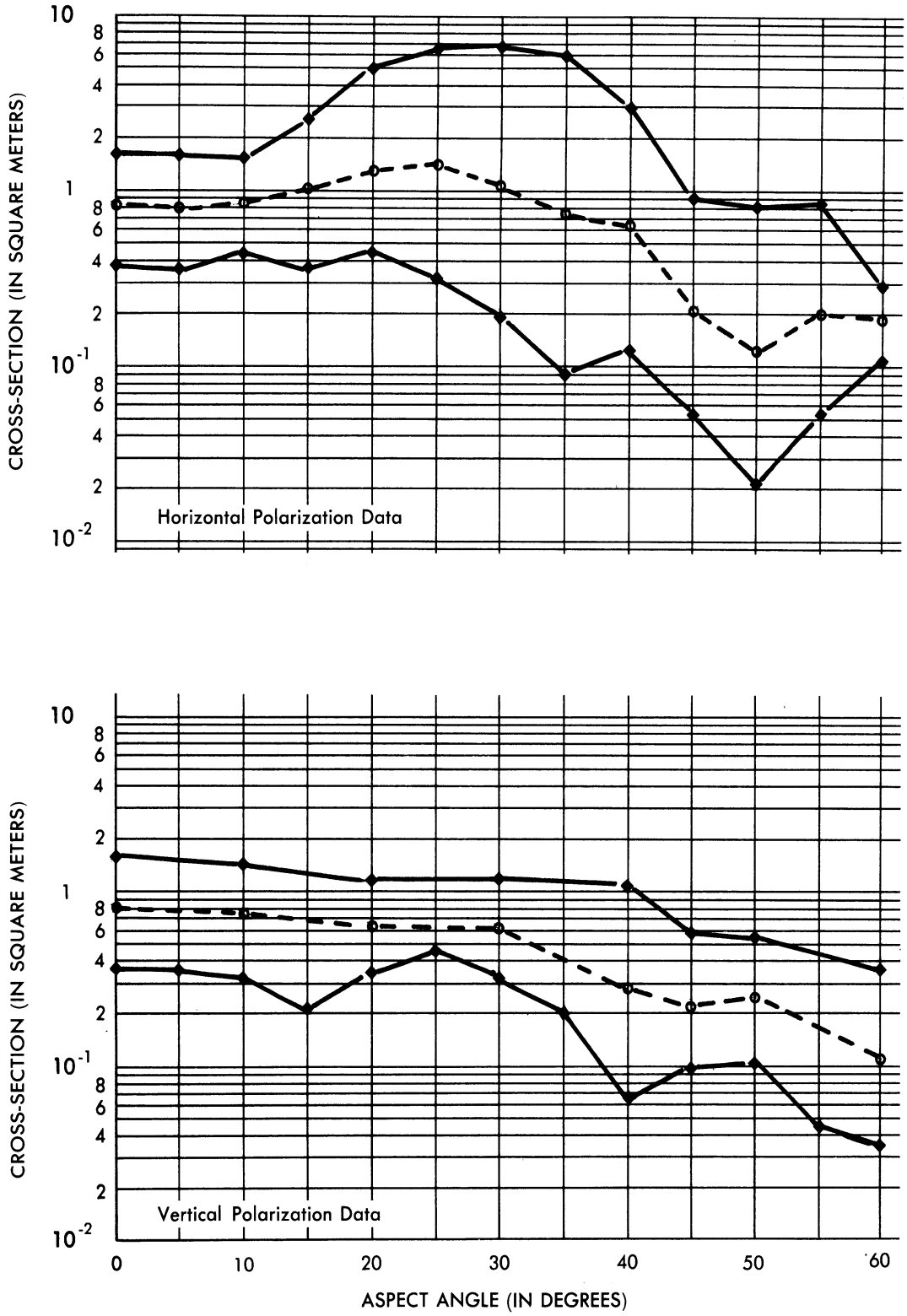

FIG. A.4-3 LARGEST, SMALLEST, AND AVERAGE CROSS-SECTIONS — CARROT AND CONE EXPERIMENTAL DATA (200 Mc)

A.4.3 Experimental Data for the 7-OC

Static experiments on 7-OC-type missiles were performed by the Microwave Radiation Company, Inc. (MRC), and by the Evans Signal Laboratory (ESL) at the instigation of Project Wizard. These data (scaled to full 7-OC dimensions) are given in Reference 1.

Using the 7-OC 75 Mc data appearing in Reference 1 and scaling it to 200 Mc yields data for the three configurations shown in Figure A.4-4. Here we have three configurations for which (at 200 Mc)

$$L/\lambda = 1.54,\ 1.46, \text{ and } 1.27; \text{ and}$$

$$D/\lambda = 0.346,\ 0.360, \text{ and } 0.346.^{1}$$

As in the Carrot and Cone experiments, the number of configurations is increased (over the aspect range of interest) by considering the model rotated through 180 degrees to be a different configuration. Combining the data from the two sources (MRC and ESL) yields ten experimental curves both for horizontal and vertical polarization:

1. 7-OC Model—nose in front (MRC data),
2. 7-OC Model—nose in front (ESL data),
3. 7-OC Model—tail in front (MRC data),
4. 7-OC Model—tail in front (ESL data),
5. 7-OC (Hemispherical Stern)—nose in front (MRC data),
6. 7-OC (Hemispherical Stern)—nose in front (ESL data),
7. 7-OC (Hemispherical Stern)—tail in front (MRC data),
8. 7-OC (Hemispherical Stern)—tail in front (ESL data),

---

[1]Compare with the $0.93 \leqslant L/\lambda \leqslant 1.43$ and $D/\lambda = 0.67$ ratios for the six R-W re-entry designs.

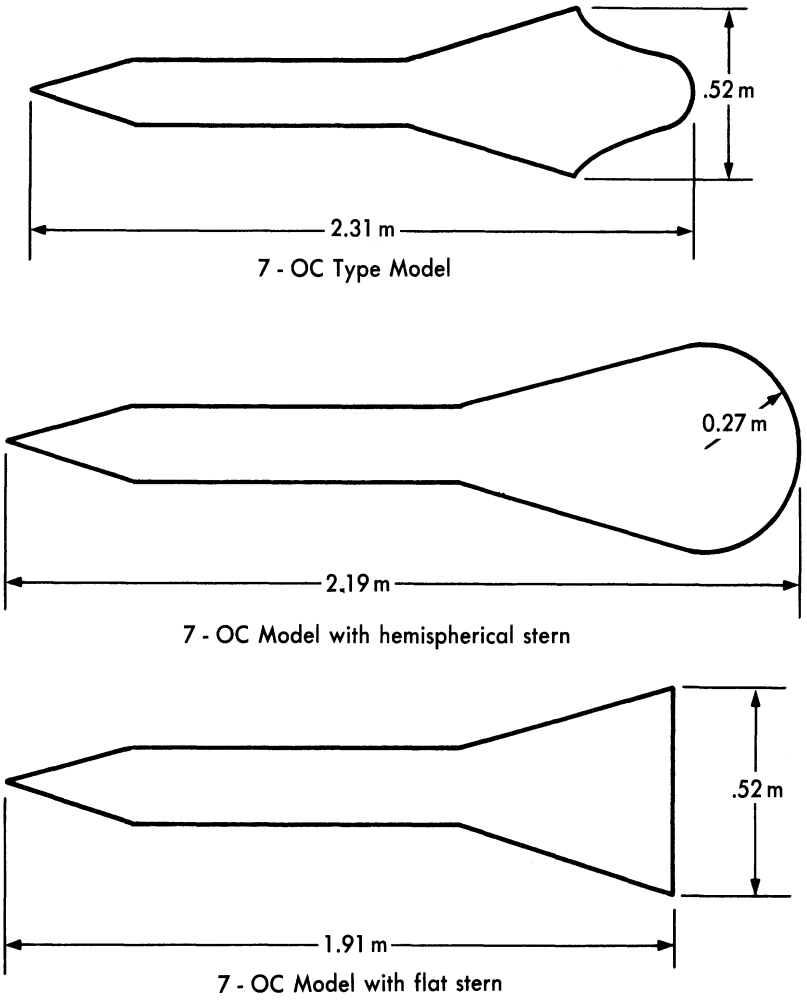

(The Dimensions are obtained by scaling the 75 Mc data from Ref. 1 to 200 Mc)

FIG. A.4-4 7-OC TYPE MODELS

9. 7-OC (Flat Stern)—nose in front (MRC data), and

10. 7-OC (Flat Stern)—tail in front (MRC data).

Figure A.4-5 shows the largest, smallest, and average values obtained for the cross-sections of the ten shapes listed above by scaling the 75 Mc—7-OC data to 200 Mc. (Table A.4-1 contains the data from which Fig. A.4-5 was constructed.)

A.4.4 Summary of Experimental Data for Carrots, Cones, and the 7-OC

By grouping the 7-OC and Carrot and Cone data and considering each of the models both from the front and the back, fourteen experimental cross-section vs. aspect curves are obtained for ten different configurations. In some cases these ten configurations differ markedly (compare Fig. A.4-1 and A.4-4), but the length (L) and maximum diameter (D) of each satisfy the conditions:

$$1.27 < L/\lambda < 2.00 \text{ and } 0.34 < D/\lambda < 0.50.$$

All of the data for vertical polarization are grouped in Figure A.4-6, which shows the range of values of σ (largest and smallest) as a function of aspect, together with an average curve. All of the data lie within a factor of five of the average curve.

The horizontal polarization data for the five "cone-nosed" configurations are grouped in Figure A.4-7 in a similar manner. In this case the average curve fits the data to within a factor of six, except for the aspect angle range of 10 to 40 degrees.

The remaining horizontal polarization data are grouped in Figure A.4-8. The average curve lies within a factor of five of all the data.

The experimental data examined in this section indicates that the cross-section of a configuration does not vary to any appreciable extent with changes in configuration shape if the L/λ and D/λ ratios are restricted by the above inequalities. (This is especially true for vertical polarization.) The configurations involved in these experiments were

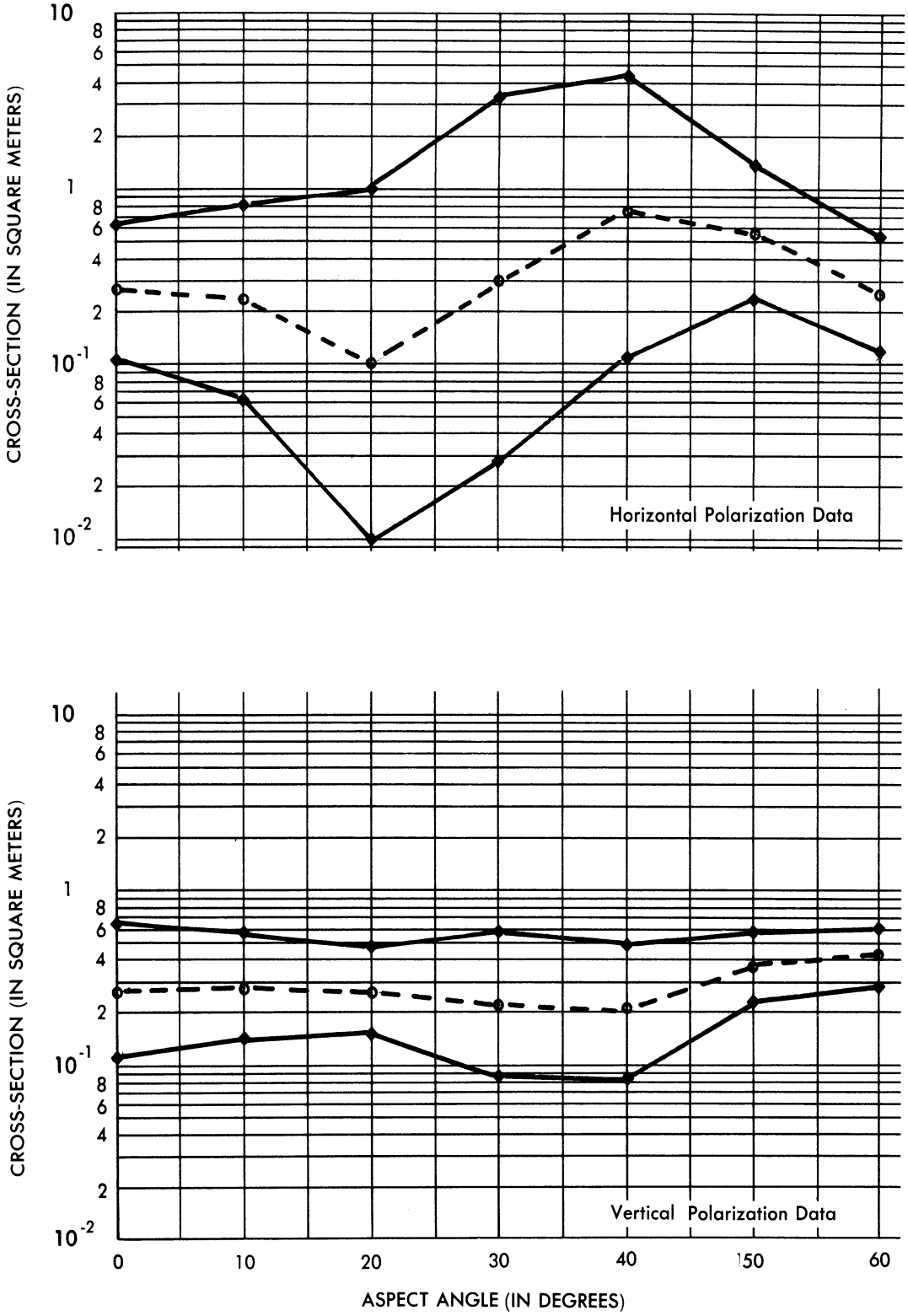

FIG. A.4-5 LARGEST, SMALLEST, AND AVERAGE CROSS-SECTIONS — 7-OC EXPERIMENTAL DATA (200 Mc)

TABLE A.4-1

CROSS-SECTION DATA FOR CONFIGURATIONS SHOWN IN FIGURE A.4-4 AT 200 Mc (in m^2)

Configuration	Source	Pol.	Aspect						
			0^o	10^o	20^o	30^o	40^o	50^o	60^o
7-OC model—nose in front	MRC	H	.12	.07	.01	.03	.31	.44	.53
7-OC model—nose in front	ESL	H	.17	.12	.01	.07	.24	.27	.42
7-OC model—tail in front	MRC	H	.17	.22	.60	2.1	2.5	.93	.27
7-OC model—tail in front	ESL	H	.14	.34	.92	2.2	2.9	1.0	.42
7-OC (Hemi. Stern)—nose in front	MRC	H	.19	.18	.19	.13	.04	.25	.38
7-OC (Hemi. Stern)—nose in front	ESL	H	.28	.31	.30	.22	.11	.38	.49
7-OC (Hemi. Stern)—tail in front	MRC	H	.31	.42	1.0	2.2	3.3	1.4	.13
7-OC (Hemi. Stern)—tail in front	ESL	H	.32	.32	.90	3.3	4.2	1.2	.13
7-OC (Flat Stern)—nose in front	MRC	H	.36	.40	.49	.77	.85	.70	.21
7-OC (Flat Stern)—tail in front	MRC	H	.62	.81	1.0	1.2	.77	.28	.28
7-OC model—nose in front	MRC	V	.13	.14	.15	.08	.08	.24	.34
7-OC model—nose in front	ESL	V	.12	.15	.17	.13	.12	.24	.34
7-OC model—tail in front	MRC	V	.20	.21	.19	.22	.21	.36	.34
7-OC model—tail in front	ESL	V	.14	.16	.18	.19	.19	.34	.29
7-OC (Hemi. Stern)—nose in front	MRC	V	.22	.24	.27	.23	.15	.25	.42
7-OC (Hemi. Stern)—nose in front	ESL	V	.18	.22	.27	.27	.21	.25	.40
7-OC (Hemi. Stern)—tail in front	MRC	V	.42	.38	.42	.56	.31	.46	.56
7-OC (Hemi. Stern)—tail in front	ESL	V	.20	.20	.22	.23	.23	.42	.42
7-OC (Flat Stern)—nose in front	MRC	V	.33	.35	.33	.27	.28	.36	.42
7-OC (Flat Stern)—tail in front	MRC	V	.62	.56	.46	.44	.49	.56	.40

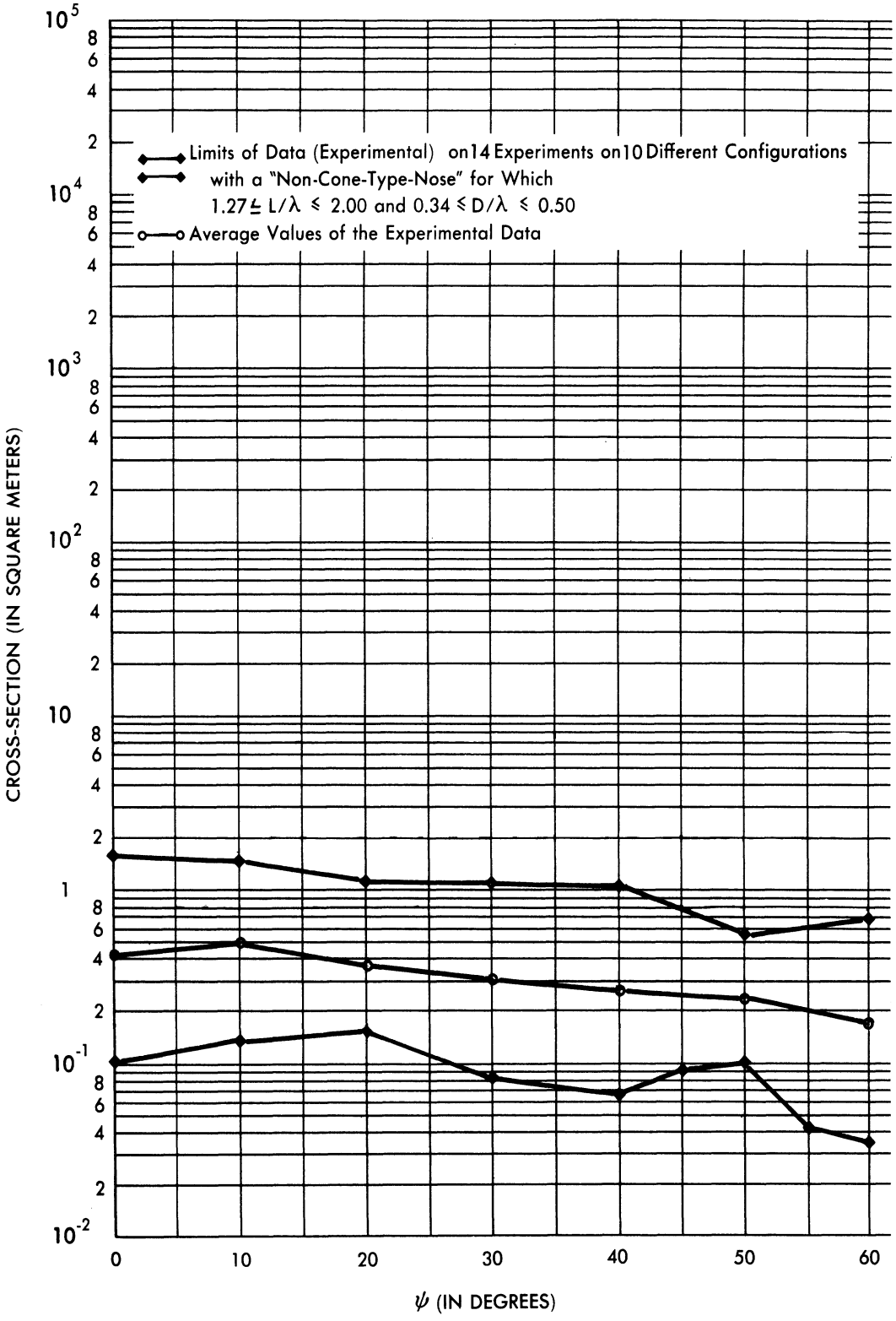

FIG. A.4-6 CROSS-SECTION DATA AT 200 Mc (VERTICAL POLARIZATION)

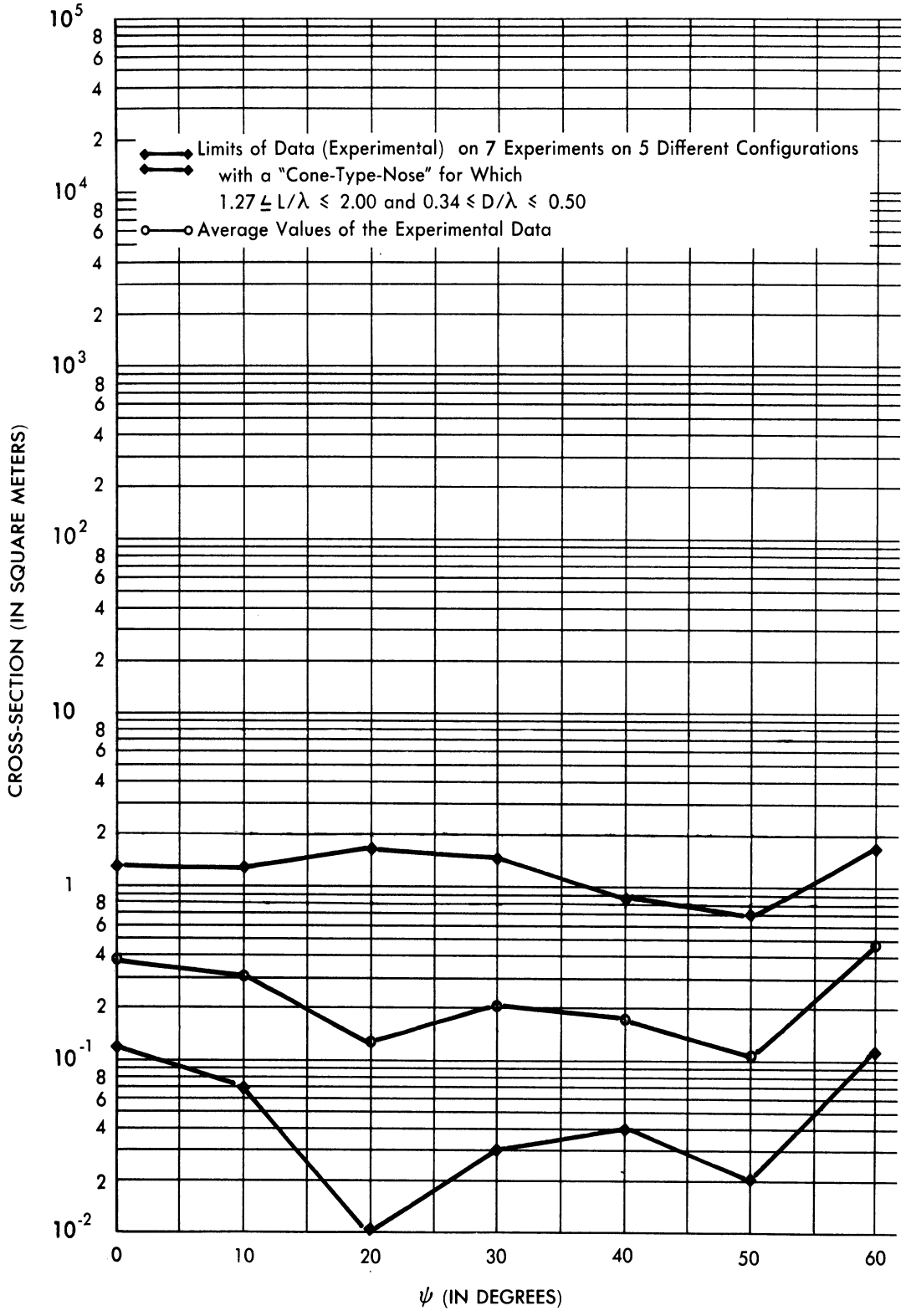

FIG. A.4-7 CROSS-SECTION DATA AT 200 Mc (HORIZONTAL POLARIZATION) - I

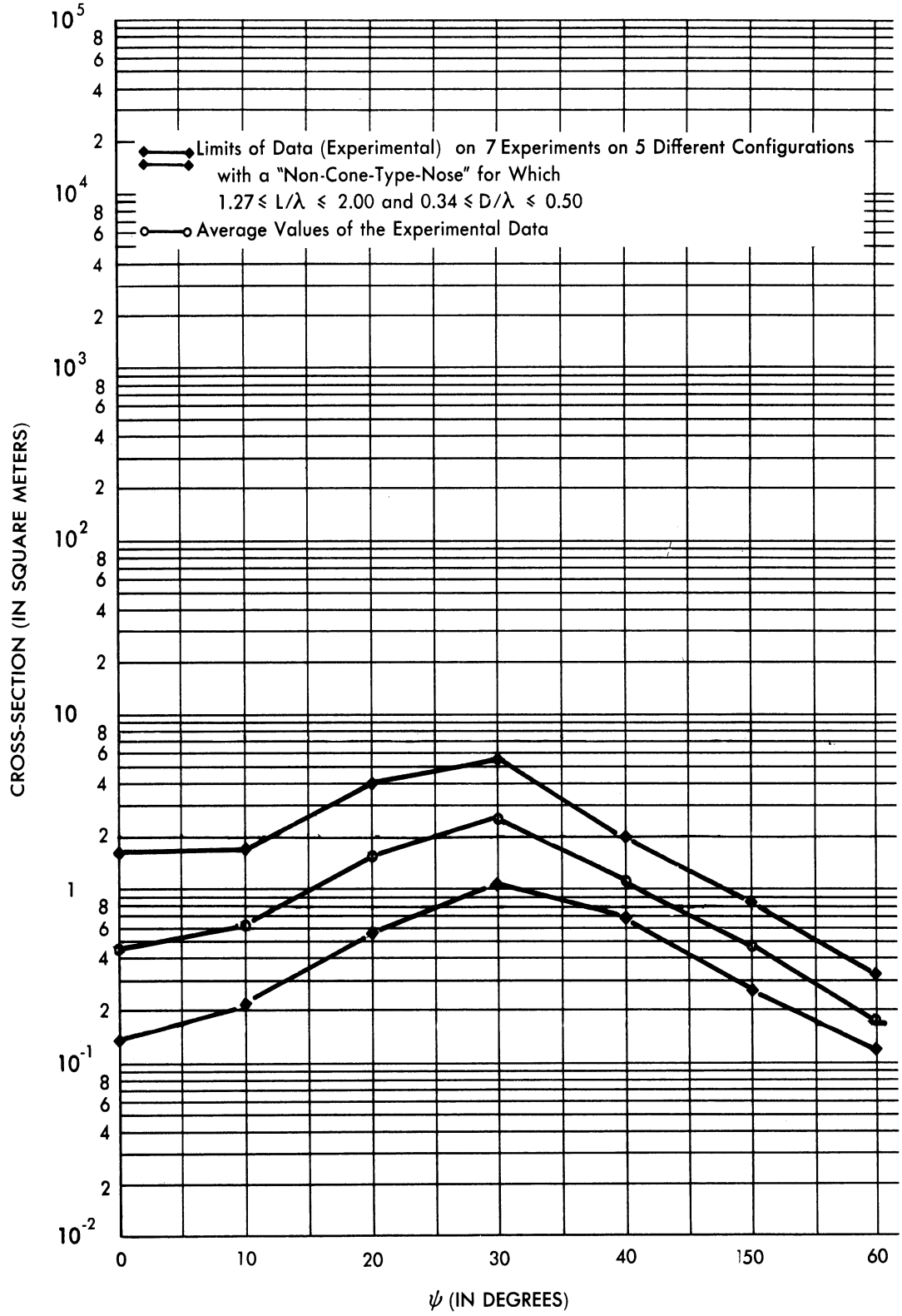

FIG. A.4-8' CROSS-SECTION DATA AT 200 Mc (HORIZONTAL POLARIZATION)-II

all pointed at one end only. If the body were pointed at both ends, other data indicate that this relative constancy of the cross-section in the 0- to 60-degree aspect interval would be expected not to be as pronounced (see Ogive data in App. B).

APPENDIX B

EFFECT OF PERTURBATION TO THE SHAPE OF THE RE-ENTRY BODY ON THE CROSS-SECTION IN THE 200 TO 3000 Mc RANGE

B.1 INTRODUCTION

A part of The University of Michigan Project No. 2428 was the determination of perturbations to the six R-W re-entry designs which might reduce the radar cross-section at 200, 1000, and 3000 Mc for aspect angles out to 60 degrees off-nose.

In this perturbation study eight modifications, Configurations A through H, were considered. Configurations A, C, E, and G are modifications of Configurations I—III, and Configurations B, D, F, and H are modifications of Configurations IV—VI. These eight perturbations are shown in Figures B.1-1 through B.1-4.

Configurations A and B are obtained from the R-W re-entry designs by capping the nose with a cone; Configurations C and D enclose the re-entry shape except the rear hemisphere in an ogive; Configurations E and F are obtained from Configurations I—VI by capping the nose with a cone and filling in and rounding off the step; and Configurations G and H are obtained from the R-W designs by capping both the nose and the tail with cones as well as filling in and rounding off the step.

It is intended that these "caps" be made of a material which will vaporize upon re-entry so that the configurations will reduce to the R-W design. Figure B.1-5 displays the process of rounding off the step in the case of Configuration G.

In what follows the computational procedures are outlined and the results obtained are compared with the results for Configuration I. (It will be recalled from Appendix A that of the six R-W re-entry designs, Configuration I yields the smallest cross-section.) A summary of the nose-on cross-section data is given in Section B.4.

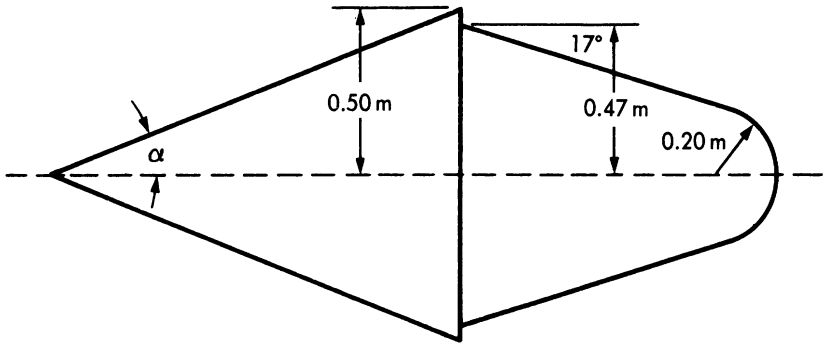

FIG. B.1-1 CONFIGURATIONS A AND B
(α=20° for Conf. A and α=40° for Conf. B)

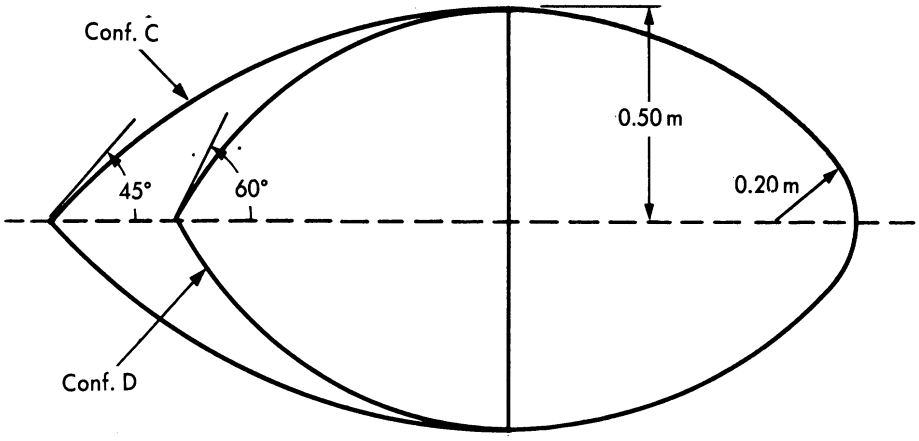

FIG. B.1-2 CONFIGURATIONS C AND D
(Ogives faired into the hemispherical stern)

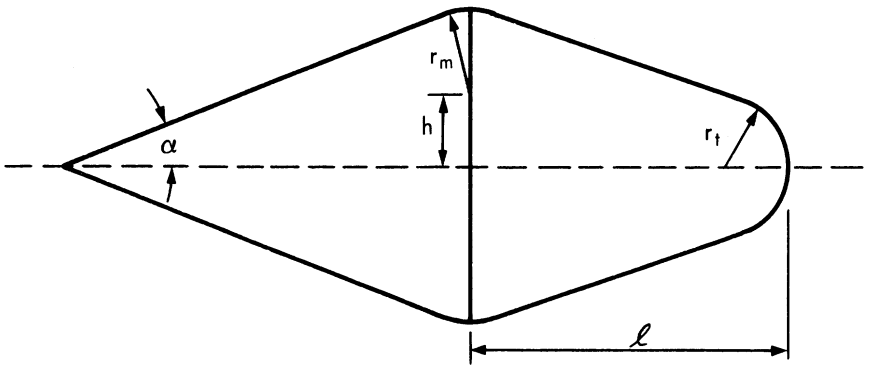

Conf.	α	h (m)	r_m (m)	r_t (m)	ℓ (m)
E	20°	0.22	0.28	0.20	1.03
F	40°	0.43	0.07	0.20	1.03

FIG. B.1-3 CONFIGURATIONS E AND F

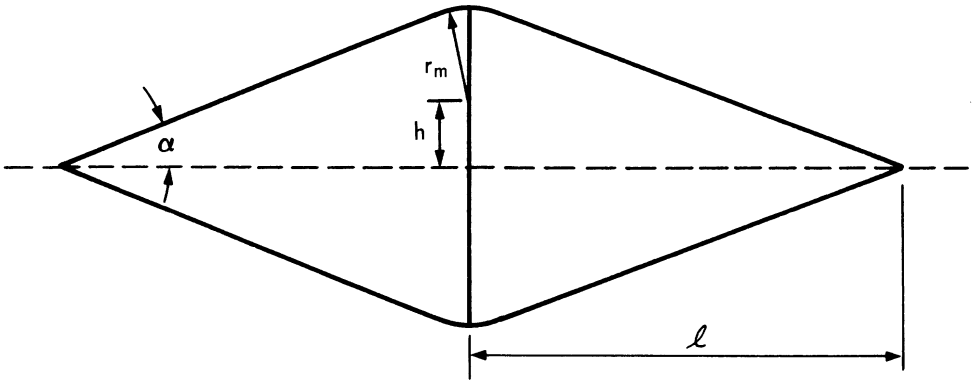

Conf.	α	r_m (m)	h (m)	ℓ (m)
G	20°	0.28	0.22	1.45
H	40°	0.07	0.43	1.45

FIG. B.1-4 CONFIGURATIONS G AND H

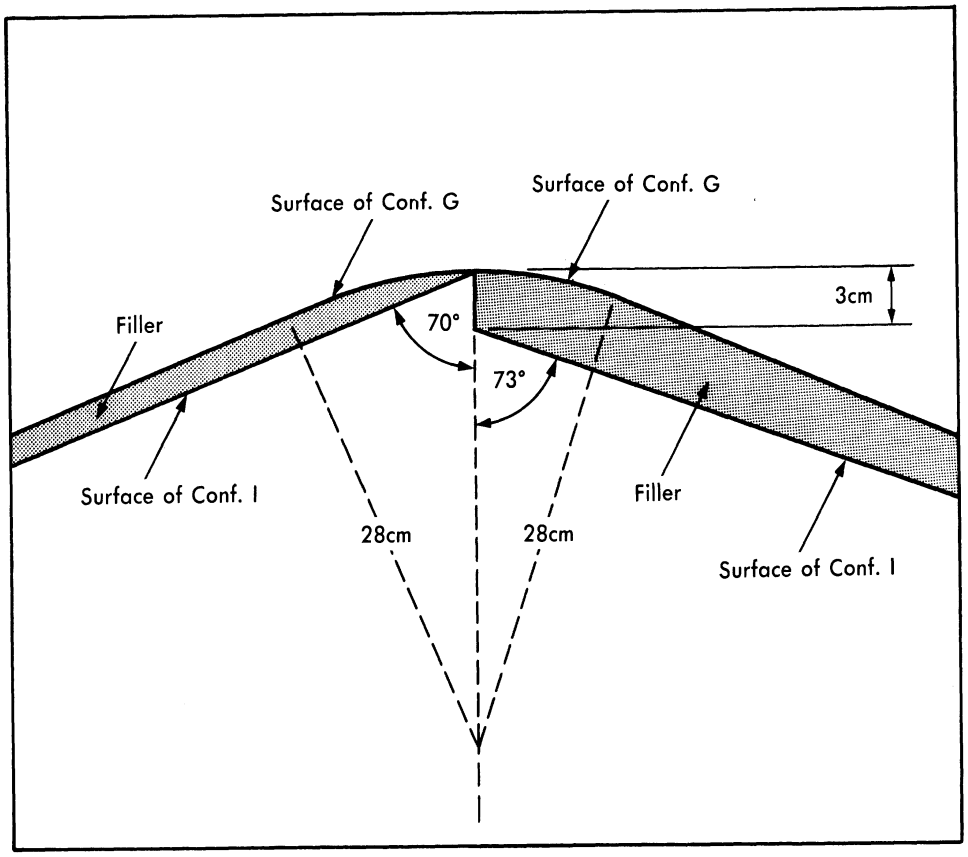

FIG. B.1-5 THE ROUNDED STEP IN CONFIGURATION G

B.2 COMPUTATIONAL PROCEDURES (1000–3000 Mc)

The techniques employed in determining the cross-sections at 1000 and 3000 Mc were based upon physical optics.[1] As mentioned in Appendix A, the cross-sections of Configurations I–VI were determined by two methods, one yielding average cross-sections and the other taking into account phase differences. The same approach was used for Configurations A and B.

---

[1]The basic theory involved is discussed in detail in Appendix A of Reference 5.

B.2.1 Computational Procedures for Configurations I–VI, A and B

The formulas used in the computation of the cross-sections of Configurations I–VI, A, and B are listed below by method.[1] (Since the procedure was applied for aspect angles out to ψ = 180 degrees for 3000 Mc, under University of Michigan Project 2360, the required formulas for the additional values of ψ are also included.) The meanings of the various parameters involved in these formulas are defined in Figure B.2-1.

B.2.1.1 Method I ($0 \leqslant \psi < \pi/2$)

For $\psi = 0^o$

$$\sigma = \pi R_n^2 + \pi R_2^2 \tan^2 a_n \ .$$

For $0^o < \psi \leqslant a_n$

$$\sigma = \pi R_n^2 + \frac{\lambda R_2}{8\pi \sin\psi}\left[\tan^2(a_n + \psi) + \tan^2(a_n - \psi)\right] \ .$$

For $a_n \leqslant \psi < \frac{\pi}{2} - a_n$

$$\sigma = \pi R_n^2 + \frac{\lambda R_2}{8\pi \sin\psi}\left[\tan^2(a_n + \psi)\right] \ .$$

For $\psi = \frac{\pi}{2} - a_n$

$$\sigma = \frac{8\pi\left[R_2^{3/2} - R_n^{3/2}\cos^{3/2}(a_n)\right]^2}{9\lambda \sin^2 a_n \cos a_n} \ .$$

For $\frac{\pi}{2} - a_n < \psi < \frac{\pi}{2}$

$$\sigma = \frac{\lambda R_2 \tan^2(a_n + \psi)}{8\pi \sin\psi} \ .$$

[1] An improvement on the approach used here to estimate the "finite cone" contributions will be discussed in the next report on this contract.

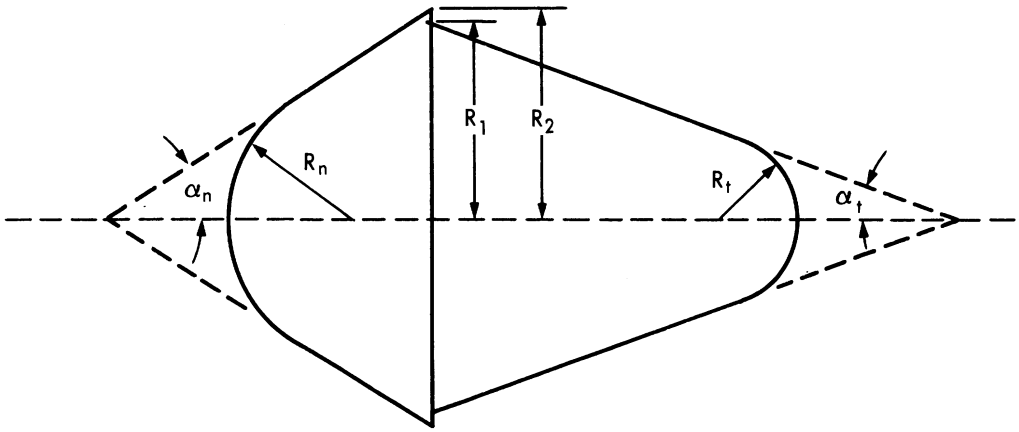

Configuration	α_n	R_n (m)	α_t	R_t (m)	R_2 (m)	R_1 (m)
I	20°	0.15	17°	0.20	0.50	0.47
II	"	0.30	"	"	"	"
III	"	0.45	"	"	"	"
IV	40°	0.15	"	"	"	"
V	"	0.30	"	"	"	"
VI	"	0.45	"	"	"	"
A	20°	0	"	"	"	"
B	40°	0	"	"	"	"

FIG. B.2-1 THE R-W RE-ENTRY DESIGNS (CONFIGURATIONS I - VI) AND CONFIGURATIONS A AND B

B.2.1.2 Method II ($0 \leqslant \psi < \pi/2$)

For $\psi = 0^{o}$

$$\sigma = \sigma_1 + \sigma_2 + 2\sqrt{\sigma_1 \sigma_2}\cos(\phi_1' - \phi_2) \ .$$

For $0 < \psi \leqslant \alpha_n$

$$\sigma = \sigma_1 + \sigma_3 + \sigma_4 + 2\sqrt{\sigma_1 \sigma_3}\cos(\phi_1 - \phi_3)$$

$$+ 2\sqrt{\sigma_1 \sigma_4}\cos(\phi_1 - \phi_4) + 2\sqrt{\sigma_3 \sigma_4}\cos(\phi_3 - \phi_4) \ .$$

For $\alpha_n \leqslant \psi < \frac{\pi}{2} - \alpha_n$

$$\sigma = \sigma_1 + \sigma_3 + 2\sqrt{\sigma_1 \sigma_3}\cos(\phi_1 - \phi_3) \ ;$$

where

$$\sigma_1 = \pi R_n^2 \ ,$$

$$\sigma_2 = \pi R_2^2 \tan^2 \alpha_n \ ,$$

$$\sigma_3 = \frac{\lambda R_2 \tan^2(\alpha_n + \psi)}{8\pi \sin\psi} \ ,$$

$$\sigma_4 = \frac{\lambda R_2 \tan^2(\alpha_n - \psi)}{8\pi \sin\psi} \ ,$$

$$\phi_1' = \frac{4\pi R_n}{\lambda}\left(\frac{1}{\sin\alpha_n} - 1\right) + \frac{\pi}{2} ,$$

$$\phi_1 = \frac{4\pi R_n}{\lambda}\left(\frac{\cos\psi}{\sin\alpha_n} - 1\right) + \frac{\pi}{2} ,$$

$$\phi_2 = \frac{4\pi R_2}{\lambda \tan\alpha_n} - \frac{\pi}{2} ,$$

$$\phi_3 = \frac{4\pi R_2 \cos(\alpha_n + \psi)}{\lambda \sin\alpha_n} + \frac{\pi}{4} , \text{ and}$$

$$\phi_4 = \frac{4\pi R_2 \cos(\alpha_n - \psi)}{\lambda \sin\alpha_n} - \frac{\pi}{4} .$$

B.2.1.3 Computations For $\frac{\pi}{2} < \psi \leqslant \pi$

In applying Methods I or II in the aspect range out to $\psi = 180$ degrees, the formulas listed below are employed.

For $\frac{\pi}{2} < \psi < \frac{\pi}{2} + \alpha_t$

$$\sigma = \sigma_4 + \sigma_5 + \sigma_6 - 2\sqrt{\sigma_4\sigma_5}$$

$$- \frac{\lambda\sqrt{R_1 R_2}\left[\tan(\psi - \alpha_t) + \frac{1}{\tan\psi}\right]}{4\pi \sin\psi \tan\psi} \cos\left[\frac{4\pi}{\lambda}(R_2 - R_1)\sin\psi\right] ;$$

where

$$\sigma_4 = \frac{\lambda R_1 \tan^2(\psi - \alpha_t)}{8\pi \sin\psi} ,$$

$$\sigma_5 = \lambda R_1/8\pi \sin\psi \tan^2\psi \text{ , and}$$

$$\sigma_6 = \lambda R_2/8\pi \sin\psi \tan^2\psi \text{ .}$$

For $\psi = \pi/2 + \alpha_t$

$$\sigma = \frac{8\pi \left[R_1^{3/2} - R_t^{3/2} \cos^{3/2}\alpha_t\right]^2}{9\lambda \sin^2\alpha_t \cos\alpha_t} \text{ .}$$

For $\frac{\pi}{2} + \alpha_t < \psi \leqslant \pi - \alpha_t$

$$\sigma = \sigma_7 + \sigma_4 + \sigma_5 + \sigma_6$$
$$+ 2\sqrt{\sigma_7\sigma_4}\cos(\phi_7 - \phi_4)$$
$$+ 2\sqrt{\sigma_7\sigma_5}\cos(\phi_7 - \phi_5)$$
$$+ 2\sqrt{\sigma_7\sigma_6}\cos(\phi_7 - \phi_6)$$
$$+ 2\sqrt{\sigma_4\sigma_5}\cos(\phi_4 - \phi_5)$$
$$+ 2\sqrt{\sigma_4\sigma_6}\cos(\phi_4 - \phi_6)$$
$$+ 2\sqrt{\sigma_5\sigma_6}\cos(\phi_5 - \phi_6) \text{ ;}$$

where

$$\sigma_7 = \pi R_t^2 \text{ ,}$$

$\frac{\pi}{2} + \alpha_t < \psi \leqslant \pi - \alpha_t$ (cont.)

$$\sigma_4 = \frac{\lambda R_1 \tan^2(\psi - \alpha_t)}{8\pi \sin\psi} \quad ,$$

$$\sigma_5 = \lambda R_1 / 8\pi \sin\psi \tan^2\psi \quad ,$$

$$\sigma_6 = \lambda R_2 / 8\pi \sin\psi \tan^2\psi \quad ,$$

$$\phi_7 = \frac{4\pi R_t}{\lambda}\left(\frac{\cos\psi}{\sin\alpha_t} - 1\right) + \frac{\pi}{2} \quad ,$$

$$\phi_4 = \frac{4\pi R_1}{\lambda}\left(\frac{\cos\left[\alpha_t - \psi\right]}{\sin\alpha_t}\right) - \frac{\pi}{4} \quad ,$$

$$\phi_5 = \phi_4 + \pi \quad , \text{ and}$$

$$\phi_6 = \phi_4 - \frac{4\pi(R_2 - R_1)\sin\psi}{\lambda} \quad .$$

For $\pi - \alpha_t \leqslant \psi < \pi$

$$\begin{aligned}\sigma = {} & \sigma_7 + \sigma_4 + \sigma'_5 + \sigma''_5 + \sigma'_6 + \sigma''_6 + \sigma_8 \\ & + 2\sqrt{\sigma_7\sigma_4}\cos(\phi_7 - \phi_4) + 2\sqrt{\sigma_7\sigma'_5}\cos(\phi_7 - \phi'_5) \\ & + 2\sqrt{\sigma_7\sigma''_5}\cos(\phi_7 - \phi''_5) + 2\sqrt{\sigma_7\sigma'_6}\cos(\phi_7 - \phi'_6) \\ & + 2\sqrt{\sigma_7\sigma''_6}\cos(\phi_7 - \phi''_6) + 2\sqrt{\sigma_7\sigma_8}\cos(\phi_7 - \phi_8) \\ & + 2\sqrt{\sigma_4\sigma'_5}\cos(\phi_4 - \phi'_5) + 2\sqrt{\sigma_4\sigma''_5}\cos(\phi_4 - \phi''_5)\end{aligned}$$

$\pi - \alpha_t \leq \psi < \pi$ (cont.)

$$+ 2\sqrt{\sigma_4\sigma'_6}\cos(\phi_4 - \phi'_6) + 2\sqrt{\sigma_4\sigma''_6}\cos(\phi_4 - \phi''_6)$$

$$+ 2\sqrt{\sigma_4\sigma_8}\cos(\phi_4 - \phi_8) + 2\sqrt{\sigma'_5\sigma''_5}\cos(\phi'_5 - \phi''_5)$$

$$+ 2\sqrt{\sigma'_5\sigma'_6}\cos(\phi'_5 - \phi'_6) + 2\sqrt{\sigma'_5\sigma''_6}\cos(\phi'_5 - \phi''_6)$$

$$+ 2\sqrt{\sigma'_5\sigma_8}\cos(\phi'_5 - \phi_8) + 2\sqrt{\sigma''_5\sigma'_6}\cos(\phi''_5 - \phi'_6)$$

$$+ 2\sqrt{\sigma''_5\sigma''_6}\cos(\phi''_5 - \phi''_6) + 2\sqrt{\sigma''_5\sigma_8}\cos(\phi''_5 - \phi_8)$$

$$+ 2\sqrt{\sigma'_6\sigma''_6}\cos(\phi'_6 - \phi''_6) + 2\sqrt{\sigma'_6\sigma_8}\cos(\phi'_6 - \phi_8)$$

$$+ 2\sqrt{\sigma''_6\sigma_8}\cos(\phi''_6 - \phi_8) \ ;$$

where

$$\sigma_7 = \pi R_t^2 \ ,$$

$$\sigma_4 = \frac{\lambda R_1 \tan^2(\psi - \alpha_t)}{8\pi \sin\psi} \ ,$$

$$\sigma'_5 = \sigma''_5 = \lambda R_1 / 4\pi \sin\psi \tan^2\psi \ ,$$

$$\sigma'_6 = \sigma''_6 = \lambda R_2 / 4\pi \sin\psi \tan^2\psi \ ,$$

$$\sigma_8 = \frac{\lambda R_1 \tan^2(\psi + \alpha_t)}{8\pi \sin\psi} \ ,$$

$$\phi_7 = \frac{4\pi R_t}{\lambda}\left(\frac{\cos\psi}{\sin\alpha_t} - 1\right) + \frac{\pi}{2} \ ,$$

$\pi - \alpha_t \leq \psi < \pi$ (cont.)

$$\phi_4 = \frac{4\pi R_1}{\lambda}\left(\frac{\cos\,[\alpha_t - \psi]}{\sin\alpha_t}\right) - \frac{\pi}{4} \quad ,$$

$$\phi_8 = \frac{4\pi R_1}{\lambda}\left(\frac{\cos\,[\alpha_t + \psi]}{\sin\,\alpha_t}\right) + \frac{\pi}{4} \quad ,$$

$$\phi_5' = \phi_4 + \pi \quad ,$$

$$\phi_5'' = \phi_8 + \pi \quad ,$$

$$\phi_6' = \phi_4 + \frac{4\pi\,(R_2 - R_1)\sin\psi}{\lambda} \quad ,$$

and

$$\phi_6'' = \phi_8 + \frac{4\pi\,(R_2 - R_1)\sin\psi}{\lambda} \quad .$$

For $\psi = \pi$

$$\sigma = \sigma_7 + \sigma_9 + \sigma_{10} + 2\sqrt{\sigma_7\sigma_9}\,\cos\,(\phi_7' - \phi_9)$$

$$+ 2\sqrt{\sigma_7\sigma_{10}}\,\cos\,(\phi_7' - \phi_{10}) + 2\sqrt{\sigma_9\sigma_{10}}\,\cos\,(\phi_9 - \phi_{10}) \quad ;$$

where

$$\sigma_7 = \pi R_t^{\,2} \quad ,$$

$$\sigma_9 = \pi R_1^{\,2}\tan^2\alpha_t \quad ,$$

$\psi = \pi$ (cont.)

$$\sigma_{10} = \frac{4\pi^3}{\lambda^2} \left(R_2^2 - R_1^2\right)^2 ,$$

$$\phi'_7 = \frac{4\pi R_t}{\lambda} \left(\frac{1}{\sin \alpha_t} - 1\right) + \frac{\pi}{2} ,$$

$$\phi_9 = \frac{4\pi R_2}{\lambda \tan \alpha_t} - \frac{\pi}{2} , \quad \text{and} \quad \phi_{10} = \frac{4\pi R_2}{\lambda \tan \alpha_t} .$$

The formulas as listed above are used in Method II. To apply Method I it is necessary to delete all of the "cosine terms" from the above formulas (i.e., each factor of $\cos(\phi_i - \phi_j)$ is a measure of the relative phase and should be replaced by zero).

B.2.2 Computations for Configurations C, D, E, F, G, and H

Configurations C and D, being ogival in the front, were computed using the ogive formulas of Reference 5, which are listed below (b = maximum radius = 0.50 m and α = 1/2 nose angle)[1]:

$$\rho = b \left(\frac{1 + \cos \alpha}{\sin^2 \alpha}\right) ;$$

$$h = (b \cos \alpha) \left(\frac{1 + \cos \alpha}{\sin^2 \alpha}\right) .$$

For $0 \leqslant \psi < \frac{\pi}{2} - \alpha$

$$\sigma = \frac{\lambda^2 \tan^4 \alpha}{16\pi \cos^6 \psi \left(1 - \tan^2 \alpha \tan^2 \psi\right)^3} .$$

[1] An extensive discussion of the determination of the cross-section of an ogive and a summary of ogive experimental data will be contained in the next report on this contract.

For $\psi = \frac{\pi}{2} - \alpha$

$$\sigma = \frac{b^2}{4\pi \tan^2(\alpha/2)} \quad .$$

For $\frac{\pi}{2} - \alpha < \psi \leq \frac{\pi}{2}$

$$\sigma = \pi\rho^2 \left(1 - \frac{h}{\rho \sin\psi}\right) \quad .$$

For Configurations E, F, G, and H, the techniques for C and D were employed in the vicinity of $\psi = 0$ degrees, and the basic procedure used on Configurations A and B (Method I) were employed in the vicinity of $\psi = \pi/2 - \alpha_n$. The cross-section curve is faired in between the two points determined.

B.2.3 Cross-Section Data at 1000 and 3000 Mc

The data for Configurations I – VI, A, and B are given in Figures A.3-1 – A.3-9. The cross-sections of Configurations A – H at 1000 and 3000 Mc are shown in Figures B.2-2 and B.2-3. In examining Figures B.2-2 and B.2-3 it should be recalled that the cross-section of Configuration I is approximately 10^{-1} m^2 throughout the aspect interval.

B.3 CROSS-SECTIONS FOR CONFIGURATIONS A – H IN THE 200 TO 500 Mc RANGE

B.3.1 Configurations A – F

In Appendix A the nose-on cross-sections of Configurations I – VI were computed by a "creeping-wave" method. Applying this technique for Configurations A – F, the results shown in Table B.3-1 are obtained. The contribution from the rear, σ_2, is the same for Configurations A – F as it was for Configurations I – VI, but the nose contribution, σ_1,

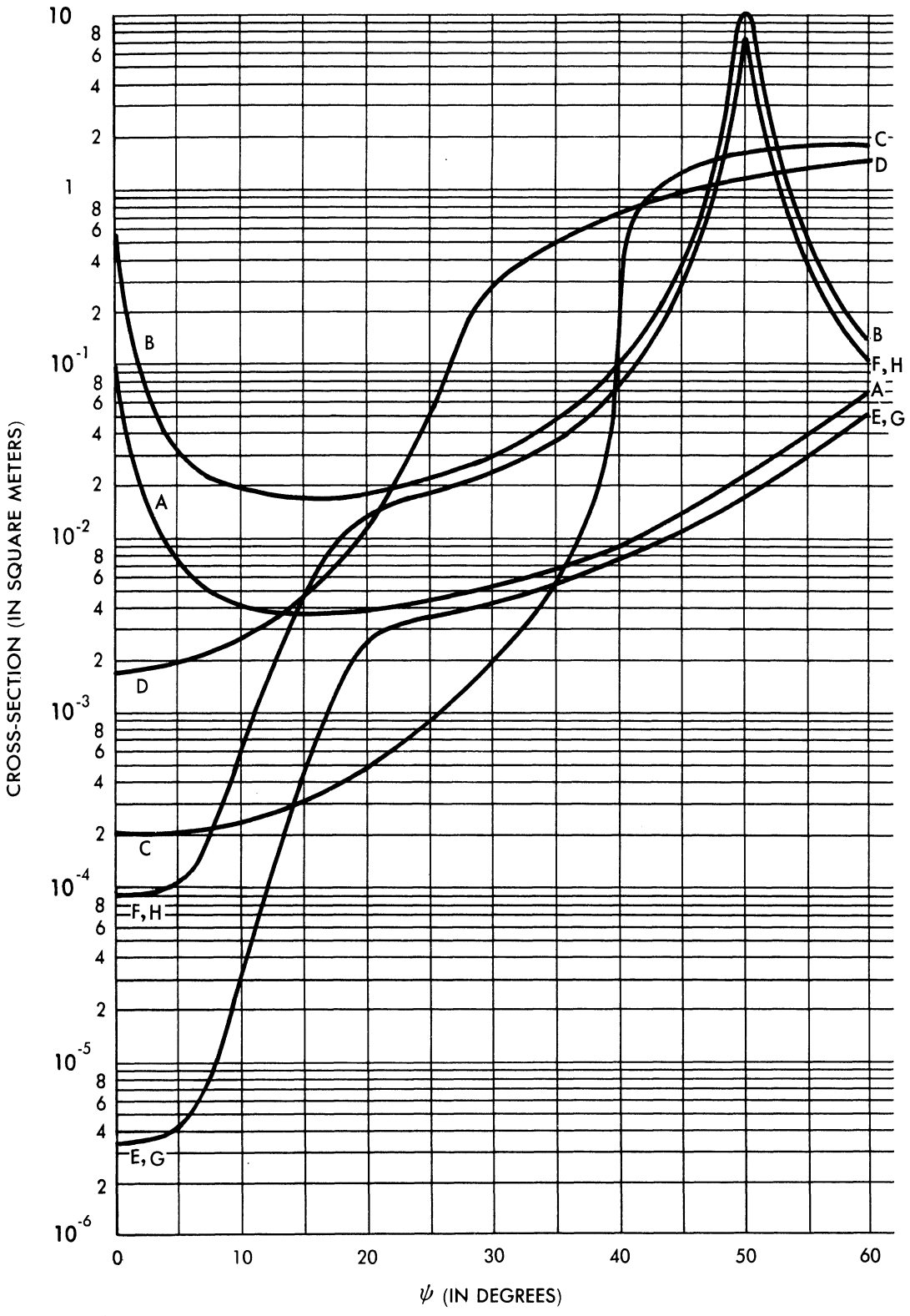

FIG. B.2-2 CROSS-SECTIONS OF CONFIGURATIONS A - H AT 3000 Mc
($\lambda = 0.1$ m)

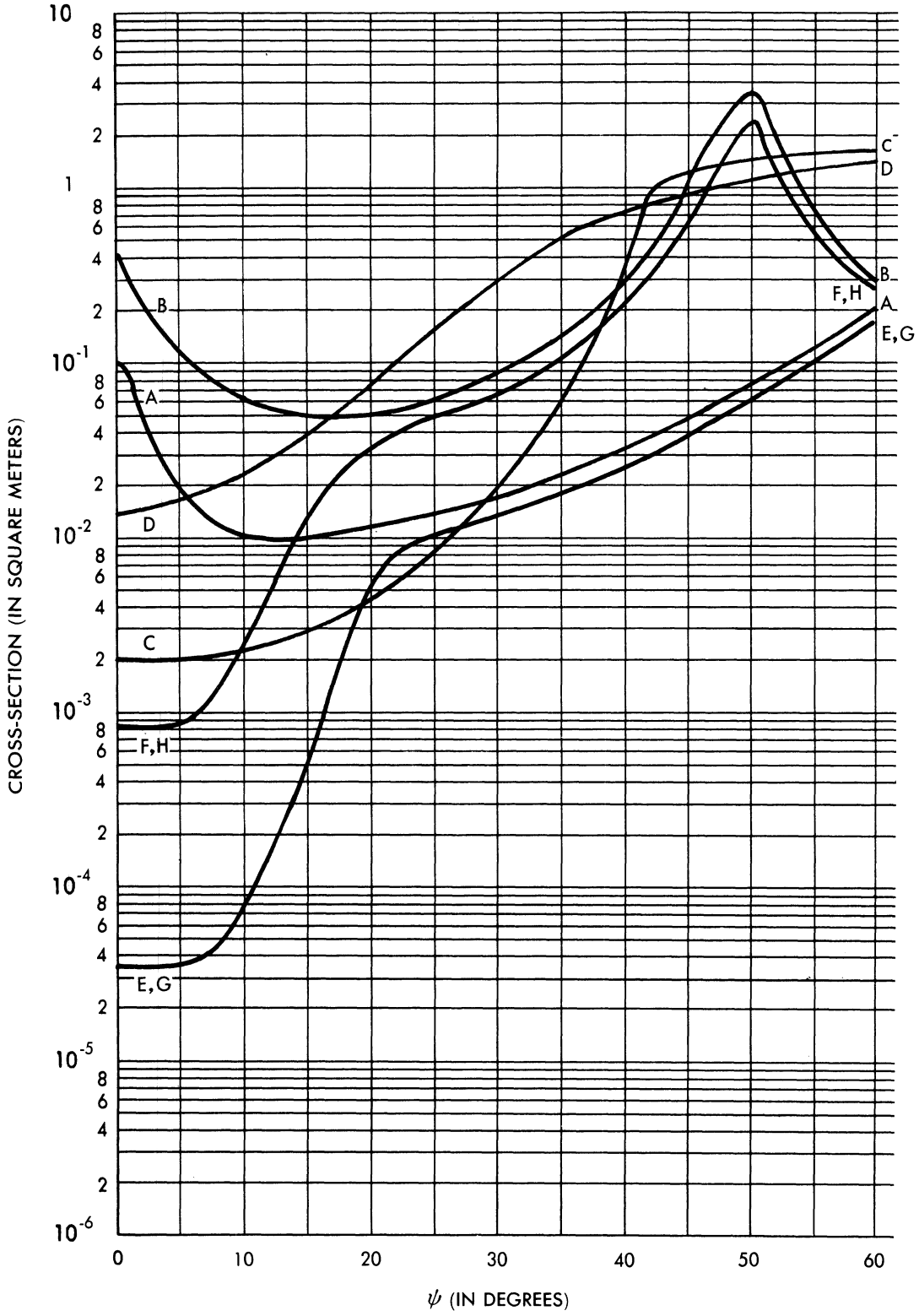

FIG. B.2-3 CROSS-SECTIONS OF CONFIGURATIONS A - H AT 1000 Mc
($\lambda = 0.3$ m)

TABLE B.3-1

NOSE-ON CROSS-SECTIONS (in Square Meters) OF CONFIGURATIONS A – F

	200 Mc			350 Mc			500 Mc		
	Lower Bound	Average	Upper Bound	Lower Bound	Average	Upper Bound	Lower Bound	Average	Upper Bound
A	.11	.13	.15	.026	.032	.038	.011	.013	.016
B	.047	.15	.26	.0086	.039	.069	.0029	.017	.030
C	.017	.18	.34	.0023	.048	.094	.00053	.021	.042
D	.077	.53	1.19	.034	.16	.29	.019	.077	.13
E	.11	.13	.15	.026	.032	.038	.011	.013	.016
F	.047	.15	.26	.0086	.039	.069	.0029	.017	.030

is in most cases less for Configurations A – F.[1] The determination of σ_1 and σ_2 for each configuration yields, as it did in Appendix A for Configurations I – VI, an average cross-section, $\sigma_1 + \sigma_2$, and bound estimates, $(\sqrt{\sigma_1} \pm \sqrt{\sigma_2})^2$. These three values are given in Table B.3-1. A comparison of these results with those for Configurations I – VI appears in Figures B.3-1 – B.3-3.

Examination of these figures indicates that little can be gained, cross-section-wise, at 200, 350, or 500 Mc, by changing the re-entry shapes to those of Configurations A – F.[2]

B.3.2 Configurations G and H

Although the cross-sections of Configurations A – F are not significantly less than those of the original Rudolph design, Configurations G and H, due to their ogival shape, can be expected to yield large reductions in cross-section even at 200 Mc.

B.3.2.1 Experimental Ogive Data at 200 Mc

Experimental ogive data obtained by Ohio State University, and reported in Reference 15, included measurements made at 3000 Mc

[1]The reader is referred to Section A.2.1 for a discussion of this creeping wave method. Its application to Configurations A – F is similar to its use on Configurations I – VI in that the contribution from the rear, σ_2, is approximated by that from a sphere of radius equal to 0.5 m for each of the Configurations A – F. The differences revolve around the determination of the contribution from the nose, σ_1. For Configurations I – VI the nose is spherical and thus σ_1 in those cases is given by πR_n^2 where R_n is the radius of the spherical nose; for Configurations A – F the nose is pointed and thus the contribution, σ_1, is given by

$$\frac{\lambda^2 \tan^4 \alpha}{16\pi} .$$

[2]This conclusion is also verified by the experimental data on the Carrot, the Cone, and the 7-OC models discussed in Section A.4.

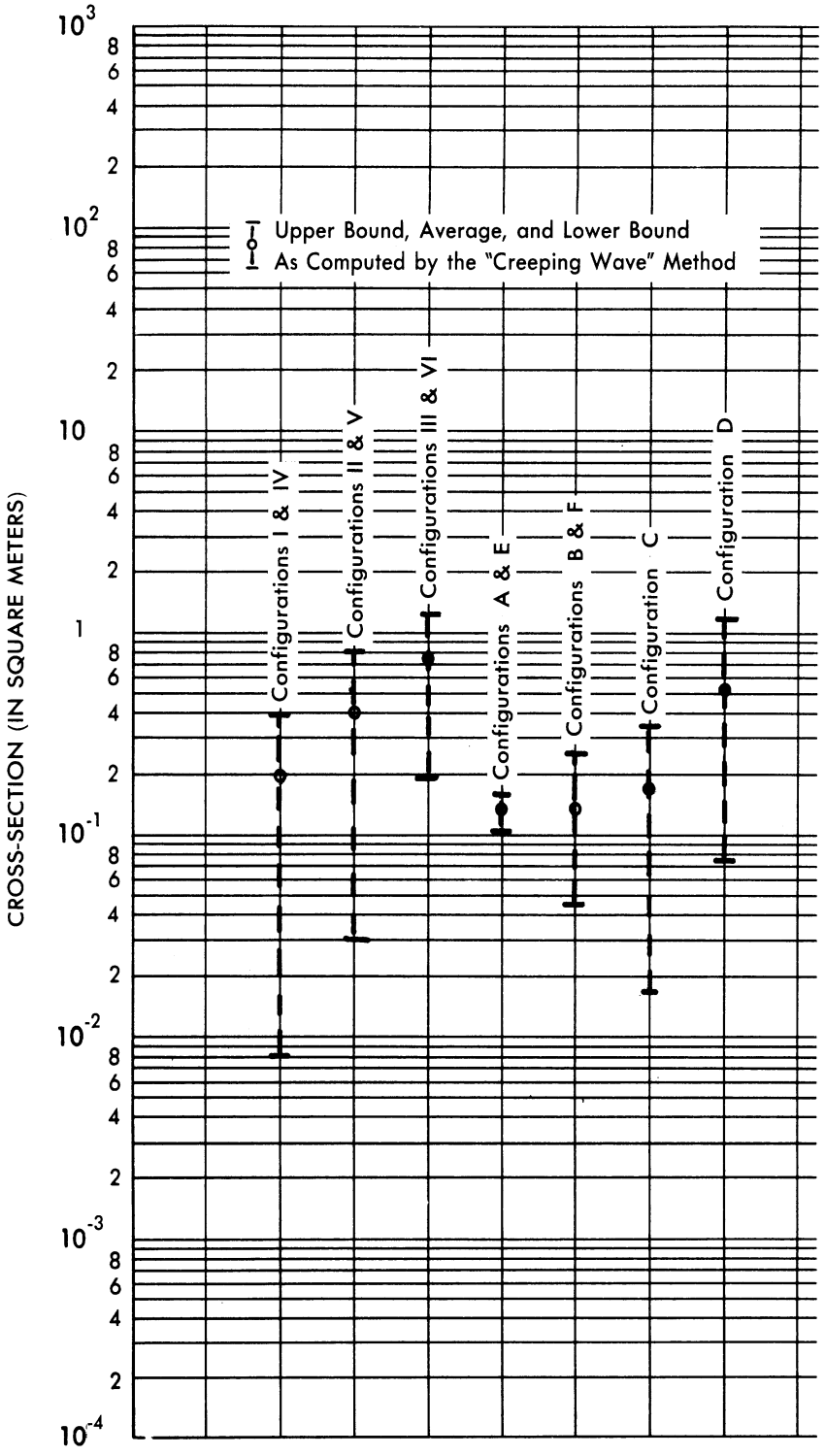

FIG. B.3-1 NOSE-ON CROSS-SECTIONS OF CONFIGURATION I - VI AND CONFIGURATIONS A - F AT 200 Mc

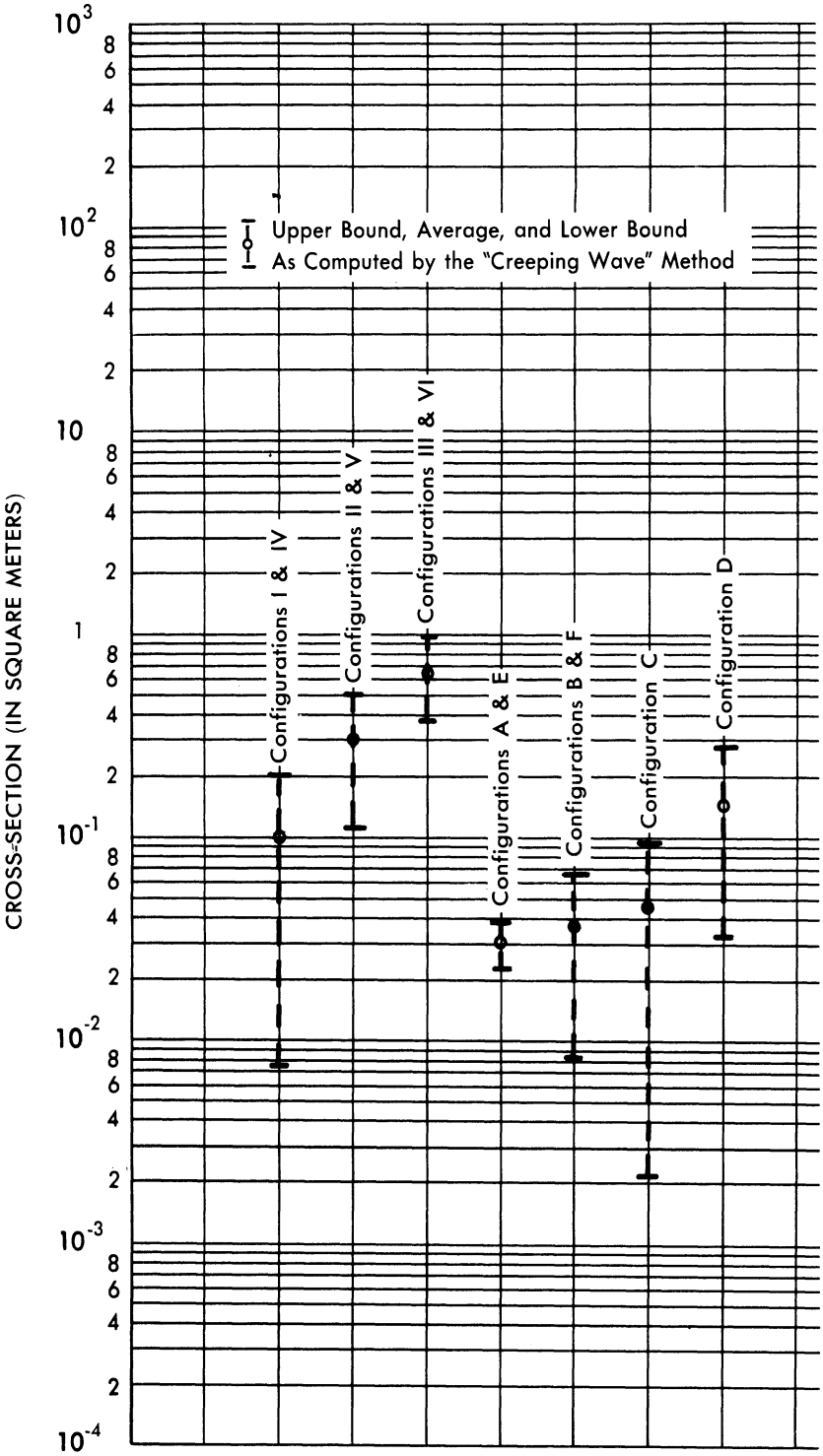

FIG. B.3-2 NOSE-ON CROSS-SECTIONS OF CONFIGURATION I - VI AND CONFIGURATIONS A - F AT 350 Mc

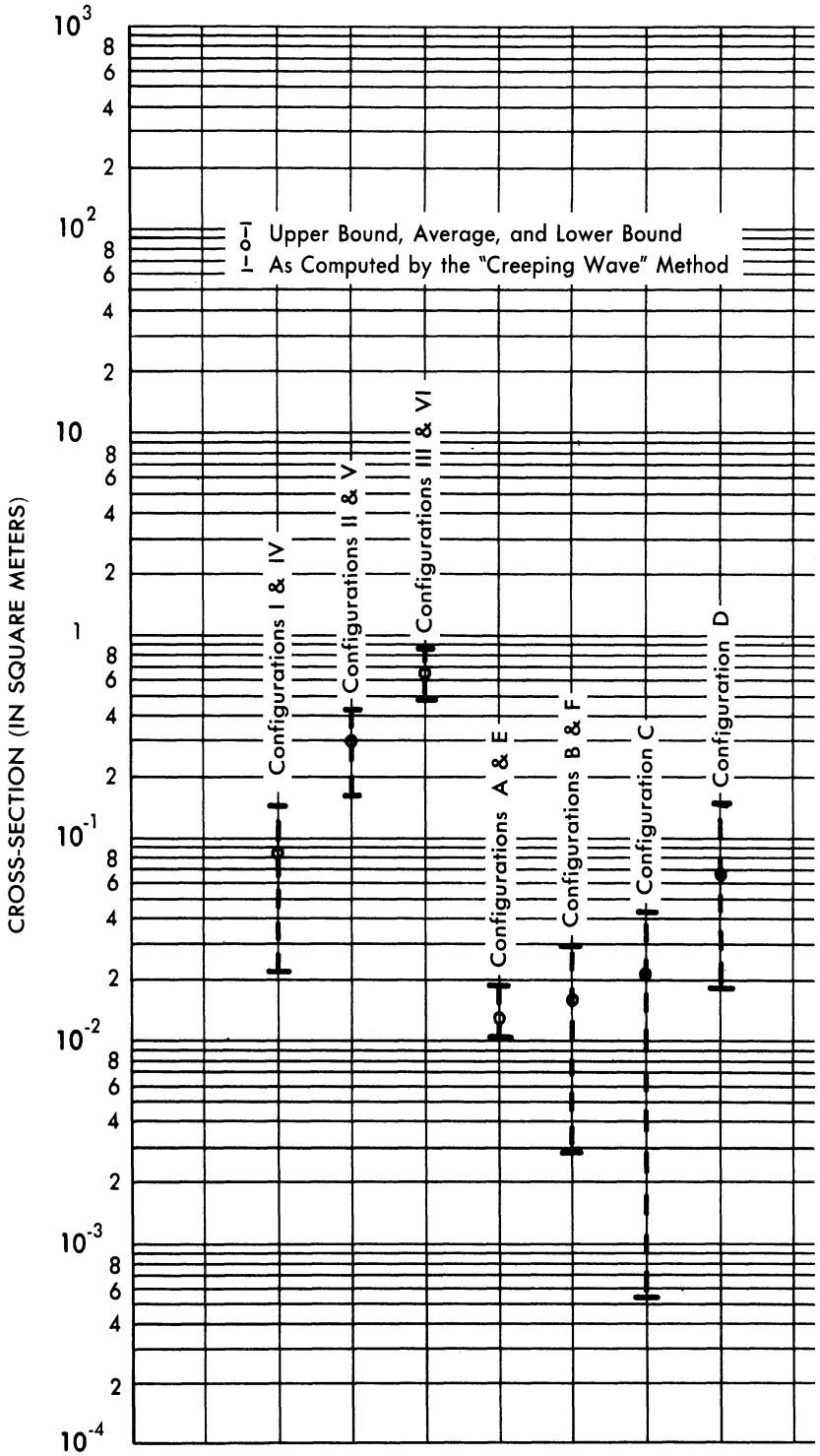

FIG. B.3-3 NOSE-ON CROSS-SECTIONS OF CONFIGURATION I - VI AND CONFIGURATIONS A - F AT 500 Mc

(λ = 10 cm) on two ogives: one of length 10 cm and maximum diameter 2.05 cm, and the other of length 20 cm and maximum diameter 5.18 cm. Upon scaling this data to 200 Mc, one obtains ogives comparable in size and shape to Configuration G. Table B.3-2 contains a comparison between the dimensions of Configuration I (the unperturbed Rudolph shape), Configuration G, and these two ogives, denoted as "Ogive A" and "Ogive B".

The data given in Reference 15 yield values of cross-section for the 10 cm ogive at four values of ψ(0, 34, 75, and 90 degrees), and for the 20 cm ogive at eight values of ψ(0, 15, 20, 43, 45, 50, 85, and 90 degrees).

Figure B.3-4 contains these data scaled to 200 Mc. In drawing these curves only the points defined by the angles mentioned above were used. Figure B.3-4 also contains the theoretical (physical-optics) curves for Ogives A and B. The theoretical curves do not differ from the experimental curves by more than a factor of 10 over most of the interval.

TABLE B.3-2

COMPARISON OF DIMENSIONS

(L = total length; D = maximum diameter; and α = 1/2 nose angle)

Configuration	L (in m)	D (in m)	α
I	2.14	1.00	–
G	2.91	1.00	20°
Ogive A	1.50	.31	23°
Ogive B	3.00	.78	29°

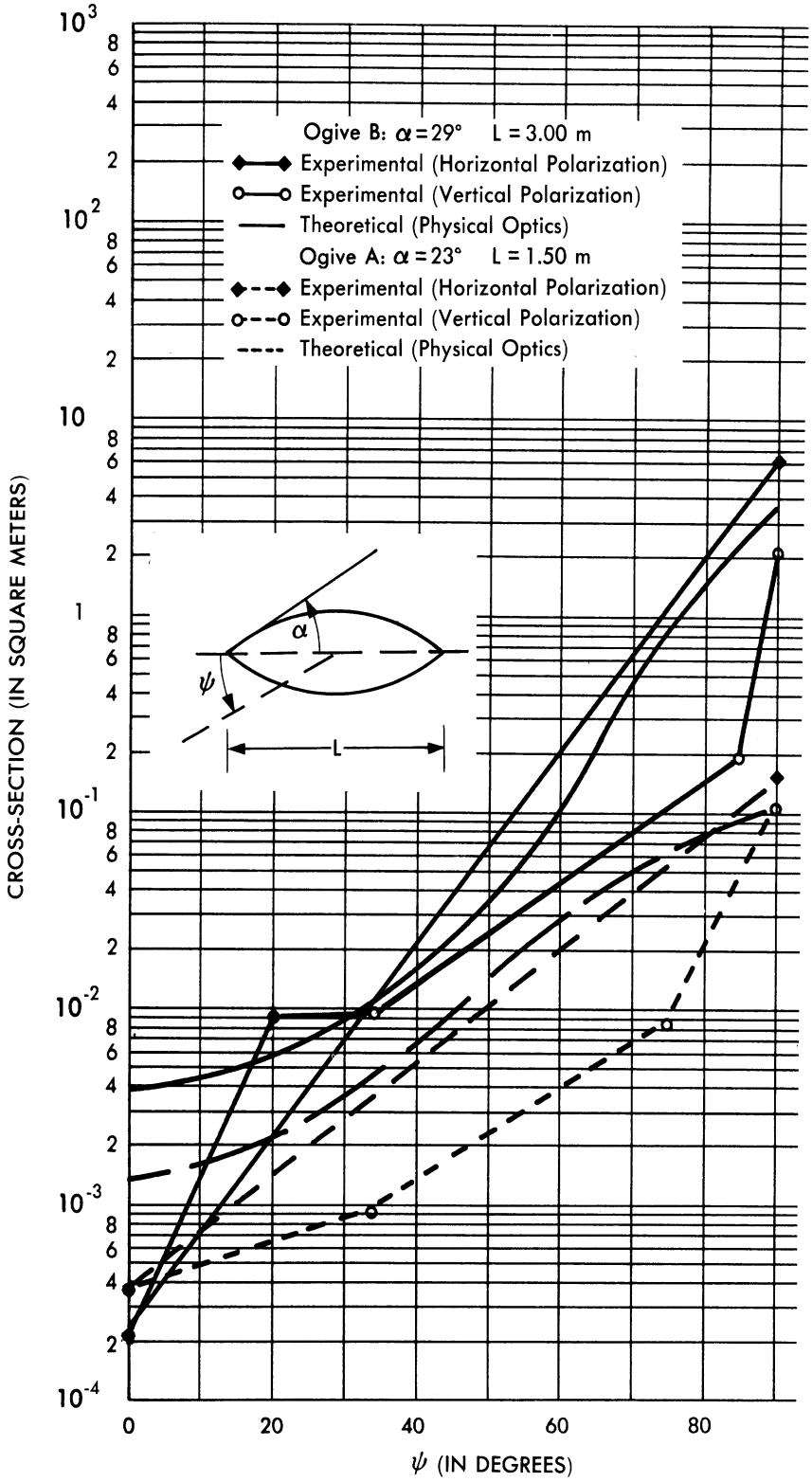

FIG. B.3-4 CROSS-SECTION OF OGIVES AT 200 Mc ($L/\lambda = 1$ AND 2)

B.3.2.2 Cross-Sections of Configurations G and H at 200 Mc

In view of the agreement between experimental and theoretical results for ogives shown in Section B.3.2, physical optics ogive methods were used for Configurations G and H at 200 Mc.[1] The results obtained are shown in Figure B.3-5, where they are compared with the Configuration I data .

B.4 CONCLUSION

The perturbation analysis described above has indicated that, of the perturbations considered, the one referred to as Configuration G yields the largest reductions in cross-section in the aspect interval $0^{o} \leqslant \psi < 60^{o}$. Capping the nose with a cone without adding any additional protuberances to the Rudolph shape does not decrease the nose-on cross-section of the warhead to any appreciable extent. Capping the nose with a cone and rounding-off the step results in large reductions in the nose-on cross-section at the larger frequencies, but at 200 Mc no appreciable reduction is obtained. If, in addition to capping the nose of the warhead with a cone and rounding-off the step, the rear of the warhead is also capped with a cone (as in Configuration G), then comparatively large reductions in the nose-on cross-section can be obtained at 200 Mc also. This is illustrated in Figure B.4-1 for Configurations A, C, E, and G, compared with Configuration I. The other four perturbations (B, D, F, and H) are not included in this graphic comparison, since they would not enclose Configuration I.

It is seen from Figure B.4-1 that the nose-on cross-section of Configuration G is smaller than that of Configuration I by factors of approximately 10^{5} at 3000 Mc, 10^{4} at 1000 Mc, and 10^{2} at 200 Mc.

---

[1]The use of these ogive methods at small wavelengths has been shown to be valid by the work of Sletten (Ref. 14) and by the work presented in Reference 40. Since there is some contradictory evidence in recent O.S.U. work, additional discussion on this point will be made in the next report under this contract.

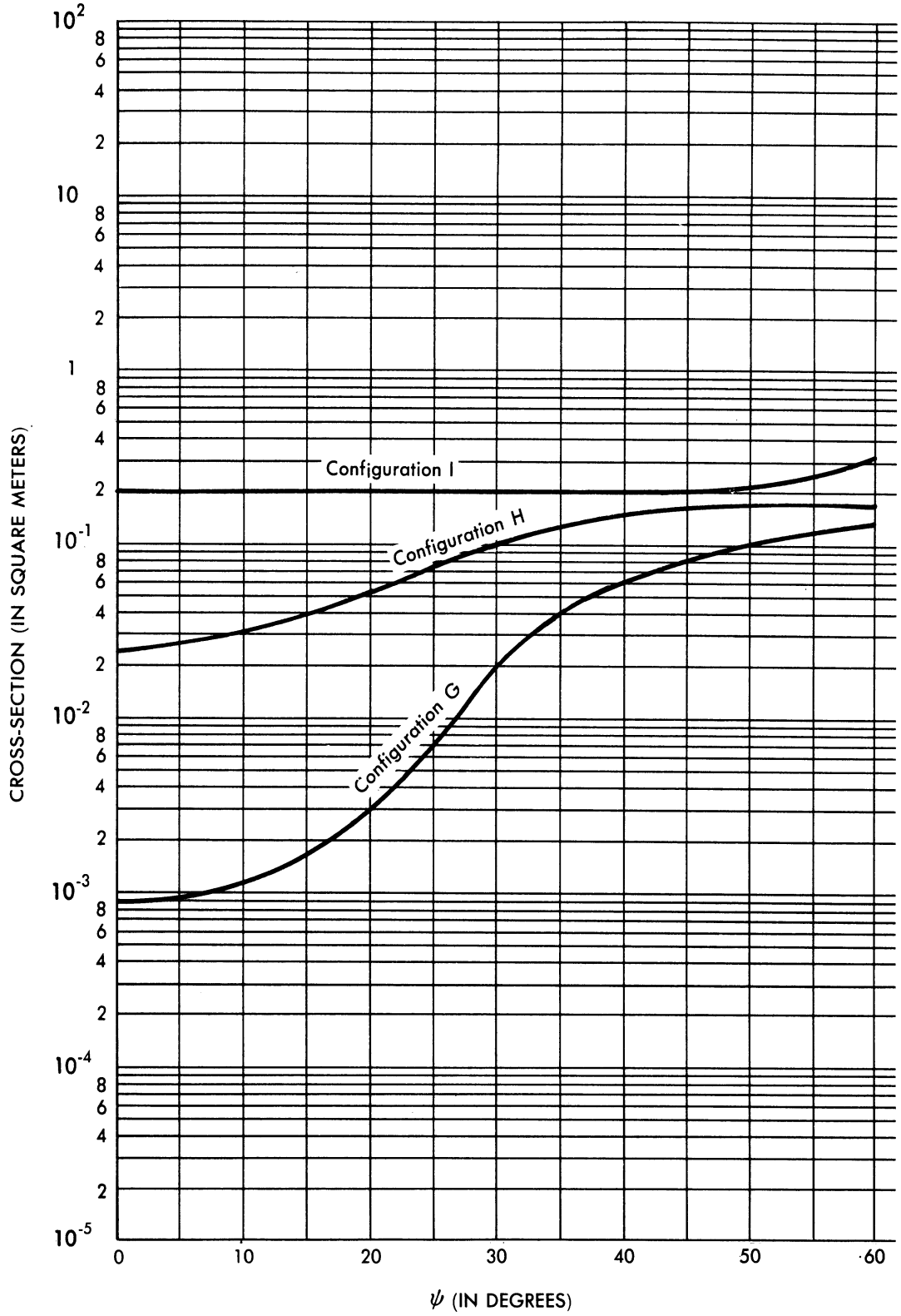

FIG. B.3-5 CROSS-SECTION OF CONFIGURATION I COMPARED WITH THE CROSS-SECTIONS OF CONFIGURATION G AND H AT 200 Mc

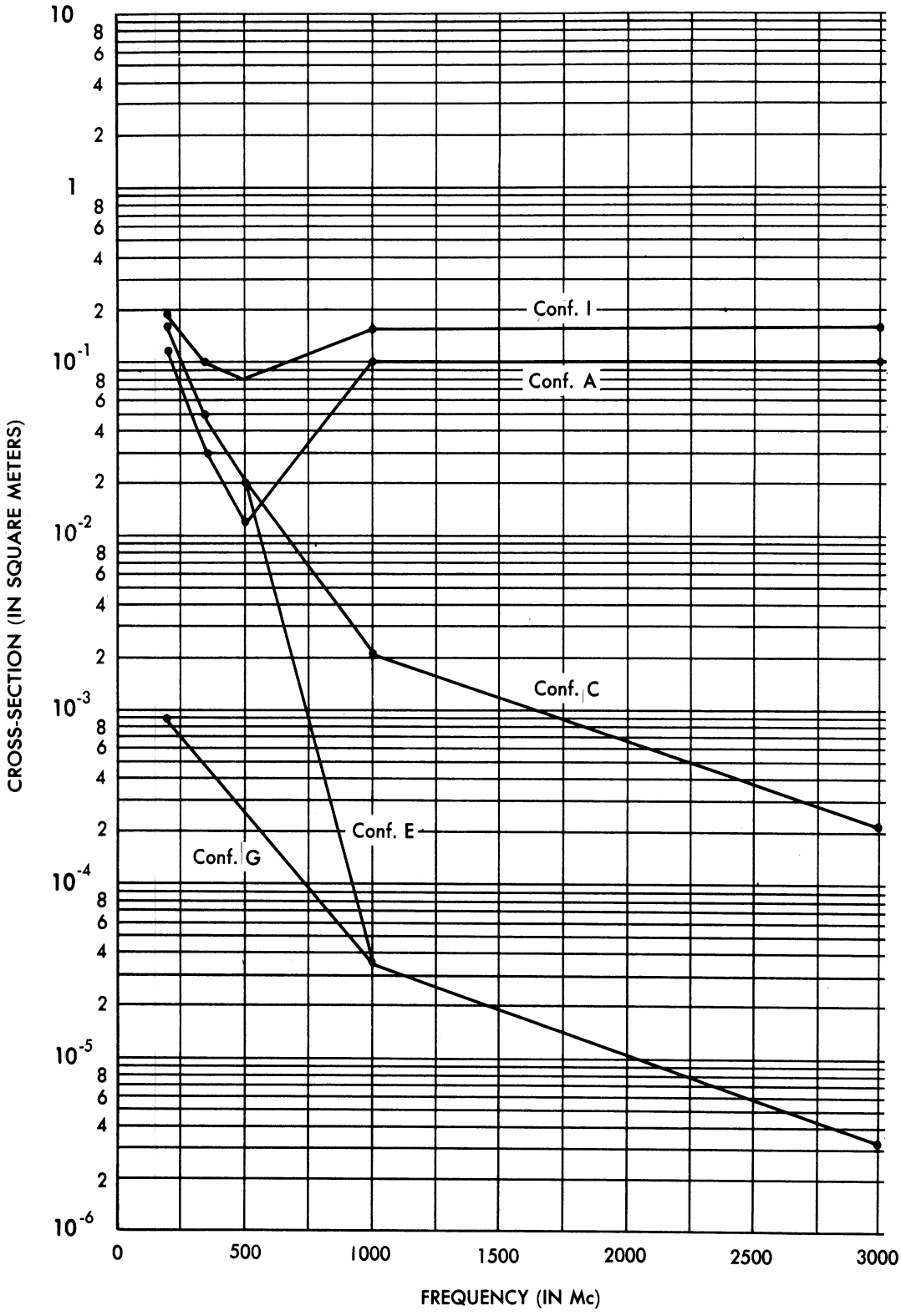

FIG. B.4-1 THEORETICAL NOSE-ON CROSS-SECTIONS AS A FUNCTION OF FREQUENCY FOR CONFIGURATIONS A, C, E, AND G COMPARED WITH THE CROSS-SECTIONS OF CONFIGURATION I

APPENDIX C

CAMOUFLAGE MATERIALS

A radar absorbing material has been developed by the Deutsche Magnesit, AG, Munich, Germany. Representatives of this company were invited by the Rome Air Development Center to fabricate their absorbing material at RADC and then apply it to models furnished by RADC. The results are very good when the material is manufactured for use in one small frequency region lying in the S- to K-band region. In fact, it was claimed that there was a 26 db reduction in cross-section at X-band.

The German scientists had no mass production methods available for the fabrication of their material. They also had no method available for making broadband materials, but they thought they could do so without too much difficulty. They attempted to do this while at RADC. The results were not good, but this may be because of the insufficient time available.

After they had left, work was started at RADC under the direction of J. Vogelman, Director of Electronic Warfare Laboratory, to find out why the obtained reduction existed and to analyze its division into absorption and increased scattering at other than the back-scattering direction. It was found that half the decrease in db was due to absorption and the other half was due to off-angle scattering.

Due to the newness of this material, and due to the fact that broadband techniques have not yet been completed, the only conclusion to be drawn at this time is that the Deutsche Magnesit material may be usable for camouflaging missiles and aircraft. Since RADC is continuing its investigation of this material for the U. S. Air Force, it is felt that its analyses will show how good or bad this material is. At this time the authors do not recommend any further action than that which is presently going on at RADC. It is recommended that people in the ICBM field follow RADC's latest results on this material for possible applications to ICBM.

APPENDIX D

UTILIZATION OF FISSION WASTE PRODUCTS FOR DECOY PURPOSES

D. 1 INTRODUCTION

Fission waste products are radioactive and therefore produce ionization. It has been conjectured that if the wastes are carried in a decoy, the radar cross-section of the decoy might be sufficiently enhanced to improve the chance of the decoy being confused with the primary vehicle by proximity-fused interceptors. Also, if the decoys were used to draw off enemy defenses to a false location by confusing ground-based radars, one would want to increase their detectability. This idea is considered here for two types of missiles and found impracticable. Another group has reached the same conclusion (Ref. 16) for sowing the wastes from airplanes as a sort of chaff.

The first type of missile considered is a hypothetical intercontinental ballistic missile. The following properties, which should be duplicated by an effective decoy, are assumed: a velocity of 10 km/sec, and flight altitudes ranging from ground level to above 200 km. Since in its nose-on descent such a missile would not have a large cross-section, it is assumed that something between π and 10 π square meters would be a reasonable radar cross-section to simulate.

The second type is a V-2, representative of the shorter-range missiles. Experimental data quoted in Reference 17 indicate typical altitudes up to about 90 km and velocities ranging from about 3.25 km/sec down to about 0.5 km/sec at different altitudes. The size of the cross-section to be simulated is the same as above.

D. 2 PHYSICAL PRINCIPLES INVOLVED

D. 2. 1 Critical Density

Upon solving the propagation equations in an ionized medium for a given radar frequency, it is found that if the electron density exceeds a

critical value the surface bounding this dense region acts as a perfect reflector (Ref. 18). This critical density is given (Ref. 1) by $N_c = (f^2/81) \times 10^6$ electrons/cm^3, where f is the frequency in megacycles. A sub-critical-density region surrounding the critical-density contour acts as a diffuse reflector, reducing the back scattering from the critical-density region. (The cross-section of a region which nowhere attains critical density is very much less than that of a geometrically identical critical-density region.) The critical-density region should be at least a few wavelengths thick if the propagation equations are to have meaning. A radius of about one meter should be sufficient, even down to L-band.

D.2.2 The Nature of the Fission Waste Products

The radioactivity of the fission waste products consists almost exclusively of β- and γ-radiation. Therefore, other types of radiation do not come into consideration. A representative figure for the power released is 100 watts/gm, divided equally between the β's and γ's. This figure, based on radiochemical analysis, does not take into account the loss of output due to self-absorption in a bulk source. The mean energy of both types of radiation is 0.7 Mev, the maximum β-energy about 5 Mev (Ref. 19[1]).

D.2.3 Range-Energy Relations For β's and γ's

For electron energies such that $v \approx c$ (since $v/c = 0.5$ corresponds to less than 80 KV, this covers nearly all of the β-activity present here), the energy loss of a β per g cm^{-2} of absorber is given by (Ref. 20)

$$k = 4\, N(Z/A)\, \pi r_e^2\, m_e\, c^2 \left[\ln \left(\frac{\pi E_T^{3/2}}{E_o^{1/2}\, I(Z)} \right) - 1.45 \right] ,$$

[1]The authors wish to express their thanks to J. V. Nehemias for communicating these results to them.

where N = Avogadro's number

$Z/A = \frac{\text{atomic number}}{\text{atomic weight}}$, for the stopping element,

$r_e = e^2/m_e c^2$, the classical electron radius,

m_e = electron rest mass,

E_T = total electron energy,

E_o = rest energy, $m_e c^2$, and

I(Z) = ionization potential of stopping material.

Since k varies monotonically by less than 30 per cent from 0 up to 5 Mev, it may be taken as constant at its value for the mean β energy of 0.7 Mev with little error. Using as order of magnitude figures for the fission products Z/A = 0.45 and I(Z) = 8 ev gives k = 1.6 Mev/g cm^{-2}. Using a density ρ = 5g cm^{-3} for the wastes yields a loss rate of 8 Mev/cm, or a range of about 1 mm for 0.7 Mev β's in the source. For ranges in air, Z/A = 0.5 may be used, and little error is involved in taking I(Z) = 13.5 ev, correct for atomic oxygen. ρ must correspond to the altitude considered.

The range of the electrons in the waste material being so small, absorption of the electrons in the source itself (self-absorption) will greatly reduce the power output of the source into the air, allowing only those electrons originating near the surface to escape. For electrons of given energy, consider a strip of area A and thickness t equal to the range, and compute what fraction of their energy will escape through the outer side of the strip (averaging over points of origin). This fraction is F=1-(s/t), where s is the mean path of the electron in the strip (since energy loss is proportional to path length).

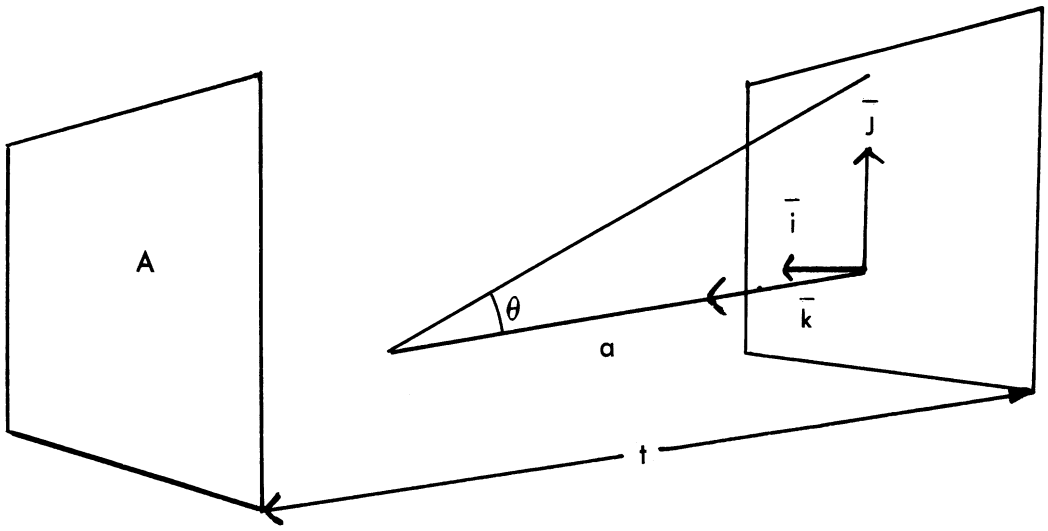

Then,

$$F = \frac{2\pi}{4\pi\, At^2} \int_0^t Ada \int_0^{\cos^{-1}(a/t)} \sin\theta d\theta (t - a/\cos\theta)$$

$$= \frac{1}{2t^2} \int_0^t da \left[t(1 - a/t) + a \ln (a/t) \right] = \frac{1}{2t^2} \left[t^2 - t^2/2 - t^2/4 \right] = \frac{1}{8}.$$

This derivation involves the assumption that the thickness of the strip is small compared to its radius of curvature (which agrees with the actual dimensions considered later), and assumes a straight-line path. If a thicker strip is used, only electrons originating within a distance t from the surface will contribute. Neglecting range straggling, electrons originating at a distance from the surface greater than their range will be absorbed before they reach the surface. The use of a thinner strip is not advisable, since the reduction of surface activity due to the presence of less source more than counterbalances the lowered self-absorption.

For a 0.7 Mev electron in air, k = 1.5 Mev/g cm^{-2}. Near sea level, the air density is about 10^{-3} g/cm^3. Thus the energy loss per unit path length is 1.5×10^{-3} Mev/cm, and the range is about 500 cm or 5 m. As the altitude increases, the air density drops off more and more rapidly (e.g., 10^{-12} g/cm^3 at 170 km) and the range increases proportionately.

Gamma-rays can be considered as attenuated as exp(-μx) (at least, for μx of order unity or less). For the γ-energies of interest, the interaction of the gamma-rays with matter is practically all due to the Compton effect (pair production competes prominently only at much higher energies, the photoelectric effect only at very much lower ones). The absorption coefficient, μ, for the Compton effect is (Ref. 21)

$$\mu = 2\pi N \rho \frac{Z}{A} r_e^2 \left\{ \frac{1+\alpha}{\alpha^2} \left[\frac{2(1+\alpha)}{1+2\alpha} - \frac{1}{\alpha} \ln (1+2\alpha) \right] + \frac{1}{2\alpha} \ln (1+2\alpha) - \frac{1+3\alpha}{(1+2\alpha)^2} \right\},$$

where α = γ-energy in units of the electron rest mass.

For a 0.7 Mev γ-ray in air near sea level, $\mu = 4 \times 10^{-5}$ cm^{-1}; hence, the γ-ray loses ~63 per cent of its energy in about 300 meters. This distance varies with air density (consequently with altitude) in the same manner as the electron range. Thus, the γ-rays are about 100 times less efficient than the β's in producing ionization.

Inasmuch as the available power is evenly divided between β's and γ's, and that portion of it in the form of β's is far more effective, consideration is limited to the electrons alone.[1]

In view of the high self-absorption of the source for electrons, the power output per gram quoted above (neglecting absorption) is not directly applicable to a bulk source. Instead, the useful quantity is the power output per unit area of the source. There are 50 watts/gm emitted in the form of β's. Using a density ρ = 5 g/cm^3 for the waste products,

[1]The overly generous assumption that all the radiation is in the form of β's would reduce the source size by less than a factor of two, leaving the conclusions unchanged.

as before, this is 250 watts/cm^3. From the discussion of self-absorption above, the power released by a layer of thickness t cm, equal to the range, is $1/8 \times 250 \times t$ watts/cm^2, and deeper-lying material does not contribute. Since the rate of energy loss is 8 Mev/cm, t = E/(8 Mev/cm) and the output is (250/64) E watts/cm^2, where E = electron kinetic energy in Mev. Averaging E over the electron spectrum gives 2.7 watts/cm^2. This is the surface activity to be expected from a thickness equal to at least the range of the most energetic β's (about 6 mm). A thinner strip will give less surface activity and a thicker one will yield no more.

D. 3 COMPUTATIONS

D. 3. 1 Introduction

This section contains a computation of the source strength required to maintain a critical density of ionization over a volume adequate for decoy purposes. It will be shown that an impractically large source is needed. Since this consideration alone rules out the use of fission wastes, others need not be treated quantitatively. However, these additional limitations are stated here.

First, there is the fact that the β-energy spectrum is continuous. This implies a continuous distribution of ranges, and therefore an ion density distribution which tails off away from the source. Thus, beyond the region of critical density a subcritical density is present which reduces the radar cross-section.

Further, the phenomena of recombination and attachment to form negative ions have been ignored. These would work to lower the electron density and require a larger source. On the other hand, if recombination is not sufficiently rapid behind the moving source, an ion trail may be formed. In the latter case, the radar reflection from the ionization produced by the decoy would not resemble a moving missile.

The fact that the β's must be relied on to produce the ionization raises a problem as to mounting the source on the decoy. As was indicated in the discussion of self-absorption, one centimeter of solid

material would stop all the β's. This effectively precludes carrying the source inside the decoy.

The nature of the fission waste products raises serious handling problems. The high level of radioactivity would make the loading of the decoy unpleasant and result in contamination difficulties at the launching site. The effects of this radioactivity upon the chemical fuels powering the decoy should also be considered. Finally, the large amount of power dissipated in self-absorption would create significant thermal problems.

D. 3. 2 Source Strength Requirements for Critical Density

To simulate a missile, ionization of at least critical density must be made to fill a volume comparable with the volume of the missile. Hence, at any moment, a critical density region of radius r_1 (ideally a couple of meters) is required. As the decoy moves, the region that has to be filled changes. If the missile velocity is L cm/sec, a cylinder of radius r_1 and length L cm must be filled in one second. Since the source is located on the axis of the cylinder, the ion density decreases as the distance from the axis increases. Therefore, critical density must be achieved near the surface of the cylinder (which will result in a higher density being present further inside). For simplicity, assume the source to be a sphere of radius r_0 (this shape also minimizes reabsorption, in one part of the source, of electrons that have escaped the surface at another point). To fool the radar, the ionized layer must be at least a meter thick, requiring that $r_1 - r_0 \geqslant 100$ cm.

Given a source whose power output per unit surface area is 2.7 watts/cm^2, subject to the conditions just enumerated, the minimum r_0 required will now be computed. The calculation is not carried out exactly; instead, a lower bound to the answer is obtained in three different ways (which is the most restrictive depends on the altitude and velocity considered).

D. 3. 2. 1 ICBM (near sea level)

To maintain the critical density out to r_1, it is necessary to supply,

every second, a cylindrical shell of radius r_1 and thickness dr with an amount of energy

$$\mathcal{E} = 2\pi r_1 \, L \, dr \, D \, I(Z)$$

where D = critical density, and

I(Z) = ionization potential (13.5 volts).

Let f(E) dE = number of electrons supplied by the source, with energy lying between E and E + dE,

k(E) = energy loss of electrons per unit path length (approximately independent of E),

ds = path length of electron through the cylindrical shell ($ds \geqslant dr$), and

E' = minimum energy of electron at source if it is to have a range sufficient to arrive at the cylindrical shell.

Then

$$\mathcal{E} = k \int_{E'}^{\infty} f(E)dE \; ds$$

$$= k \int_{E'}^{\infty} Ef(E)dE \; \frac{ds}{E}$$

$$< k \; \frac{ds}{E'} \int_{E'}^{\infty} Ef(E)dE$$

$$< k \frac{ds}{E'} \int_0^\infty Ef(E)dE.$$

For different orientations of the electron path, ds is proportional to the path length traveled in order to reach the cylindrical shell (minimum range), which in turn is proportional to the minimum required energy E'. Hence, ds/E' is independent of direction and can be replaced by dr/E_1, where E_1 is the minimum energy for radial motion. If the dimensions of the source are small compared with r_1, $E_1 = kr_1$. Hence,

$$\varepsilon < k \frac{ds}{E'} \int_0^\infty Ef(E)dE$$

$$= k \frac{dr}{E_1} \int_0^\infty Ef(E)dE$$

$$= \frac{dr}{r_1} \int_0^\infty Ef(E)dE$$

and $$\int_0^\infty Ef(E)dE > 2\pi r_1^2 \, L \, D \, I(Z).$$

The energy supplied, $\int_0^\infty Ef(E)dE$, comes from a sphere of radius r_0.

In one second, this source supplies 2.7 joules per cm^2 of area or a total of $2.7 \times 4\pi r_0^2$ joules = $2.12 \times 10^{20}\ r_0^2$ ev. For minimum energy input for the ICBM ($L = 10^6$ cm),

$$2.12 \times 10^{20}\ r_0^2 \text{ ev} = 2\pi r_1^2\ 10^6 \text{cm} \times 6.9 \times 10^{11} \times 13.5 \text{ ev}$$

$$\frac{r_0^2}{r_1^2} = 0.28$$

$$r_0 = 0.53\ r_1 .$$

Since $r_1 - r_0 \geqslant 100$ cm for simulation, the minimum $r_0 = 110$ cm, so the diameter of the sphere has to be more than two meters. Thus at low altitudes, the fission products ionization source is at best no more effective as a decoy than a metallic object of comparable size would be.

Neglect of the source dimensions is not essential.

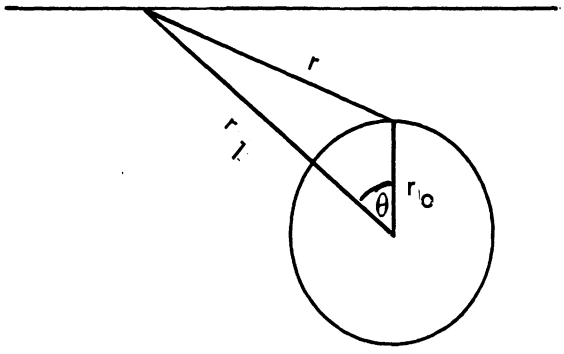

The path difference of an electron arriving at a point on the cylinder from different places on the source can be taken into account. Assuming isotropy of emission direction from the source, the correction factor is

$$\left(\frac{r}{r_1}\right)_{av.} = \frac{1}{r_1} \frac{\int_0^{\theta_{max}} \sin\theta d\theta \; r}{\int_0^{\theta_{max}} \sin\theta d\theta} .$$

From the geometry, $r^2 = r_1^2 + r_0^2 - 2r_0 r_1 \cos\theta$ and $\theta_{max} = \cos^{-1} \frac{r_0}{r_1}$.

Let $x = \frac{r_0}{r_1}$, $\cos\theta = u$, then

$$\frac{r}{r_1} = \sqrt{1 + x^2 - 2x\,u}$$

$$\left(\frac{r}{r_1}\right)_{av} = \frac{\int_x^1 \sqrt{1 + x^2 - 2x\,u}\, du}{\int_x^1 du} = \frac{(1-x)^{1/2}}{3x}\left[(1+x)^{3/2} - (1-x)^{3/2}\right].$$

For $x = \frac{1}{2}$,

$$\left(\frac{r}{r_1}\right)_{av} = 0.7.$$

The minimum diameter of the sphere is changed to 1 1/2 meters. The conclusions are unaltered.

D. 3. 2. 2 ICBM (higher altitudes)

At low air densities where the range of most of the source electrons greatly exceeds r_1, the replacement of ds/E by ds/E' represents a gross underestimate of the source strength required. Instead, 1/E is left inside the integral and a mean value of ds, or better ds/dr, is used:

$$\frac{ds}{dr} = \frac{s}{r_1} = \frac{1}{\cos\theta}$$

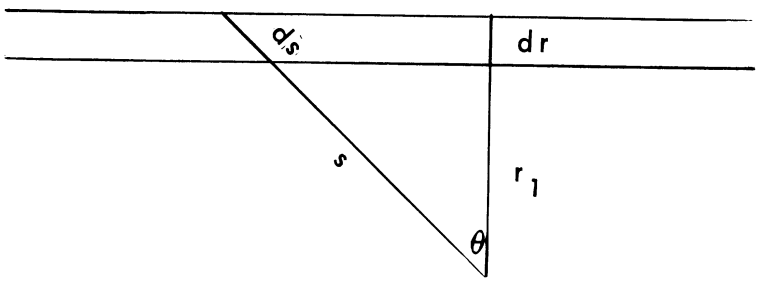

Electrons will leave the cylinder at angle θ ranging from zero to a maximum value such that s is the electron range. An overestimate is obtained by choosing $s_{max} = E_{max}/k$ and assuming an equal number of electrons leaving at all values of θ in the range so defined (i.e., $0 \leq \theta \leq \theta_{max} = \cos^{-1}(kr_1/E_{max})$).

Then

$$\left(\frac{ds}{dr}\right)_{av} < \frac{\int_0^{\theta_{max}} \frac{d\theta}{\cos\theta}}{\int_0^{\theta_{max}} d\theta} = \frac{1}{\theta_{max}} \ln\left(\tan\theta_{max} + \sec\theta_{max}\right)$$

$$= \frac{1}{\theta_{max}} \ln \frac{1 + \sin \theta_{max}}{\cos \theta_{max}} = \left(\cos^{-1} \frac{kr_1}{E_{max}}\right)^{-1} \ln \frac{1 + \sqrt{1 - \left(\frac{kr_1}{E_{max}}\right)^2}}{\frac{kr_1}{E_{max}}} .$$

At low densities, $kr_1 \ll E_{max}$, and

$$\left(\frac{ds}{dr}\right)_{av} = \frac{2}{\pi} \ln \frac{2\ E_{max}}{kr_1}$$

$$\mathcal{E} = k \int_{E'}^{\infty} f(E)dE\ ds < \frac{2}{\pi} k\ dr \ln \frac{2\ E_{max}}{kr_1} \int_{E'}^{\infty} f(E)dE$$

$$< \frac{2}{\pi} k\ dr \ln \frac{2\ E_{max}}{kr_1} \int_{0}^{\infty} f(E)dE$$

$$= \frac{2}{\pi} \frac{k}{\bar{E}} dr \ln \frac{2\ E_{max}}{kr_1} \int_{0}^{\infty} E\ f(E)dE,$$

where $\bar{E}$ is the mean energy.

$$\int_{0}^{\infty} E\ f(E)dE > \pi^2 \frac{r_1\ L\ D\ I(z)\ \bar{E}}{k \ln \frac{2E_{max}}{kr_1}} ,$$

and, at the minimum,

$$r_0^2 = \frac{1.89 \times 10^{-8} L r_1}{\rho \ln \frac{6.25}{\rho r_1}} .$$

The condition $kr_1 \ll E_{max}$ means $1.6 \times 10^6 \rho r_1 \ll 5 \times 10^6$ or $\frac{1}{\rho} \gg r_1$.

Thus, $\ln \frac{6.25}{\rho r_1} = \ln \frac{1}{\rho} - \ln \frac{r_1}{6.25} \approx \ln \frac{1}{\rho}$, and

$$\frac{r_0^2}{r_1} = \frac{1.89 \times 10^{-8} L}{\rho \ln \frac{1}{\rho}} .$$

Near sea level, $\rho \approx 10^{-3}$ gm/cm^3 and a reasonable r_1 is 200 cm, so that $kr_1/E_{max} \approx 0.06$. At higher altitudes, the inequality is even better satisfied. For the minimum r_0, impose again the condition that $r_1 - r_0 = 100$ cm (minimum ionization layer for simulation),

$$\frac{r_0^2}{r_0 + 100} = \frac{1.89 \times 10^{-8} L}{\rho \ln \frac{1}{\rho}} .$$

For the ICBM at different altitudes, the source size is given below:

Altitude in km	Air Density in gm/cm^3 (Ref. 22)	Diameter
10	4.21×10^{-4}	0.5 m
20	9.34×10^{-5}	1.2 m
50	1.16×10^{-6}	26 m
100	8.60×10^{-10}	21 km
200	1.71×10^{-13}	7.5×10^4 km

Thus, while this lower bound on the source is somewhat less stringent than the previous one at low altitudes, it imposes far greater (in fact, quite unattainable) limitations at the higher altitudes.

It would appear at first sight that the large value of r_0 obtained at the higher altitudes conflicts with the omission of source dimension considerations from the derivation. This is not correct. Indeed, including these considerations results in changing the maximum of s to $(E_{max}/k) + r_0$. This simply makes

$$\theta_{max} = \cos^{-1} \frac{r_1}{\frac{E_{max}}{k} + r_0} = \cos^{-1} \frac{kr_1}{E_{max}\left(\frac{1+kr_0}{E_{max}}\right)}.$$

Since $kr_0 < kr_1 \ll E_{max}$, this correction factor can be neglected.

D. 3. 2. 3 The V-2

The V-2 has a lower velocity than an ICBM. Furthermore, its maximum altitude is only about 150 km, which is considerably less than that of an ICBM. These differences reduce somewhat the power requirements. Applying the calculation of Section D. 2,

Altitude in km	20	32	48	63	88
Velocity in km/sec (Ref. 17)	0.995	1.49	1.32	1.08	3.25
Density in gm/cm^3 (Ref. 22)	9.34×10^{-5}	1.37×10^{-5}	1.48×10^{-6}	2.42×10^{-7}	5.65×10^{-9}
Diameter	.16 m	1.1 m	3.8 m	13 m	1.1 km

As the altitude increases, θ_{max} reaches a cutoff value due to the size of the cylinder, namely $\theta_{max} = \tan^{-1}(L/2r_1)$.

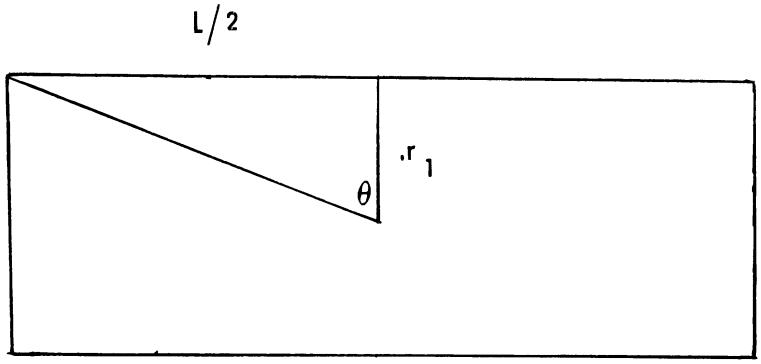

Then $$\left(\frac{ds}{dr}\right)_{av} < \frac{1}{\theta_{max}} \ln(\tan\theta_{max} + \sec\theta_{max})$$

$$= \frac{1}{\tan^{-1}\frac{L}{2r_1}} \ln\left(\frac{L}{2r_1} + \sqrt{1 + \left(\frac{L}{2r_1}\right)^2}\right) .$$

For $(L/2)^2 \gg r_1^2$, this leads to a maximum value:

$$\left(\frac{ds}{dr}\right)_{av} = \frac{2}{\pi} \ln \frac{L}{r_1} .$$

Then

$$2.12 \times 10^{20}\, r_0^2 = \frac{\pi^2 r_1 L D I(z) \bar{E}}{k \ln \frac{L}{r_1}} = \frac{4.02 \times 10^{12} r_1 L}{\rho \ln \frac{L}{r_1}} ,$$

$$\frac{r_0^2 \ln \frac{L}{r_1}}{r_1} = \frac{1.9 \times 10^{-8} L}{\rho} .$$

Set $r_1 = r_0 + 100$ cm (minimum):

$$\frac{r_0^2 \ln \frac{L}{r_0 + 100}}{r_0 + 100} = \frac{1.9 \times 10^{-8} L}{\rho} .$$

Results obtained in this way are:

Altitude in km	32	48	63
Diameter in m	1 1/2	7	40

At an altitude of 88 km, this approach becomes meaningless because $r_0 > L$.

D.4 CONCLUSIONS

The proposal to utilize fission waste products in decoys to simulate the radar cross-section of conventional missiles or the ICBM has been examined. From source strength (and size) considerations alone, the idea has been shown to be impractical. Even near sea level, a lower limit on the power required leads to a source of size comparable to that of a metallic object giving the same cross-section. At higher altitudes (over most of the range for the V-2 and practically all of the range for the ICBM), the source required is unattainably large. Other difficulties, mentioned but not treated quantitatively, raise further doubts as to the feasibility of the proposal.

APPENDIX E

DECOYS

Before considering possible defenses against decoys from the radar cross-section point of view, we will summarize the work which has been done for the aircraft case.

One first computes the radar cross-section of the aircraft. Then one investigates means of simulating its radar cross-section and flight characteristics with a smaller body. In Reference 5, the radar cross-sections of the B-47 and B-52 were computed from 65 Mc through X-band. It was found that an object of approximately 1/100th the volume of the aircraft could be used to reproduce the radar cross-section; the object could also reproduce the flight trajectory for one flight. In Reference 2 the possible defensive methods outlined below and analyses for the design of decoys to simulate the reflection characteristics of the aircraft were presented. In Reference 6, the scattering matrix of the B-47 was determined at S-band. The latter was useful in discussing polarization methods of distinguishing between decoys and aircraft. If one assumes that the defense has linearly polarized monostatic radars of fixed frequency (L-band or higher), then the radar cross-section of the aircraft can be simulated through the use of corner reflectors in decoys.

However, the enemy may then use frequency comparison methods to determine whether the vehicle is an aircraft or a decoy. For example, if the enemy's main radar is at S-band and its frequency comparator radar is at X-band, one would expect the cross-section of the aircraft to remain approximately the same for the two radars while the cross-section of the decoy would increase by a factor of 10 from S-band to X-band, due to the fact that the cross-section of a corner reflector depends on wavelength approximately as $1/\lambda^2$. On the other hand, it has been our experience (Ref. 23) that the radar cross-sections of aircraft such as the B-47 and the F-86 are only slowly varying functions of wavelength as soon as the wavelength becomes small with respect to the major dimensions of the aircraft.

This detection scheme can be countered as follows. Corner reflectors with appropriately curved faces will simulate the aircraft at S-band but cannot be recognized by the above technique. This is so because curvature of the faces of a corner reflector greatly modifies the behavior of its cross-section as a function of λ. A feeling for this can be gotten by observing that the angle error formulas for corner reflectors are wavelength-dependent, and thus changes in angle which are insignificant at one wavelength can cause severe reduction in the radar cross-section at smaller wavelengths. It has been shown that a corner reflector with spherical faces can be designed that eliminates the $1/\lambda^2$ wavelength dependence. The beauty of the spherical face idea is that after one matches the cross-section at one frequency it remains essentially a constant for all higher frequencies.

Another means of "unmasking" corner reflectors in decoys is the use of a transmitter which is circularly polarized (e.g., to the right), together with two receiving antennas, one of which is right-circularly polarized and the other of which is left-circularly polarized. When the corner reflectors are so oriented that single or triple reflections dominate, the left-circular polarization receiver will get 10 to 20 times as much power as the right polarized receiver. When double reflections dominate, the reverse situation applies. In any practical case, one of these orientations will occur. Thus, decoys using corner reflectors could easily be differentiated from aircraft (for which the power distribution between the two receivers varies between 3:2 and 2:3). This method of detection can be countered by the use of dielectric material on one of the faces of the corner reflector (Ref. 24). The procedure consists of properly coating one of the faces with a dielectric, so that the ray picture remains essentially unchanged, but the polarization is rotated in such a manner that the return is now distributed between the two receivers in roughly the ratio expected from aircraft. Another means of defeating this method of detection is by the use of holes of appropriate size in one of the corner-reflector faces or the use of one-half-wavelength protuberances. These last two approaches are not as efficient as the Ohio State University technique (Ref. 24) because they cause a significant degradation in the energy returned.

Another possible means of discriminating between decoys and aircraft would be the use of bistatic radars (Ref. 25 and 26). Bistatic radars are presently being used in the McGill Fence and the DEW line. Discrimination is based, in this case, on having one receiver near the transmitter and one or more receivers at a distance from the transmitter. In the case of aircraft (assumed to fly between the remote receiver and the transmitter), the radar cross-section at the remote site is often much larger than, and in almost all cases at least comparable to, the radar cross-section at the receiver which is near the transmitter. In the case of decoys, the cross-section at the transmitter site is always much larger than the cross-section at the distant receiver, due to the property of the corner reflector of reradiating energy into the quadrant from which it came. Some tentative schemes (obviously not fully adequate) have been discovered to counter this method of detection (Ref. 2).

Two other methods for the detection of decoys have been brought forward; one involves scintillation and glint and the other broadside discrimination (it is assumed in the discussion that the frequency of detection is above 1000 Mc). The power spectra for one-third-scale V-2 type ballistic missiles are contained in this report. The authors have no reason to believe that the power spectra which would be obtained for the Rudolph missile would be significantly different from these. In fact, if one analyzes the return from aircraft like the B-52 and B-47 (Ref. 27), he finds the shapes of the power spectra are rather similar to those for the missiles. This, of course, does not mean that special equipment cannot be built to detect spectral differences. However, it would be extremely difficult to do this without a thorough knowledge of the structural behavior of the enemy's missile and the enemy's decoy. The broadside discrimination method is more applicable to the aircraft problem than the missile problem, since in the search phase the Rudolph missile would be out of the sensible atmosphere, and as a result Rudolph never would have to "put its broadside forward." In fact, one of the best methods of reducing the cross-section of the Rudolph missile would be to guarantee that its nose is always pointing in the general direction of the enemy's search radars, with the temporary alteration of the metallic skin described in this report applied, so that the cross-section of the Rudolph warhead in the nose-on direction would be significantly reduced.

In the case of low frequency detection (e.g., the 60 to 100 Mc range), the decoys must carry barrage jammers if they are to duplicate the low frequency cross-sections of the Rudolph missile. However, the background due to cosmic noise, meteors, and stray ionization sharply limits the feasibility of detection by search radars in that range. It has been said that if American radars were operated at 60 Mc, it might be possible for the "Commissar of Jamming of the USSR" to push a button and create so much radiation that he could jam out all our receivers in this frequency range. Due to the great range of propagation at these low frequencies, it is clear that the above statement has an aura of truth about it.

The bistatic method for detecting decoys is not presently being countered. However, the data-gathering and data-processing equipment necessary for the use of this method would tax our national economy. Although it has been assumed that the United States has more computing equipment and data-processing equipment available than the Russians, it is felt that even the United States could not afford in the next few years to use a great many remote receivers and the associated data-processing equipment in order to discriminate between decoys and aircraft. Thus, it seems reasonable to assume that the USSR also will not be able to afford such defensive procedures. It appears, therefore, that decoys could substantially increase the "probability of kill" of the ICBM. Of course, until one is sure that the enemy can defend against such missiles, the necessity for a decoy effort would not seem to be established. However, if one waits until the knowledge is obtained that a defense is possible, it might easily be too late to design and build the necessary number of decoys.

Decoys, of course, can be used for both the long-range and short-range efforts; they can be used against search radars and against local defense radars. It may be possible to store decoys in the tanks section (if it is not far removed from the warhead) which can be used against either set of radars. It is possible to make decoys which are aerodynamically more highly performing than the Rudolph warhead (they might even catch up with and pass the warhead in flight after re-entry into the atmosphere).

APPENDIX F

FURTHER ANALYSIS OF THE UNIVERSITY OF MICHIGAN DROP-TEST DATA (POWER SPECTRA FOR EXPERIMENTAL DATA)

F.1 INTRODUCTION AND SUMMARY

As stated in Section IV and in Appendix E, one method the defense might attempt to employ to discriminate between decoys and aircraft is based upon possible differences in the fine structure of the radar return. An investigation of this possibility involves a thorough study of the fine structure of the radar return from aircraft, decoys, and missiles. Others have expressed the belief that power spectra associated with the radar return from these vehicles would be of significance in this detection problem.

Power spectra for manned aircraft have previously been studied (Ref. 27); to the best knowledge of the authors, the power spectra presented here are the first that have been computed for the radar return from missiles. The experimental data involved in the present analysis are the measurements made during The University of Michigan's drop tests reported in References 1 and 3. These computations were sponsored by the Bendix Aviation Corporation under Purchase Order No. S-96527.

The one-third-scale V-2-type models involved in the experiments are referred to here as Objects 59, 61, 62, 64, and 65. The first three models had swept-back fins and the last two had rectangular fins.

Three separate items were determined under this study: a frequency distribution of the radar cross-sections of each model at each wavelength; the autocorrelation function for each run; and the power spectrum for each run. (The procedures employed and the data obtained appear in Sec. F.2 – F.4.)

The study brings into focus two basic questions: first, whether or not a fine structure analysis for the missile-decoy problem can be expected to provide significant information; and second, the question of

whether or not the power spectra are the correct quantities to consider in this analysis. This study deals with finite samples. The classical theory is based upon a sample of infinite size. A certain amount of arbitrariness is involved when the theory is modified for application to a finite sample. Alternative definitions of the power spectrum and autocorrelation function have been given in the literature (Refs. 28 and 31). It is pointed out that these definitions are definitely not equivalent (Sec. F.5).

The power spectra obtained by the procedure outlined in this appendix are displayed graphically in Section F.4. Even though the main contribution to the radar cross-sections of V-2-type missiles usually comes from the fins, the variation in the shapes of the curves found for Objects 59, 61, and 62 (swept-back fins) appears to be as great as the variation between these and Objects 64 and 65 (rectangular fins)[1].

It is possible that a study of a larger sample of missile runs by the approach used here might begin to display a pattern of differences between power spectra. An attempt to obtain greater discrimination by lengthening the time of observation for a given run would have no bearing on the practical defense problem, since the times available are even less than the intervals of observation used in the drop tests. The practical problem is further restricted, if a pulse-modulated radar is used, since the accessible frequency interval is limited; for the drop-test data, the upper limit was approximately 400 cps.

Some other approach to the question of how the infinite sample theory can be modified for application to a finite sample might conceivably yield spectra which are more sensitive to differences between radar returns for different objects.

If one is convinced that the fine structure of the target return is the most important information available for discriminating between aircraft

[1]In fact, there appears to be little difference between the spectra found here for missiles and those obtained for a B-47 aircraft (Ref. 27).

and decoys, it seems clear that much further analysis is necessary before one can hope to instrument this concept into a feasible discriminator between decoys and aircraft. Such an investigation should include an analysis of the mathematical functional representation of the fine structure to yield the maximum amount of information. After the above method of representation is established and a method of presentation is fixed, one should determine (probably experimentally) whether the differences in the fine structure between missile and decoy are greater than the differences between missile and missile. The latter differences are expected because of differences in the conditions under which the observations are made or unanticipated alterations in enemy missiles (as to structure or structural behavior). If this investigation is to be used to analyze vehicles which are out of the atmosphere for almost all of their trajectories, one should bear in mind the possibility that transient effects (which disappear rapidly in flights through only the sensible atmosphere) might not be damped out. It is clear that, for economic reasons, vehicles cannot be fired out of the atmosphere to analyze transient effects which, by their very nature, may not be reproducible from air frame to air frame.

In short, one should first complete a theoretical investigation to determine the best method of collecting fine structure data, assembling it, representing it, and then displaying it. When this is done, one should see whether, after considering the physics of the ICBM problem, the observables are really significant and physically meaningful in the optimal theory.

F.2 THE FREQUENCY DISTRIBUTIONS

The frequency distributions obtained for each of the ten runs appear in Tables F.2.1 – F.2.10. Each value of cross-section was computed by averaging the power received over consecutive groups of six pulses each. The aspect angles for the measurements contained in these tables are such that the aspect angle never exceeds 15 degrees off-nose and in most cases is between 5 and 10 degrees.

TABLE F.2-1

FREQUENCY DISTRIBUTION – OBJECT 59(S-band)

σ Interval (m^2)	No. of values in interval
0.00 - 0.01	208
0.01 - 0.02	107
0.02 - 0.03	45
0.03 - 0.04	20
0.04 - 0.05	12
0.05 - 0.06	8
0.06 - 0.07	16
0.07 - 0.08	26
0.08 - 0.09	6
	448

TABLE F.2-2

FREQUENCY DISTRIBUTION – OBJECT 59(X-band)

σ Interval (m^2)	No. of values in interval	σ Interval (m^2)	No. of values in interval
0.00 - 0.01	45	0.17 - 0.18	4
0.01 - 0.02	50	0.18 - 0.19	5
0.02 - 0.03	55	0.19 - 0.20	5
0.03 - 0.04	54	0.20 - 0.21	5
0.04 - 0.05	48	0.21 - 0.22	4
0.05 - 0.06	28	0.22 - 0.23	3
0.06 - 0.07	28	0.23 - 0.24	4
0.07 - 0.08	16	0.24 - 0.25	3
0.08 - 0.09	19	0.25 - 0.26	1
0.09 - 0.10	19	0.26 - 0.27	1
0.10 - 0.11	16	0.27 - 0.28	4
0.11 - 0.12	10	0.29 - 0.30	3
0.12 - 0.13	5	0.31 - 0.32	1
0.13 - 0.14	5	0.59 - 0.60	4
0.14 - 0.15	5	0.64 - 0.65	3
0.15 - 0.16	9		463
0.16 - 0.17	1		

TABLE F.2-3

FREQUENCY DISTRIBUTION – OBJECT 61 (S-band)

σ Interval (m^2)	No. of values in interval
0.00 - 0.01	40
0.01 - 0.02	44
0.02 - 0.03	27
0.03 - 0.04	16
0.04 - 0.05	8
0.05 - 0.06	13
0.06 - 0.07	14
0.07 - 0.08	22
0.08 - 0.09	17
0.09 - 0.10	6
0.10 - 0.11	5
0.11 - 0.12	4
0.12 - 0.13	3
0.13 - 0.14	2
	221

TABLE F.2-4

FREQUENCY DISTRIBUTION – OBJECT 61(X-band)

σ Interval (m^2)	No. of values in interval
0.00 - 0.01	49
0.01 - 0.02	47
0.02 - 0.03	17
0.03 - 0.04	22
0.04 - 0.05	12
0.05 - 0.06	12
0.06 - 0.07	5
0.07 - 0.08	4
0.08 - 0.09	3
0.09 - 0.10	10
0.10 - 0.11	9
0.11 - 0.12	6
0.12 - 0.13	8
0.13 - 0.14	4
0.14 - 0.15	5
0.15 - 0.16	3
0.16 - 0.17	1
0.17 - 0.18	3
0.18 - 0.19	2
0.19 - 0.20	1
	223

TABLE F.2-5

FREQUENCY DISTRIBUTION – OBJECT 62(S-band)

σ Interval (m^2)	No. of values in interval
0.00 - 0.01	123
0.01 - 0.02	107
0.02 - 0.03	117
0.03 - 0.04	62
0.04 - 0.05	55
0.05 - 0.06	48
0.06 - 0.07	46
0.07 - 0.08	21
0.08 - 0.09	14
0.09 - 0.10	12
0.10 - 0.11	15
0.11 - 0.12	3
0.12 - 0.13	6
0.13 - 0.14	4
0.14 - 0.15	4
0.16 - 0.17	2
0.17 - 0.18	2
	641

TABLE F.2-6

FREQUENCY DISTRIBUTION – OBJECT 62(X-band)

σ Interval (m^2)	No. of values in interval	σ Interval (m^2)	No. of values in interval
0.00 - 0.01	152	0.15 - 0.16	3
0.01 - 0.02	115	0.16 - 0.17	6
0.02 - 0.03	80	0.17 - 0.18	2
0.03 - 0.04	74	0.18 - 0.19	3
0.04 - 0.05	43	0.19 - 0.20	2
0.05 - 0.06	35	0.20 - 0.21	5
0.06 - 0.07	25	0.21 - 0.22	3
0.07 - 0.08	13	0.22 - 0.23	2
0.08 - 0.09	15	0.25 - 0.26	1
0.09 - 0.10	19	0.27 - 0.28	1
0.10 - 0.11	12	0.35 - 0.36	1
0.11 - 0.12	8	0.36 - 0.37	1
0.12 - 0.13	10	0.39 - 0.40	3
0.13 - 0.14	9		649
0.14 - 0.15	6		

TABLE F.2-7

FREQUENCY DISTRIBUTION – OBJECT 64(S-band)

σ Interval (m^2)	No. of values in interval	σ Interval (m^2)	No. of values in interval
0.00 - 0.01	49	0.27 - 0.28	6
0.01 - 0.02	129	0.28 - 0.29	4
0.02 - 0.03	147	0.29 - 0.30	3
0.03 - 0.04	123	0.30 - 0.31	6
0.04 - 0.05	65	0.31 - 0.32	2
0.05 - 0.06	52	0.32 - 0.33	2
0.06 - 0.07	51	0.33 - 0.34	2
0.07 - 0.08	59	0.34 - 0.35	3
0.08 - 0.09	61	0.35 - 0.36	3
0.09 - 0.10	73	0.36 - 0.37	3
0.10 - 0.11	60	0.37 - 0.38	5
0.11 - 0.12	28	0.38 - 0.39	4
0.12 - 0.13	33	0.39 - 0.40	2
0.13 - 0.14	19	0.41 - 0.42	1
0.14 - 0.15	15	0.42 - 0.43	5
0.15 - 0.16	21	0.43 - 0.44	6
0.16 - 0.17	14	0.44 - 0.45	6
0.17 - 0.18	18	0.45 - 0.46	3
0.18 - 0.19	18	0.46 - 0.47	4
0.19 - 0.20	6	0.47 - 0.48	1
0.20 - 0.21	11	0.48 - 0.49	7
0.21 - 0.22	9	0.49 - 0.50	4
0.22 - 0.23	7	0.50 - 0.51	7
0.23 - 0.24	8	0.51 - 0.52	3
0.24 - 0.25	7	0.52 - 0.53	1
0.25 - 0.26	6		1192
0.26 - 0.27	10		

TABLE F.2-8

FREQUENCY DISTRIBUTION – OBJECT 64(X-band)

σ Interval (m^2)	No. of values in interval	σ Interval (m^2)	No. of values in interval
0.00 - 0.01	56	0.44 - 0.45	6
0.01 - 0.02	61	0.45 - 0.46	4
0.02 - 0.03	54	0.46 - 0.47	4
0.03 - 0.04	60	0.47 - 0.48	4
0.04 - 0.05	52	0.48 - 0.49	4
0.05 - 0.06	39	0.49 - 0.50	6
0.06 - 0.07	46	0.50 - 0.51	4
0.07 - 0.08	39	0.51 - 0.52	1
0.08 - 0.09	33	0.52 - 0.53	2
0.09 - 0.10	30	0.53 - 0.54	2
0.10 - 0.11	41	0.54 - 0.55	5
0.11 - 0.12	26	0.55 - 0.56	1
0.12 - 0.13	26	0.57 - 0.58	4
0.13 - 0.14	21	0.59 - 0.60	1
0.14 - 0.15	33	0.60 - 0.61	1
0.15 - 0.16	27	0.61 - 0.62	1
0.16 - 0.17	33	0.63 - 0.64	3
0.17 - 0.18	35	0.65 - 0.66	1
0.18 - 0.19	26	0.66 - 0.67	2
0.19 - 0.20	25	0.67 - 0.68	1
0.20 - 0.21	34	0.69 - 0.70	1
0.21 - 0.22	27	0.70 - 0.71	1
0.22 - 0.23	30	0.74 - 0.75	1
0.23 - 0.24	34	0.75 - 0.76	1
0.24 - 0.25	21	0.80 - 0.81	2
0.25 - 0.26	16	0.81 - 0.82	2
0.26 - 0.27	15	0.83 - 0.84	2
0.27 - 0.28	10	0.84 - 0.85	1
0.28 - 0.29	11	0.85 - 0.86	1
0.29 - 0.30	13	0.87 - 0.88	1
0.30 - 0.31	13	0.88 - 0.89	3
0.31 - 0.32	12	0.89 - 0.90	1
0.32 - 0.33	14	0.94 - 0.95	1
0.33 - 0.34	6	1.00 - 1.01	1
0.34 - 0.35	18	1.04 - 1.05	3
0.35 - 0.36	14	1.10 - 1.11	2
0.36 - 0.37	6	1.12 - 1.13	1
0.37 - 0.38	10	1.13 - 1.14	3
0.38 - 0.39	8	1.16 - 1.17	3
0.39 - 0.40	6	1.27 - 1.28	1
0.40 - 0.41	5	1.28 - 1.29	1
0.41 - 0.42	5	1.30 - 1.31	1
0.42 - 0.43	6	1.36 - 1.37	1
0.43 - 0.44	3		1192

TABLE F.2-9

FREQUENCY DISTRIBUTION – OBJECT 65(S-band)

σ Interval (m^2)	No. of values in interval	σ Interval (m^2)	No. of values in interval
0.00 - 0.01	78	0.20 - 0.21	7
0.01 - 0.02	44	0.21 - 0.22	5
0.02 - 0.03	63	0.22 - 0.23	3
0.03 - 0.04	74	0.23 - 0.24	6
0.04 - 0.05	81	0.24 - 0.25	7
0.05 - 0.06	65	0.25 - 0.26	2
0.06 - 0.07	75	0.26 - 0.27	5
0.07 - 0.08	61	0.27 - 0.28	4
0.08 - 0.09	44	0.28 - 0.29	6
0.09 - 0.10	35	0.29 - 0.30	5
0.10 - 0.11	31	0.30 - 0.31	4
0.11 - 0.12	38	0.31 - 0.32	5
0.12 - 0.13	21	0.32 - 0.33	8
0.13 - 0.14	31	0.33 - 0.34	5
0.14 - 0.15	15	0.34 - 0.35	1
0.15 - 0.16	9	0.35 - 0.36	2
0.16 - 0.17	7	0.36 - 0.37	3
0.17 - 0.18	14	0.37 - 0.38	3
0.18 - 0.19	7	0.38 - 0.39	2
0.19 - 0.20	4		880

TABLE F.2-10

FREQUENCY DISTRIBUTION – OBJECT 65(X-band)

σ Interval (m^2)	No. of values in interval	σ Interval (m^2)	No. of values in interval
0.00 - 0.01	32	0.29 - 0.30	13
0.01 - 0.02	49	0.30 - 0.31	9
0.02 - 0.03	33	0.31 - 0.32	8
0.03 - 0.04	33	0.32 - 0.33	5
0.04 - 0.05	43	0.33 - 0.34	6
0.05 - 0.06	51	0.34 - 0.35	10
0.06 - 0.07	33	0.35 - 0.36	12
0.07 - 0.08	38	0.36 - 0.37	7
0.08 - 0.09	36	0.37 - 0.38	3
0.09 - 0.10	31	0.38 - 0.39	9
0.10 - 0.11	31	0.39 - 0.40	5
0.11 - 0.12	33	0.40 - 0.41	1
0.12 - 0.13	25	0.41 - 0.42	5
0.13 - 0.14	27	0.42 - 0.43	9
0.14 - 0.15	24	0.43 - 0.44	6
0.15 - 0.16	20	0.44 - 0.45	1
0.16 - 0.17	17	0.45 - 0.46	2
0.17 - 0.18	23	0.46 - 0.47	4
0.18 - 0.19	16	0.47 - 0.48	3
0.19 - 0.20	19	0.48 - 0.49	7
0.20 - 0.21	22	0.49 - 0.50	2
0.21 - 0.22	16	0.50 - 0.51	1
0.22 - 0.23	20	0.52 - 0.53	1
0.23 - 0.24	15	0.53 - 0.54	2
0.24 - 0.25	23	0.55 - 0.56	2
0.25 - 0.26	17	0.60 - 0.61	1
0.26 - 0.27	12	0.62 - 0.63	1
0.27 - 0.28	13	0.67 - 0.68	1
0.28 - 0.29	10		898

F.3 THE DEFINITIONS OF THE AUTOCORRELATION FUNCTION, $R(\tau)$, AND THE POWER SPECTRUM, $S(\omega)$, USED IN THE COMPUTATIONS

In this section, a brief summary of pertinent facts concerning the usual $R(\tau)$ and $S(\omega)$, the definitions of $R(\tau)$ and $S(\omega)$ used in the computations, the relationship between $R(\tau)$ and $S(\omega)$, and one aspect of the significance of the definitions are presented.

When a real random function $y(t)$ is known for all times t from 0 to ∞, the autocorrelation function $R_\infty(\tau)$ and power spectrum, $S_\infty(\omega)$, are defined as

$$R_\infty(\tau) = \lim_{T \to \infty} \frac{1}{T} \int_0^T y(t)\, y(t+\tau)\, dt \quad , \tag{F.3-1}$$

and

$$S_\infty(\omega) = \lim_{T \to \infty} \frac{2\left|A(\omega, T)\right|^2}{T} \quad , \tag{F.3-2}$$

where

$$A(\omega, T) = \frac{1}{\sqrt{2\pi}} \int_0^T y(t) e^{-i\omega t}\, dt \quad . \tag{F.3-3}$$

Note that

$$S_\infty(\omega) \geq 0 \quad , \qquad \left|R_\infty(\tau)\right| \leq R_\infty(0) \quad , \tag{F.3-4}$$

and

$$S_\infty(\omega) = \frac{2}{\pi} \int_0^\infty R_\infty(\tau) \cos \omega \tau\, d\tau \quad . \tag{F.3-5}$$

The last equation is known as the Wiener-Khinchine Theorem.

For a random function $y(nT_o)$, $n = 0, 1, \ldots, N$ (that is, for a finite set of data), the autocorrelation function, $R(\tau, T)$, and the power spectrum, $S(\omega)$, will be defined here by

$$R(\tau_s, T) = \frac{1}{N} \sum_{n=0}^{N-s} y(nT_o)\, y(nT_o + \tau_s) , \quad 0 \leq \tau_s \leq NT_o$$

$$= 0 , \quad \tau_s < 0 \text{ and } \tau_s > NT_o , \qquad \text{(F. 3-6)}$$

where

$$\tau_s = sT_o , \qquad s = 0, 1, \ldots, N, \text{ and}$$

$$S(\omega) = \frac{2}{T} \left| F(\omega, T) \right|^2 , \qquad \text{(F. 3-7)}$$

where

$$F(\omega, T) = \frac{T_o}{\sqrt{2\pi}} \sum_{n=0}^{N} y(nT_o) e^{-i\omega nT_o} . \qquad \text{(F. 3-8)}$$

Note that the summation in $R(\tau_s, T)$ is divided by N, the total number of values for $y(nT_o)$, rather than by $N - s$, the number of values of $y(nT_o) \times y(nT_o + \tau_s)$ in the summation. The reason for this is to preserve the relation

$$S(\omega) = \frac{2T_o}{\pi} \left\{ \sum_{s=0}^{N} R(sT_o, T) \cos \omega sT_o - \frac{1}{2} R(0, T) \right\} , \qquad \text{(F. 3-9)}$$

which is the analogue of the Wiener-Khinchine relation. A proof of Equation F. 3-9 is the following:

Using the definition of $F(\omega, T)$ given in Equation F. 3-8,

$$\left|F(\omega, T)\right|^2 = \frac{T_o^2}{2\pi} \sum_{n=0}^{N} \sum_{m=0}^{N} y(nT_o)\, y(mT_o) e^{i\omega(n-m)T_o}$$

$$= \frac{T_o^2}{2\pi} \sum_{n=0}^{N} \sum_{s=n-N}^{n} y(nT_o)\, y\left[(n-s)T_o\right] e^{i\omega s T_o}$$

$$= \frac{T_o^2}{2\pi} \left\{ \sum_{s=0}^{N} \sum_{n=s}^{N} y(nT_o)\, y\left[(n-s)T_o\right] e^{i\omega s T_o} \right.$$

$$\left. + \sum_{s=-N}^{-1} \sum_{n=0}^{N+s} y(nT_o)\, y\left[(n-s)T_o\right] e^{i\omega s T_o} \right\}$$

$$= \frac{T_o^2}{2\pi} \left\{ \sum_{n=0}^{N} y^2(nT_o) + 2 \sum_{s=1}^{N} \sum_{n=s}^{N} y(nT_o)\, y\left[(n-s)T_o\right] \cos\omega s T_o \right\} .$$

From the definition of $R(\tau_s, T)$

$$R(sT_o, T) = \left(\frac{T_o}{T}\right) \sum_{n=s}^{N} y(nT_o)\, y\left[(n-s)T_o\right] ,$$

where

$$T = NT_o .$$

Thus

$$S(\omega) \equiv \frac{2}{T}\left|F(\omega, T)\right|^2 = \frac{T_o}{\pi}\left\{R(o, T) + 2\sum_{s=1}^{N} R(sT_o, T)\cos\omega sT_o\right\}$$

from which Equation F. 3-9 immediately follows.

One aspect of the significance of the definition of $F(\omega, T)$ may be seen from the following considerations. $R(\tau_s, T)$ and $S(\omega)$ were computed according to the above equations, using for $y(nT_o)$ the averaged values of cross-section described in Section F. 2; that is, each $\bar{\sigma}$ is the average over six successive values of σ with no overlap in neighboring $\bar{\sigma}$'s. Consider the Fourier analysis of an arbitrary function f(t) which passes through a given set of points f_{nm} defined at the times t_{nm}, m = 0, 1, ..., M, n = 0, 1, ..., N, and f(t) = 0 for $t < t_{oo}$ and $t > t_{N, M+1}$. (The f_{nm} correspond to the σ values, M + 1 of these being used to obtain a value of $\bar{\sigma}$.) The Fourier transform of f(t) is given by

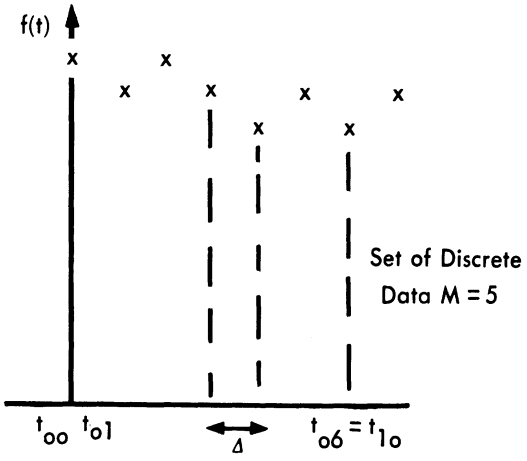

$$F(\omega) = \left(\frac{1}{\sqrt{2\pi}}\right)\int_{t_{oo}}^{t_{N, M+1}} f(t)e^{-i\omega t}\,dt = \left(\frac{1}{\sqrt{2\pi}}\right)\sum_{n=0}^{N}\sum_{m=0}^{M}\int_{t_{nm}}^{t_{n, m+1}} f(t)e^{-i\omega t}\,dt,$$

the latter expression being valid provided $t_{n, M+1} = t_{n+1, o}$ (this insures that the whole integration range be covered).

If

$$t_{n,m+1} - t_{n,m} = \Delta \text{ and } t_{oo} = 0 \ ,$$

then

$$t_{nm} = n(M+1)\,\Delta + m\Delta \ ,$$

and

$$t_{n,m+1} = n(M+1)\,\Delta + (m+1)\,\Delta \ ,$$

$$\int_{t_{nm}}^{t_{n,m+1}} f(t)e^{-i\omega t}\,dt = e^{-i\omega t_{nm}} \int_0^{\Delta} dt'\, f(t'+t_{nm})e^{-i\omega t'} \ .$$

If $\omega\Delta \ll 1$,

$$F(\omega) \cong \left(\frac{\Delta}{\sqrt{2\pi}}\right) \sum_{n=0}^{N} \sum_{m=0}^{M} e^{-i\omega\left[n(M+1)\,\Delta + m\Delta\right]} \tilde{f}_{nm} \ ,$$

where

$$\tilde{f}_{nm} = \left(\frac{1}{\Delta}\right) \int_{t_{nm}}^{t_{n,m+1}} f(t)\,dt \ .$$

If further $\omega M\Delta \ll 1$,

$$F(\omega) \cong \frac{T_o}{\sqrt{2\pi}} \sum_{n=0}^{N} \bar{f}_n\, e^{-i\omega n T_o} \ ,$$

where

$$T_o = (M+1)\,\Delta$$

and

$$\bar{f}_n = \frac{1}{M+1} \sum_{m=0}^{M} \tilde{f}_{nm} \ .$$

The formal similarity between this expression for $F(\omega)$ and $f(\omega, T)$ as defined in Equation F.3-8 is apparent. If now f(t) is slowly varying over time intervals of length Δ (i.e., f(t) is band limited with $\omega_{maximum} \ll 1/\Delta$), then $\tilde{f}_{nm} \cong f_{nm} \cong \tilde{f}_{n,\,m+1}$; that is, $\tilde{f}_{nm}$ may be replaced by f_{nm}, in which case $\bar{f}_n$ is merely the average of the M+1 values: $f_{n0}, f_{n1}, \ldots, f_{nM}$. Thus, the definition of $F(\omega, T)$ given above and used in the computations gives the power spectrum, for $\omega \ll 1/T_o$ (T_o is the interval over which the data are averaged), of a function which is zero outside the observation interval and which passes through all the points of the data before averaging. It is assumed that the function is band limited with maximum frequency $\ll 1/\Delta$ (Δ is the pulse repetition period of the radar used in obtaining the original data). In this case, $\Delta = 1/409.75$ sec. and $T_o = 6\Delta$ (M = 5).

In actual practice, the following procedure was used:

$$R(\tau) = R(sT_o) = \left(\frac{1}{N}\right) \sum_{n=0}^{N-s} \bar{\sigma}(nT_o)\, \bar{\sigma}\left((n+s)\,T_o\right) \ ,$$

where values of s used were

s = 0(5)150(25)1250 for S-band ,

s = 0(5)200(25)1250 for X-band .

These are the values shown on the accompanying list.

Then $S(\omega)$ for $\omega \leq 2\pi$ was approximated as

$$S(\omega) = \frac{2T_o}{\pi} \sum_{s=0}^{N} a_s \, R(sT_o) \cos(\omega s T_o) \quad ,$$

where

$$a_o = 5/2 \quad ,$$

$$a_s = 5 \quad \text{for} \begin{cases} 5 \leq s \leq 145 & \text{for S-band} \\ 5 \leq s \leq 195 & \text{for X-band} \end{cases} ,$$

$$a_s = 15 \quad \text{for} \begin{cases} s = 150 & \text{for S-band} \\ s = 200 & \text{for X-band} \end{cases} ,$$

$$a_s = 25 \quad \text{for} \begin{cases} 175 \leq s \leq 1250 & \text{for S-band} \\ 225 \leq s \leq 1250 & \text{for X-band} \end{cases} .$$

This procedure was used to obtain $S(\omega)$ for $\omega/2\pi = 0(.1)1.0$ cycles per second; for larger values of ω, the method must be altered, inasmuch as taking s at intervals of 25 does not yield sufficient accuracy. In the interest of economy of time and money, it was decided to return to the basic definition of the power spectrum, namely

$$S(\omega) \equiv \frac{2}{T} \left| F(\omega, T) \right|^2 \quad .$$

Numerically, this means

$$S(\omega) = \frac{25\,T_o}{\pi N} \left\{ \left[\sum_{n=0}^{[N/5]} \bar{\sigma}(5nT_o) \cos(5n\omega T_o) \right]^2 + \left[\sum_{n=0}^{[N/5]} \bar{\sigma}(5nT_o) \sin(5n\omega T_o) \right]^2 \right\} .$$

This is the formula used to obtain $S(\omega)$ for $\omega/2\pi = 1.1, 1.2, 1.5, 2.0, 3.0, 4.0, 5.5, 6.0, 6.5, 7.5$ cycles per second. To get $S(\omega)$ for higher values of ω would require taking more than every fifth value of $\bar{\sigma}$ which was not considered warranted.

F.4 COMPUTATIONAL RESULTS FOR R(τ) AND S(ω)

The results of the computations of the autocorrelation functions and spectra for the various objects are given in Tables F.4-1 – F.4-4 and Figures F.4-1 – F.4-20. There are two curves for each object and frequency, one of which shows all of the computed values and is faired in at $\omega/2\pi$ = 1.1 cycles per second, the other of which shows the region $\omega \leq 2\pi$ in more detail.

The spectra, as expected, all show a large peak at $\omega = 0$. They then drop off rapidly and then oscillate more or less randomly. For only three of the ten cases did the ratio of the second largest peak to that at $\omega = 0$ exceed 1/10: for Object 59 at S-band this ratio is $\sim$0.2; for Object 61 at S-band it is $\sim$0.3; and for Object 61 at X-band, there are two large subsidiary peaks with ratios to the zero-frequency peak of $\sim$0.5 and 0.2. The observation times for Objects 59 and 61 were considerably less than for the others. (The sample lengths were approximately 7, 3, and 3 seconds for Object 59 at S-band, Object 61 at S-band, and Object 61 at X-band, respectively. For the other objects, the sample length was >10 seconds.)

Before interpreting the peaks in terms of physical characteristics of the missile, one should take into account the fact that the zero-frequency signal from the missile will, for short observation times, contribute appreciable subsidiary peaks to the spectrum (in addition to the one at $\omega = 0$). When this is done, it is found that the results are not inconsistent with the assumption that the spectra are due merely to a zero-frequency signal with superimposed noise characteristics inherent to the small sample. If the missile generates any other frequencies, these are not likely to be detected from the power spectra.

F.5 FURTHER ANALYSIS OF R(τ) AND S(ω)

The finite nature of the sample involved in these computations of the autocorrelation function and power spectrum for the radar cross-section data obtained in the drop tests necessitates a more detailed study, which is presented in this section.

TABLE F.4-1

$R(n T_o)$ – S-BAND – SWEPT BACK FINS

n	Object 59	Object 61	Object 62
0	.0008453	.0029390	.0023321
5	0008353	0023537	0018821
10	0008000	0017303	0013379
15	0007538	0011459	0009538
20	0006946	0007092	0007803
25	0006308	0005899	0007903
30	0005674	0005798	0008497
35	0005087	0006064	0009763
40	0004469	0007060	0010370
45	0003924	0007693	0010078
50	0003453	0008243	0009771
55	0003045	0009202	0010260
60	0002761	0010578	0010491
65	0002554	0012257	0010660
70	0002460	0014454	0010257
75	0002395	0013674	0009476
80	0002451	0011573	0008434
85	0002522	0009491	0007511
90	0002656	0006780	0007332
95	0002725	0005560	0007779
100	0002775	0005202	0008361
105	0002768	0004491	0008304
110	0002732	0003977	0007481
115	0002676	0003463	0007005
120	0002540	0004005	0007566
125	0002395	0005413	0008530
130	0002230	0006821	0009498
135	0002076	0008294	0010403
140	0001864	0009101	0010378
145	0001721	0009339	0009784

TABLE F.4-1 (Cont.)

$R(n T_o)$ – S-BAND – SWEPT BACK FINS

n	Object 59	Object 61	Object 62
150	.0001623	.0007954	.0008917
175	0001308	0005069	0006795
200	0001248	0002642	0007798
225	0001098	0006688	0006138
250	0001533	0000477	0006063
275	0001949	0000812	0007759
300	0001547	0003202	0007138
325	0000730	0000193	0005265
350	0000348	0000615	0007893
375	0000442		0005356
400	0000435		0003522
425	0000129		0006118
450	0000000		0003889
475			0003649
500			0003116
525			0002660
550			0002799
575			0002389
600			0003582
625			0003334
650			0002809
675			0002497
700			0001704
725			0002867
750			0000575
775			0002067
800			0000082

TABLE F.4-2

$R(n\,T_o)$ – X-BAND – SWEPT BACK FINS

n	Object 59	Object 61	Object 62
0	.0141270	.0046145	.0050741
5	0071525	0041448	0025862
10	0070421	0034787	0020497
15	0059138	0028063	0017938
20	0053559	0021480	0021512
25	0044026	0015557	0025621
30	0054613	0010679	0021173
35	0043404	0006991	0018398
40	0040270	0004715	0018803
45	0045957	0003385	0023149
50	0041832	0002416	0022695
55	0033812	0001878	0016563
60	0034853	0001489	0018283
65	0033959	0001520	0018065
70	0032140	0002208	0019548
75	0034870	0003448	0022300
80	0036184	0004371	0017712
85	0036834	0005240	0021593
90	0044616	0005950	0017755
95	0055883	0007081	0017029
100	0056242	0008855	0016308
105	0056562	0011552	0018463
110	0049853	0014348	0017689
115	0041834	0016783	0017517
120	0039607	0018905	0015197
125	0036294	0020430	0015692
130	0037868	0022077	0019122
135	0037045	0022308	0018591
140	0036235	0020588	0017432
145	0033121	0017566	0017085
150	0029456	0014172	0014481
155	0026168	0009584	0014074
160	0024110	0005271	0012283
165	0024711	0002434	0010523

TABLE F.4-2 (Cont.)

$R(n T_o)$ – X-BAND – SWEPT BACK FINS

n	Object 59	Object 61	Object 62
170	.0026162	.0001081	.0010752
175	0026965	0000774	0012779
180	0027853	0000973	0013834
185	0029782	0001878	0011650
190	0032698	0003357	0013454
195	0035881	0003873	0010824
200	.0039490	.0003661	.0011133
225	0034259	0003475	0011588
250	0022680	0002882	0009446
275	0021086	0001199	0007613
300	0022799	0000566	0006469
325	0023015	0001348	0008158
350	0013603	0001063	0006938
375	0012445		0005678
400	0009518		0004964
425	0007890		0003596
450	0002006		0004875
475			0004372
500			0004175
525			0004257
550			0004977
575			0003584
600			0005147
625			0003615
650			0002293
675			0002339
700			0001387
725			0000443
750			0000183
775			0000331
800			0000000

TABLE F.4-3

$R(n T_o)$ – S-BAND – SQUARE FINS

n	Object 64	Object 65
0	.0213705	.0135879
5	0200862	0102389
10	0178543	0066842
15	0156342	0061679
20	0138965	0063365
25	0125703	0068854
30	0115042	0075865
35	0106352	0079173
40	0098932	0077494
45	0092760	0064617
50	0088143	0057250
55	0085914	0060818
60	0087777	0065239
65	0091778	0066173
70	0095362	0067007
75	0096523	0067176
80	0095611	0061667
85	0093766	0054871
90	0091029	0055849
95	0087031	0063276
100	0082757	0073871
105	0078319	0073213
110	0073477	0058965
115	0068420	0049297
120	0064605	0047688
125	0063129	0051110
130	0063519	0058077
135	0064878	0059460
140	0067283	0058439
145	0071034	0057026

TABLE F.4-3 (Cont.)

$R(n\,T_o)$ – S-BAND – SQUARE FINS

n	Object 64	Object 65
150	.0075680	.0052668
175	0089139	0053268
200	0077239	0059709
225	0060214	0045687
250	0063744	0037299
275	0066082	0042200
300	0045265	0044469
325	0061719	0036720
350	0070511	0036091
375	0056870	0037898
400	0045454	0040035
425	0045930	0028989
450	0041060	0029714
475	0040726	0032119
500	0048994	0039226
525	0048728	0029245
550	0043212	0025457
575	0062451	0028174
600	0067761	0038098
625	0050572	0022803
650	0062977	0026753
675	0072518	0038686
700	0056768	0028555
725	0039070	0018952
750	0035771	0017655
775	0032301	0015259
800	0027729	0009849
825	0026783	0007866
850	0051205	0007180
875	0035928	0008692

TABLE F.4-3 (Cont.)

$R(n T_o)$ – S-BAND – SQUARE FINS

n	Object 64	Object 65
900	.0019334	.0004677
925	0036836	0001206
950	0027423	
975	0013044	
1000	0020053	
1025	0023112	
1050	0016797	
1075	0007424	
1100	0005445	
1125	0009259	
1150	0002440	
1175	0002134	
1200	0006488	
1225	0006437	

TABLE F.4-4

$R(n\,T_o)$ – X-BAND – SQUARE FINS

n	Object 64	Object 65
0	.0731492	.0401553
5	0496405	0269065
10	0415901	0257876
15	0418286	0257512
20	0359315	0245474
25	0301876	0238165
30	0310012	0244880
35	0311995	0242412
40	0350713	0226309
45	0377331	0255553
50	0422809	0256857
55	0432972	0253318
60	0370850	0232201
65	0359330	0252210
70	0362422	0235390
75	0348520	0251941
80	0299206	0224900
85	0289381	0217394
90	0330233	0238443
95	0332032	0240687
100	0329484	0243688
105	0400315	0241638
110	0364368	0232737
115	0347348	0216312
120	0358902	0237124
125	0335385	0218293
130	0290651	0205318
135	0272524	0213441
140	0280468	0226513
145	0301092	0235193

TABLE F.4-4 (Cont.)

$R(n\,T_o)$ – X-BAND – SQUARE FINS

n	Object 64	Object 65
150	.0291169	.0237621
155	0333597	0222940
160	0355673	0209540
165	0326777	0225274
170	0333055	0221028
175	0351747	0212266
180	0319484	0205320
185	0296904	0199072
190	0284441	0206678
195	0282039	0225460
200	.0279145	.0220419
225	0300524	0190359
250	0251444	0181058
275	0272144	0174472
300	0260056	0159126
325	0256764	0159699
350	0250086	0152185
375	0246935	0145686
400	0261566	0139706
425	0237105	0112744
450	0274815	0114447
475	0204867	0109566
500	0229171	0098070
525	0226876	0098986
550	0204659	0084603
575	0185845	0081030
600	0181684	0063576
625	0173128	0052469

TABLE F.4-4 (Cont.)

$R(n T_o)$ – X-BAND – SQUARE FINS

n	Object 64	Object 65
650	.0151293	.0049851
675	0148216	0041182
700	0137398	0037598
725	0133801	0032464
750	0088473	0021562
775	0089325	0017225
800	0077180	0013484
825	0069846	0008427
850	0080214	0007767
875	0073055	0008462
900	0052689	0003787
925	0053285	0002023
950	0040715	
975	0039828	
1000	0035806	
1025	0026802	
1050	0031196	
1075	0031564	
1100	0024238	
1125	0020768	
1150	0019607	
1175	0014503	
1200	0011415	
1225	0003088	

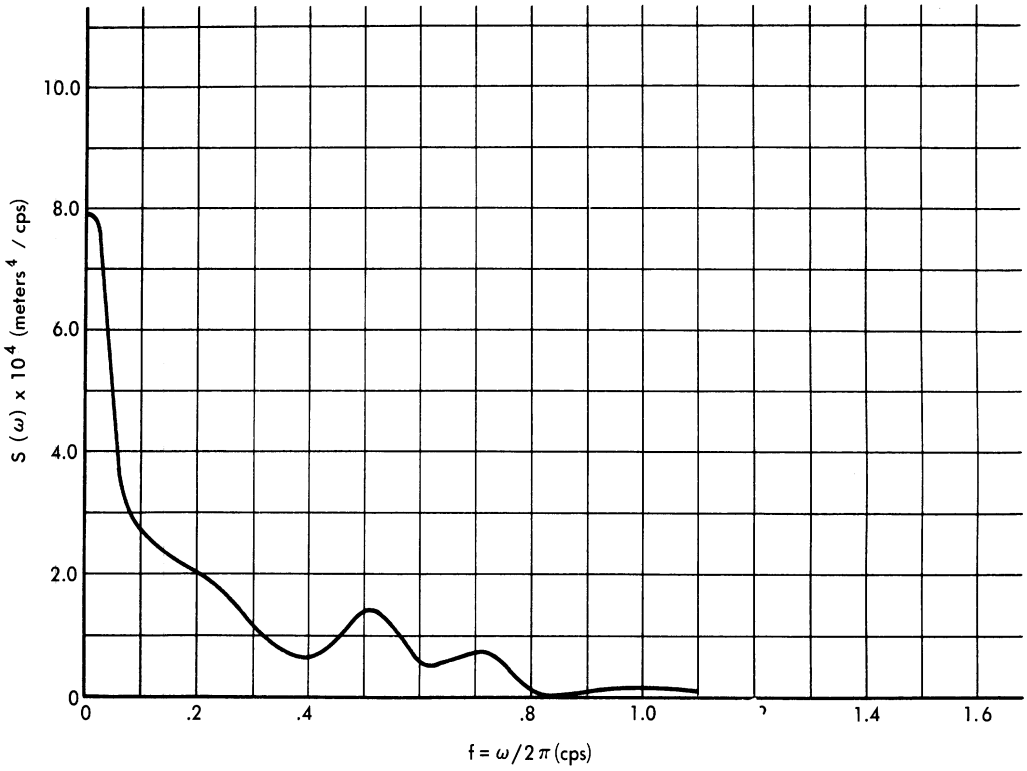

FIG. F.4-1 S (ω) FOR OBJECT 59 S-BAND

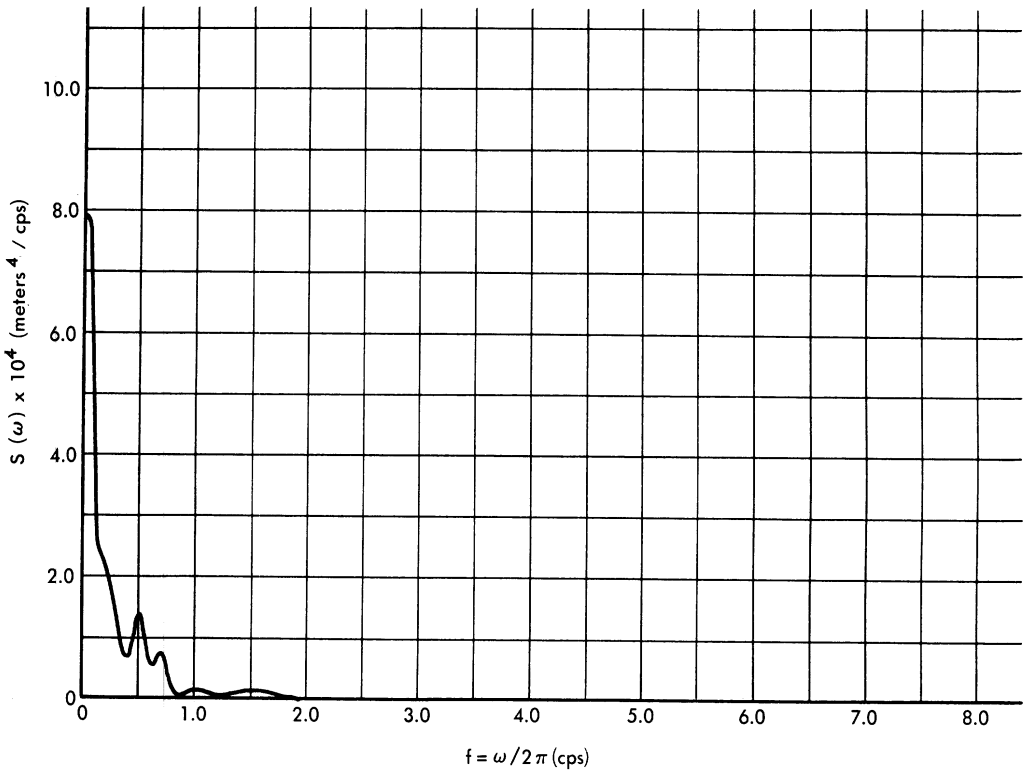

FIG. F.4-2 S (ω) FOR OBJECT 59 S-BAND

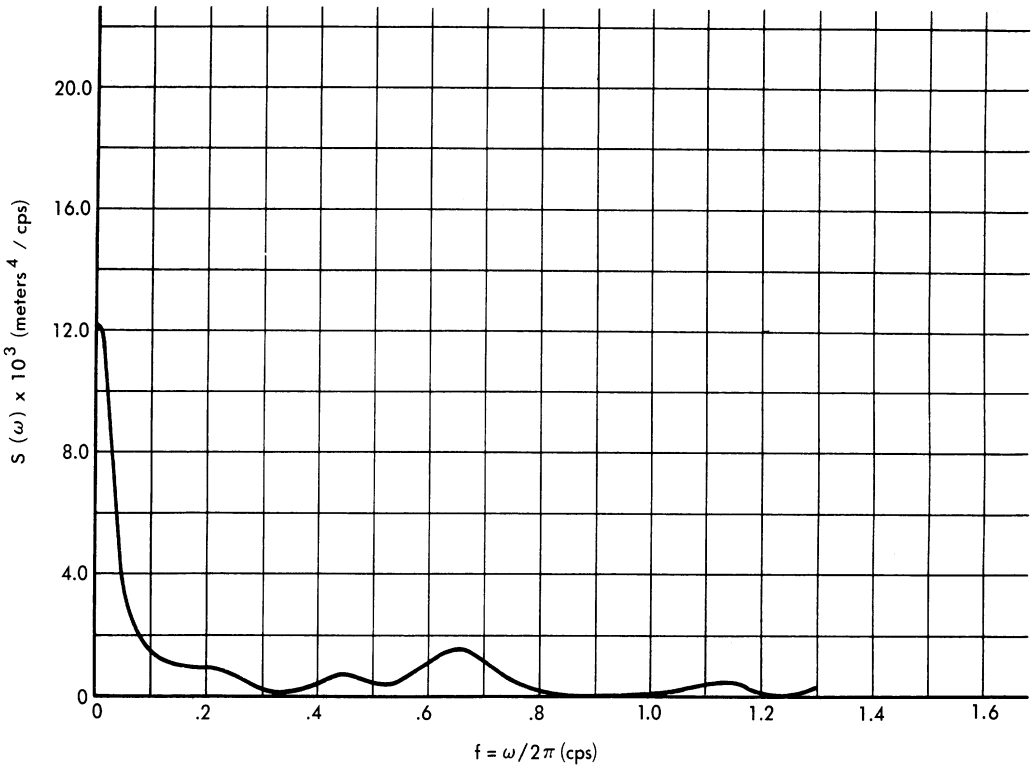

FIG. F.4 - 3 S (ω) FOR OBJECT 59 X - BAND

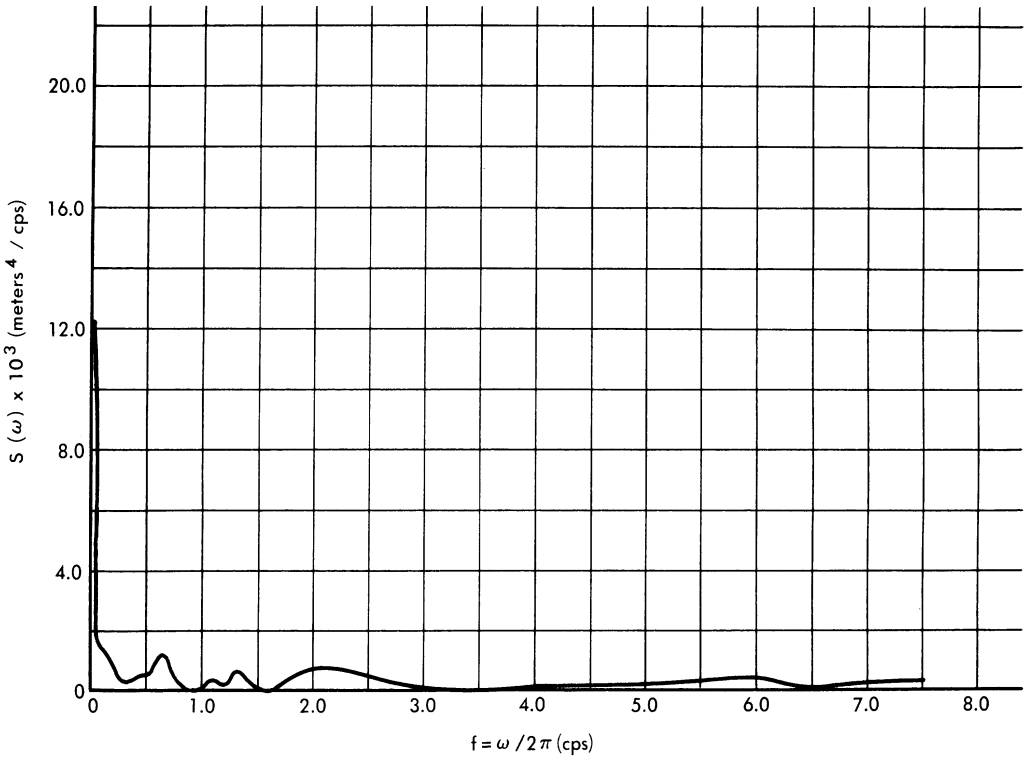

FIG. F.4 - 4 S (ω) FOR OBJECT 59 X - BAND

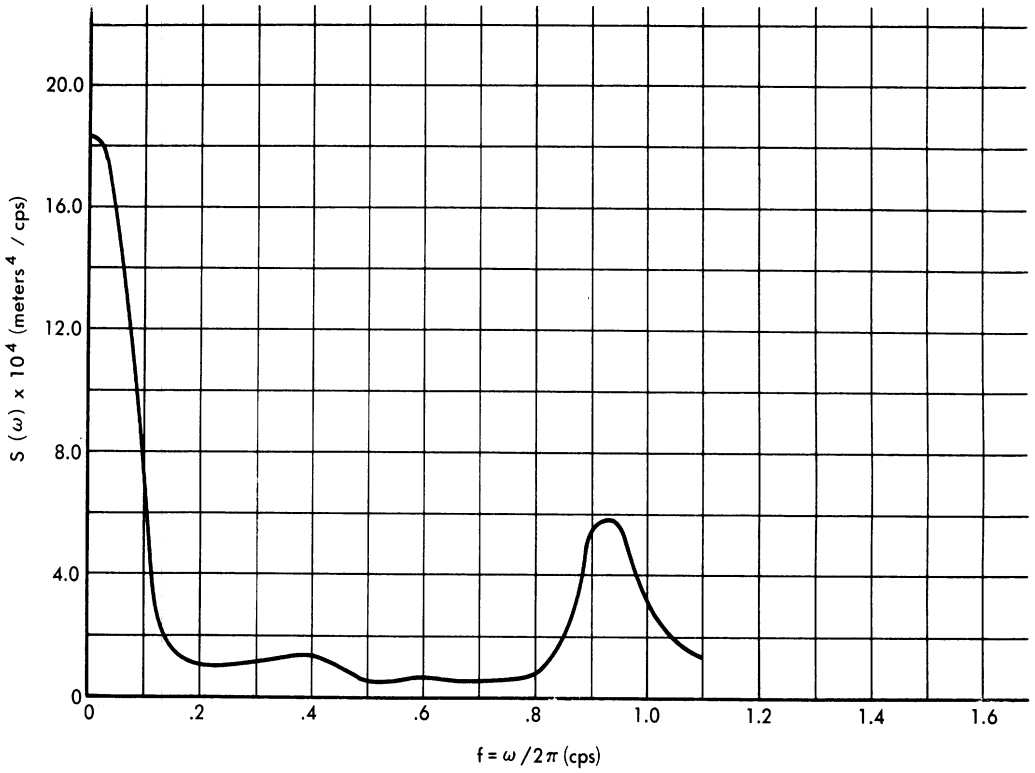

FIG. F.4-5 S (ω) FOR OBJECT 61 S-BAND

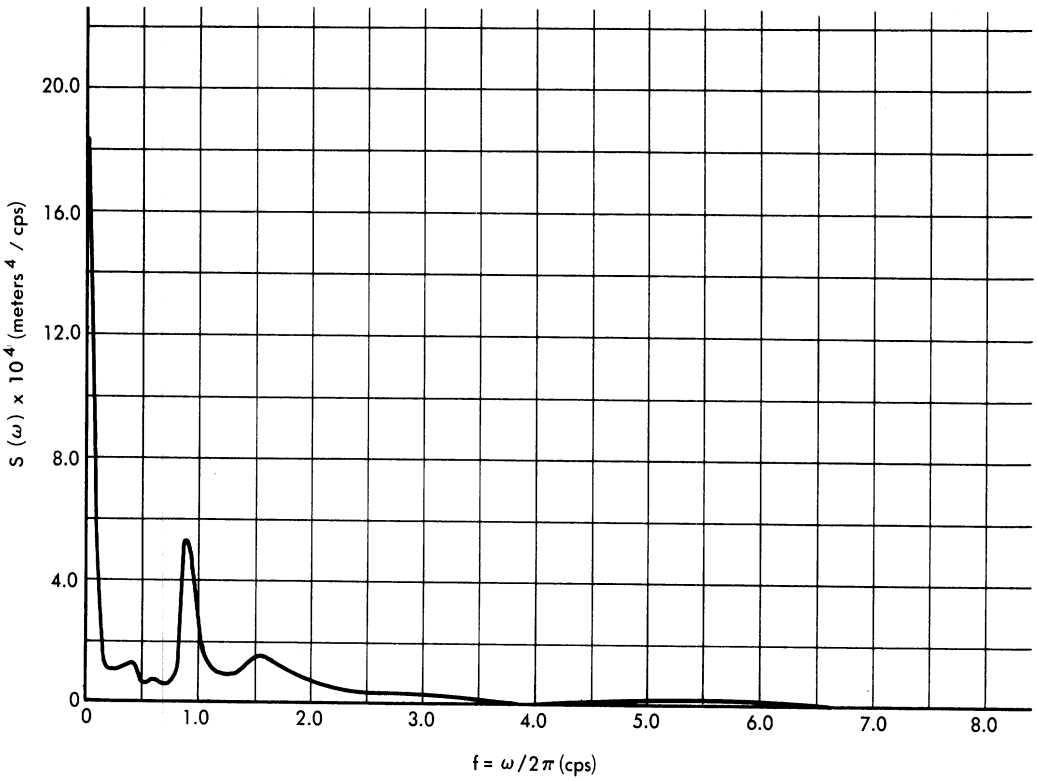

FIG. F.4-6 S (ω) FOR OBJECT 61 S-BAND

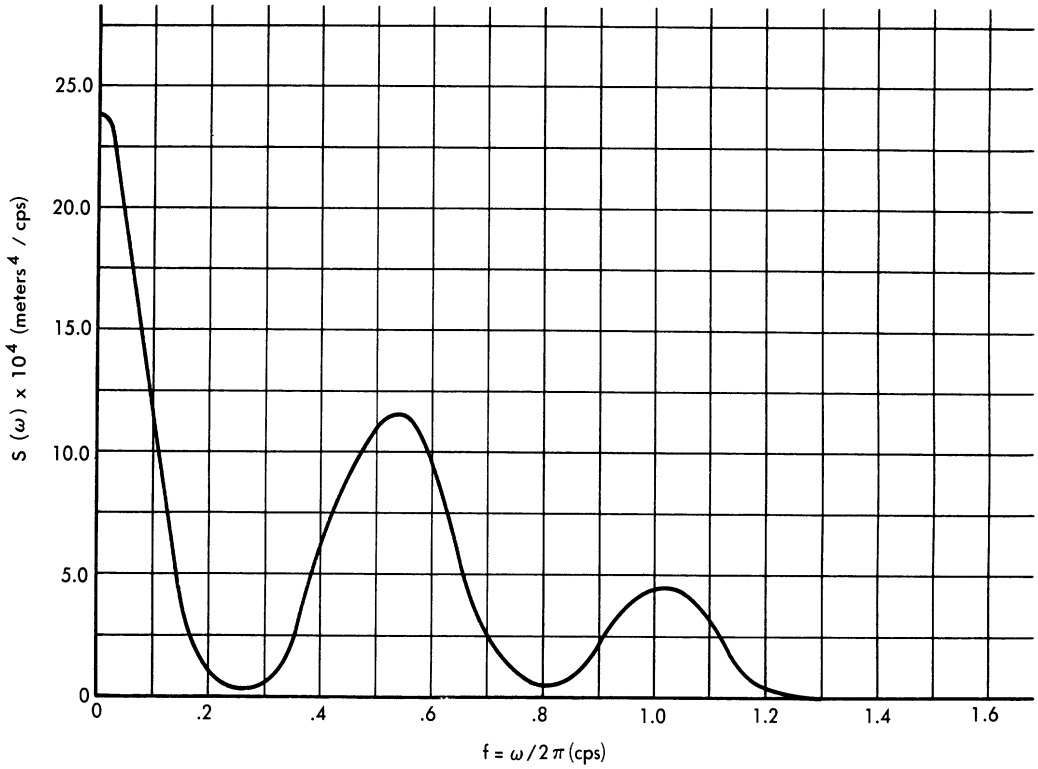

FIG. F.4-7 S (ω) FOR OBJECT 61 X-BAND

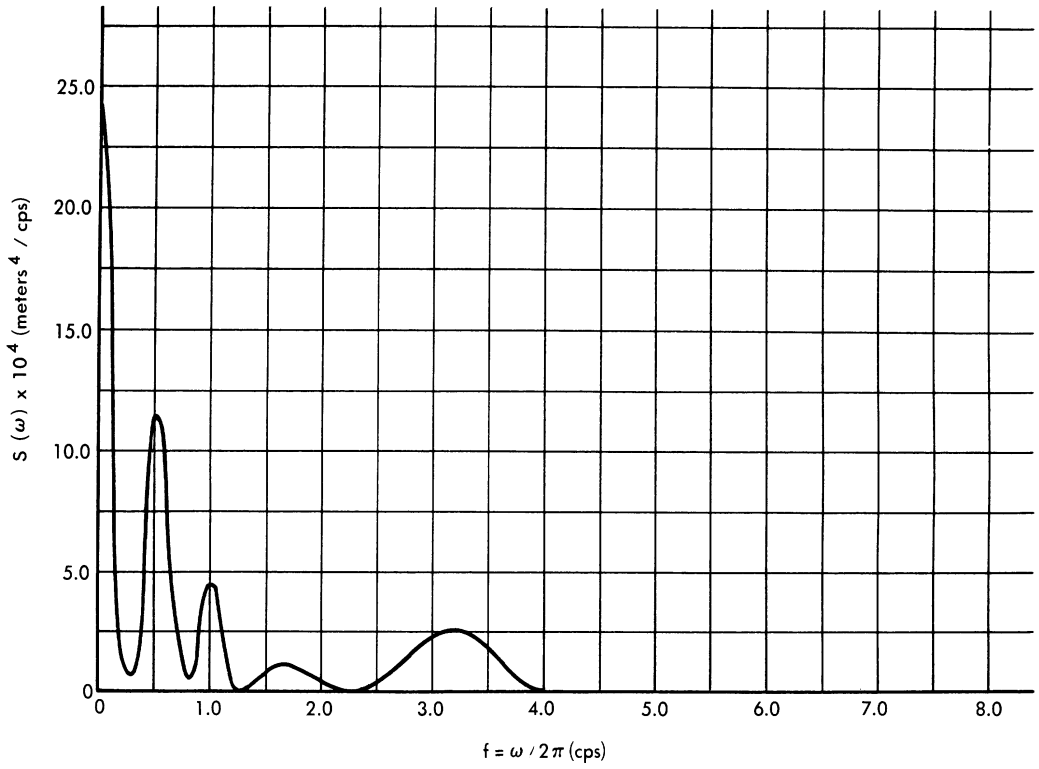

FIG. F.4-8 S (ω) FOR OBJECT 61 X-BAND

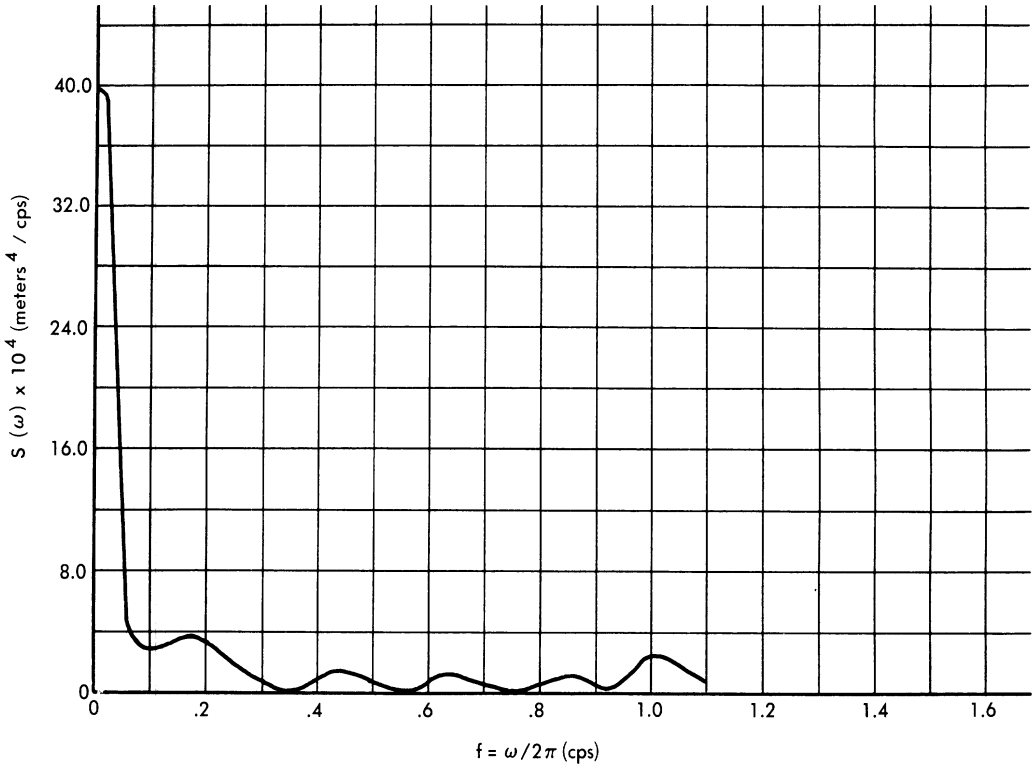

FIG. F.4-9 S (ω) FOR OBJECT 62 S-BAND

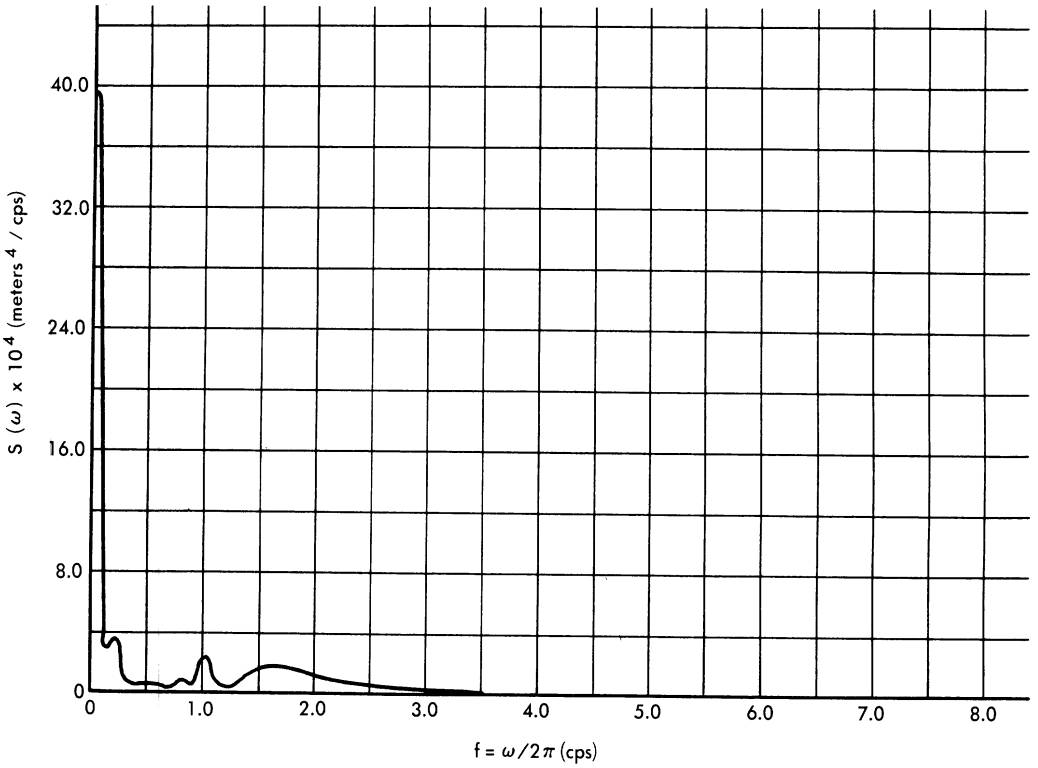

FIG. F.4-10 S (ω) FOR OBJECT 62 S-BAND

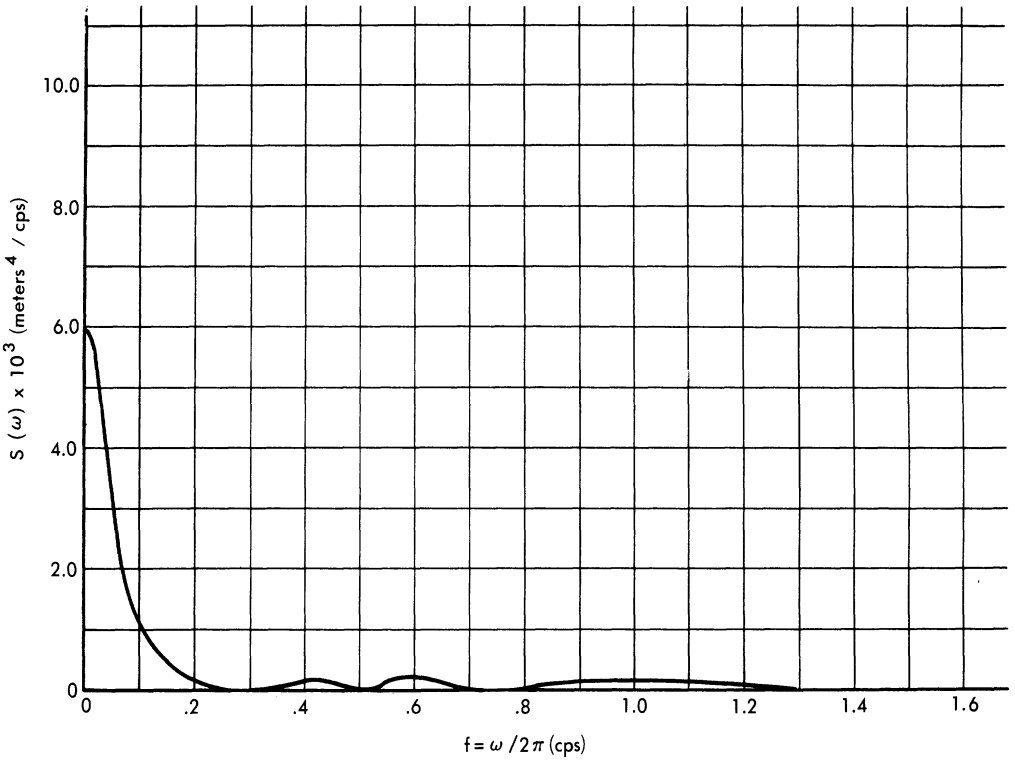

FIG. F.4-11 S (ω) FOR OBJECT 62 X-BAND

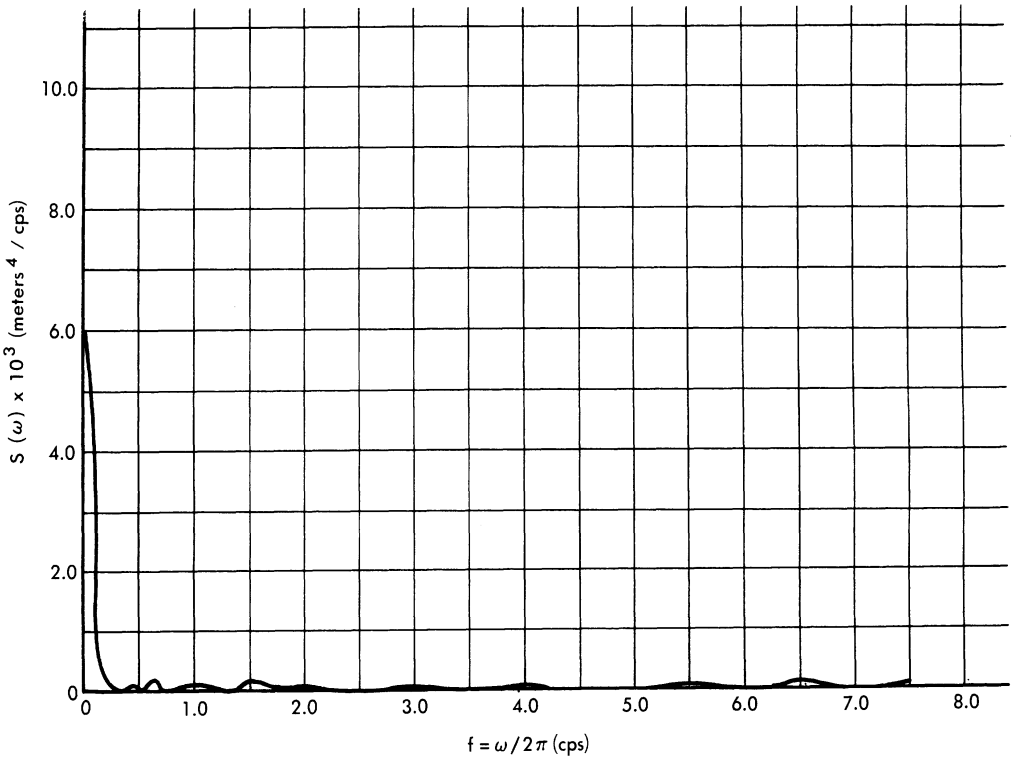

FIG. F.4-12 S (ω) FOR OBJECT 62 X-BAND

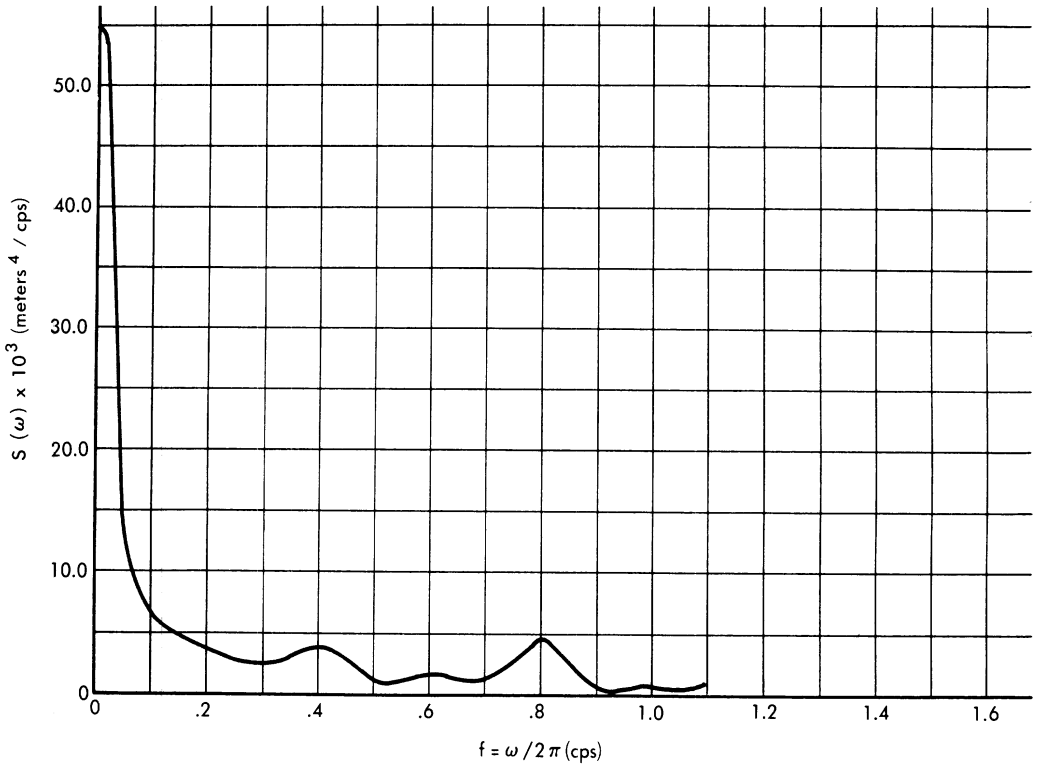

FIG. F.4-13 S (ω) FOR OBJECT 64 S-BAND

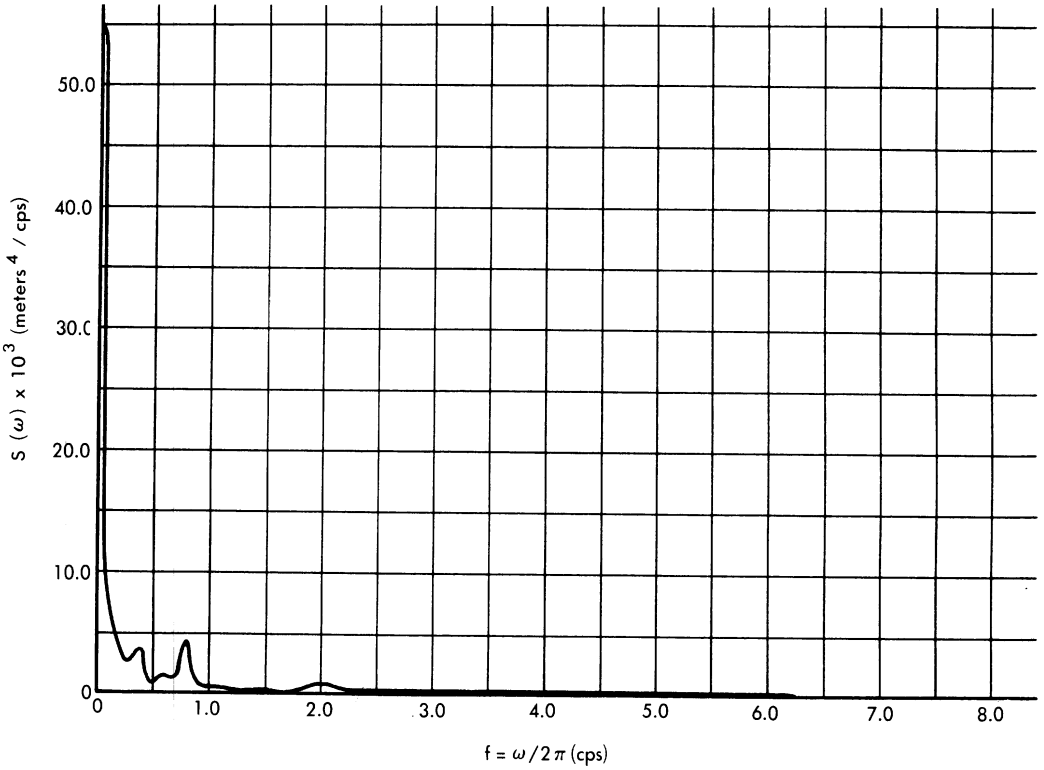

FIG. F.4-14 S (ω) FOR OBJECT 64 S-BAND

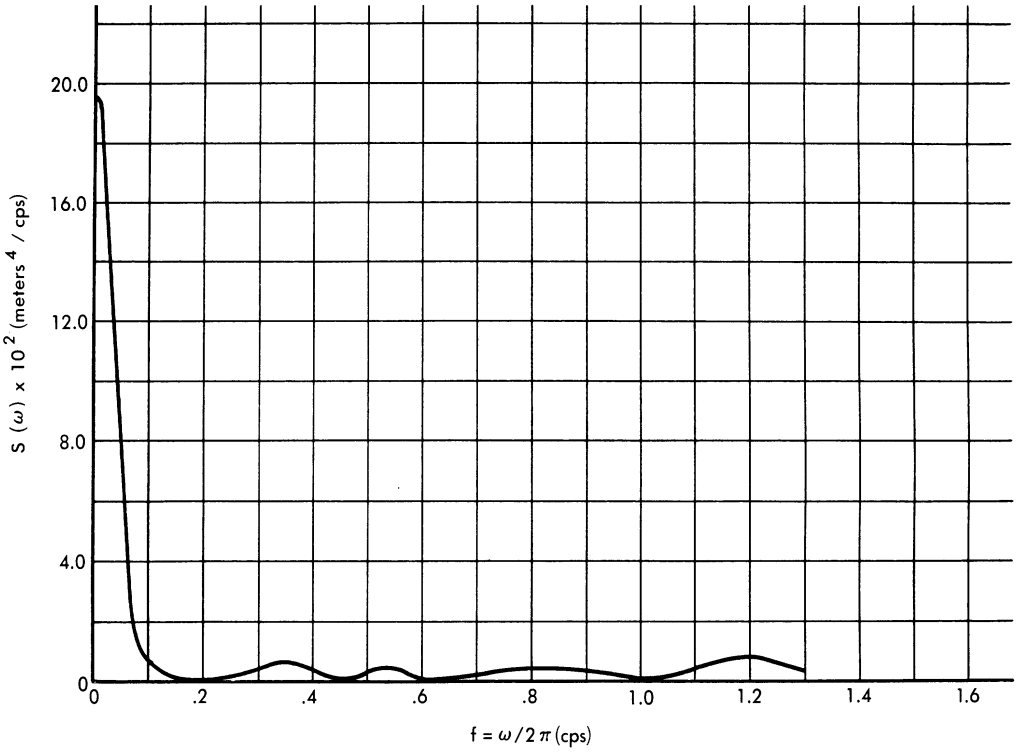

FIG. F-4 - 15 S (ω) FOR OBJECT 64 X - BAND

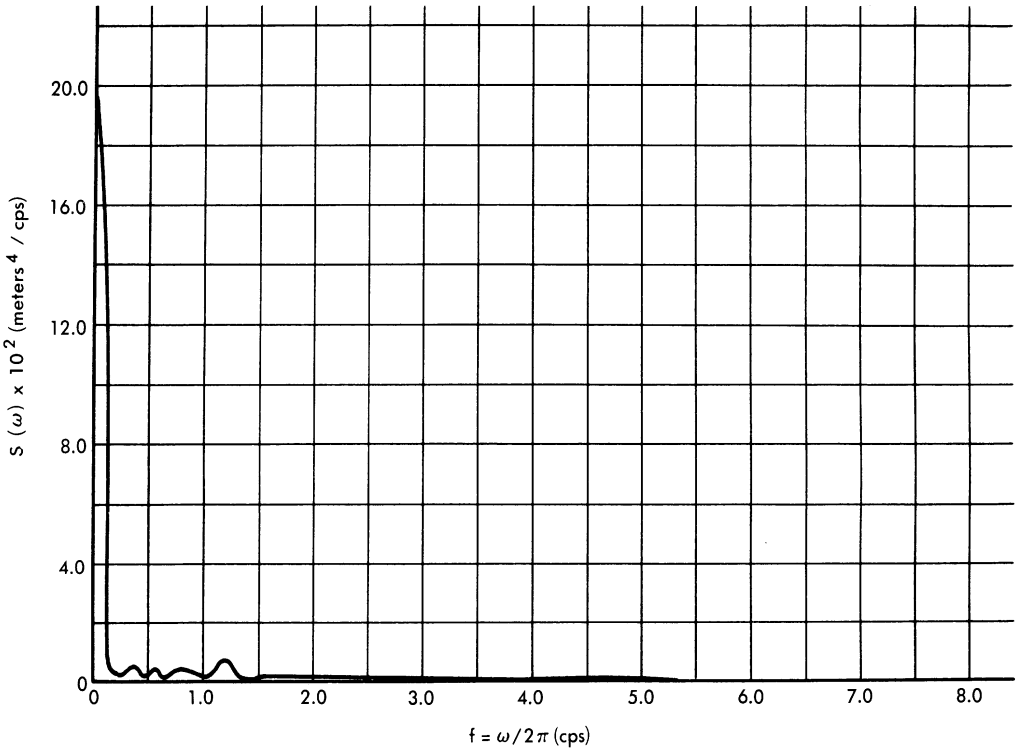

FIG. F-4 - 16 S (ω) FOR OBJECT 64 X - BAND

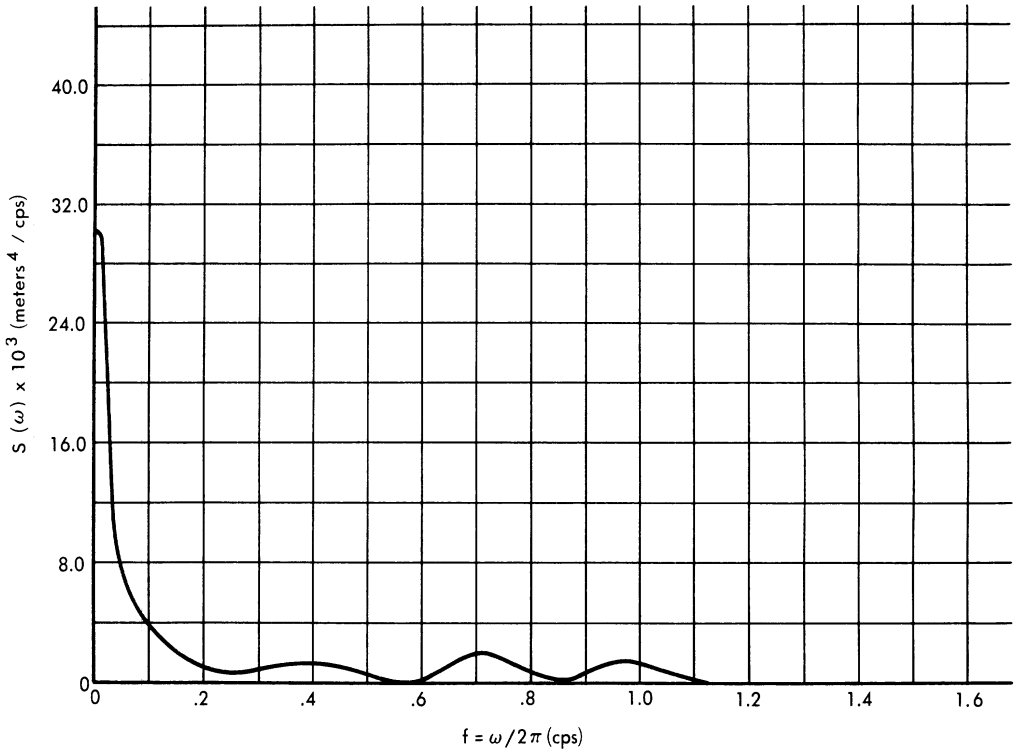

FIG. F.4-17 S (ω) FOR OBJECT 65 S-BAND

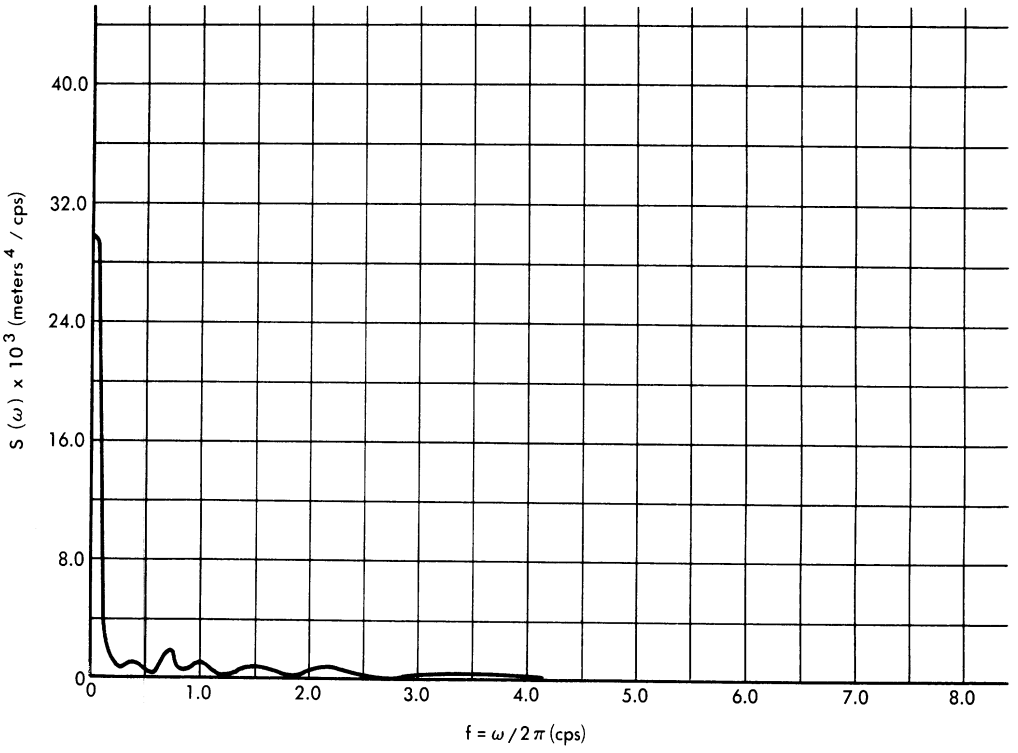

FIG. F.4-18 S (ω) FOR OBJECT 65 S-BAND

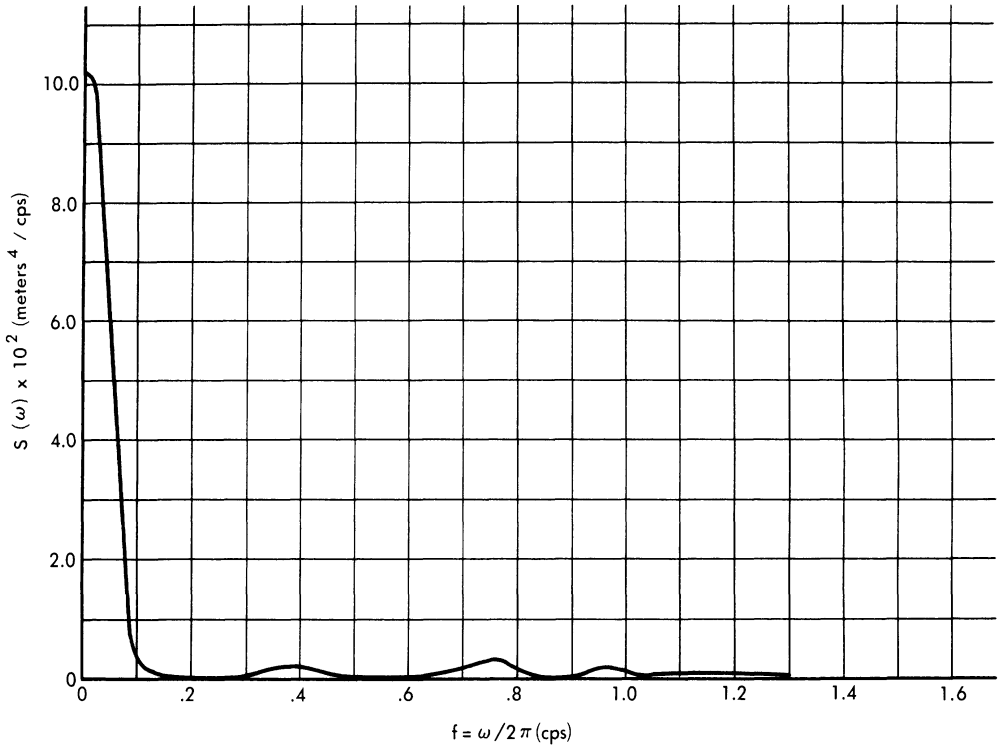

FIG. F.4-19 S (ω) FOR OBJECT 65 X-BAND

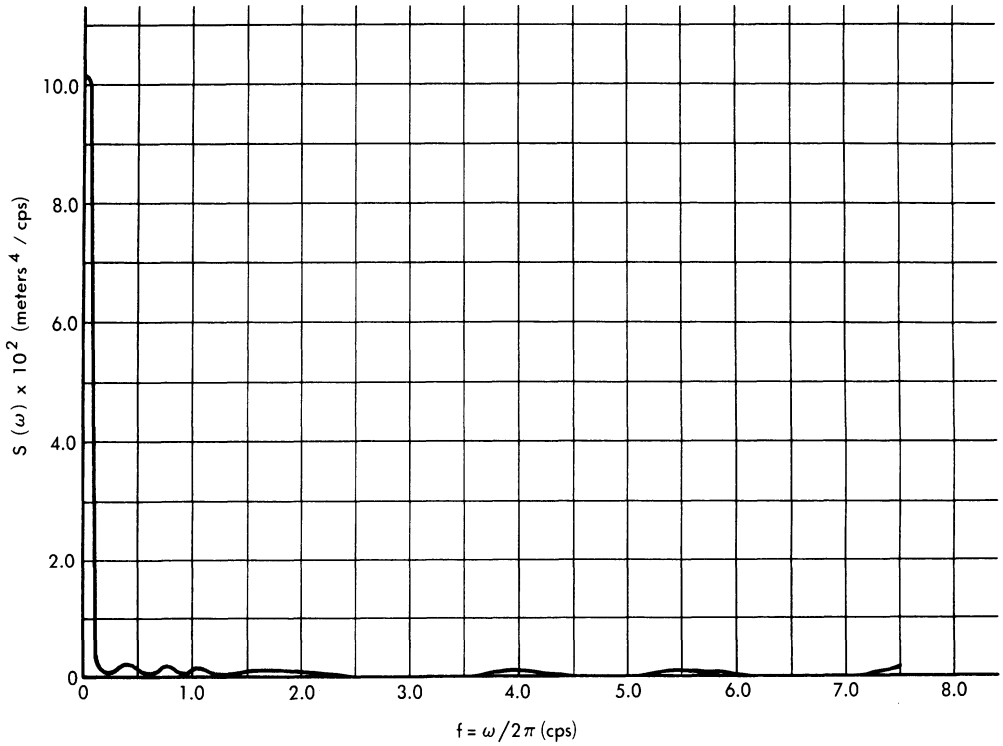

FIG. F.4-20 S (ω) FOR OBJECT 65 X-BAND

F.5.1 Definition of the Autocorrelation Function and Power Spectrum for a Continuous Sample on a Finite Interval

In defining the spectral density (power spectrum) and autocorrelation function when the data is given for only a finite interval (2T), these quantities must approach, continuously, the corresponding definitions given in Equations F.3-1 and F.3-2 as T becomes larger. Definitions for the continuum corresponding to those of Section F.3 are

$$S_1(\omega, T) = \frac{\left|F_1(\omega, T)\right|^2}{T} \quad , \tag{F.5-1}$$

$$R_1(\tau, T) = \frac{1}{2T} \int_{-\infty}^{\infty} y(t, T)\, y(t+\tau, T)\, dt \quad , \tag{F.5-2}$$

where

$$F_1(\omega, T) = \frac{1}{\sqrt{2\pi}} \int_{-T}^{T} y(t) e^{-i\omega t}\, dt \quad ,$$

$$y(t, T) = \begin{cases} y(t), & |t| \leq T \\ 0, & |t| > T \end{cases} \quad . \tag{F.5-3}$$

These functions have the properties $S_1(\omega, T) \geq 0$, $R_1(\tau, T) = R_1(-\tau, T)$, $R_1(0, T) \geq R_1(\tau, T)$, and they satisfy the Wiener-Khinchine relation:

$$S_1(\omega, T) = \frac{2}{\pi} \int_0^{\infty} R_1(\tau, T) \cos \omega\tau\, d\tau \quad . \tag{F.5-4}$$

The proof of Equation F.5-4: By definition,

$$S_1(\omega, T) = \frac{1}{2\pi T} \int_{-\infty}^{\infty} dt \int_{-\infty}^{\infty} dt'\, y(t, T)\, y(t', T) e^{-i\omega(t-t')}$$

$$= \frac{1}{2\pi T} \int_{-\infty}^{\infty} dt\, y(t, T) \int_{-\infty}^{\infty} d\tau\, y(t+\tau, T) e^{i\omega\tau}$$

$$= \frac{1}{\pi} \int_{-\infty}^{\infty} d\tau e^{i\omega\tau} R_1(\tau, T) \quad . \qquad \text{(F.5-5)}$$

From Equation F.5-2, it follows that $R_1(-\tau, T) = R_1(\tau, T)$, so that Equation F.5-5 implies Equation F.5-4. Inverting, we have

$$R_1(\tau, T) = \frac{1}{2} \int_{-\infty}^{\infty} d\omega e^{-i\omega\tau} S_1(\omega, T) \quad . \qquad \text{(F.5-6)}$$

Thus,

$$\left| R_1(\tau, T) \right| \leq \frac{1}{2} \int_{-\infty}^{\infty} d\omega\, S_1(\omega, T) \quad ,$$

or

$$\left| R_1(\tau, T) \right| \leq R_1(0, T) \quad . \qquad \text{(F.5-7)}$$

Since the limiting value, $R(\tau)$, is the time average of the product $y(t)\ y(t+\tau)$, another reasonable definition, $R_2(\tau, T)$, would be

$$R_2(\tau, T) = \frac{1}{2T - |\tau|} \int_{-\infty}^{\infty} y(t,\ T)\ y(t+\tau, T)\ dt\ ; \qquad \text{(F.5-8)}$$

that is, the integral

$$\int_{-\infty}^{\infty} y(t, T)\ y(t+\tau, T)\, dt = \int_{-T}^{T-\tau} y(t)\ y(t+\tau)\, dt,\ \tau \geq 0$$

is divided by the interval used in averaging $y(t)\ y(t+\tau)$. Note that $|R_2(\tau, T)|$ can be greater than $R_2(0, T)$. For example, if $y(t)$ is as shown in the figure, $R_2(0, T) = t_o/T$, whereas $R_2(2T-t_o, T) = 1 > R_2(0, T)$ for $0 < t_o < T$.

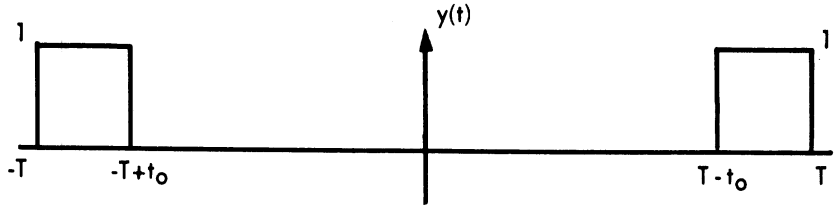

One could also define a spectral density as the transform of $R_2(\tau, T)$:

$$S_2(\omega, T) = \frac{2}{\pi} \int_{-\infty}^{\infty} R_2(\tau, T) \cos \omega\tau\, d\tau\ . \qquad \text{(F.5-9)}$$

That $S_2(\omega, T)$ is not non-negative may be seen by the example $y(t) = 1$. Then $R_2(\tau, T) = 1$, and $S_2(\omega, T) = (2/\pi\omega) \sin 2\omega T$. Note that

$$S_1(\omega, T) = \frac{2}{\pi} \int_0^{2T} \left(1 - \frac{\tau}{2T}\right) R_2(\tau, T) \cos\omega\tau d\tau \ ,$$

i.e., $S_1(\omega, \infty)$ is the first order Césaro sum of $S_2(\omega, \infty)$, so that when the latter exists it is equal to $S_1(\omega, \infty)$.

Before comparing the relative merits of these various definitions, the question as to what is desirable in the approximate quantities must be discussed. Clearly the $S(\omega, T)$ and $R(\tau, T)$ which minimize $|S(\omega, T)-S(\omega)|$ and $|R(\tau, T)-R(\tau)|$, for all ω and τ, respectively, would be the most desirable. On the other hand, the usual types of criteria, wherein a single parameter such as

$$L_1 = \int_0^{\infty} \left| S(\omega, T)-S(\omega) \right| d\omega$$

or

$$L_2 = \int_0^{\infty} \left[S(\omega, T)-S(\omega) \right]^2 d\omega$$

is minimized would not necessarily yield the most desirable approximate function. For example, if $y(t)$ consists of a random (noise) component and a signal made up of a finite number of sine waves, and the purpose is to detect this signal and determine the frequencies, one would choose the $S(\omega, T)$ which gave the "sharpest" peaks at (or near) those frequencies, provided it did not give sharp peaks at other frequencies. It can be shown that, in general, neither L_1 nor L_2 are good comparison parameters for an analysis of this kind.

Criteria involving $S(\omega)$ and $R(\tau)$, the true spectrum and correlation function, cannot be applied directly to problems such as the data analysis for the Bendix Aviation Corporation, since the limitation to a finite sample excludes the possibility of knowing $S(\omega)$ and $R(\tau)$. However, it is conceivable that some process of guessing the statistics and finding optimum definitions for $R(\tau, T)$ and $S(\omega, T)$ could lead one to better definitions (Ref. 29)[1]. This approach, which seems worthy of investigation, will not be considered further here.

---

[1]In Reference 29, the finite time average,

$$\frac{1}{T}\int_0^T Z(t)\,dt,$$

where $Z(t)$ is some functional of $y(t)$ (both $y(t)$ and $Z(t)$ are assumed to be stationary) is generalized to

$$\int_0^T g(t)\,Z(t)\,dt \equiv M(T);\ \text{the quantity } \left[\langle M(T)^2\rangle - \langle M(T)\rangle^2\right]\Big/\langle M(T)\rangle^2 \equiv L$$

is then minimized ($\langle\ \rangle$ denotes an ensemble average). This leads to an integral equation for the "optimum" $g(t)$, having the autocorrelation function $\langle Z(t)\,Z(t+\tau)\rangle$ as its kernel. One can apply this to the autocorrelation function $\langle y(t)\,y(t+\tau)\rangle$ by taking $Z(t) = y(t)\,y(t+\tau)$ and, in addition, modifying the limits of integration to

$$\int_0^{T-\tau} .$$

However, the process of deriving the spectrum from the optimum autocorrelation function through the Wiener-Khinchine relation does not, in general, give an optimum definition for the spectrum. Further, the analysis of Reference 29 is of no help in trying to minimize L directly for the spectrum, i.e., taking

$$Z(t) = \int_{-T}^{T} K(t)\,y(t)e^{i\omega t}\,dt.$$

Other properties which might be considered desirable are those described by Equation F. 3-4. These will not be assumed here (if they were, then the pair $R_2(\tau, T)$ and $S_2(\omega, T)$ would immediately be ruled out). Instead, $y(t) = A\cos\omega_0 t + N(t)$ will be investigated, where the function $N(t)$ is assumed to have some standard noise properties. $S(\omega, T)$ will be required to consist of a continuous (noise) component plus a peak[1] located near $\omega = \omega_0$ (the purpose of the peak is to allow one to say whether or not the signal, $A\cos\omega_0 t$, is present and, further, to determine the value of ω_0). This will be done for the two functions $S_1(\omega, T)$ and $S_2(\omega, T)$; it will be seen that the nature of the signal peak, and in fact the whole function, is essentially different for these two definitions. Some remarks about the comparison of $R_1(\tau, T)$ and $R_2(\tau, T)$ will also be made.

For y(t) of the form

$$y(t) = \sigma(t) + \eta(t) \qquad \text{(F. 5-10)}$$

($\sigma(t)$ is considered to be signal, $\eta(t)$ to be noise),

$$R_1(\tau, T) = \frac{1}{2T}\int_{-\infty}^{\infty} U(t, T)\, U(t+\tau, T)\left[\sigma(t) + \eta(t)\right]\left[\sigma(t+\tau) + \eta(t+\tau)\right] ,$$

where

$$U(t, T) = \begin{cases} 1, & |t| \le T \\ 0, & |t| > T \end{cases} .$$

[1]It is tempting to consider the peaked component an approximation to the Dirac δ-function. Care should be taken in this respect, however, since there the manner in which the approximation approaches the δ-function is important. For example, the function $\delta(\omega, T) = \sqrt{2/\pi}\, T\cos\omega^2 T^2$ satisfies the integral property

$$\int_{-\infty}^{\infty} \delta(\omega - \omega')\, f(\omega')\, d\omega' = f(\omega)$$

in the limit $T \to \infty$ for most well-behaved functions f(x), but this $\delta(\omega, T)$ would not be satisfactory for our purposes.

Thus,

$$R_1(\tau, T) = R_1^{\sigma}(\tau, T) + R_1^{\eta}(\tau, T) + \frac{1}{2T} \int_{-T}^{T-\tau} \left[\sigma(t)\ \eta(t+\tau) + \sigma(t+\tau)\ \eta(t) \right] dt,$$

$$2T \geq \tau \geq 0 \ , \qquad \text{(F.5-11)}$$

where

$$R_1^{\beta}(\tau, T) = \frac{1}{2T} \int_{-T}^{T-\tau} \beta(t)\ \beta(t+\tau)\, dt. \qquad \beta = \sigma, \eta \ .$$

Taking the ensemble average,

$$\langle R_1(\tau, T) \rangle = R_1^{\sigma}(\tau, T) + \langle R_1^{\eta}(\tau, T) \rangle + \frac{\langle \eta \rangle}{2T} \int_{-T}^{T-\tau} \left[\sigma(t) + \sigma(t+\tau) \right] dt,$$

$$0 \leq \tau \leq 2T \ , \qquad \text{(F.5-12)}$$

where $\eta(t)$ is assumed to be a stationary random process; this assumption also leads to

$$\langle R_1^{\eta}(\tau, T) \rangle = \left(1 - \frac{\tau}{2T}\right) R^{\eta}(\tau), \qquad 0 \leq \tau \leq 2T \ , \qquad \text{(F.5-13)}$$

where

$$R^{\eta}(\tau) = \langle \eta(t)\ \eta(t+\tau) \rangle \ . \qquad \text{(F.5-14)}$$

Noting that

$$R_2(\tau, T) = \frac{2T}{2T - |\tau|} R_1(\tau, T) \ , \qquad \text{(F.5-15)}$$

and

$$S_k^{\beta}(\omega, T) = \frac{2}{\pi} \int_0^{2T} R_k^{\beta}(\tau, T) \cos\omega\tau d\tau \ ,$$

then

$$\langle S_1(\omega, T)\rangle = S_1^{\sigma}(\omega, T) + \langle S_1^{\eta}(\omega, T)\rangle + \frac{\langle\eta\rangle}{\pi T} \int_0^{2T} d\tau \cos\omega\tau \int_{-T}^{T-\tau} \left[\sigma(t) + \sigma(t+\tau)\right] dt$$

$$= S_1^{\sigma}(\omega, T) + \langle S_1^{\eta}(\omega, T)\rangle + \frac{\langle\eta\rangle}{\pi\omega T} \int_0^{2T} d\tau \sin\omega\tau \left[\sigma(T-\tau) + \sigma(\tau-T)\right] \ ,$$

(F.5-16)

and

$$\langle S_2(\omega, T)\rangle = S_2^{\sigma}(\omega, T) + \langle S_2^{\eta}(\omega, T)\rangle + \frac{2\langle\eta\rangle}{\pi} \int_0^{2T} d\tau \frac{\cos\omega\tau}{2T-\tau} \int_{-T}^{T-\tau} dt \left[\sigma(t) + \sigma(t+\tau)\right] \ .$$

(F.5-17)

Clearly

$$\langle S_1^{\eta}(\omega, T)\rangle = \frac{2}{\pi} \int_0^{2T} \left(1 - \frac{\tau}{2T}\right) R^{\eta}(\tau) \cos\omega\tau d\tau \ , \qquad \text{(F.5-18)}$$

and

$$\langle S_2^{\eta}(\omega, T)\rangle = \frac{2}{\pi} \int_0^{2T} R^{\eta}(\tau) \cos\omega\tau d\tau = \langle S_1^{\eta}(\omega, T)\rangle + \frac{1}{\pi T} \int_0^{2T} \tau R^{\eta}(\tau) \cos\omega\tau d\tau \ .$$

(F.5-19)

Assuming $\langle \eta \rangle = 0$, the autocorrelation functions and spectra are simply sums of the contributions due to signal alone and noise alone. Furthermore, from Equation F.5-19 it follows that for $T >>$ the correlation time of the noise,

$$\langle S_1^{\eta}(\omega, T) \rangle \cong \langle S_2^{\eta}(\omega, T) \rangle \ .$$

Consider the part of the correlation function and spectrum due to signal alone. For

$$\sigma(t) = A \cos \omega_o t \ , \qquad \text{(F.5-20)}$$

simple integration leads to

$$R_1^{\sigma}(\tau, T) = A^2 \frac{2T-\tau}{4T} \left[\cos \omega_o \tau + \frac{1}{2T-\tau} \frac{\sin \omega_o (2T-\tau)}{\omega_o} \right] , \ 0 \le \tau \le 2T \ , \qquad \text{(F.5-21)}$$

$$R_2^{\sigma}(\tau, T) = A^2 \frac{1}{2} \left[\cos \omega_o \tau + \frac{1}{2T-\tau} \frac{\sin \omega_o (2T-\tau)}{\omega_o} \right] , \ 0 \le \tau \le 2T \ , \qquad \text{(F.5-22)}$$

$$S_1^{\sigma}(\omega, T) = \frac{A^2}{2\pi T} \left[\frac{\sin^2 (\omega-\omega_o)T}{(\omega-\omega_o)^2} + \frac{\sin^2 (\omega+\omega_o)T}{(\omega+\omega_o)^2} + 2 \frac{\sin(\omega-\omega_o)T \sin(\omega+\omega_o)T}{(\omega-\omega_o)(\omega+\omega_o)} \right] . \qquad \text{(F.5-23)}$$

Calculating $S_2^{\sigma}(\omega, T)$ from the definition,

$$S_2^{\sigma}(\omega, T) = \frac{A^2}{2\pi} \left[\frac{\sin 2(\omega-\omega_o)T}{\omega-\omega_o} + \frac{\sin 2(\omega+\omega_o)T}{\omega+\omega_o} \right] + \frac{A^2}{\pi \omega_o} \ I(\omega, T) \ , \qquad \text{(F.5-24)}$$

where

$$I(\omega, T) = \int_0^{2T} d\tau \, \frac{\cos \omega\tau \sin \omega_o(2T-\tau)}{2T-\tau} .$$

It is easy to show that

$$I(\omega, T) = \frac{\cos 2\omega T}{2} \left\{ Si\left[2(\omega+\omega_o)T\right] - Si\left[2(\omega-\omega_o)T\right] \right\} + \frac{\sin 2\omega T}{2} \left\{ \psi\left[2(\omega-\omega_o)T\right] \right\} ,$$

(F.5-25)

where

$$Si(x) = \int_0^x \frac{\sin t}{t} \, dt ,$$

$$\psi(x) = \int_0^x \frac{1-\cos t}{t} \, dt = \ln \gamma x - Ci(x) ,$$

$$Ci(x) = -\int_x^\infty \frac{\cos t}{t} \, dt , \quad \text{and}$$

$\gamma = 1.781072$, Euler's constant.

Consider first the spectra for the case $\omega_o = 0$. Then

$$S_1^\sigma(\omega, T) = \frac{2A^2}{\pi} \, \frac{\sin^2 \omega T}{\omega^2 T} \qquad (F.5-26)$$

and $(\omega_o = 0)$

$$S_2^\sigma(\omega, T) = \frac{2A^2}{\pi} \, \frac{\sin 2\omega T}{\omega}$$

(since $I(\omega, T)/\omega_o = (\sin 2\omega T)/\omega$ when $\omega_o = 0$). The interesting feature here is that, while for $T \to \infty$ both functions satisfy, to within a normalization constant, the property

$$\int_{-\infty}^{\infty} \delta(\omega)\, f(\omega)\, d\omega = f(0)$$

(for most well-behaved $f(\omega)$), they differ in a number of other essential properties. Some of these are advantageous (from the viewpoint of signal detection and resolution) for one, some for the other. For example, the fact that $S_2^\sigma(\omega, T)$ is twice as high as $S_1^\sigma(\omega, T)$ at $\omega = 0$, and half as wide (i.e., the first zero of $S_2^\sigma(\omega, T)$ occurs at half that of $S_1^\sigma(\omega, T)$), works in favor of $S_2^\sigma(\omega, T)$. On the other hand, the property $S_1^\sigma(\omega, T) \xrightarrow[T\to\infty]{} 0$, ω = constant $\neq 0$, which is not exhibited by $S_2^\sigma(\omega, T)$, tends to favor $S_1^\sigma(\omega, T)$. Another property which favors $S_1^\sigma(\omega, T)$ is that the ratio of the height of the peak at $\omega = 0$ to that of the neighboring peak (which occurs at $\omega = \omega_1' \cong 3\pi/2T$) is almost three times the corresponding ratio for $S_2^\sigma(\omega, T)$:

$$\frac{S_1^\sigma(0, T)/S_1^\sigma(\omega_1', T)}{S_2^\sigma(0, T)/S_2^\sigma(\omega_2', T)} = \frac{9\pi^2/4}{5\pi/2} = \frac{9\pi}{10} \cong 2.8 \quad . \tag{F.5-27}$$

Consider $\omega_o > 0$. Then,

$$S_1^\sigma(\omega, T) = \frac{A^2 T}{2\pi}\left[\frac{\sin^2(\omega-\omega_o)T}{(\omega-\omega_o)^2 T^2} + \Delta_1(\omega, T)\right] \quad , \tag{F.5-28}$$

$$S_2^\sigma(\omega, T) = \frac{A^2 T}{\pi}\left[\frac{\sin 2(\omega-\omega_o)T}{2(\omega-\omega_o)T} + \Delta_2(\omega, T)\right] \quad , \tag{F.5-29}$$

where the functions

$$\Delta_1(\omega, T) = 2\,\frac{\sin(\omega-\omega_o)T\,\sin(\omega+\omega_o)T}{(\omega-\omega_o)T\,(\omega+\omega_o)T} + \frac{\sin^2(\omega+\omega_o)T}{(\omega+\omega_o)^2 T^2} \quad , \tag{F.5-30}$$

$$\Delta_2(\omega, T) = \frac{\sin 2(\omega+\omega_o)T}{2(\omega+\omega_o)T} + \frac{I(\omega, T)}{8\,\omega_o T} \quad , \qquad \text{(F.5-31)}$$

tend to distort the peaks; these peaks are represented by the terms

$$(A^2/2\pi T)\left[\sin^2(\omega-\omega_o)T\right] \Big/ (\omega-\omega_o)^2$$

and

$$(A^2/2\pi)\left[\sin 2(\omega-\omega_o)T\right] \Big/ (\omega-\omega_o)$$

in $S_1^\sigma(\omega, T)$ and $S_2^\sigma(\omega, T)$, respectively, which are simply 1/4 the functions for $\omega_o = 0$ (Eq. F.5-26), but centered around ω_o. Clearly there is not much distortion in $S_1^\sigma(\omega, T)$ for $\omega_o T \gg \pi$; for example, $\Delta_1(\omega, T) = 0(\omega_o^{-1} T^{-1})$ at $\omega = \omega_o$. To estimate the distortion in $S_2^\sigma(\omega, T)$, examine the asymptotic expressions (Ref. 30)

$$\mathrm{Si}(x) \approx \frac{\pi}{2} - \frac{\cos x}{x}, \qquad \psi(x) \approx \ln \gamma\, x - \frac{\sin x}{x} \quad ,$$

valid for $x \gtrsim 2\pi$. Considering again the value at $\omega = \omega_o$,

$$\Delta_2(\omega, T) \approx \left[(\ln 4\gamma\,\omega_o T)\sin 2\,\omega_o T + \frac{\pi}{2}\cos 2\omega_o T\right] + \frac{\sin 4\,\omega_o T}{4\,\omega_o T} \quad , \qquad \text{(F.5-32)}$$

which goes to zero as $\omega_o T \to \infty$; the logarithmic term, however, tends to cause more distortion in the case of $S_2^\sigma(\omega, T)$.

Thus the two functions, $S_1(\omega, T)$ and $S_2(\omega, T)$, which differ in several essential respects, both show peaks at the signal frequency, plus other maxima which are less than 1/7 the height of the signal peak. For the purpose of the Bendix contract, wherein the only a priori information was that there was a large zero-frequency component, with the object

being to discover any other components if they existed, the choice between the various definitions was a matter of indifference.

Before concluding this section, one further remark concerning the two definitions of the autocorrelation functions remains to be made. $R_1(\tau, T)$ is identically zero for $\tau \geqq 2T$ and is near zero for $\tau \cong 2T$, whereas $R_2(\tau, T)$ will not generally approach zero as $\tau \to 2T$ ($\tau < 2T$). Therefore, $R_2(\tau, T)$ could be considered, in general, a better approximation to the true $R(\tau)$. However, as $\tau \to 2T$, the length of sample used in computing either $R(\tau, T)$ goes to zero, so that the results for $\tau \cong 2T$ will be statistically unreliable; hence, essentially nothing is lost in this respect by using $R_1(\tau, T)$.

F.5.2 The Autocorrelation Function and Power Spectrum for a Finite Sample

The drop-test data, being the result of measurement with a pulsed radar (prr $\cong 400$ sec^{-1}), yielded a finite number of values of the cross-section spaced at intervals $\Delta \cong 1/400$ sec. The problem of defining the autocorrelation function and power spectrum in terms of such data is essentially the same as in the case of a continuous sample of finite length with the exception that, in the discrete case, one must make an assumption as to band limitation. This corresponds to the fact that $\cos(\omega_1 t)$ and $\cos(\omega_2 t)$ will look precisely the same if sampled at times $t_n = n\Delta (n = 0, 1, \ldots, N)$ if $\omega_2 = \omega_1 + 2s\pi/\Delta$, s any integer. The limitation imposed by the discrete observations is not restricted, a priori, to low frequencies. It is necessary only that two frequencies differing by $2s\pi/\Delta$ be indistinguishable (no matter how large N may be). However, physical considerations lead to the assumption that the function being sampled is essentially band-limited by $\omega < 2\pi/\Delta \cong 400$ cps (that is, the amplitudes of the higher frequency components are much less than the amplitudes of those within this band). The actual computation was not based on the original data, but on a reduced set obtained from the original by averaging, with no overlap, successive sets of six points. Hence, the data used was at intervals of $T_0 = 6\Delta$. One may ask whether it is necessary to assume a band limitation of $\omega < 2\pi/T_0 \cong 66$ cps. It was shown in Section F.3 that, in terms of the definitions used, this was not

the case – one need assume only the band limitation imposed by the spacing of the original data, provided that the spectrum is computed for $\omega \ll 2\pi/T_o$.

Analogously to the case of a continuous sample, there are, as alternatives, the definitions of Section F. 3:

$$R'(\tau_s, T) = \frac{1}{N-s+1} \sum_{n=0}^{N-s} y(nT_o)\, y(nT_o + \tau_s)$$

and

$$S'(\omega) = \frac{2T_o}{\pi} \left\{ \sum_{s=0}^{N} R'(sT_o, T) \cos \omega s T_o - \frac{1}{2} R'(0, T) \right\} .$$

For the case $y(t) = 1$, the summations are easily carried out, yielding

$$S(\omega) = \frac{T_o}{(N+1)\pi} \frac{\sin^2 \frac{(N+1)\omega T_o}{2}}{\sin^2 \frac{\omega T_o}{2}},$$

$$S'(\omega) = \frac{T_o}{\pi} \left\{ \frac{\sin \omega N T_o}{\sin \frac{\omega T_o}{2}} + \cos N\omega T_o \right\} .$$

Hence, the remarks of Section F. 5. 1 concerning the comparison of the various definitions apply here as well.

APPENDIX G

THE CROSS-SECTION OF THE TANKS

G.1 INTRODUCTION

The cross-section of the terminal propulsion unit (tanks) at 200 Mc was determined by essentially three different methods of approach:

1. Using previously obtained theoretical and experimental data on the 7-OC booster (Ref. 1),
2. Using physical optics methods on the breakdown of the tanks shown in Figure G.1-1 (a drawing of the tanks appears in Fig. 2-4[1]), and
3. Using physical optics methods on a modification of the breakdown used in Method 2.

In the consideration of the problem by Methods 2 and 3, the cross-section was determined for the tanks with the warhead attached, with the warhead removed, and with both the warhead and hat section removed.

G.2 METHOD 1 – SCALED 7-OC BOOSTER DATA

This section contains an estimate of the radar cross-section of the terminal propulsion unit (tanks) at 200 Mc based upon the results obtained previously on the 7-OC booster. Experimental and theoretical data on the cross-section of the 7-OC booster appear in Reference 1. If the 7-OC booster is scaled down by a factor of 5/6 (Fig. G.2-1), the resulting model closely resembles that of the tanks. The dimension of the 5/6-scale 7-OC booster and the tanks are compared in Table G.2-1.

[1]The drawing of the tanks shown in Figure 2-4 shows the warhead in the shape of a cone rather than as one of the Rudolph parameterizations. Thus, the Method 2 approach, in computing the cross-section with the warhead attached, assumes the warhead to be in the shape of the cone shown on Figure 2-4.

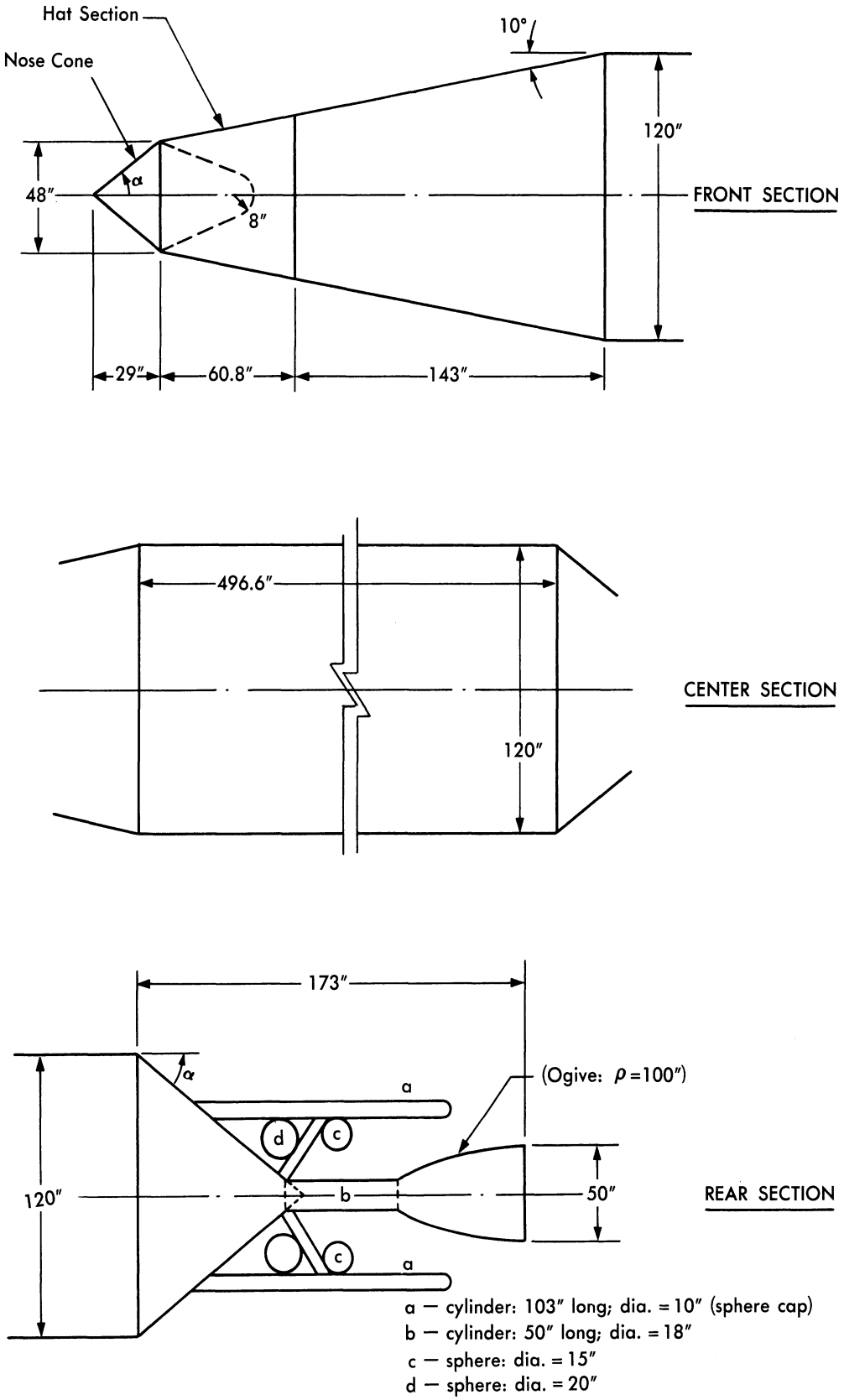

FIG. G.1-1 GEOMETRY OF "TANKS" USED IN COMPUTATIONS

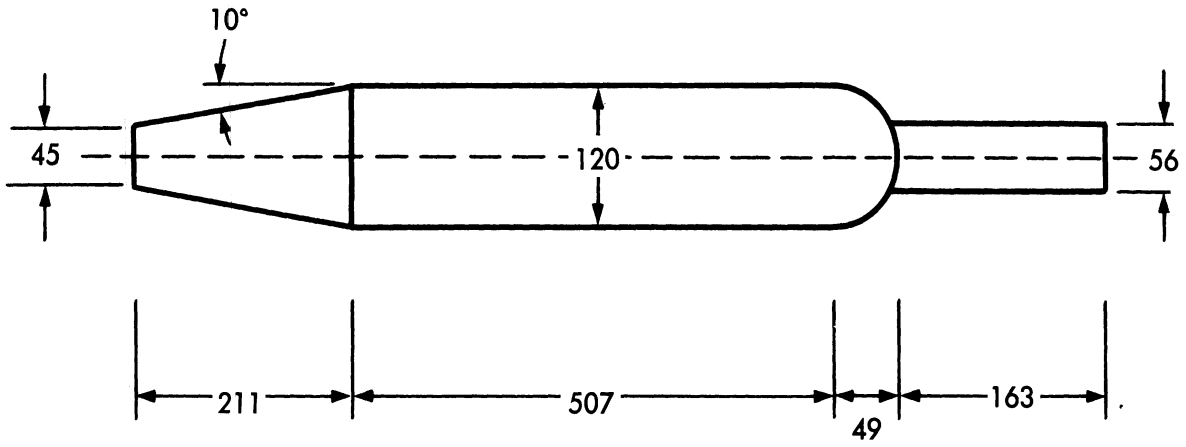

(all dimensions are in inches)

FIG. G.2-1 A 5/6 -SCALE MODEL OF THE 7-OC BOOSTER

TABLE G.2-1

COMPARISON OF DIMENSIONS BETWEEN THE TANKS AND THE 5/6-SCALE MODEL OF THE 7-OC BOOSTER

	Tanks	7-OC Booster
Maximum diameter	120 in.	120 in.
Front diameter	48 in.	45 in.
Rear diameter	50 in.	56 in.
Length-truncated cone	204 in.	211 in.
Length-cylinder section	497 in.	507 in.
Length-rear sloped section	45 in.	49 in.
Length-tail cylinder	128 in.	163 in.
Nose angle (truncated cone)	10^{o}	10^{o}

Application of modeling theory to the data for the 7-OC booster given in Reference 1 yields cross-section data on the "5/6-scale 7-OC booster" (and thus on the tanks) at 90, 270, 720, and 1200 Mc. Figure G.2-2 shows the theoretical cross-section (average σ) of the "5/6-scale 7-OC booster" at 270, 720, and 1200 Mc, as scaled from the data of Reference 1.

The theoretical curves given in Figure G.2-2 for the cross-section, combined with the experimental data shown in Figures G.2-3 and G.2-4[1], yield a reasonably good estimate of the cross-section pattern to be expected for the tanks at 200 Mc in the interval $0 \leqslant \psi \leqslant 90^{o}$.

G.3 METHOD 2 – PHYSICAL OPTICS CROSS-SECTION OF THE TANKS

G.3.1 Cross-Sections

The physical optics method was applied to the determination of the cross-sections of the tanks using the formulas given in Section G.3.2 which were evolved from the breakdown of the tanks by the methods of Appendix A of Reference 5. The cross-sections were determined at 200 Mc for the tanks with:

1. The nose-cone attached;
2. The nose-cone removed and the resulting hole assumed to be:
   a. Filled with an absorbing material so that no return is received from the interior of the hole,
   b. Lined on the inside with an inverted hemisphere, and
   c. Empty up to the end of the hat section, so that from the nose-on aspect the return would be like that from a flat plate; and
3. Both the nose-cone and hat section removed.

[1]Figures G.2-2 – G.2-4 were taken directly from Reference 1, with the appropriate scale factors introduced.

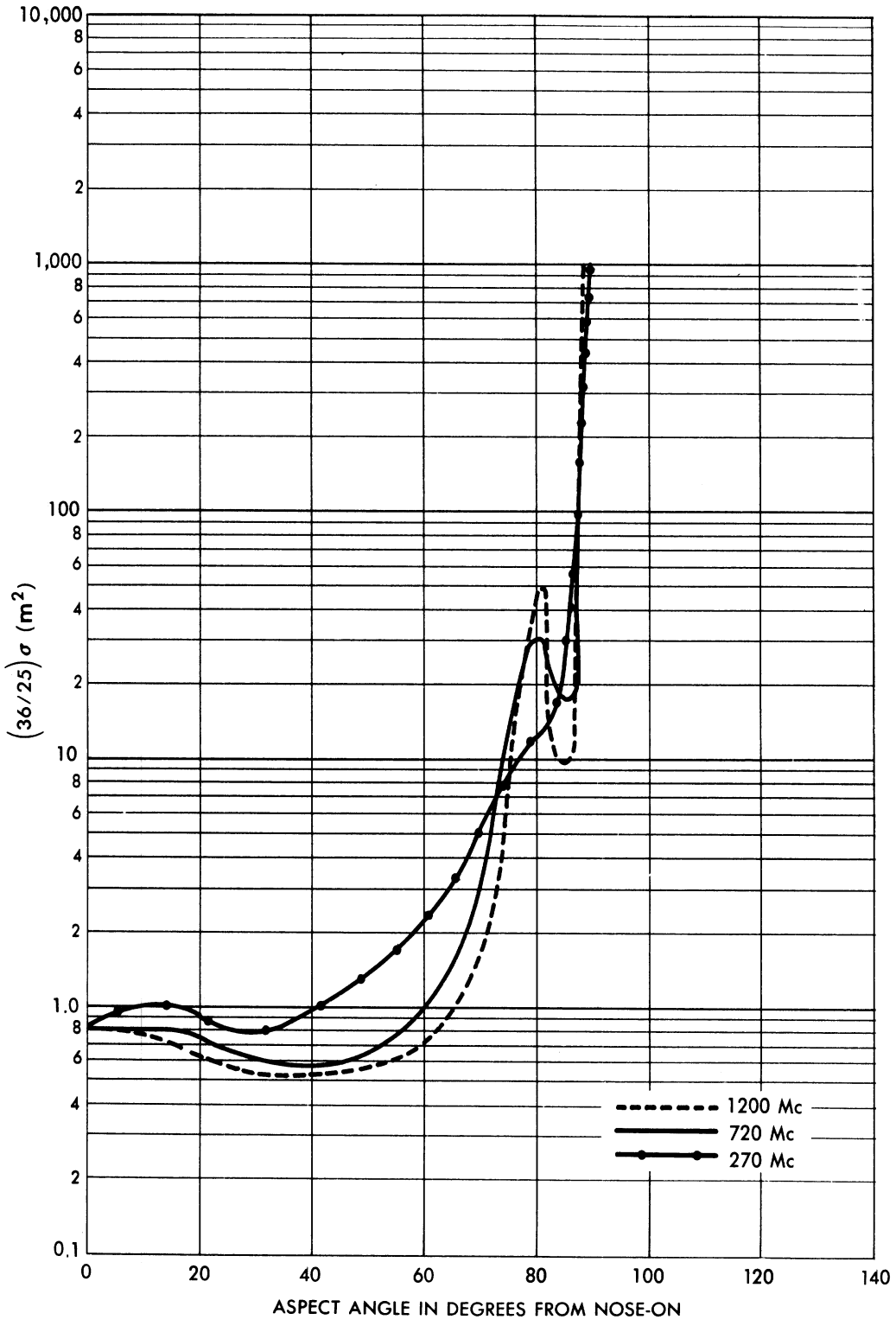

FIG. G.2-2 THEORETICAL CROSS-SECTIONS OF THE TANKS
(Based upon a 5/6-scale model of the 7-OC Booster)

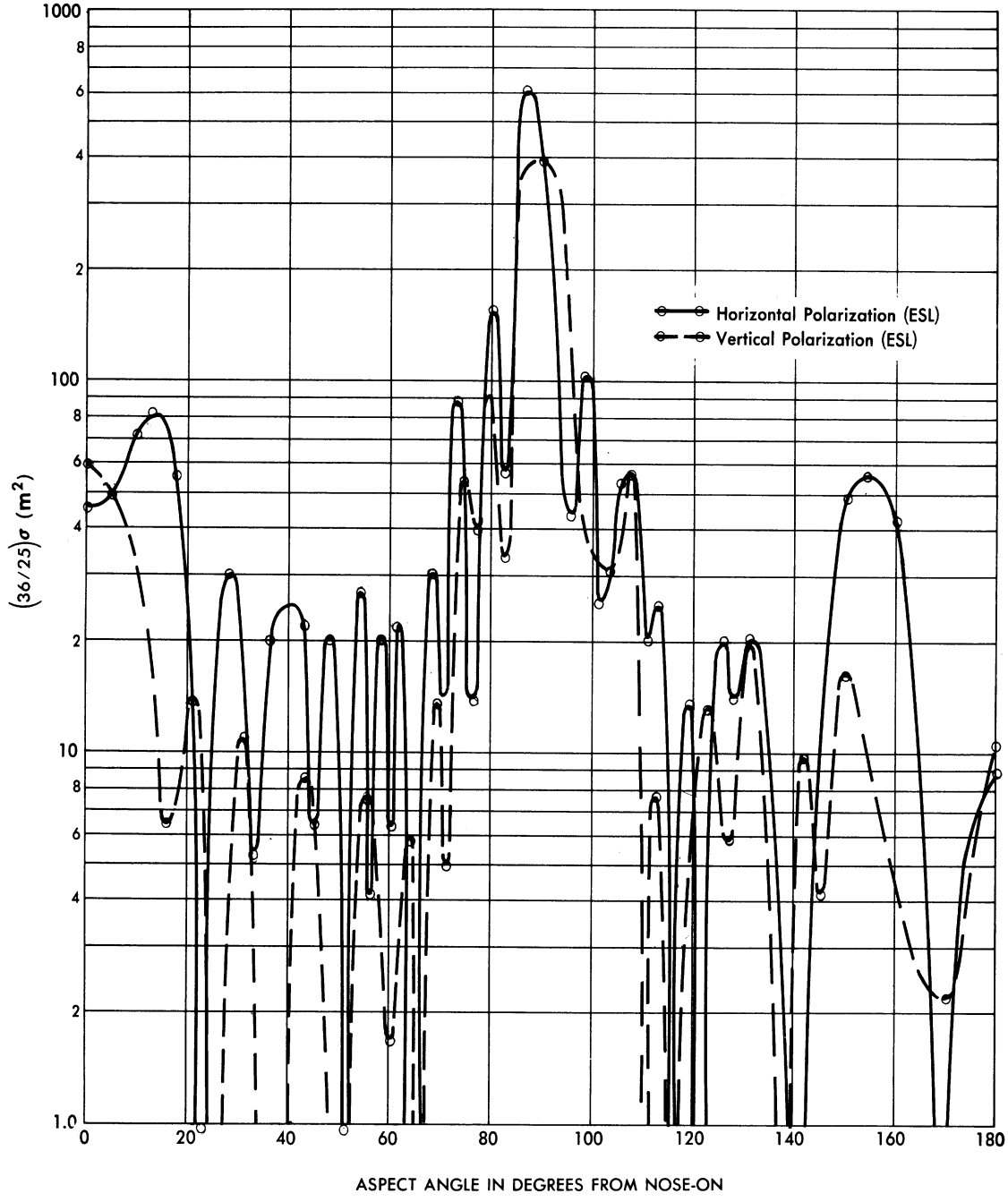

FIG. G.2-3 CROSS-SECTION OF THE TANKS (NOSE-CONE REMOVED) AT 90 Mc
(Based upon a 5/6-Scale Model of the 7-OC Booster)

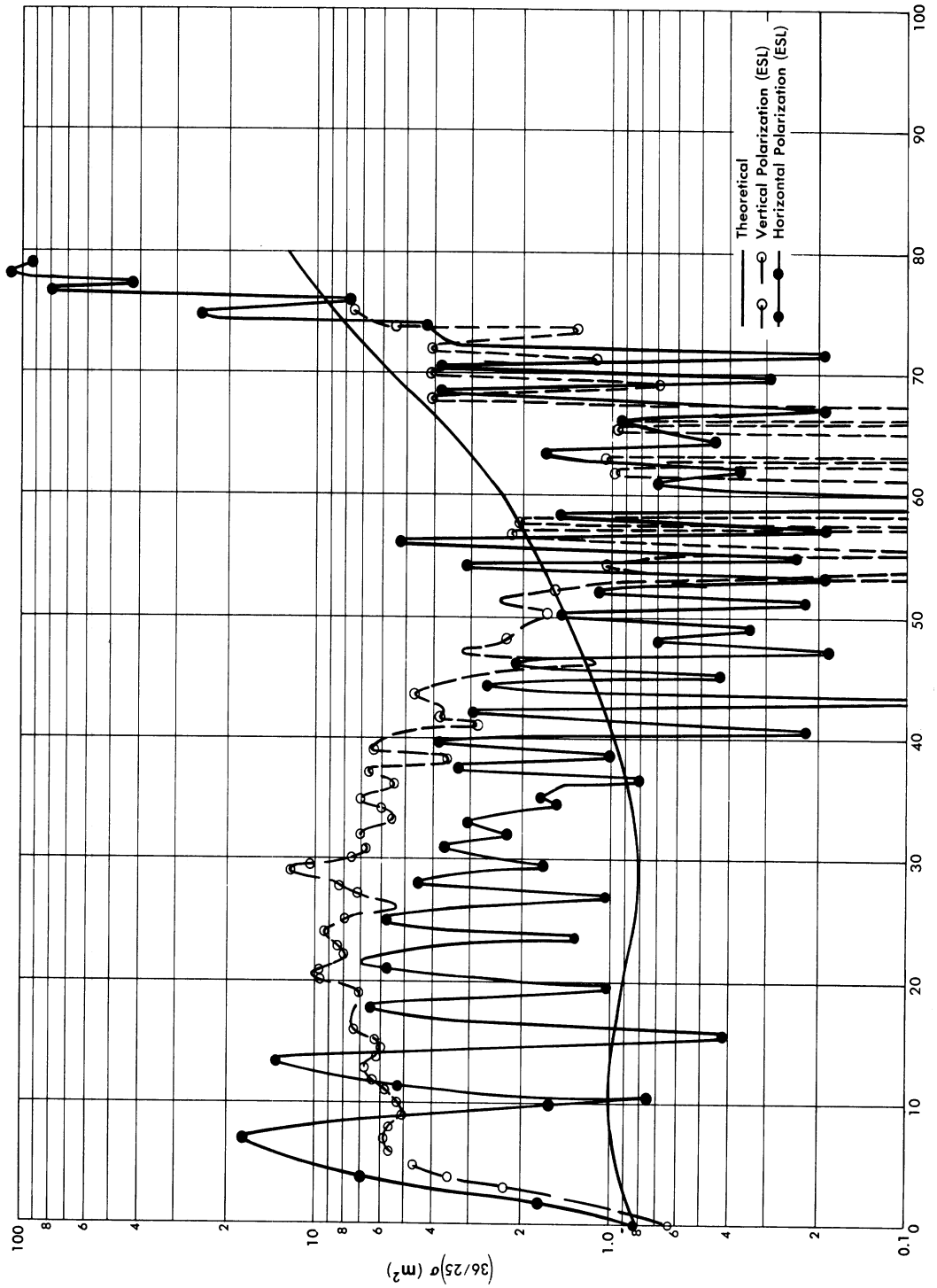

FIG. G.2-4 CROSS-SECTION OF THE TANKS (NOSE-CONE REMOVED) AT 270 Mc
(Based upon a 5/6-scale model of the 7-OC Booster)

The results obtained are shown in Figure G.3-1.

G.3.2 Computational Procedures For the Tanks

In determining the cross-section, using the breakdown shown in Figure G.1-1, the primary contributions to the cross-section were assumed to come from:

1. The tip of the nose-cone (σ_1),
2. The junction of the nose-cone and the hat section (σ_3 and σ_4),
3. The junction of the extended hat section and the central cylindrical portion (σ_2 and σ_5),
4. The junction of the cylindrical portion and the rear conical surface (σ_6 and σ_8), and
5. The engine breakdown back of the rear cone (σ_7).

At certain aspects (namely those which are normal to the conical or cylindrical surfaces), other formulations were involved.

The formulas involved are listed below:

$$\sigma = \sigma_1 + \pi R_2^2 \tan^2(10^\circ) + \pi R_1^2 \left[\tan\alpha - \tan(10^\circ)\right]^2 \text{, for } \psi = 0^\circ$$

$$\sigma = \sum_{i=1}^{5} \sigma_i \text{, for } 0^\circ < \psi < 10^\circ$$

$$\sigma = \sigma_1 + \sum_{i=3}^{6} \sigma_i \text{, for } 10^\circ < \psi < \alpha$$

$$\sigma = \sigma_1 + \sum_{i=4}^{7} \sigma_i \text{, for } \alpha < \psi < 90^\circ - \alpha$$

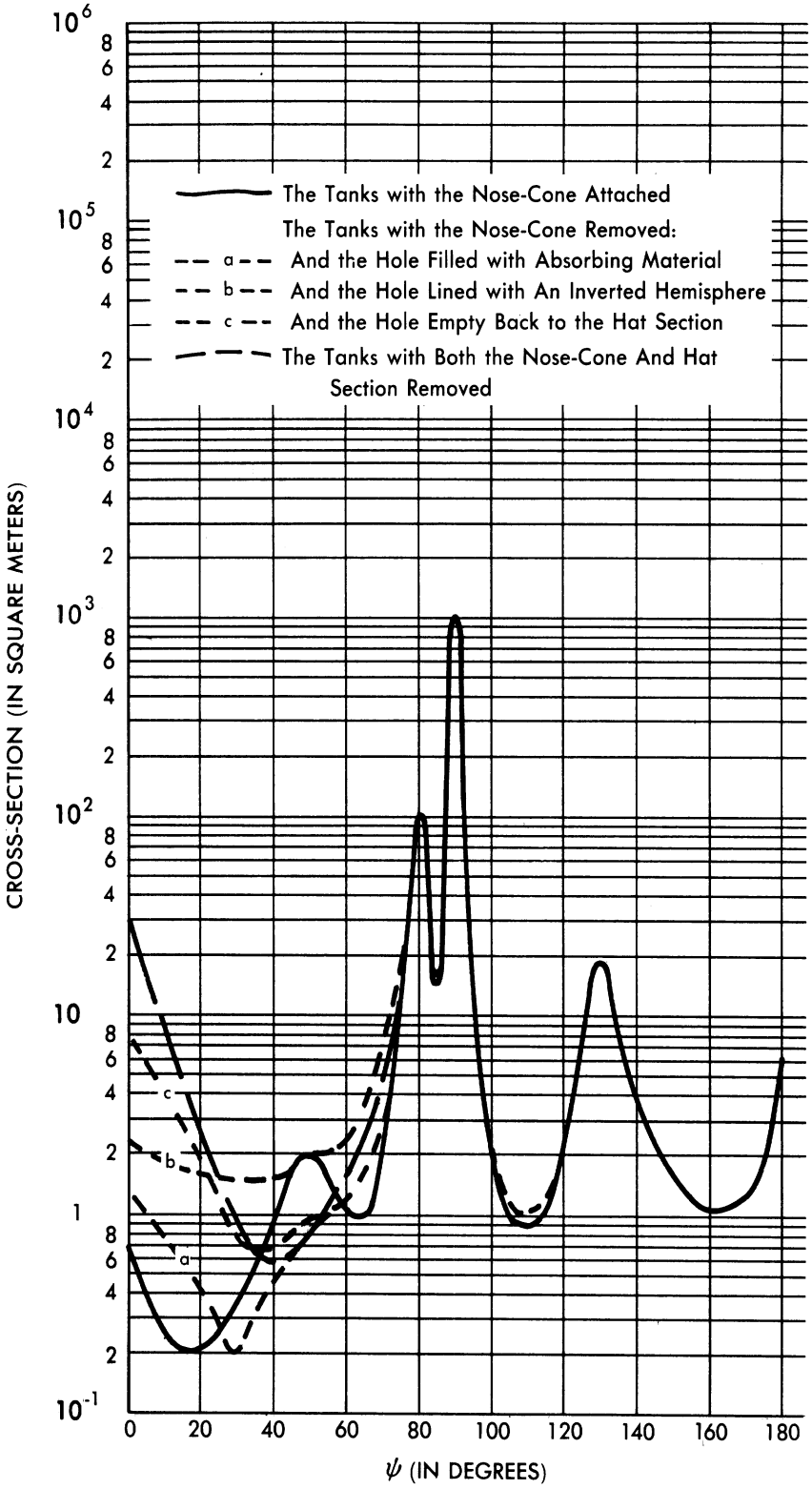

FIG. G.3-1 CROSS-SECTION OF THE TANKS AT 200 Mc (METHOD 2)

$$\sigma = \frac{8\pi R_1^{\,3}}{9\lambda \sin^2\alpha \cos\alpha} + \sum_{i=5}^{7} \sigma_i \quad , \text{ for } \psi = 90^o - \alpha$$

$$\sigma = \sum_{i=4}^{7} \sigma_i \quad , \text{ for } 90^o - \alpha < \psi < 80^o$$

$$\sigma = \frac{8\pi \left[(R_2)^{3/2} - (R_1)^{3/2}\right]^2}{9\lambda \sin^2(10^o) \cos(10^o)} + \sigma_6 + \sigma_7 \quad , \text{ for } \psi = 80^o$$

$$\sigma = \sum_{i=4}^{7} \sigma_i \quad , \text{ for } 80^o < \psi < 90^o$$

$$\sigma = \frac{2\pi L^2 R_2}{\lambda} + \sigma_4 + \sigma_7 \quad , \text{ for } \psi = 90^o$$

$$\sigma = \sum_{i=4}^{7} \sigma_i \quad , \text{ for } 90^o < \psi < 90^o + \alpha$$

$$\sigma = \frac{8\pi \left[(R_2)^{3/2} - (r)^{3/2}\right]^2}{9\lambda \sin^2\alpha \cos\alpha} + \sigma_4 + \sigma_5 + \sigma_7 \quad , \text{ for } \psi = 90^o + \alpha$$

$$\sigma = \sum_{i=4}^{7} \sigma_i \quad , \text{ for } 90^o + \alpha < \psi < 180^o - \alpha$$

$$\sigma = \sum_{i=5}^{7} \sigma_i \quad , \text{ for } 180^o - \alpha < \psi < 170^o -$$

$$\sigma = \sum_{i=6}^{8} \sigma_i \quad , \text{ for } 170^o < \psi < 180^o$$

$$\sigma = \pi(r_t)^2 + \pi(R_2)^2 \tan^2 a + \sigma_7 \quad , \text{ for } \psi = 180^o$$

where

$$\lambda = 1.5 \text{ m}$$

$$a = \tan^{-1}(24/29)$$

$$R_1 = 0.61 \text{ m}$$

$$R_2 = 1.52 \text{ m}$$

$$r = 0.23 \text{ m}$$

$$r_t = 0.63 \text{ m}$$

and

$$\sigma_1 = \frac{\lambda^2 \tan^4 a}{16\pi} \left[\frac{1 + \cos(2a)}{\cos(2\psi) + \cos(2a)}\right]^3$$

$$\sigma_2 = \frac{\lambda R_2 \tan^2(10^o - \psi)}{8\pi \sin\psi}$$

$$\sigma_3 = \frac{\lambda R_1}{8\pi \sin\psi}\left[\tan\ (a - \psi) - \tan(10^o - \psi)\right]^2 \quad , \text{ for } 0^o < \psi < 10^o$$

$$= \frac{\lambda R_1}{8\pi \sin\psi}\left[\tan^2(a - \psi)\right] \quad , \text{ for } 10^o < \psi < a$$

$$\sigma_4 = \frac{\lambda R_1}{8\pi |\sin\psi|}\left\{|\tan(a + \psi)| - |\tan(10^o + \psi)|\right\}^2$$

$$\sigma_5 = \frac{\lambda R_2}{8\pi |\sin\psi|}\left\{|\tan(10^o + \psi)| - |\tan\psi|\right\}^2$$

$$\sigma_6 = \frac{\lambda R_2}{8\pi |\sin\psi|}\left\{\tan^2\psi\right\} \quad , \text{ for } 10^o < \psi < a$$

$$= \frac{\lambda R_2}{8\pi |\sin\psi|}\left\{|\tan\psi| - |\tan(\psi - a)|\right\}^2 \quad , \text{ for } a < \psi < 180^o - a \quad (\psi \neq \frac{\pi}{2} \text{ or } \frac{\pi}{2} + a)$$

$$\sigma_7 = \frac{\pi}{2}\left[(.51)^2 + (.37)^2\right], \text{ for } a < \psi < 90^o$$

$$= \frac{\pi}{2}\left[(.51)^2 + (.37)^2 + (.25)^2\right] \quad , \text{ for } 90^o < \psi < 180^o$$

$$= \pi\left[(.37)^2 + (.25)^2\right] \quad , \text{ for } \psi = 180^o$$

$$\sigma_8 = \frac{\lambda R_2}{8\pi |\sin\psi|}\left\{\tan^2(a + \psi)\right\}$$

The formulas above were applied for the tanks with the nose-cone attached. In considering the cases of the tanks with the nose-cone removed, the expressions for σ_i, i = 1, 3, and 4 had to be changed and, at the aspect $\psi = 90^o - a$, the normal incidence term deleted.

The new forms of σ_3 and σ_4 are

$$\sigma_3' = \frac{\lambda R_1}{8\pi \sin\psi}\tan^2(10^o - \psi), \quad 0^o < \psi < 10^o \ ,$$

$$\sigma_4' = \frac{\lambda R_1}{8\pi \sin\psi}\tan^2(10^o + \psi), \quad \psi \neq 80^o \ ;$$

and σ_1 is replaced by:

1. The wire loop formula for the case cited in (2a) of Section G.3.1,
2. The wire loop and sphere formulas for the case cited in (2b), and
3. The wire loop and circular flat plate formulas for the case cited in (2c).

In determining the cross-section for the tanks with both warhead and hat section removed, the approach outlined above for the case cited in (2c) was employed, with the value of R_1 changed to 0.88.

G.4 METHOD 3 – CROSS-SECTION OF MODIFIED TANKS

In performing the analysis and computations for the Method 2 approach, it was observed that the base of the nose-cone shown on the drawing furnished to us of the terminal propulsion unit was larger in diameter than the maximum diameter of the Rudolph warhead. Thus, the tanks were modified slightly (the hat section was lengthened), and the computations were repeated. The warhead used in these computations is Configuration IV.

Configuration IV was chosen because it most closely resembled the nose-cone shown on the "tanks" drawing. One further modification was made in the breakdown, and that involved the breakdown of the "engine configuration." (This latter modification had no effect upon the cross-section curves obtained.)

The new breakdown, as it pertained to the front portion of the tanks, is shown in Figure G.4-1.

The computations were performed for:

1. The tanks with the warhead (Configuration IV) attached,

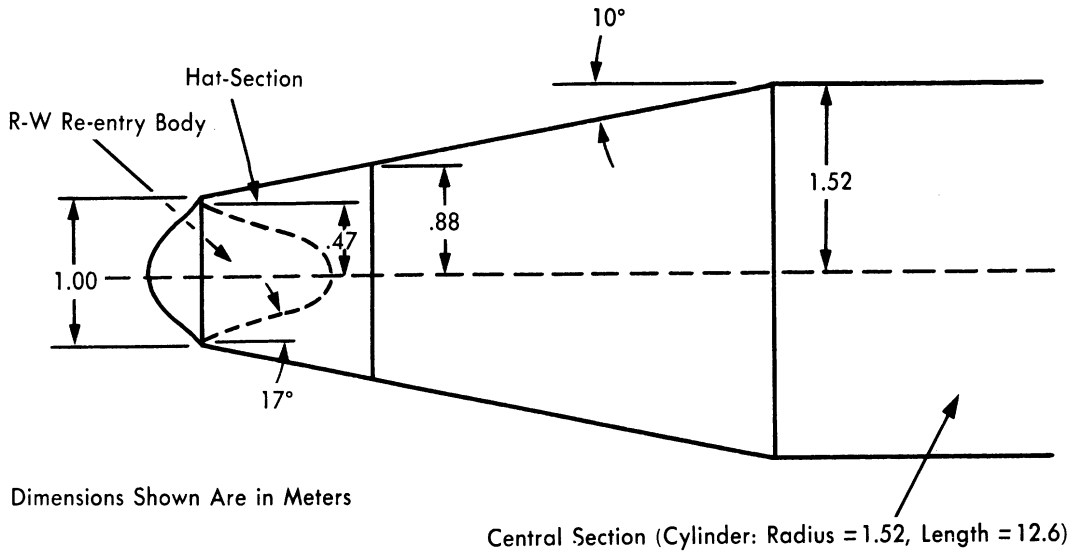

FIG. G.4-1 GEOMETRY OF THE MODIFIED TANKS USED FOR COMPUTATIONAL PURPOSES

2. The tanks with the warhead removed, the resulting "hole" being the mirror image of the rear of Configuration IV, and

3. The tanks with warhead and hat section removed.

The lengthening of the hat section led to a slightly larger value for the cross-sections for Cases 1 and 2 at $\psi = 80^{o}$. Otherwise, the only noticeable changes from the results of the Method 2 approach are in the cross-sections for $\psi = 0^{o}$.

For Case 1, the σ_1 of Section G.3.2 was replaced by the nose contribution of Configuration IV (App. A); and for Case 2, σ_1 was replaced by the wire loop formula used in Method 2 plus a contribution from the inside of the hole (estimated to be equivalent to that obtained from a sphere of radius 0.2 m, the radius of the rear hemisphere of Configuration VI). Case 3 was identical to the Case 3 of Method 2.

The results obtained are shown in Figure G.4-2.

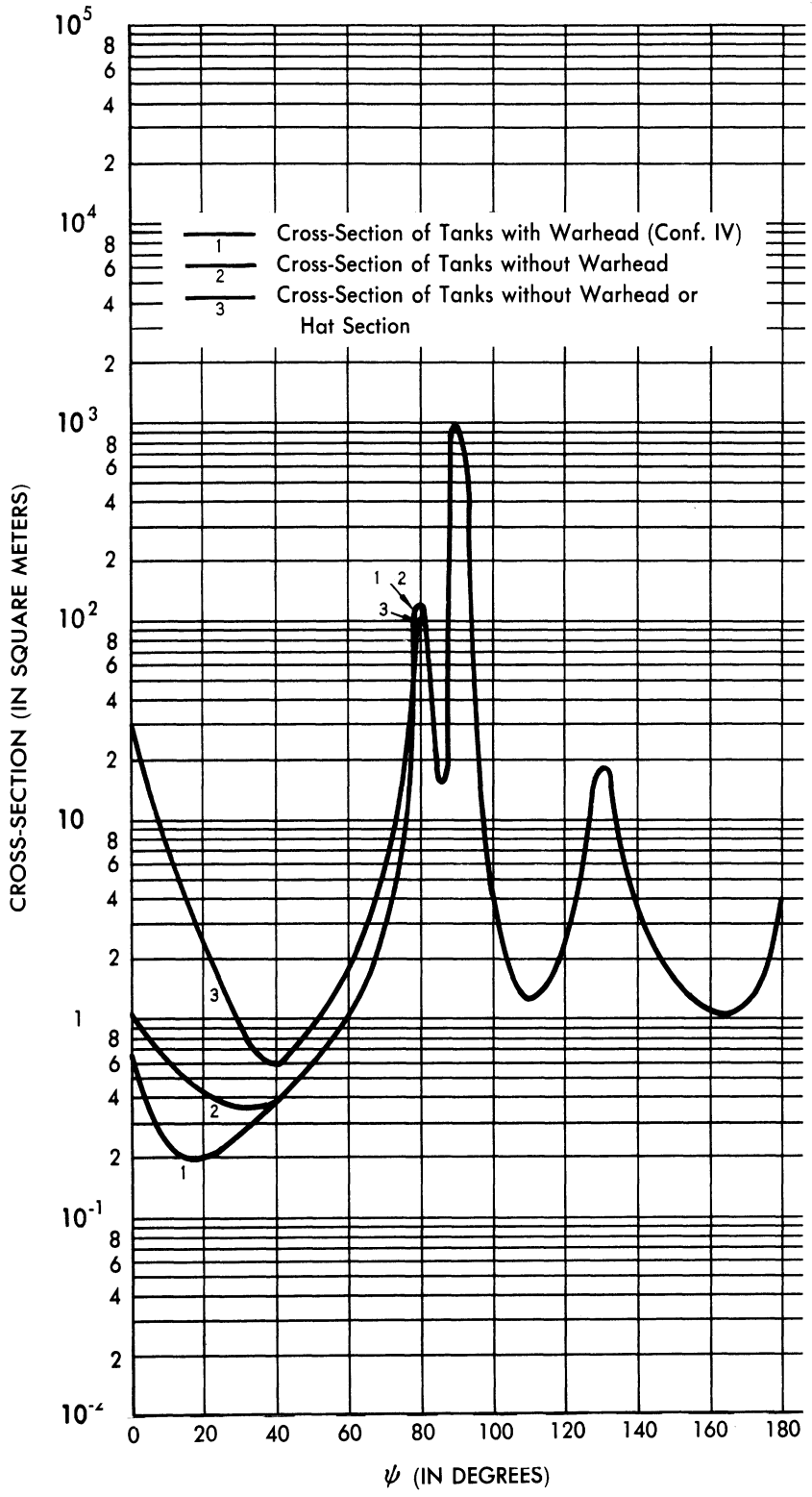

FIG. G.4-2 CROSS-SECTION OF THE TANKS AT 200 Mc (METHOD 3)

APPENDIX H

IONIZATION AND RELATED TOPICS

H. 1 INTRODUCTION

The ionization which appears about a high-speed missile as it descends through the atmosphere could be a contributor to the radar reflections from the missile. An analysis of this problem was begun in Reference 1 and the results of that analysis are summarized below. Other related investigations carried out since the publication of Reference 1 are also discussed.

H. 2 SUMMARY OF IONIZATION STUDIES REPORTED IN REFERENCE 1

This section contains a summary of the work on ionization produced by a ballistic missile performed at The University of Michigan and reported in Reference 1. This study was necessitated by the fact that, if missiles produced sufficient ionization, their radar cross-section might be significantly enhanced. Further, if they formed persistent ion trails, they might be confused with meteors in radar observation.

The work was based on the fact that, to have perfect reflection from an ion cloud, the electron density must exceed a critical value given by

$$N_c = \frac{f^2}{81} \times 10^6 \text{ electrons/cm}^3,$$

where f is the observing radar frequency, measured in Mc. Operation at 25 Mc was assumed; in practice a higher frequency would certainly be used, and thus a greater electron density would be required.

The ionization was assumed to be caused by secondary collisions, in which atmospheric particles struck by the missile rebound elastically and ionization occurs in their collisions with other atmospheric particles. The primary collisions were treated by two opposite approximations: rigid

binding, where the missile atoms may be assigned infinite mass; and no binding, in which they are taken as free. Ionization in the primary collision is energetically forbidden, and no other mechanisms were clearly established as physically significant.

The ion distribution about the missile nose is shown to resemble a hyperboloid. Supracritical density is assumed within such a contour, and the effect of the subcritical density outside, which would reduce the radar cross-section, is neglected. At other points in the computation, approximations favorable to ion production are made. A missile velocity of 10 km/sec at an altitude of 200 km was assumed. Maintenance of a contour large enough to enhance the missile's nose-on cross-section by πm^2 was shown to require a probability > 1 for ionization in a sufficiently energetic secondary collision. It was therefore concluded that the nose-on cross-section of a 10 km/sec missile at that altitude would not be enhanced by ionization.

It was further shown that the broadside cross-section would not be enhanced, since few electrons would be produced along the sides of the missile. Also, the electron density produced is too small to form a significant trail behind the missile.

Since the relative importance of the possible mechanisms for ionization is affected by altitude and speed, the fact that meteors are observed by radar reflection does not constitute an objection to the conclusions reached in Reference 1. Meteor observations by radar usually take place for meteor altitudes lower than 120 km (Ref. 32) and most meteor speeds greatly exceed the missile speeds considered. (Reference 33 contains a summary of the theoretical work done on the meteor problem.)

H. 3 SHOCK WAVES

H. 3. 1 Reflections from Shock Waves

Reflections from shock waves were also considered in Reference 1 where it was concluded that, for almost all missile cross-section problems of interest, the effects of shock fronts may be neglected.

H. 3. 2 Shape of Shock Waves During Ascent and Descent of an ICBM

It has been conjectured that the shape of the shock wave associated with an ICBM might differ on the ascending and descending portions of its trajectory. Using trajectory data given (Ref. 34) for Atlas, this section will demonstrate the validity of the conjecture.

The problem is simple for the initial portion of the ascent. Once the transonic region is traversed, a normal, attached, acute-angled shock will be present. On the basis of some photographs made at the Aberdeen ballistic range, and quoted by von Kármán (Ref. 35), it is estimated that the normal pattern is established by about Mach 2. This pattern should persist until the missile leaves the continuum regime of aerodynamics and enters the slip-flow regime. The shock will then become diffuse, gradually reaching a state in which its existence is questionable.

Using the Atlas trajectory data, the time history of the shock during the missile's ascent is determined below.

First, consider the 5500-nautical-mile trajectory data given on page II-114 of Reference 34. After about 60 seconds, the transonic region has been traversed. A reasonable criterion for the lower limit of the slip-flow regime is (Ref. 17) $M \lambda/\ell = 0.02$, where M = free-stream Mach number, λ = mean free path, and ℓ is a characteristic length of the missile. The velocity of sound and mean free path at higher altitudes are taken from a Rocket Panel paper (Ref. 22). Computation then shows this missile to enter the slip-flow regime at an altitude of about 70 km, about 160 seconds after launching. Thus, on the way up, the missile is subsonic for the first 40 seconds, transonic for the next 20 or so, and finally exhibits supersonic flow with a narrow shock for about the next 100 seconds. Starting at about that time, the shock gradually becomes diffuse and disappears.

We consider next the ascent of the midwing-configuration glide missile (p. II-119, Ref. 34) for 5500-nautical-mile range. Here the transonic region is passed about 60 seconds after launching, and this configuration never attains sufficient altitude to leave the continuum regime of aerodynamics. Thus, it retains its narrow conical shock.

The powered-flight trajectory for maximum range is given on page II-125 of Reference 34. This missile's speed exceeds Mach 2 after 60 seconds, and it leaves the continuum regime about 140 seconds after launching, at an altitude of about 80 km.

Finally, consider (p. II-127, Ref. 34) the trajectory for the 1000-nautical-mile range. Here, Mach 2 is passed after about 62 seconds, and the missile remains always in the continuum regime. Now consider the descent portions of these trajectories. For the glide missile, and the 1000-nautical-mile trajectory, unless a blunt re-entry shape gives rise to a detached shock, the shock configuration of the ascent is retained. This, however, is not true in the other two cases. For those cases, consider the possibility that a gas cap forms before the missile re-enters the continuum regime where a shock can exist. If this should happen, the shock would form around the rounded contour of the gas cap and therefore be rounded or possibly detached.

The criterion for the existence of a gas cap, formed by trapped air molecules, is (Ref. 36)

$$\frac{\lambda V}{rv} \lesssim 1,$$

where λ is the mean free path and V the thermal velocity of air constituents, v the missile velocity, and r the missile nose radius if it were spherical. Since the authors have not located the assumptions underlying the analyses of Herlofson (Ref. 39), they have not followed his work here, but have used the less recent Reference 36. Here r will be taken as 3 inches; for an order of magnitude calculation this should suffice.

For the 5500-nautical-mile powered-flight trajectory, use of the Rocket Panel data and the trajectories given by Convair indicate that the gas cap begins to form at about 110 km. The shock, however, doesn't begin to form until the missile has descended to about 60 km. Therefore, since the gas cap exists prior to the shock formation, a rounded or detached shock is to be expected.

Finally, examine the powered-flight trajectory for maximum range. The Convair trajectories do not present the portion of the flight immediately preceding re-entry, but the curves given are sufficiently similar to those for the 5500-nautical-mile range that the conclusions drawn for the latter retain qualitative validity.

H.4 WORK PERFORMED AT OTHER ESTABLISHMENTS

H.4.1 Lincoln Laboratory of the Massachusetts Institute of Technology

Reference 1 contains a list of references containing additional material on ionization and related studies. Included here is the work of the Lincoln Laboratory of the Massachusetts Institute of Technology. Their work on meteors and the ICBM is reported in Reference 37. Some of the conclusions reached to date are:

1. For the megawatt radars being contemplated for ICBM, one may expect meteor echoes at the rate of several thousand per hour. These meteor trail echoes will have a Doppler character during the trail formation, and will persist as relatively stationary target echoes for several seconds after formation. Unless the radar is specifically designed to reject meteor echoes, these can be a serious clutter and false-alarm problem.

2. On the basis of the available meteor-rate data it appears that the number of meteors seen by a radar should not increase with antenna gain but will increase with transmitter power. Hence, to get longer-range radars without increasing meteor background, one has more to gain from higher gain antennas than higher power transmitters.

3. The need for further experiments is indicated, particularly with higher-powered radars and shorter wavelengths than have been used until now. Such data are needed to establish the extent to which the meteor background is cut down by using higher frequencies and to determine the distribution of meteors corresponding to the smaller ion density trails.

4. The probability of a meteor hitting an offensive missile is negligible.

Other work performed at the Lincoln Laboratory on the ICBM problem is reported in Reference 38.

H.4.2 Poulter Laboratories of the Stanford Research Institute

Information relative to experimental work on "Extreme Velocity Pellets" performed at the Poulter Laboratories of the Stanford Research Institute has been received in personal correspondence from Dr. Poulter to one of the authors. Dr. Poulter states that much work remains to be done to develop the controls for velocity, pellet shape, etc., but that they believe the solutions of these problems are rather straight-forward and that the methods which they have employed offer a possibility of obtaining any fragment velocity that will be required in missile studies.

By using a Mach stem detonation along the axis of a comparatively small-angle concave conical detonation front (apparently one of the most effective means of collecting and concentrating energy into a very small space) and using 1.5 pounds of explosive, the Poulter Laboratories have consistently been able to photograph with the framing camera 0.2-gram pellets having velocities of approximately 12 mm/μ sec. In one case, the pellet was traveling in a lucite tube in which the air pressure was reduced to 50 microns. The luminous pellet, at the time the pictures were taken, was traveling at the tip of the jet. From the scale in the pictures and a camera speed of one frame per microsecond, a velocity of 13.2 km/sec was calculated.

In a second case the pellet was traveling in an atmosphere of helium at a pressure of one atmosphere. The luminous conical shock pulse surrounding this pellet was clearly visible in the pictures and was seen to travel 230 mm in 17μ sec, giving a velocity of 13.5 km/sec.

One picture was taken prior to firing the charge for purposes of reference, the next one was taken only a few microseconds after the detonation front struck the rear of the metal liner and before the central

portion of the center of the liner had moved perceptibly. An approximate velocity can therefore be determined for the pellet in terms of the velocity of the central portion of the liner and the distance that the center of the plate has traveled. The most conservative value that it is possible to obtain from this picture is in excess of 60 km/sec. Thus, the Poulter Laboratories feel that this offers a feasible method of obtaining extremely high-velocity pellets in the range of from 10 to more than 50 km/sec.

REFERENCES

Number	
1	K. M. Siegel, M. L. Barasch, J. W. Crispin, I. V. Schensted, W. C. Orthwein, and H. Weil, "Studies in Radar Cross-Sections XIV – Radar Cross-Section of a Ballistic Missile", The University of Michigan, Engineering Research Institute, Report No. UMM-134 (September 1954). SECRET
2	K. M. Siegel, M. L. Barasch, J. W. Crispin, R. F. Goodrich, A. H. Halpin, A. L. Maffett, W. C. Orthwein, C. E. Schensted, and C. J. Titus, "Studies in Radar Cross-Sections XVIII – Airborne Passive Measures and Countermeasures", The University of Michigan, Engineering Research Institute, Report No. 2260-29-F (January 1956). SECRET
3	K. M. Siegel and J. M. Wolf, "Studies in Radar Cross-Sections XIII – Description of a Dynamic Measurement Program", The University of Michigan, Engineering Research Institute, Report No. UMM-128 (July 1954). CONFIDENTIAL
4	W. B. Graham, "A Preliminary Discussion of Intercontinental Ballistic Missile Defense", The Rand Corporation, Report RM-1388 (January 1955). SECRET, RESTRICTED DATA
5	C. E. Schensted, J. W. Crispin, and K. M. Siegel, "Studies in Radar Cross-Sections XV – Radar Cross-Sections of B-47 and B-52 Aircraft", The University of Michigan, Engineering Research Institute, Report No. 2260-1-T (August 1954). CONFIDENTIAL
6	A. L. Maffett, M. L. Barasch, W. E. Burdick, R. F. Goodrich, W. C. Orthwein, C. E. Schensted and K. M. Siegel, "Studies in Radar Cross-Sections XVII – Complete Scattering Matrices and Circular Polarization Cross-Sections for the B-47 Aircraft at S-Band", The University of Michigan, Engineering Research Institute, Report No. 2260-6-T (June 1955). CONFIDENTIAL

REFERENCES (Cont.)

Number

7 H. Weil, R. R. Bonkowski, T. A. Kaplan, and M. Leichter, "Studies in Radar Cross-Sections XVI – Microwave Reflection Characteristics of Buildings", The University of Michigan, Engineering Research Institute, Report No. 2255-12-T (May 1955). SECRET

8 W. H. Emerson, A. G. Sands, and M. V. McDowell, "Development of Broadband Absorbing Materials For Frequencies as Low as 500 Mc", Naval Research Laboratory, Report No. 300 (May 1954). UNCLASSIFIED

9 D. E. Kerr, Propagation of Short Radio Waves, McGraw-Hill (1951).

10 K. M. Siegel, B. H. Gere, I. Marx, and F. B. Sleator, "Studies in Radar Cross-Sections XI – The Numerical Determination of the Radar Cross-Section of a Prolate Spheroid", The University of Michigan, Engineering Research Institute, Report No. UMM-126 (December 1953). UNCLASSIFIED

11 W. Franz and K. Deppermann, "Theory of Diffraction by a Cylinder as Affected by the Surface Wave", Annalen der Physik, 10, 361 (1952).

12 "The Equivalent Echoing Area of a Rocket Missile Near Head-on Aspect", Radar Research and Development Establishment, RRDE Report 370 (August 1952). CONFIDENTIAL

13 "Radar System Analysis – Comparative Performance Study of Pulse, F-M, and Doppler C-W Techniques for Ground Based Long-Range Search and MTI Radar Systems", Sperry Gyroscope Company, Sperry Report No. 5223-1109 (June 1948). SECRET

14 C. J. Sletten, "Electromagnetic Scattering From Wedges and Cones", Air Force Cambridge Research Center, Report CRC-E-5090 (July 1952). UNCLASSIFIED

REFERENCES (Cont.)

Number

15 "Determination of Echoing Area Characteristics of Various Objects", The Ohio State University Research Foundation, Report 302-7 (October 1947). CONFIDENTIAL

16 "Fifth Quarterly Progress Report on Development of Chaff Material – 10 July to 10 October 1955", The University of Michigan, Engineering Research Institute, Report No. 2273-9-P. SECRET

17 K. M. Siegel, "Boundaries of Fluid Mechanics", Journal of Aeronautical Sciences, 17, 191 (1950).

18 J. Stratton, Electromagnetic Theory, McGraw-Hill (1941).

19 J. V. Nehemias, "Use of Computers in Determining Time-Dependence of Fission Product Distribution", Nuclear Energy Conference in Geneva (1955).

20 D. H. Menzel, Fundamental Formulas of Physics, Prentice-Hall (1955).

21 C. M. Davisson and R. D. Evans, "Gamma Ray Absorption Coefficients", Reviews of Modern Physics, 24, 79 (1952).

22 "Pressures, Densities, and Temperatures in the Upper Atmosphere", The Rocket Panel, Physical Review, 88, 1027 (1952).

23 K. M. Siegel, "Radar Cross-Section of Aircraft", to be presented 1 March 1956 at the Naval Research Laboratory at a symposium on Radar Detection Theory. CONFIDENTIAL

24 "Quarterly Progress Report – Polarization Dependence of Radar Echoes, Contract AF-30(635)-2811, Period Ending 31 March 1955", The Ohio State University Research Foundation, Antenna Laboratory, Report No. 612-2 (16 March 1955). UNCLASSIFIED

REFERENCES (Cont.)

Number

25 K. M. Siegel, "Studies in Radar Cross-Sections V – An Examination of Bistatic Early Warning Radars", The University of Michigan, Engineering Research Institute, Report No. UMM-98 (19 August 1952). SECRET

26 E. A. Sloane, E. S. Candidus, J. Salerno, M. Skolnik, "A Bistatic CW Radar", Massachusetts Institute of Technology, Lincoln Laboratory, Technical Report No. 82 (6 June 1955). SECRET

27 B. L. Lewis, "Radar Characteristics of Jet Exhaust Gases", Tracking Branch, Radar Division, Naval Research Laboratory, Report 4438 (2 December 1954). SECRET

28 J. L. Lawson and G. E. Uhlenbeck, Threshold Signals, McGraw-Hill (1950).

29 W. B. Davenport, Jr., R. A. Johnson, and D. Middleton, "Statistical Errors in Measurements on Random Time Functions", Journal of Applied Physics, Vol. 23, No. 4, 377 (April 1952).

30 E. Jahnke and F. Emde, Tables of Functions, Dover (1945).

31 James, Nichols, and Phillips, Theory of Servomechanisms, Radiation Laboratory Series, Volume 25, McGraw-Hill Book Company, Inc.

32 "Thumper Project: The Meteor Problem (In connection with High Altitude, High-Velocity, Anti-Missile Research)", General Electric Company, Report No. TR-55038 (April 1947). CONFIDENTIAL

33 T. R. Kaiser, "Radio Echo Studies of Meteor Ionization", Advances in Physics, Vol. 2, No. 8, 495 (October 1953).

REFERENCES (Cont.)

Number

34 "Summary Report ZM-7-011, Project Atlas", Consolidated Vultee Aircraft Corporation (January 1952). SECRET

35 T. von Kármán, "Supersonic Aerodynamics – Principles and Applications", Journal of Aeronautical Sciences, 14, 373 (1947).

36 F. A. Lindemann and G. M. B. Dobson, "A Theory of Meteors and the Density and Temperature of the Outer Atmosphere to Which it Leads", Proceedings of the Royal Society, 102, 411 (1923).

37 D. L. Falkoff, "Meteors and Intercontinental Ballistic Missiles", Massachusetts Institute of Technology, Lincoln Laboratory, Group Report No. 23.10 (4 February 1954). SECRET

38 D. L. Falkoff, E. C. Lerner, "Intercontinental Ballistic Missiles", Massachusetts Institute of Technology, Lincoln Laboratory, Group Report No. 23.2 (28 December 1953). SECRET

39 N. Herlofson, Physical Society Report on Progress in Physics, 11, 44 (1948).

40 K. M. Siegel, H. A. Alperin, R. R. Bonkowski, J. W. Crispin, A. L. Maffett, C. E. Schensted, and I. V. Schensted, "Bistatic Radar Cross-Sections of Surfaces of Revolution", Journal of Applied Physics, 26, 297 (1955).

DISTRIBUTION

To be distributed in accordance
with the terms of the contract.

Confidential